Dissertation

submitted to the

Combined Faculty of Natural Sciences and Mathematics

of Heidelberg University, Germany

for the degree of

Doctor of Natural Sciences

Put forward by

M.Sc. Johannes Wolfram Blumberg

born in: Karlsruhe

Oral examination: 17$^{\text{th}}$ of October 2023

Leveraging elasticity theory to calculate cell forces:

From analytical insights to machine learning

Referees: Prof. Dr. Ulrich Schwarz

Prof. Dr. Tristan Bereau

Zusammenfassung

Lebende Zellen sind in der Lage, mechanische Einflüsse ihrer Umgebung wahrzunehmen und auf diese zu reagieren. In der Zellkraftmikroskopie wird die Zughaftung von Zellen auf elastischen Substraten anhand der Substratverformung sichtbar gemacht, die durch die Bewegung von eingebetteten Markierungskügelchen gemessen wird. Werden Substrate mit Hilfe der Elastizitätstheorie beschrieben, können wir die Adhäsionskräfte berechnen und so unser Verständnis der Zellfunktionen und des Zellverhaltens vertiefen. In dieser Dissertation kombiniere ich analytische Lösungen mit numerischen Methoden und Techniken des maschinellen Lernens, um die Vorhersage der Zugspannung in einer Reihe von experimentellen Anwendungen zu verbessern. Ich beschreibe, wie die normale Zugkraftkomponente in regularisierungsbasierte Fourier-Ansätze einbezogen werden kann, die ich auf experimentelle Daten anwende. Ich vergleiche die vorherrschenden Strategien zur Kraftrekonstruktion, die direkte Methode und inverse, regularisierungsbasierte Ansätze, und lege dar, dass letztere präziser und erstere resistenter gegenüber Rauscheffekten sind. Ich demonstriere, wie eine punktkraftbasierte Rekonstruktion verwendet werden kann, um die Entwicklung des Kräftegleichgewichts als Reaktion auf das Ziehen mit Mikronadeln zu untersuchen, wobei ein Übergang von einer dipolaren zu einer monopolaren Kraftanordnung zu erkennen ist. Schließlich lege ich da, wie ein konditionales, invertierbares neuronales Netzwerk nicht nur adhäsive Bereiche lokalisierter rekonstruiert, sondern auch räumliche Korrelationen und Variationen in der Zuverlässigkeit von Traktionsrekonstruktionen aufzeigt.

Abstract

Living cells possess capabilities to detect and respond to mechanical features of their surroundings. In traction force microscopy, the traction of cells on an elastic substrate is made visible by observing substrate deformation as measured by the movement of embedded marker beads. Describing the substrates by means of elasticity theory, we can calculate the adhesive forces, improving our understanding of cellular function and behavior. In this dissertation, I combine analytical solutions with numerical methods and machine learning techniques to improve traction prediction in a range of experimental applications. I describe how to include the normal traction component in regularization-based Fourier approaches, which I apply to experimental data. I compare the dominant strategies for traction reconstruction, the direct method and inverse, regularization-based approaches and find, that the latter are more precise while the former is more stress resilient to noise. I find that a point-force based reconstruction can be used to study the force balance evolution in response to microneedle pulling showing a transition from a dipolar into a monopolar force arrangement. Finally, I show how a conditional invertible neural network not only reconstructs adhesive areas more localized, but also reveals spatial correlations and variations in reliability of traction reconstructions.

Contents

List of Figures

Acronyms

AdNFM adaptive near field method.

ADP adenosine diphosphate.

AFM atomic force microscopy.

ATP adenosine triphosphate.

BEM boundary element method.

cINN conditional invertible neural network.

CLSM confocal laser scanning microscopy.

CME clathrin-mediated endocytosis.

DM direct method.

ECM extracellular matrix.

FEM finite element method.

FFD free form deformation.

FTTC Fourier transform traction cytometry.

GCV generalized cross-validation.

GDP guanosine diphosphate.

GTP guanosine triphosphate.

hiPSC human induced pluripotent stem cell derived cardiomyocytes.

IF intermediate filaments.

IM inverse method.

KLP Kanade-Lucas-Tomasi optical flow algorithm.

LSFM light sheet fluorescence microscopy.

ML machine learning.

MTOC microtubule-organizing center.

NM II non-muscle myosin II.

NN neural network.

PAA polyacrylamide.

PDMS polydimethylsiloxane.

PIV particle image velocimetry.

ReLU rectified linear unit.

SF stress fibers.

SGD stochastic gradient descent.

SIM structured illumination microscopy.

SSD sum of squared distances.

STED stimulated emission depletion.

TFM traction force microscopy.

TIRF total internal reflection fluorescence.

TRFP traction reconstruction with point forces.

Chapter 1

Introduction

The ability to create setups where the transfer of energy, material and information occurs in a regulated and thermal equilibrium evading fashion is one of the principal aspects of live [1]. Biological research has revealed a wide range of chemical aspects to these processes. However, as cells exist in a universe governed by the principles of physics, the mechanical aspects of cellular interactions with their surrounding cannot be neglected. Together with external applied forces, cells generate forces to modulate their various actions, which not only include adhesion and migration but also differentiation and immune functions [2, 3]. Research in the last decades has even revealed that mechanical forces may affect biochemical activity directly, a process known as mechanotransduction [4].

Given the substantial role of mechanics in understanding cellular behavior, the ability to observe cell forces has become an essential ingredient in the research of biological systems. Atomic force microscopy (AFM) [5], bio-membrane force probes [6], magnetic and optical tweezers [7] and traction force microscopy (TFM) [8] are only some of the techniques devised.

One of the earliest attempts to attribute cellular forces with an observable quantity was made by Harris *et al.* [9]: Using a thin silicon rubber as a substrate, they observed fibroblasts to create elastic wrinkles in the silicon layer when crawling. This showed that the cells had used the substrate-cell interactions to exchange traction forces in order to propel themselves forward. Some estimates could be made in terms of traction magnitude by comparing the winkling to the one caused by a microneedle. Unfortunately, this process overall could only be used as a qualitative measure, as the surface wrinkling is a nonlinear and complex process, making it difficult to accurately estimate forces.

A more quantitative method, traction force microscopy (TFM) was devised by Dembo and Wang [8, 10] to measure the forces exerted by fibroblast cells on their substrate during cell migration. Using a substrate of polyacrylamide gel with embedded fluorescent beads, they could observe the deformation of the substrate in response to cellular forces during the locomotion of fibroblast. By segmenting the cell into a mesh of bi-linear shape functions, they were able to obtain a traction map of the cell. This technique forms the basis of traction force microscopy (TFM) in the modern sense. Since then, while the basic technique has remained constant, a variety of more advanced variations of their principle technique have been devised, each improving upon different aspects of the overall procedure.

Early on, improvements were made focusing on variations in the way the deforma-

tion field is modeled: Schwarz *et al.* [11] used vinculin staining to detect individual adhesion sites, modeled them as point forces and used the far field deformation to assign a force vector to each of them. Butler *et al.* [12] introduced a Fourier space description to predict traction distribution in more detail, which has since become the standard approach for reconstructing traction forces on planar substrates. Other efforts focused on including more information into the procedure by looking into traction forces together with modeling intracellular force generation [13] or focused on how exactly to select a good reconstruction [14]. Finally, it was explored how the overall setup could be made more flexible by the investigating inclusion of normal force [15–17], thin substrates [18] and the setups with non-planar interfaces between the cell and a fibrous environment [19–22]. Most recently, improvements have been made using data driven approaches for cell force reconstruction [23–26].

Nowadays, the term traction force microscopy describes not a single method, but encompasses a range of techniques. All of these have certain things in common: They observe deformations in a mechanically well understood material, the substrate, in mechanical contact with the to be observed cell or biological material by using non-invasive optical imaging. In most cases, fluorescent markers are employed to improve deformation registration abilities [3].

In this dissertation, I will focus on how to further refine and link up some of the approaches in TFM mentioned. First, I will use some analytical calculations that will give us a deep understanding about the force-deformation relationship in elastic substrates. Using this information, I will show how the present techniques for TFM that also consider a normal force component can be described more elegantly when compared to previous approaches. I will then move on to show how these extended techniques can be deployed in practice to study clathrin-mediated endocytosis of nanoparticles at the cellular ventral side.

After that, I will introduce the direct method for TFM. This technique involves calculating the strain and stress tensors directly from the displacement data and in principle is very flexible with respect to the underlying substrate geometry and its elastic properties. I then compare it to the normal-force including technique introduced in the prior chapter. Through this comparison, I aim to establish a relationship between these two techniques and analyze their respective capabilities in handling displacement data noise. By exploring the performance of these techniques and their response to varying levels of noise, we can gain insights into their strengths and limitations and are able to compare the performance of both traditional planar methods and the methods commonly used in three-dimensional variants of TFM.

In the next part of my study, I will highlight some of the fundamental limitations Fourier-based methods are facing when cells are put under the influence of external forces. I will present a variation of the point force method that avoids many of the difficulties faced in the original approach by making use of the extensive insight previously gained into the force-deformation relation in substrates. By combining this technique with microneedle shearing at the apical cell surface, I will then use this technique to quantify intracellular force transmission. Together with my experimental collaborators, I will then study the response of cells to known shear forces exerted with a calibrated microneedle.

Finally, I investigate recent neural-network based techniques and describe a new fully probabilistic approach, trained on simulated data. This will not only improve upon the preexisting analytical methods for traction force reconstruction, but also

investigate the variability of the obtained solution revealing insight into the effects of inhomogeneities and noise on the reconstruction.

1.1 Force generation in biological cells

1.1.1 Cytoskeletal structures

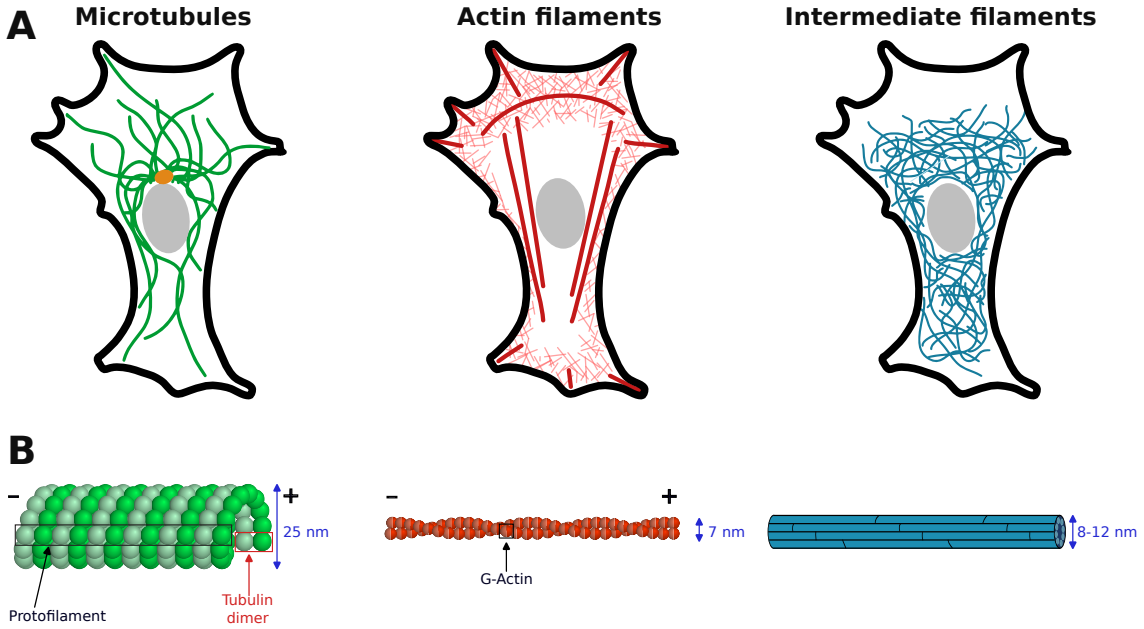

Figure 1.1: The three different components of the cytoskeleton. (A) Schematic drawing of to the distribution of the three different cytoskeleton networks within the cell. The microtubules (green) form rigid structures originating in the *centromere* (yellow) which is located close to the nucleus. The actin filaments form both linear bundles (stress fibers) as well as networking structures concentrated in the nuclear *cortex*. Intermediate filaments may serve different roles, but some types span the cytoplasm, giving the entire cell mechanical stiffness [27]. (B) At the molecular level, microtubules are hollow cylinders formed from tubulin dimers. Actin filaments display a helical shape formed from actin subunits. Both microtubules and actin filaments are polar and formed from globular subunits. In contrast, intermediate filaments are non-polar and are formed from filamentous subunits. — A is replicated from [27], B is modeled after [28] and [29] with modifications.

Cells must be able to achieve a wide range of mechanical objectives. They must be able to obtain a desired shape and put up a stiff response against indentation and maintain their internal structure, but they must also be able to change their shape and relocate themselves and their internal structure if needed. In order to do so, cells employ multiple active and continuously reconfiguring protein filament networks. These are collectively known as the cytoskeleton [28]. There are three main types of protein filaments in the cytoskeleton: Microtubules, actin filaments, and intermediate filaments. Each of them has unique mechanical and functional properties that allow it to carry out specific tasks within the cell. It is the combination of the different filament types that enables the cell to achieve their specific objectives. In Fig 1.1, I compare the three filament structures.

All three network types are polymers that can be described by the worm-like chain model and as such their mechanical properties can be described by their persistence

length l_p [30]. This length describes the correlation between the tangential vectors, $\boldsymbol{t}(s_1)$ and $\boldsymbol{t}(s_2)$, at two different points, s_1 and s_2, on the polymer parameterized by the polymer's arc length [31]:

$$< \boldsymbol{t}(s_2) \cdot \boldsymbol{t}(s_1) >= \exp\left(-\frac{|s_2 - s_1|}{l_p}\right). \tag{1.1}$$

The persistence length determines the length scale in which the polymer appears more or less rigid.

Microtubules

Microtubules form by a spiraling polymerization of tubulin dimers as seen in Fig 1.1, left column. This creates a pipe shaped structure with a diameter of 25 nm and a persistence length of over 1 mm. This makes them the largest and strongest of the three filaments. As such, they play a primary role in maintaining the cells shape and internal organization. However, they are also involved in the process of cell division and intracellular transport processes.

Tubulin dimers form from two monomers known as α- and β-tubulin. As all dimers are incorporated with the same orientation, the two ends of the microtubule differ, the α-tubulin faces towards the so-called minus-end, the β-tubulin towards the so called plus-end. The microtubule constantly grows and shrinks by polymerization and depolymerization of dimers at both ends of the polymer tube [28]. The net addition rate is controlled by guanosine triphosphate (GTP) and guanosine diphosphate (GDP), both of which can bind to β-tubulin. The energy rich GTP facilitates the incorporation of new monomers into the microtubule, while GDP increases the unbinding rate. Dimers typically bind only if they carry GTP, however, this quickly hydrolyzes into GDP upon incorporation into the microtubule. This creates a dynamical instability: As long as the ratio of GTP-carrying dimers is high, microtubule growth outpaces the hydrolysis front. However, if the dimer addition rate decreases due to GTP depletion in the dimer pool, the hydrolysis front may reach the end of the microtubule and the filament subsequently starts to break up. As addition of dimers at the plus end is generally faster than on the minus end, the critical concentration is lower for the plus end than for the minus end. More details can be found in literature [32].

In most cases, only the plus end of a microtubule is free and grows. Its minus end is bounded to a protein complex known as microtubule-organizing center (MTOC). This binding prevents the microtubule disassembly at the minus end. Animal cells typically have one single MTOC known as the centrosome located in proximity of their nucleus from which microtubules grow radially in all directions ascertaining a certain cell shape. Other kinds of MTOCs are also known. A detailed overview over microtubule organization can be found in literature [33].

Microtubules provide a structure for accessory proteins to attach to. For example, motor proteins like kinesin can perform locomotion along microtubules. By doing so, they actively transport molecules along the microtubules which thus serve as track ways for intracellular transport. Other accessory proteins cross-link between microtubules as well as create relative traction. More details on accessory proteins can be found in literature [34].

Actin filaments

Actin filaments, also known as microfilaments, are polar actin polymers build in a right-handed double-helix structure, as show in Fig 1.1, center column. This form of actin is also known as filamentous actin (F-actin). They have a diameter of 8 nm and a persistence length in the range of 10 µm [35]. This makes them the smallest and most flexible kind of cytoskeleton filaments. As such, they are primarily involved in cell motility, but they do also provide mechanical support.

The actin monomer, known as globular actin (G-actin), is non-symmetric, resulting in the actin filaments having a so-called barbed (+) and pointed (-) ends. Monomers predominantly attach to the barbed end [28]. Actin filament growth is controlled by adenosine triphosphate (ATP) concentration with monomers typically carrying ATP which enhances binding affinity but hydrolyses into to adenosine diphosphate (ADP) upon integration of the actin monomer into the polymer chain. ADP carrying actin monomers show a higher unbinding rate [36]. Under normal physiological conditions the actin concentration is such that the unbinding rate is lower than the binding rate on the barbed end, with the reverse being true at the pointed end. This results in a net growth at the barbed and a net shrinkage at the pointed end. This results in a process known as treadmilling and results in the filament's center of mass traversing the cell, without much movement of the individual monomers, while the overall length of the filament at any given time remains constant. This process makes the actin filament structure highly adaptive without compromising rigidity or plasticity at the same time [37].

Actin filaments are dispersed throughout the cell, but are most highly concentrated just beneath the cell membrane. Actin filaments can cluster together to form a variety of either one-dimensional linear bundles, two-dimensional networks or three-dimensional hydrogels [28]. Actin bundles can further be classified into parallel and antiparallel bundles. A typical example for actin bundles are stress fibers (SF). These structures comprise between 10 and 30 actin filaments arranged in an antiparallel fashion, crosslinked by both passive crosslinkers like α-actinin and active myosin II crosslinkers. This allows stress fibers to generate contractile forces between anchoring points. The mechanism behind myosin II crosslinkers will be explained in the subsequent section. Filopodia are a typical example for parallel actin bundles. They are dense spike-like protrusions mostly located at the leading edge of the cell, the edge facing the direction the cell is moving towards to, and consist of actin filaments connected by fascin and formin. Filopodia play an important role in migrating cells [38], but they can also appear during the spreading of thrombocytes [39].

Network-like structures can be classified into cross-linked networks like the actin cortex and branched networks like the lamellipodium. The actin cortex is connected to the inner cell membrane by membrane-anchoring proteins. Similar to stress fibers, it contains passive and active cross-linking proteins, such as α-actinin and myosin II. This particular design enables the cell to tightly control its cell shape in order to resist mechanical disturbances and change shape during cell migration and division. The branched actin network known as the lamellipodium is located at the leading edge of the cell and uses actin polymerization at the leaves of the actin network to propel the cell envelope forward [28].

Intermediate filaments

Intermediate filaments (IF) have properties in between those of actin filaments and microtubules. They are a diverse group, made up of different kinds of filament forming proteins. IF include filaments made of various keratins, neurofilaments and vimentin-like filaments. IF often show unique mechanical properties, which include high tensile strength and resistance to compression. IF are built up of α helical monomers that group into coiled coil dimers. These dimers then stack together slightly asymmetrically to form a tetramer. Eight of these tetramers form the threads of a single intermediate filament building block. The distribution and structure of an IF is presented in Fig 1.1, right column. In contrast to the other cytoskeleton components, they do not undergo treadmilling or dynamic instability and hence show much less dynamic reconfiguration, making them a more passive component of the cytoskeleton with slower dynamics [40].

1.1.2 The actomyosin complex

Cell-generated forces are largely driven by the interaction between the actin filaments and myosin motors, a structure known collectively as the actomyosin complex [41].

Myosin motors are formed by a protein known as myosin II, which is shown in Fig 1.2. A single myosin II molecule is composed of two heavy chains, around 2000 amino acids long domains. These are intertwined to form a coiled-coil of two connected α-helices. Each heavy chain has one open end, known as C-terminus and one other end where it is connected to two light chains (hence four light chains in total). Each light chain ends in a globular head domain, known as the motor head domain. The end where the motor head is located is also known as the N-terminus [28].

Myosin motors can bind to actin filaments with their motor heads and can generate forces through a sequence of conformational changes known as the *cross-bridging cycle*. This process involves the binding of an ATP to the myosin motor head domain, which triggers changes in the conformation of the motor head. These changes cause the motor head to dissociate from the actin filament and changes the relative angle between the motor head and the rest of the myosin molecule. The subsequent hydrolysis of ATP to ADP and phosphate causes a reassociation between the motor head and the actin filament. The subsequent release of both ADP and phosphate provokes a conformational change during which the myosin is regaining its original configuration. This is known as *power stroke* and releases mechanical energy leading to the generation of force and movement along the actin filament. The whole process is visualized in Fig 1.2.

1.1.3 Cell adhesions

In normal biological circumstances, cells anchor themselves in their environment using the so-called extracellular matrix (ECM) or by linking themselves to neighboring cells [28]. The ECM is mainly composed of two classes of macromolecules, proteoglycans and fibrous proteins. The dominant fibrous protein is collagen which may constitute up to 30% of the total protein mass of a multicellular animal. Other fibrous proteins include elastins, fibronectins, and laminins. Together, they are the main structural elements, providing tensile strength, regulating cell adhesion, and directing tissue development. In contrast, proteoglycans fill most of the extracellular space within the tissue in the form of a hydrated gel and show a wide variety of hydration, binding, and force-resistance properties [44]. The ECM is primarily produced and maintained by fibroblasts, the most common cell type found in connective tissue [28]. Physical

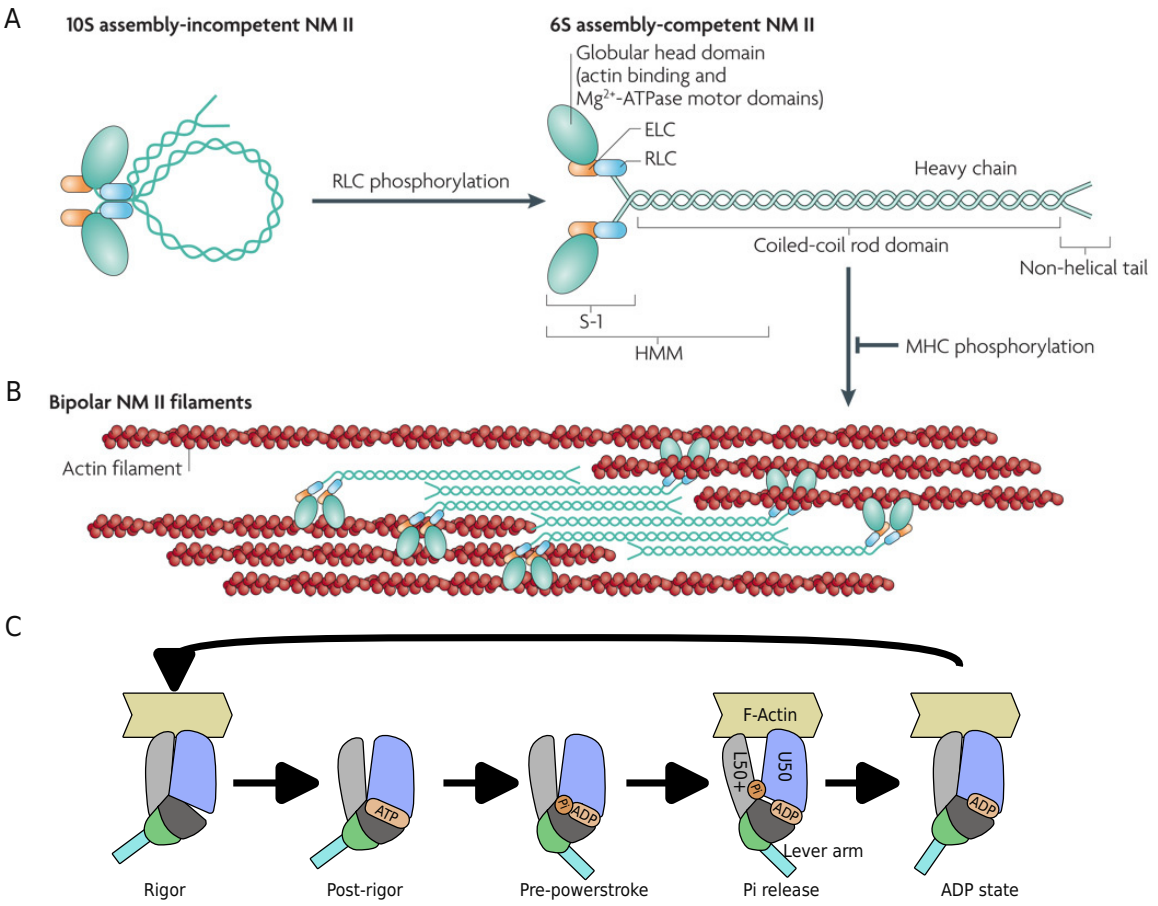

Figure 1.2: Structure and function of non-muscle myosin II (NM II). (A) Structure of NM II with its subunit and domain organization. NM II consists of two heavy chains that form a dimer by interacting with each other through α-helical coiled-coil rod domains. The globular head domain contains actin-binding regions and enzymatic motor domains. The essential light chains (ELCs) and regulatory light chains (RLCs) connect the head and rod domains. Together they form the S-1 fragment. In the absence of RLC phosphorylation, NM II adopts a compact, ring-like form (10S) through head-to-tail interactions, which is incapable of associating with other NM II dimers. However, when the RLCs are phosphorylated, the 10S structure unfolds, transforming into an assembly-competent form (6S). (B) NM II bind to actin filaments using their motor domain and link up using their motor domain. By means of the cross-bridging cycle they can cause a confocal change to the actin configuration. (C) Visualization of the cross-bridging cycle. The dissolution of ATP into ADP and phosphate cause the motor head to move forward along the actin filament. — A and B are replicated from [41], C is adapted and modified from [42].

connections between the ECM and cells are known as cell-matrix connection. Both actin filaments as well as intermediate filaments can be linked to the matrix in this fashion. At least four different types of these have been established in fibroblasts: Focal complexes, focal adhesions, fibrillar adhesions, and 3D-matrix adhesions [43]. These structures differ in the protein complexes they consist of as visualized in Fig 1.3.

In experiments, cells are often cultivated on top of 2D ECM-coated substrates.

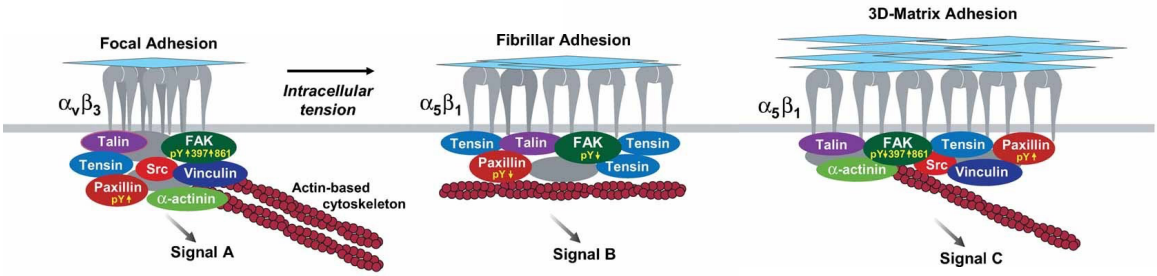

Figure 1.3: Schematic drawing of the different kinds of cell adhesion, focal adhesions, fibrillar adhesions, and 3D-matrix adhesions. All three types of adhesions recruit different protein components which causes each of them to show different kinds of behavior. — Adapted and modified from [43]

When fibroblasts are observed in this kind of setup the first kind of adhesive structure observed starting from the leading edge, close to the lamellipodium are the focal complexes. These are small dot-like adhesions that provide initial attachment at the newly covered area and have a typical diameter of around 100 nm. Focal complexes may stabilize and subsequently turn into focal adhesions. This kind of cell-matrix adhesion has a typical contact area of a few square micrometers and are usually connected to stress fibers which causes them to obtain an elongated shape. Physiologically, they have been observed in blood vessels next to high fluid shear stresses. Focal adhesion may further develop into fibrillar adhesions which are commonly found near the cell center [45]. Fibroblasts in physiological 3D setups also show the 4th type of cell-matrix adhesion, known as 3D-matrix adhesions that display enhanced cell biological activities and a reduced integrin use [46].

Cells can also connect directly to neighboring cells using intercellular connections without the need for ECM mediation [43]. Anchoring cell-cell junctions that link to actin filaments are known as adherence junctions, while those that have intermediate filaments as their intercellular cytoskeletal attachment are known as desmosome. A detailed description can be found e.g., in Alberts *et al.* [28].

1.2 Quantifying contractility in cells using traction force microscopy

1.2.1 Traction force microscopy

Traction force microscopy (TFM) represents the most widely used technique for measuring cell forces [47]. One of the principal strengths of this method is its applicability over multiple length scales: The method is able to generate continuous qualitative traction maps that can be used to describe forces from the low micrometer regime of individual cells (e.g. [8]) up to the range of tissue monolayers (e.g. [48]). Another advantage is, that it requires only minor modifications to the growth of the existing tissue culture.

Like mentioned above, cells adhere to sufficiently prepared hydrogel substrate in a fashion that mimics natural cell adhesion to the ECM or neighboring cells. Typical substrate materials used are polyacrylamide (PAA) or polydimethylsiloxane (PDMS), which can be tuned to obtain for a wide range of stiffness. TFM commonly relies on fluorescent beads, embedded during preparation or attached to the substrates surface.

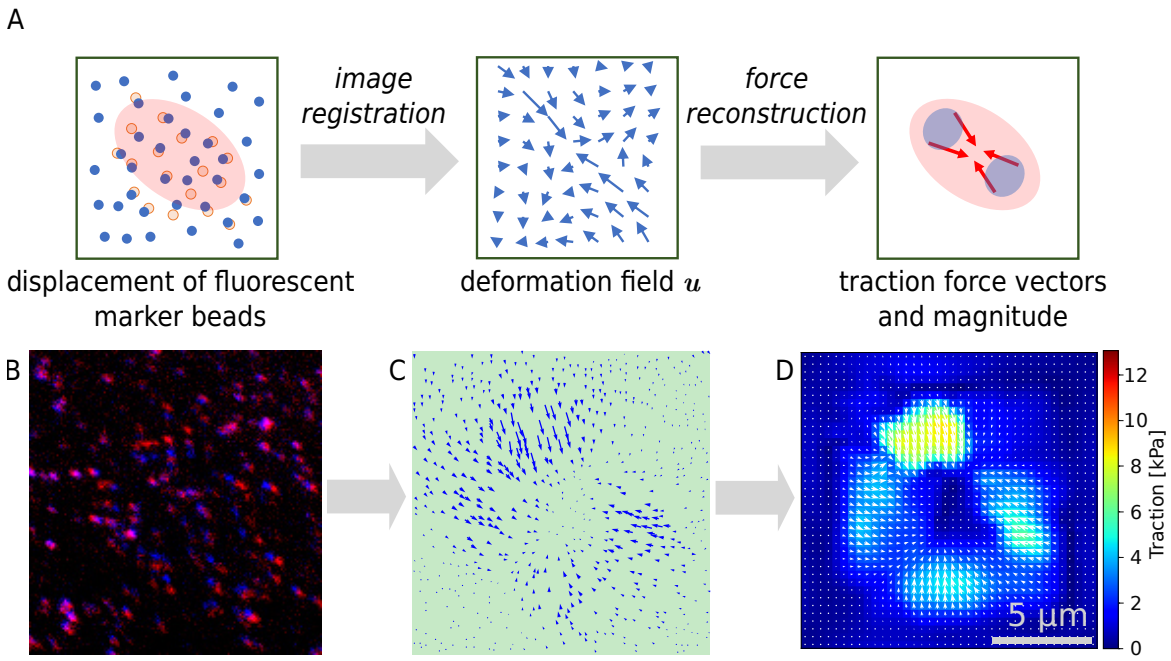

Figure 1.4: Main steps in TFM. (A) The reconstruction of cell forces is commonly separated into two individual tasks. In a first step, an image registration algorithm is used to track the movement of the different fluorescent beads and reconstruct a deformation field. Then, using methods from continuum mechanics, the deformation field is used to reconstruct a traction field. (B) Overlay of the fluorescent images showing bead configurations in the relaxed and loaded state: Red describes the reference configuration, blue describes the deformation vectors. (C) reconstructed deformation field using a Kanade-Lucas-Tomasi (KLT) optical flow algorithm (D) Reconstructed traction field using FTTC. — Experimental data presented in manuscript 4.

These then serve as fiducial markers for optical tracking in space and time [49]. A TFM experiment typically consists of at least two distinct image acquisition phases: During the first phase, the bead configuration is measured in a loaded state, when the cell is exerting contractile tension onto the substrate material. This phase may consist of a single recording or a sequence of recordings to compare the contractility of the cell at different moments (e.g. [50]). Then the cells attachment to the substrate needs to be severed to also observe the substrate in its stress-free reference configuration. Usually, the cell is removed from the substrate by enzymatic means. In particular, trypsin is commonly employed [51]. More recently a light induced release mechanism has been introduced that enables a selective detachment of cell using controlled doses of UV light. This technique, which I personally contributed to, is known as local UV illumination traction force microscopy (LUVI-TFM) and is described in manuscript 2.

Care must be taken to ensure that not only the cell itself but also the neighboring substrate area is in the field of view during the first step of image acquisition, such that the deformation decays to zero when approaching the image boundary [52]. This is because stress calculations close to the image edge become less reliable and may result in artifacts, but is also highly beneficial in properly aligning the two images in subsequent steps.

After cell detachment a second recording is made that then describes the stress-free reference configuration. The reconstruction of traction forces generally is conducted as a sequence of two subsequent steps as visualized in Fig 1.4: In a first step, the bead

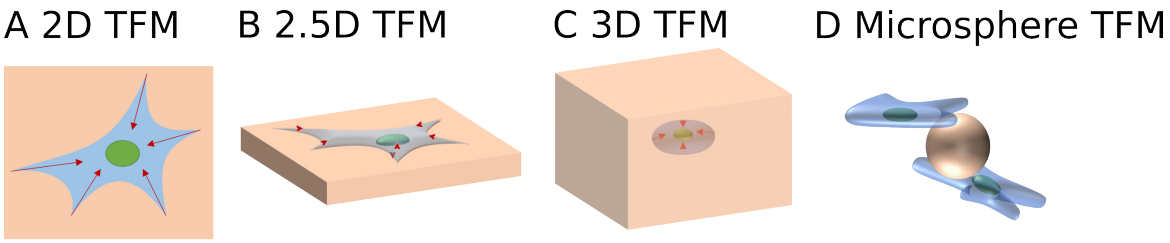

Figure 1.5: Different dimensional variants in TFM (A) Two-dimensional TFM considers traction forces as a purely planar problem only focusing on tangential tractions and deformations within the substrate. (B) 2.5D TFM maintains the planar setup of the cell sitting on top of a substrate but extends the image registration and force reconstruction by a third dimension considering the three-dimensional force generation of cells. (C) 3D TFM abandons the planar substrate entirely and observes the forces acting on cells embedded in a 3D environment closely mimicking the ECM. (D) Micro-sphere TFM observes the forces on spherical force sensors making the method more suitable for organoid and *in vivo* observations.

configuration in the reference configuration is compared to the one in the loaded state and by means of image processing techniques and a deformation field is obtained. I will describe the different approaches for this in section 1.2.3. Then, in a second step, the actual traction field is reconstructed. It is this second task on which I predominantly focused in this work and a brief introduction is given in 1.2.4.

A wide range of variations has been introduced. One common variation is to selectively designate adhesive and non-adhesive regions on the substrate using micropatterning techniques to study cellular response to specific anchoring modes onto the substrate. Examples of this approach can be found in the works of Pasqualini *et al.* [53] who applied a PDMS micro-contact stamp in order to selectively deposit fibronectin onto a PAA substrate. Balaban *et al.* [54] used lithographic approaches to create not only selectively coated PDMS substrates, but also to create relief profiles at the surface.

Another variation is reference-free TFM. This approach introduced by Bergert *et al.* [55] bypasses the acquisition of the reference image using nanodrip printing of quantum dots into confocal monocrystalline arrays on the surface of PDMS substrate. These substitute the fluorescent beads as individually identifiable light sources. Since the quantum dots were originally printed in form of a highly structured lattice, linking the points up with a mesh and relaxing it back to its highly symmetric structure reveals the deformation at each sampling point from which tractions can be derived.

Finally, some approaches combine the force reconstruction directly with a modelling of the force generation framework. These approaches are known as model-based TFM. One common variant, used in TFM observations of cell monolayers is monolayer-stress microscopy [56–59]. This technique models the cell monolayer as a thin elastic sheet and jointly solves the equations for the in-sheet stresses and the traction forces. Similar techniques have also been used for single cell observations [13].

Originally, TFM methods created purely two-dimensional reconstructions of in-plane traction fields of cells by neglecting normal deformations and traction components [10, 11]. This approach is referred to as *2D TFM* and visualized in Fig 1.5 A. However, these normal forces turn out to be relevant in a variety of biological processes, such as tissue migration and tumor invasion [60]. For example, it could be shown that normal traction is more likely to occur below distal and proximal focal ad-

hesions [61]. To conduct these kinds of observations, a technique has been developed that maintains the planar geometry but includes the full three-dimensional interaction at the interface. This technique is known as *2.5D TFM* [20, 62] and is presented in Fig 1.5 B. We further discuss two techniques used for *2.5D TFM* in chapter 3 and 4 of this dissertation.

Techniques that go beyond planar substrates have also been devised. Since *in vivo* cells are usually navigating and adhering in three-dimensional ECM environments, these methods aim to reconstruct force applied by cells onto fibrous matrices that surround the cell. Techniques that deploy these kinds of 3D substrates are shown in Fig 1.5 C and are referred to as *3D TFM* [19–22]. We study one technique used in 3D TFM, the direct method, in chapter 4 of this dissertation. 3D TFM requires a 3D image volume in order to be able to reconstruct the full stress tensor. This is often challenging given the anisotropic point spread functions of standard microscopes and the time required to acquire image stacks.

Recently, another three-dimensional variant has been developed: Rather than embedding the cells in a hydrogel environment, the setup is inverted by using elastic beads deformed by cell traction [63–65]. We scratch the layout of these techniques in Fig 1.5 D.

1.2.2 Imaging techniques

TFM generally leverages a multitude of imaging techniques commonly used in microbiology [66] to track beads within the substrate.

Underlying to all microphotographic techniques for TFM is the concept of fluorescence microscopy. Rather than observing light that is emitted by an external light source, that is then subsequently scattered by an observed object, this microscopic technique uses fluorophores, which can absorb energy when being irradiated by an external light source and subsequently emit light with a characteristic frequency [66]. By selectively observing only the emitted frequency, a good resolution and contrast ratio can be achieved. Fluorophores occur naturally in some species and a range of fluorescent dyes with different emission frequencies is available. Many fluorescence microscopes are capable of selectively imaging multiple frequency ranges (channels) simultaneously, enabling the concurrent observation not only of the TFM-microbeads, but also fluorescently stained cellular structures. Fluorophores may be attached to antibodies, which can then bind to a multitude of structures allowing the highlighting of specific structures of cells or organisms [55].

Confocal laser scanning microscopy (CLSM) uses a laser as a high intensity, correlated light source. The laser radiation is redirected using a dichroic mirror and then passed through a focusing lens, causing the light to only reach a significant intensity in a plane separated from the focusing lens by its focal length. By ensuring that the fluorophores are only stimulated in this high intensity area, a selected slice can be imaged. By variations in the distance of the probe and the focusing lens a three-dimensional intensity map can be obtained. This is essential for 3D and most 2.5D TFM techniques.

Light sheet fluorescence microscopy (LSFM) provides an alternative to CLSM to obtain three-dimensional intensity maps: In this method the laser light source is arranged orthogonal to the imaging setup next to the probe and a cylindrical lens is used to focus light into a thin sheet such that only a selective plane within the probe is illuminated. This selective excitation minimizes the loss of fluorophores due

to excessive irradiation (fluorophore bleaching) and phototoxic effects.

When PDMS substrates are used, Total Internal Reflection Fluorescence (TIRF) microscopy [67, 68] can avoid illuminating the cell entirely: Here, the light source is placed below the sample. Using a lens, that is connected to the substrate basin via a film of immersion oil, the light is refracted in such a way, that it enters the substrate basin in an almost vertical angle. Because the lens, the immersion oil, the glass basin and the PDMS substrate all show a similar refractive index, the light is passing through them with only minor refraction and the fluorescent beads get stimulated. However, due to the significant change in the refractive index between substrate ($n \approx 1.49$) and the cell ($n \approx 1.38$) or its water-based medium ($n \approx 1.33$), internal reflection occurs preventing the excitation light to damage the cell.

To increase spatial resolution Stimulated Emission Depletion (STED) microscopy can be used [69, 70]. This technique selectively images individual spots in the image sequentially and uses a donut-shaped depletion beam to suppress fluorescence emission from the outer regions of the excitation spot, enabling the visualization of nanoscale structures beyond the diffraction limit.

Recently, other super-resolution techniques like Structured Illumination Microscopy (SIM) [71, 72] and functional-based imaging [73] have been proposed as well. On PDMS substrates SIM has been combined with TIRF [74] bundling the benefits of both techniques for 2D TFM.

Astigmatic TFM [75] uses TIRF-SIM combined with a non-circular point-spread function. This technique allows the vertical displacement to be inferred from a single imaging plane thus extending the benefits of TIRF-SIM-TFM to 2.5D TFM techniques.

1.2.3 Image registration techniques

The first step in reconstruction is image registration or extracting a deformation field from the change in bead distribution. Microscopic data typically consists of two intensity maps I_R and I_D where high intensity is attributed to the presence of beads. The first image I_R describes the stress-free or reference situation while the second I_D describes the deformed or loaded setup. The task is now to find a vector field $\boldsymbol{u}$ describing the changes that occurred between the to images. Due to limitations in microscopic observations, beads may become blurred or moving out of the field of view during deformation. This poses additional challenges to the reconstruction and is a source of errors that need to be accounted for. The selection of technique for this task depends on the typical distance of beads when observed. In the case of low bead density, tracing should be conducted on the level of individual beads as it is very challenging to recognize the relative displacement of neighboring beads using this technique. The most straight-forward approach for low pixel resolutions is particle tracking velocimetry. This technique is particularly common in 3D approaches due to the large bead spacing as a result of three-dimensional distribution of beads [76]. It works by detecting the position of individually beads in the intensity map and then matching up individual beads detected in the force free and loaded configuration and calculate the difference in position [77]. However, optical-flow based methods [78] provide an alternative to particle tracking velocimetry, as they often have a lower number of relevant parameters and feature a significant reduction in computation costs, making them less error-prone, easier to use and more efficient in production [49].

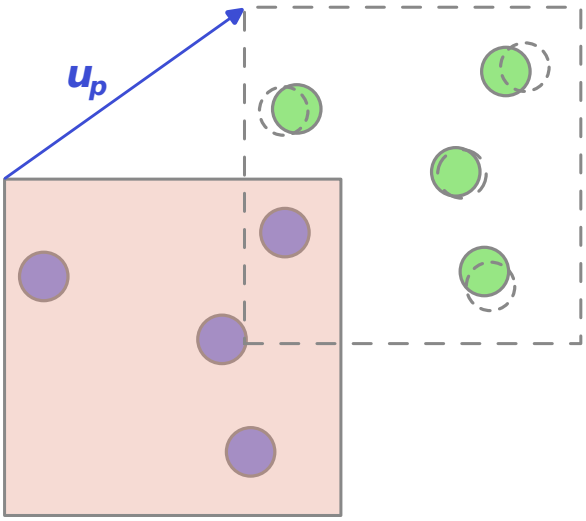

Figure 1.6: Concept of correlation tracking. Rather than tracing the displacement of beads individually, a small subset, the interrogation patch (red shaded square), of the stress-free image (blue circles) is translated until a good correlation with the loaded situation (green circles) is found. The translation vector $\boldsymbol{u}_p$ corresponds to the average deformation in the interrogation patch. By repeating the process with different interrogation patches a spatial resolved displacement vector field, the deformation field, is found.

When bead concentration is sufficiently high the correlation in displacement between neighboring beads should be considered. In this case, one can greatly improve deformation field construction by observing the collective motion of beads rather than the individual one with a decrease in spatial resolution, as shown in Fig 1.6. The dominant method used for TFM in this case (see [52]) is correlation tracking, which is also known as particle image velocimetry (PIV) [79–81], digital image correlation (DIV) [82] or digital volume correlation (DVC) [83–85].

Instead of calculating the deformations with respect to the reference frame in a single step, in time series we can also use an iterative stepping process where we find the deformation between two succeeding images and accumulate the individual deformation steps between the different frames [50].

Correlation tracking

Correlation tracking starts by covering both the traction-free or relaxed as well as the loaded or deformed bead image by several fixed-size patches. The intensity field in each patch is labeled R and D and patches have a specific window size w_R and w_D respectively. Westerweel [80] suggested selecting w_R equal or larger than four times the typical displacement of features. w_D can be chosen equal in size to w_R, may be chosen large which allows features to be found in a larger radius. In any case w_D must be chosen sufficiently large to be able to predict the largest deformation observable. Patches can be chosen in an overlapping fashion and it has been suggested that choosing an overlap of 50% optimally compromises between over and under-fitting of information [86, 87].

For each patch a bulk deformation is then determined with the help of the cross-

correlation function $C(r,s)$, which is given by

$$C(r,s) = \frac{1}{w_R^2} \cdot \sum_{i=1}^{w_R} \sum_{j=1}^{w_R} (R(i,j) - \bar{R})(D(r+i, s+j) - \bar{D}). \tag{1.2}$$

Here $\bar{R}$ and $\bar{D}$ are the average value of the respective fields in the patch and r and s are discrete indices corresponding to the tested displacement vector $\boldsymbol{u} = (r,s)^T$ when measured in pixel units. If the beads are very unevenly distributed, the correlation has to be stabilized by dividing $C(r,s)$ with the standard deviations of both R and D respectively [88]. If both images are segmented into patches of the same size $w = w_R = w_D$, the cross-correlation function can be computed efficiently using the Fast Fourier Transform [79, 88, 89]. In order to improve the granularity of the displacement reconstruction, a Gaussian fit is employed surrounding the peak value [90]. The sub-pixel accuracy displacement vector is now given by:

$$\begin{aligned} u_x &= \hat{r} + \frac{\ln C(\hat{r}-1,\hat{s}) - \ln C(\hat{r}+1,\hat{s})}{\ln C(\hat{r}-1,\hat{s}) - 4\ln C(\hat{r},\hat{s}) + 2\ln C(\hat{r}+1,\hat{s})} \\ u_y &= \hat{s} + \frac{\ln C(\hat{r},\hat{s}-1) - \ln C(\hat{r},\hat{s}+1)}{\ln C(\hat{r},\hat{s}-1) - 4\ln C(\hat{r},\hat{s}) + 2\ln C(\hat{r},\hat{s}+1)} \end{aligned} \tag{1.3}$$

Where $\hat{r}$ and $\hat{s}$ are those values for r and s that maximize the correlation function. Correlation calculation in 2.5D and 3D follows a similar pattern save for the extra dimension.

In some regions, e.g. those with low intensity difference between the bead signal and background noise or along the boundaries of the image, the algorithm will produce spurious vectors. Classification and substitution techniques can be used to detect and subsequently replace these spurious vectors. Vectors with high probabilistic ambiguity are removed by limiting the minimally accepted signal-to-noise ratio in the correlation function [91]. If the correlation shows two distinct peaks and the ratio between the highest and second highest peak is below a certain threshold, the vector is found unreliable and removed from the output. General outliers are removed by a so-called normalized median test [92]. Here, for each sampling patch, whose displacement vector we label $\boldsymbol{u}_0$, we calculate the median $\boldsymbol{u}_m$ of the displacement vectors $\boldsymbol{u}_i$ for each of the 8 adjacent patches cells: $\boldsymbol{u}_m = \text{median}(\boldsymbol{u}_i | i = 1, \ldots, 9)$. We then compare the displacement residual of the interrogated patch $r_0 = |\boldsymbol{u}_0 - \boldsymbol{u}_m|$ to the median residual of the adjacent patches $r_m = \text{median}(r_i = |\boldsymbol{u}_0 - \boldsymbol{u}_m| | i = 1, \ldots, 8)$. If now the normalized residual r_0/r_m exceeds a certain threshold, the interrogated patch is considered an outlier and its displacement vector is substituted by the mean of its neighbors.

By assigning the deformation of each patch to the center coordinate of each patch, the correlation tracking yields the deformation field of the material in a rectangular grid sampled representation. An efficient implementation for 2D TFM including the two classification and substitution techniques is implemented in the *OpenPIV* software utility [93]. This implementation both in an adapted version of its original form as well as a modification to extend it to 2.5D was used for correlation-based image registration in this work.

In the case of large deformations, iterative procedures can be used that first use a large window size to calculate macro-scale displacement $\mathbf{u}^{(0)}$ and then map the reference configuration to a slightly deformed image $I_R'(x,y) = I_R(x + u_x^{(0)}, y + u_y^{(0)})$

and repeat the calculation with a smaller window size until a sufficient resolution is reached. The full deformation can be found by accumulating the individual deformations from all iterations [85].

Optical flow algorithm

The Optical flow algorithm [78, 94] was originally developed to track continuous flow fields, but may also be used to reconstruct bead displacement fields [49]. The following description is given for the 2D scenario but can be trivially extend to the 2.5D and 3D case if needed. In a first step, trackable features (beads) are located in an image's intensity field using a *Shi-Tomasi* corner detection algorithm [95]. We first define a sum of squared differences (SSD) for a given point (i, j) which detects the level of change observed in an interrogation window under an image drift:

$$SSD(x, y) = \sum_{i,j=1}^{b} (I(i + x, j + y) - I(i, j))^2 \tag{1.4}$$

If we assume both drift parameters x and y to be small, we can use a Taylor expansion to find that

$$\begin{aligned} SSD(x, y) &\approx \sum_{i,j=1}^{b} (I(i, j) + \partial_x I(i, j)x + \partial_y I(i, j)y - I(i, j))^2 \\ &= \begin{pmatrix} x & y \end{pmatrix} \cdot \mathbf{A} \cdot \begin{pmatrix} x \\ y \end{pmatrix}, \end{aligned} \tag{1.5}$$

where we identified the structure tensor

$$\mathbf{A} = \sum_{i,j=1}^{b} \begin{pmatrix} (\partial_x I)^2 & (\partial_x I)(\partial_y I) \\ (\partial_x I)(\partial_y I) & (\partial_y I)^2 \end{pmatrix}. \tag{1.6}$$

An easy to track feature is determined by a large SSD value in all directions, meaning for any choice of (x, y). The Shi-Tomasi [95] criterion for this is $R(i, j) = \min(\lambda_1, \lambda_2)$, λ_1 and λ_2 being the eigenvalues of $\mathbf{A}$, and we can take the first N points with the largest R value to be the relevant features. In order to get discrete meaningful points, we reject features that are below a certain threshold Q below the most definitive feature ($R(i, j) < Q \cdot \max_{k,l} R(k, l)$) as well as those that are closer than a minimal distance $D_{\min}$ relative to a more prominent feature. Displacement are now calculated by means of the Kanade-Lucas-Tomasi (KLP) optical flow algorithm [94, 96]. This is based on the optical flow equation. If a feature moves from (x, y) to $x + u_x$, $y + u_y$, we find that

$$I_D(x, y, t) \approx I_R(x - u_x, y - u_y) \approx I_R(x, y, t) - \nabla_{x,y} I_R(x, y, t) \begin{pmatrix} u_x \\ u_y \end{pmatrix} \tag{1.7}$$

which effectively describes a time discretized continuum equation

$$\begin{pmatrix} u_x & u_y \end{pmatrix} \cdot \nabla_{x,y} I_R = -\Delta I. \tag{1.8}$$

Where we defined $\Delta I = I_D - I_R$. The Lucas-Kanade method now assumes that the drift remains constant over a multitude of points within a sampling window of size $w \times w$. A sampling vector can now be found by solving

$$\arg\min_{u_x,u_y} \left\| \mathbf{S} \cdot \begin{pmatrix} u_x \\ u_y \end{pmatrix} - \boldsymbol{t} \right\|_2^2, \tag{1.9}$$

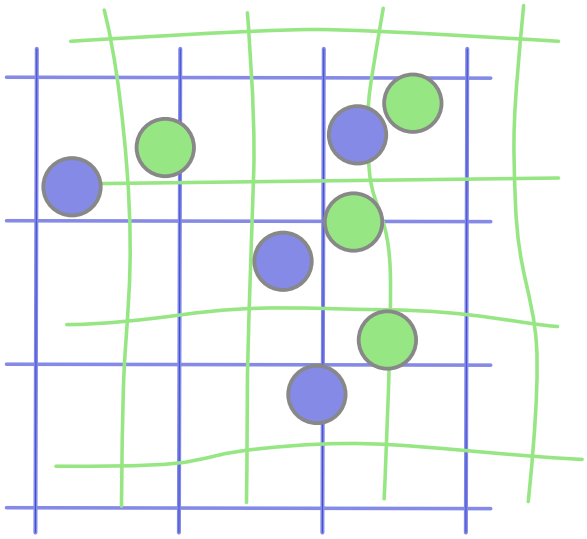

Figure 1.7: Concept of Free Form Deformation. Here the underlying coordinate mash is deformed in such a manner, that beads in reference image (marked in blue) are mapped to their counterparts in the loaded situation (marked in green).

where

$$\mathbf{S}^T = \left(\nabla_{x,y} I_R(q_1), \ldots, \nabla_{x,y} I_R(q_N)\right) \qquad \boldsymbol{t} = \left(-\Delta I(q_1), \ldots, -\Delta I(q_N)\right) \tag{1.10}$$

and the double index q_i runs over all $N = w^2$ points within the sampling window. Eq 1.9 can be solved exactly by calculating

$$\begin{pmatrix} u_x \\ u_y \end{pmatrix} = (\mathbf{S}^T\mathbf{S})^{-1}\mathbf{S}^T\boldsymbol{t}. \tag{1.11}$$

If the displacements become too large, the approximations made in Eq 1.7 are no longer valid. The pyramidal Kanade-Lucas-Tomasi (KLP) optical flow algorithm [94, 96] avoids this issue by first down-sampling the image, to find the macro-scale deformations. Then similar to iterative correlation methods, the reference image is substituted by a projection and the procedure is repeated for a finer granularity.

If the displacements become too large, the approximations made in Eq 1.7 are no longer valid. One solution is to use the above-mentioned cumulative procedure where only the displacement between cumulative steps in a time series are calculated. In this case Eq 1.7 corresponds to an effective Euler stepping which may lead to numerical instability. This issue can be resolved by also performing the optical flow analysis in the inverse direction and calculate

$$\boldsymbol{u}_i = \frac{1}{2}\left(\boldsymbol{u}_{(i-1)\to i} - \boldsymbol{u}_{i\to(i+1)}\right) \tag{1.12}$$

Advanced algorithms

More recently advanced algorithms have been devised, like the Free Form Deformation (FFD) algorithm [97], which is visualized in Fig 1.7. Here the deformation is described by a sequence of B-splines,

$$\boldsymbol{u}_{\boldsymbol{\Phi}}(\boldsymbol{x}) = \sum_{r=0}^{3}\sum_{s=0}^{3}\sum_{t=0}^{3} B_r(q)B_s(v)B_t(w)\Phi_{i+r,j+s,k+t}, \tag{1.13}$$

where $\boldsymbol{x} = (\Delta x i + 1 + q, \Delta y j + 1 + v, \Delta z k + 1 + w)^T$ such that i, j and k are integers describing pixel indices. q, v and w should be non-negative real numbers below one. The functions B_n are cubic B-spline polynomials given by:

$$B_0 = (1-q)^3/6 \qquad B_1 = (3q^3 - 6q^2 + 4)/6 \tag{1.14}$$

$$B_2 = (-3q^3 + 3q^2 + 3q + 1)/6 \qquad B_3 = q^3/6 \tag{1.15}$$

In order to find the coefficients $\Phi_{i,j,k}$, the normalized cross correlation between the loaded intensity map $I_D(\boldsymbol{x})$ and the transformed reference image $I_R(\boldsymbol{x} + \boldsymbol{u}_\Phi(\boldsymbol{x}))$ is found by a stochastic gradient descent method.

1.2.4 Traction reconstruction

A wide range of approaches has been established for traction force reconstructions. Methodically, there are two major approaches for traction force reconstruction, known as the *direct method* and the *inverse method*.

The workflow known as the *direct* (or *forward*) *method* (DM) starts from a representation of the three-dimensional displacement field. Recalling the concepts of continuum mechanics, the strain tensor can be calculated, which is a linear composition of the deformation gradient. Then, using the constitutive law of the material, it can be converted into a stress tensor. For an linear isotropic material, this step is simply a linear transformation. Finally, the surface traction follows as contraction of the stress tensor with the surface normal.

The DM has been pioneered for 2.5D TFM [15–17], but also has been applied to 3D TFM [98, 99] and to elastic beads with embedded markers that are deformed by the traction forces in cell aggregates [63]. The DM is especially suited to deal with large deformations and non-linear material laws, but it also can be used in the linear regime, which is typically used for 2D or 2.5D TFM on soft elastic substrates. In general, however, the direct method is not very commonly used, for two main reasons. First the method is intrinsically three-dimensional making it unsuitable for situations where 2D TFM is sufficient, but the requirements of 3D imaging pose a significant restriction. Secondly, it is a numerical challenge to calculate the required derivatives in the presence of the unavoidable experimental noise, especially when microscope resolution is low. In contrast, the DM seems to be an attractive choice for non-planar geometries like elastic beads, for which it is very challenging to calculate appropriate GFs [63]. Another benefit of this method is the fact that, when used in combination with advanced image registration methods, the DM may leverage their representation of the displacement field directly during the gradient taking step [99]. I will discuss the DM in more detail in chapter 4.

The more common and historically older workflows for traction reconstruction are encompassed by the term *inverse method* (IM). In order to avoid derivatives, in this approach, one does not explicitly calculate strain or stress tensors, but stays on the level of displacement fields. A solution is found, by minimizing the difference between the measured displacement field and a displacement field calculated from an estimated traction field. Doing so, which possibly requires one to calculate the deformation from estimated traction (*direct problem*) repeatedly, one arrives at the best estimate given the experimental data.

The IM includes approaches based on Green's functions as well as those based on the Finite Element Method (FEM), the former of which includes the approach first

conceived for 2D TFM by its pioneers [8, 10]. Green's function approaches use a fundamental solution of the elastic boundary value problem (Green's function) to reduce the direct problem to a simple matrix application on the deformation field. Green's functions can be used only for linear elasticity, but offer several advantages. First, the Green's function for thick elastic substrates is well known (*Boussinesq solution*) [100] and also the Green's function for a finite thickness substrate has been derived [18]. Second, for flat cells on planar substrates it is sufficient to know the displacements in a two-dimensional plane close to the gel surface. This reduces the Green's function from a 3x3 to a 2x2 matrix, which makes this approach usable for 2D TFM. And third, one can use fast Fourier methods to convert the convolution of GF and traction into a product. Due to its speed, Fourier Transform Traction Cytometry (FTTC) [12] therefore has become the method of choice for high resolution measurements. Together, these advances make the inverse method very attractive for measuring cell traction on elastic substrates.

Because elasticity theory leads to an ill-posed inverse problem due to its long-ranged deformation fields, one usually deals with the noise problem by invoking some regularization procedure, like the zero-order Tikhonov regularization [10, 11, 20, 76]. In order to choose the correct value of the regularization parameter, different schemes have been suggested, including the L-curve criterion or generalized cross-validation [13, 14]. When using FTTC, the regularization can be formulated in Fourier space and therefore many schemes can be applied to deal with the noise issue [14, 101, 102]. The need for explicit regularization can be avoided by using TFM-schemes that effectively filter the deformation data, like image smoothing [12, 59] or by using a the FEM [71, 98, 99]. I will discuss Green's function-based approaches in more detail in chapter 2.

When geometrical and material linearity can no longer be assumed, the direct problem is usually solved using FEM-based approaches. This is usually the case for 3D TFM, but might also apply to cases that simply aim to study strong cells on particularly soft substrates [21, 98, 103–105], but can also be used in 2D setups [106].

Neural-network based approaches have been the most recent edition to the collection of traction force reconstruction techniques [23, 26, 107]. These methods cannot be cataloged into the DM and IM classification. Neural network methods used for 2D TFM often use the U-Net [108], an convolutional network architecture widely applied in biomedical image segmentation tasks, similar in nature to TFM [23, 24, 109]. Neural network models are generally trained by generating a large collection of simulated force deformation pairs that mimic the adhesive profiles on real data without losing generality.

Besides for deformation-to-force reconstruction, neural networks have also been deployed for closely related force inference techniques and to study cellular force generation itself [25, 109]. For example, Schmitt *et al.* [25] used neural networks to show that cytic traction fields could be predicted from an immunostaining image of the cell's zyxin distribution, a protein found in the cell's focal adhesions. They also showed that both a short-range and a long-range correlation exists between the zyxin and traction force distribution, highlighting the role of focal adhesions as the linker between the cytoskeleton and the extracellular mechanical anchoring of the cell. Neural-network based approaches will be discussed in detail in chapter 6.

1.2.5 Quantitative evaluation of traction maps

After a traction map τ has been calculated, we can use a spatial visualization to observe the distribution of force qualitatively. For a more quantitative analysis, different metrics have been established to characterize the contractile strength, as well as specific properties of the traction pattern. For 2D TFM the following metrics have been devised.

Strain energy

The strain energy qualifies the amount of mechanical energy, that is stored in the substrate deformation and conforms to the work invested by the cell into deforming the substrate. It is defined by [12]:

$$U = \frac{1}{2} \int_C \boldsymbol{\tau} \cdot \boldsymbol{u} \, \mathrm{d}x \, \mathrm{d}y \,. \tag{1.16}$$

The integration area C should be chosen to encompass the adhesive area of the cell.

Total force

The total force [110] quantifies the cell's overall and momentary contractile activity. It is formed by accumulating the force magnitude transmitted by all adhesions, yielding

$$F_{tot} = \int_C |\boldsymbol{\tau}| \, \mathrm{d}x \, \mathrm{d}y \,. \tag{1.17}$$

Again, the integration area C should be chosen to encompass the adhesive area of the cell.

Force monopole

The force monopole describes the net directed force on the substrate, which is defined by

$$\boldsymbol{F} = \int \boldsymbol{\tau}_A \, \mathrm{d}x \, \mathrm{d}y \,. \tag{1.18}$$

If no external forces are applied onto the cell, the monopole force must be zero due to moment conservation.

Dipole moment matrix

The first order moment or dipole matrix $\mathbf{M}$ is defined by means of [12]

$$\mathrm{M}_{ij} = \int_C (x_i - x_{CP,i}) \tau_j \, \mathrm{d}x \, \mathrm{d}y \,. \tag{1.19}$$

The coordinate frame for this integral is chosen with respect to the center of force of the system, which is given by

$$\boldsymbol{x}_{\mathrm{CF}} = \left(\int |\boldsymbol{\tau}| \, \mathrm{d}x \, \mathrm{d}y \,. \right)^{-1} \int |\boldsymbol{\tau}| \boldsymbol{x} \, \mathrm{d}x \, \mathrm{d}y \,. \tag{1.20}$$

which can be calculated in any coordinate frame.

The diagonal components of the moment matrix describe the contractility of the system. The two off-diagonal components correspond to a torque relative to the center of force [12]. We define the contractile momentum by

$$\mu = \mathrm{M}_{11} + \mathrm{M}_{22}. \tag{1.21}$$

This describes the net ability to dilate or contract the cell. The net torque is defined by

$$\mathcal{M} = \mathrm{M}_{12} - \mathrm{M}_{21}. \tag{1.22}$$

Both μ and $\mathcal{M}$ are independent of the orientation of the coordinate axes and are independent of each other. In the absence of external forces, angular momentum conservation dictates that the net torque must vanish and the moment matrix must hence be symmetric. In this case, one can find an orientation of the axis such that $\mathbf{M}$ is diagonal and the eigenvalues can be used to find the directed and isotropic contractile moment of the system. The two eigenvalues are known as the dipole moments, with the one with the largest absolute magnitude being referred to as the major dipole moment and the other as the minor dipole moment. The corresponding eigenvectors form an orthogonal coordinate base and the corresponding coordinate axes are referred to as the major and minor dipole axis respectively.

Areal integrated force

The areal integrated force $\boldsymbol{F}_A$ describes the force transmitted over a specified contact area A, hence

$$\boldsymbol{F}_A = \int_A \boldsymbol{\tau} \, \mathrm{d}x \, \mathrm{d}y \tag{1.23}$$

When choosing A to be the entire area of cellular adhesion, this force is also known as the monopole force. If no external forces are applied onto the cell, the monopole force must be zero due to moment conservation.

Chapter 2

Theoretical framework

TFM relies extensively on an understanding of the mechanical behavior of the hydrogel substrates. In order to accurately interpret the traction forces exerted by cells on hydrogel substrates, it is essential to study the principles of continuum mechanics.

Continuum mechanics is a branch of physics and mathematics that provides a theoretical framework for studying the behavior of continuous materials, such as hydrogels, under the influence of external forces. By treating the hydrogel substrate as a continuous medium, continuum mechanics enables the development of mathematical models and equations that describe the mechanical properties and behavior of the substrate [111].

In the framework of TFM, continuum mechanics describes the relationship between the deformation and stress distribution within the hydrogel substrate caused by cellular forces. This information is crucial for accurately inferring the traction forces exerted by cells based on the observed substrate displacement.

In this chapter, I will give a brief overview over some fundamental concepts of continuum mechanics and also describe some analytical solutions that will be used in the subsequent sections.

2.1 Continuum description of solids

2.1.1 Elasticity theory

Elasticity theory is the area of continuum mechanics concerned with describing objects with a defined rest shape. Rather than describing the mechanics of individual atoms and molecules at an atomic scale, it uses a continuum approximation. It is hence a macroscopic field theory [100].

The underlying physical observable of all continuum mechanic theories is deformation or displacement. There exist two different ways to parameterize spatially distributed quantities. One can either describe fields by giving their values at each point in space, this is known as Eulerian specification[112]. If the system is in motion, the microscopic particles contributing to the properties at each position will thus change and propagation of properties attributed to local material quanta like local density, temperature or momentum must be tracked explicitly in the dynamic equations of each field. The main benefit of this description is that the choice of parameters is independent of the observed system and in particular does not depend on any previous state of the system. This kind of description is often used in hydrodynamics, as it considers the Marcovinan nature of fluids [113].

An alternative method of description is obtained by parameterizing the different material quanta irrespectively of their current position. The advantage of this is, that the microscopic particles contributing to the described properties will remain the same for each point in the parameter space. However, we must choose a reference configuration, based on which the material quanta are parameterized. This description is most suitable for elastic solids. Those have a dedicated relaxed state, and the motion is dominated by the difference between the current configuration and one of the relaxed state[113].

Another major advantage of using the Lagrangian description for solids is the treatment of boundary conditions. As the boundaries of a material are determined by the motion of surface material quanta, the boundary will generally remain constant in the Lagrangian description, while it will depend on the evolution of fields in the Lagrangian description. The major disadvantage of this approach is that the deformation of the coordinate system will result in the parameterization being curved and must therefore be described using methods from differential geometry[112].

We introduce a Lagrangian parameterization of a system by assigning each material quantum a set of parameters $\boldsymbol{X}$ which corresponds to its spatial position at the reference configuration. We can now describe the dynamics of the material by a field $\boldsymbol{x}(\boldsymbol{X}, t)$. If the system assumes this configuration at a specific time t_0 we thus have by construction an initial condition

$$\boldsymbol{x}(\boldsymbol{X}, t_0) = \boldsymbol{X}. \tag{2.1}$$

For a different time the positions will differ: The displacement field

$$\boldsymbol{u}(\boldsymbol{X}, t) = \boldsymbol{x}(\boldsymbol{X}, t) - \boldsymbol{X} \tag{2.2}$$

describes the change in position with respect to the initial configuration [113]. We also define the Jacobian of the displacement field and of the coordinate transformation as the displacement gradient tensor and the deformation gradient tensor respectively:

$$\mathbf{H} = \frac{\partial \boldsymbol{u}}{\partial \boldsymbol{X}} \qquad\qquad \mathbf{F} = \frac{\partial \boldsymbol{x}}{\partial \boldsymbol{X}} = \mathbf{H} + \mathbf{I} \tag{2.3}$$

Strains and Stresses

The strain tensor describes local bending, stretching and compression of the system compared to the reference configuration [114]. The (Green-Lagrangian) strain tensor is defined by:

$$\mathbf{E} := \frac{1}{2}\left(\mathbf{F}^T\mathbf{F} - \mathbf{I}\right) = \frac{1}{2}\left(\mathbf{H}^T + \mathbf{H} + \mathbf{H}^T\mathbf{H}\right) \tag{2.4}$$

If we select three neighboring points $\boldsymbol{X}$, $\boldsymbol{X} + \mathrm{d}\boldsymbol{A}$, $\boldsymbol{X} + \mathrm{d}\boldsymbol{B}$, that will move to $\boldsymbol{x}$, $\boldsymbol{x} + \mathrm{d}\boldsymbol{a}$, $\boldsymbol{x} + \mathrm{d}\boldsymbol{b}$ under the deformation, the deformation gradient tensor now can be used to estimate the changes in the relation of the separation vectors, namely:

$$\mathrm{d}\boldsymbol{a} \cdot \mathrm{d}\boldsymbol{b} - \mathrm{d}\boldsymbol{A} \cdot \mathrm{d}\boldsymbol{B} = \mathrm{d}\boldsymbol{A} \cdot \mathbf{E} \cdot \mathrm{d}\boldsymbol{B} \tag{2.5}$$

It is apparent, that this generalizes the one-dimensional concept of strain as a local increase in length to a 3d quantity.

Just like discreet bodies interact with neighboring bodies using forces, different materials and different regions of the same material can exchange forces on shared

surfaces. These forces are known as traction forces. Tractions caused by internal cohesion forces between adjunct volume elements within the same material are known as stresses. These are caused by thermodynamic pressure as well as atomic and molecular bindings. The total traction force transmitted over a surface $\mathcal{S}$ is given by

$$\boldsymbol{F}_{\mathcal{S}} = \int_{\mathcal{S}} \boldsymbol{\tau} \, \mathrm{d}a \,, \tag{2.6}$$

where $\boldsymbol{\tau}$ describes the traction or traction force per area. By geometrical consideration on finds, that at any given point the traction one surfaces with different surface normal are related and can be described by a tensor, known as the Cauchy stress tensor $\boldsymbol{\sigma}$ [113]. The traction $\boldsymbol{\tau}$ contributed by a given point on a surface with surface normal $\boldsymbol{n}$ is given by:

$$\boldsymbol{\tau} = \boldsymbol{\sigma}\boldsymbol{n}. \tag{2.7}$$

This stress tensor describes the local mechanical properties of the material and is the most commonly used tensor to describe stresses in the material. In order to preserve angular momentum, the stress tensor must also obey an additional condition $\boldsymbol{\sigma} = \boldsymbol{\sigma}^T$, meaning the Cauchy-Stress Tensor, must be a symmetric one [100]. If this would not be imposed the torque acting on an infinitesimal volume element would be finite.

Elastostatics

If the system is in a static state, meaning $\dot{\boldsymbol{u}} = 0$, the forces in each volume element must be balanced, hence:

$$-\int_{\Omega} \rho \boldsymbol{g} \, \mathrm{d}^3 x = \int_{\partial\Omega} \boldsymbol{\sigma}\boldsymbol{n} \, \mathrm{d}a \,. \tag{2.8}$$

Here the left-hand side corresponds to a potential density dependent body force due to external factors (electromagnetic interaction/gravity etc.).

In the Eulerian coordinate frame this integral equation reduces to a point-wise differential equation:

$$0 = \rho \boldsymbol{g} + \frac{\partial}{\partial \boldsymbol{x}} \boldsymbol{\sigma} \tag{2.9}$$

In the Lagrangian coordinates, the corresponding equation is written as:

$$0 = \rho_0 \boldsymbol{g} + \frac{\partial}{\partial \boldsymbol{X}} \left(\det(\mathbf{F}) \mathbf{F}^{-1} \boldsymbol{\sigma} \right) \tag{2.10}$$

The relationship between strain and stress depends on the material. In fluid like materials there is no reference configuration. As such, the stress is fully dependent on the current flow field.

An important group of materials are those, where the stress in any given point does only depend on the deformation gradient tensor, meaning $\boldsymbol{\sigma} = \boldsymbol{\sigma}(\mathbf{F})$, such materials are called (Cauchy)-elastic ones [115]. Such a material will return to its preferred configuration after external forces, that caused the material to deform, cease to apply. The stress-strain relation is known as a *constitutive relation* and completes the momentum conservation equation into a full differential equation [113]. Particular useful subgroups are hyperelastic and isotropic linear elastic materials.

In a hyperelastic material, stress is conservative and fully determined by the local deformation energy density $W(\mathbf{E})$ [115]:

$$\boldsymbol{\sigma} = \frac{1}{\det(\mathbf{F})} \frac{\partial W}{\partial \mathbf{E}} \mathbf{F}^T \tag{2.11}$$

Isotropic hydrogels can be commonly described by a Neo-Hookean model [13, 116, 117]:

$$W = \frac{E}{4(1+\nu)} \left(\bar{I}_1 - 3\right)^2 + \frac{E}{6(1-2\nu)} \left(J - 3\right)^2 \tag{2.12}$$

where $\bar{I}_1$ and J are isotropic expressions, describing the average linear stretching and the local volume compression respectively [115]

$$\bar{I}_1 = \frac{\operatorname{tr}\left(\mathbf{F}\mathbf{F}^T\right)}{\det(\mathbf{F})^{2/3}} = \frac{2\operatorname{tr}(\mathbf{E}) + 3}{\det(2\mathbf{E} + \mathbf{I})^{1/3}} \qquad J = \det(\mathbf{F}) = \sqrt{\det(2\mathbf{E} + \mathbf{I})} \tag{2.13}$$

The resulting strain-stress relation is then given by:

$$\sigma = \frac{E}{2(1+\nu)J^{5/3}} \left(\mathbf{F}\mathbf{F}^T - \frac{1}{3}\operatorname{tr}\left(\mathbf{F}\mathbf{F}^T\right)\mathbf{I}\right) + \frac{E}{3(1-2\nu)} \left(J - 1\right)\mathbf{I} \tag{2.14}$$

The material constants E and ν are known as the Young's modulus and the Poisson's ratio, respectively, and describe the stiffness and compressibility of the material.

Linearized theory

In most cases the material is stiff, and hence the deformation gradients will be very small and only need to be considered up to linear order. In this approximation, the strain tensor can be simplified to

$$\mathbf{E} \approx \boldsymbol{\varepsilon} = \frac{1}{2}\left(\mathbf{H} + \mathbf{H}^T\right). \tag{2.15}$$

For isotropic materials, the constitutive equation reduces to

$$\boldsymbol{\sigma} = \frac{E}{1+\nu}\left(\boldsymbol{\varepsilon} + \frac{\nu}{1-2\nu}\operatorname{tr}(\boldsymbol{\varepsilon})\mathbf{I}\right) \tag{2.16}$$

$$= \frac{E}{2(1+\nu)}\left(\mathbf{H} + \mathbf{H}^T + \frac{2\nu}{1-2\nu}(\nabla\mathbf{u})\mathbf{I}\right). \tag{2.17}$$

In addition, the differences of using the Eulerian and the Lagrangian parameterization will only contribute to higher order terms and can hence be neglected.

Whether a substrate is considered stiff or soft is determined by the relation between the typical traction force amplitude and the Young's modulus. The dimensionless deformation gradient will typically be in the same order of magnitude as the ratio σ_{ij}/E. We must consider the substrate to be soft, if we expect the magnitude of the traction forces to be much larger than the substrates Young's modulus. Then the linear approximation as given in Eq 2.15 does not necessarily apply anymore and has to be replaced by a more complicated (non-linear) mapping. Both PAA and PDMS substrates can be created for a wide range of stiffness. For experiments, a typical substrate stiffness is $E = 10\,\mathrm{kPa}$ while the typical range of cell contractility is in the range of 100 Pa. This means that in most cases a stiff substrate can be assumed and the linear relation is typically satisfied. Both types of substrates are usually considered to be close to incompressible, with a Poisson ratio close to 0.5. It should be noted that incompressibility implies $\nabla\mathbf{u} = 0$ in the linear case assumed in Eq 2.17. This counteracts the apparent divergence for $\nu \to 1/2$ that would otherwise occur in the last term of Eq 2.17.

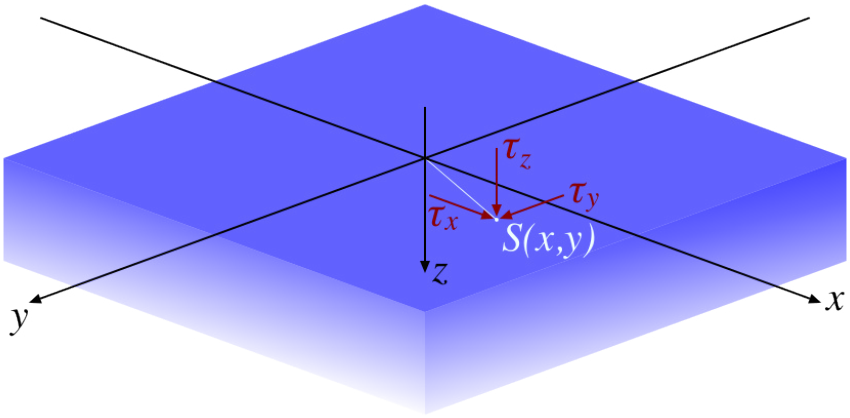

Figure 2.1: Visualization of the elastic halve-space problem. The surface lies in the x-y-plane while the z axis points into the substrate. Each point $S(x, y)$ on the halve-space surface is attributed a set of tangential surface tractions τ_x and τ_y as well as a normal pressure vector τ_z.

2.2 Analytical solutions of the elastic half-space problem

2.2.1 Modeling linear substrate

In typical TFM setups, cell-induced displacements are around two orders of magnitude smaller than the thickness of the substrate, which can usually be found in the range of 50 to 80 µm [47]. In these cases, the effects of the substrates lower surface, as well as the limited horizontal extent of the hydrogel layer can be neglected and the substrate can be described as an infinite elastic half-space due to its predominantly elastic behavior within the relevant deformation range. This assumption simplifies the modeling and analysis of traction forces exerted by cells onto the substrate interface. We also assume that the substrate behaves homogenously and isotropically in order to allow for it being treated as an elastic material with uniform properties, allowing for concise mathematical modeling and analytical solutions. In some cases, these assumptions do not uphold and boundary effects need to be discussed [18].

We must now fix a coordinate system and we model our system in such a way, that the traction stresses are exerted on the $z = 0$ plane and the substrate is confined to the $z > 0$ half-space as visualized in Fig 2.1.

The general problem of finding the deformation field in an infinite half-space with surface traction as boundary condition and no internal forces follows from Eq 2.17 and Eq 2.7 as

$$\frac{\partial}{\partial x_j}\left(\frac{\partial u_i}{\partial x_j}+\frac{\partial u_j}{\partial x_i}+\frac{2\nu}{1-2\nu}(\nabla \boldsymbol{u})\delta_{ij}\right)=0\ , \quad -\sigma_{iz}|_{z=0}=\tau_i\ , \tag{2.18}$$

where $\boldsymbol{\tau}$ describes the surface traction field corresponding to the traction exerted by the cell.

2.2.2 Green's function

A general solution to Eq 2.18 can be found using a Green's function. This approach makes use of the linearity of Eq 2.18 to relate the traction forces to the deformation

using a convolution relation with a Fredholm integral [118].

$$\boldsymbol{u}(x,y,z) = \int_S \mathbf{G}(x-x', y-y', z) \cdot \boldsymbol{\tau}(x',y')\,\mathrm{d}x'\,\mathrm{d}y'\,, \tag{2.19}$$

The Green's function $\mathbf{G}$ for the elastic half-space problem is known analytically from literature (*Boussinesq solution*) [100]:

$$\frac{2\pi E}{1+\nu}\mathbf{G}(x,y,z) = \begin{pmatrix} \frac{2(1-\nu)r+z}{r(r+z)} + \frac{(2r(\nu r+z)+z^2)x^2}{r^3(r+z)^2} & \frac{(2r(\nu r+z)+z^2)xy}{r^3(r+z)^2} & \frac{xz}{r^3} - \frac{(1-2\nu)x}{r(r+z)} \\ \frac{(2r(\nu r+z)+z^2)xy}{r^3(r+z)^2} & \frac{2(1-\nu)r+z}{r(r+z)} + \frac{(2r(\nu r+z)+z^2)y^2}{r^3(r+z)^2} & \frac{yz}{r^3} - \frac{(1-2\nu)y}{r(r+z)} \\ \frac{(1-2\nu)x}{r(r+z)} + \frac{xz}{r^3} & \frac{(1-2\nu)y}{r(r+z)} + \frac{yz}{r^3} & \frac{2(1-\nu)}{r} + \frac{z^2}{r^3} \end{pmatrix}, \tag{2.20}$$

where we used $r = \sqrt{x^2+y^2+z^2}$. Cases where the substrate is not sufficiently thick and interactions at the bottom surface of a finite-thickness substrate cannot be neglected have also been studied [18]. In these cases, the convolution relation is still valid, but a different Green's function has to be used. Note the $1/r$-dependence of this Green's function, it is the reason why the inverse problem to Eq 2.19 is ill-posed.

2.2.3 The Boussinesq-Cerruti potential functions

Finding solutions for Eq 2.18 can be simplified by introducing appropriate potential functions. An approach using harmonic potential functions is known as Boussinesq-Cerruti potential functions [113, 114]. For a given surface traction field $\boldsymbol{\tau}$, we find solutions P_1, P_2 and P_3 that each solve the boundary value problem

$$\nabla^2 P_i = 0\,, \quad \partial_z^3 P_i|_{z=0} = -\tau_i\,.. \tag{2.21}$$

It can now be shown, that if a solution P_i to this boundary value problem has been found, a solution of Eq 2.18 is now given by:

$$u_i = \sum_{j=1}^{3} u_i^{(j)}, \tag{2.22}$$

together with the x-tangential contributions

$$\begin{aligned} 2\mu u_x^{(1)} &= 2\nu\partial_x^2 P_x + 2\partial_z^2 P_x - z\partial_x^2\partial_z P_x \\ 2\mu u_y^{(1)} &= 2\nu\partial_x\partial_y P_x - z\partial_x\partial_y\partial_z P_x \\ 2\mu u_z^{(1)} &= (1-2\nu)\partial_x\partial_z P_x - z\partial_x\partial_z^2 P_x, \end{aligned} \tag{2.23}$$

the y-tangential contributions

$$\begin{aligned} 2\mu u_x^{(2)} &= 2\nu\partial_x\partial_y P_y - z\partial_x\partial_y\partial_z P_y \\ 2\mu u_y^{(2)} &= 2\nu\partial_y^2 P_y + 2\partial_z^2 P_y - z\partial_y^2\partial_z P_y \\ 2\mu u_z^{(2)} &= (1-2\nu)\partial_y\partial_z P_y - z\partial_y\partial_z^2 P_y \end{aligned} \tag{2.24}$$

and the normal (z) contributions

$$\begin{aligned} 2\mu u_x^{(3)} &= -(1-2\nu)\partial_x\partial_z P_z - z\partial_x\partial_z^2 P_z \\ 2\mu u_y^{(3)} &= -(1-2\nu)\partial_y\partial_z P_z - z\partial_y\partial_z^2 P_z \\ 2\mu u_z^{(3)} &= 2(1-\nu)\partial_z^2 P_z - z\partial_z^3 P_z. \end{aligned} \tag{2.25}$$

2.2.4 3D displacement fields for a Hertz-like force profile

In this subsection, I determine an analytical solution for the infinite halfspace problem presented in Eq 2.18 with the boundary condition

$$\boldsymbol{\tau}(\boldsymbol{x}) = \begin{cases} \frac{3}{2\pi a^3}\boldsymbol{F}\sqrt{a^2-(\boldsymbol{x}-\boldsymbol{x}_c)^2} & (\boldsymbol{x}-\boldsymbol{x}_c)^2 < a^2 \\ 0 & (\boldsymbol{x}-\boldsymbol{x}_c)^2 \geq a^2 \end{cases}, \tag{2.26}$$

with the vector notation $\boldsymbol{x} = (x, y)^T$.

This profile is identical to the one generated by a sliding Hertz contact and aims to approximate structures found in physical adhesion profiles, in particular focal adhesions. The parameter $\boldsymbol{x}_0 = (x_0, y_0)^T$ describes the center of a force transmission area, a its radius and $\boldsymbol{F}$ the total force transmitted.

In a first step, we note, that the profile can be separated into a tangential and a normal component:

$$\boldsymbol{\tau}(\boldsymbol{x}) = R(\phi)\boldsymbol{\tau}_T(F_T, R(\phi)^{-1}(\boldsymbol{x}-\boldsymbol{x}_0)) + \boldsymbol{\tau}_N(F_N, \boldsymbol{x}-\boldsymbol{x}_0). \tag{2.27}$$

$$\boldsymbol{\tau}_T(Q, \boldsymbol{x}) = \frac{3}{2\pi a^3} Q\boldsymbol{e}_x\sqrt{a^2-\boldsymbol{x}^2}\Theta(a^2-\boldsymbol{x}^2) \tag{2.28}$$

$$\boldsymbol{\tau}_N(Q, \boldsymbol{x}) = \frac{3}{2\pi a^3} Q\boldsymbol{e}_z\sqrt{a^2-\boldsymbol{x}^2}\Theta(a^2-\boldsymbol{x}^2) \tag{2.29}$$

Here, we use the definitions $F_N = F_z$ and $F_T = \sqrt{F_x^2 + F_y^2}$. The angle ϕ is chosen such that $F_x = F_T\cos(\phi)$ and $F_y = F_T\sin(\phi)$. $R(\phi)$ describes the matrix of an active rotation by an angle ϕ. Θ describes the Heaviside step function:

$$\Theta(x) = \begin{cases} 0 & x < 0 \\ \frac{1}{2} & x = 0 \\ 1 & x > 0 \end{cases} \tag{2.30}$$

Now, we only need to find the deformation field corresponding to $\boldsymbol{\tau}_T$ and $\boldsymbol{\tau}_N$.

I deal with $\boldsymbol{\tau}_N$ first. Following an ansatz put forward by [119], we first define a function

$$\mathcal{M}(x, y, z) = \int_0^a t(\xi)k(x, y, z+i\xi)\,\mathrm{d}\xi \tag{2.31}$$

k is chosen in a such a way that $\mathcal{M}$ is a complex harmonic function ($\nabla^2\mathcal{M} = 0$):

$$k(x, y, z_1) = \frac{1}{2}\left(z_1^2 - \frac{1}{2}r^2\right)\ln(z_1 + R_1) - \frac{3}{4}R_1 z_1 + \frac{1}{4}r^2 \tag{2.32}$$

I use the abbreviations $r = \sqrt{x^2+y^2}$ and $R_1 = \sqrt{z_1^2+r^2}$ and $t(\xi)$ is a function defined on the integration interval.

I will make use of the Boussinesq-Cerruti potential functions introduced in Eq 2.22 We can now find solutions to Eq 2.18 by setting

$$P_{N,x} = 0 \qquad P_{N,y} = 0 \qquad P_{N,z} = \operatorname{Im}\mathcal{M} \tag{2.33}$$

The definitions of $P_{N,x}$ and $P_{N,y}$ provide trivial solutions to their boundary value problems. The field equation for $P_{N,z}$ is already satisfied, because $P_{N,z}$ is harmonic from

being the imaginary part of a complex harmonic function. The boundary condition for $P_{N,z}$ results in an integral problem for $t(\xi)$ given by:

$$\begin{aligned}\tau_{N,z}(P,x,y) = -\partial_z^3 P_{N,z}|_{z=0} &= -\operatorname{Im}\int_0^a t(\xi)\frac{1}{\sqrt{r^2+(i\xi)^2}}\,\mathrm{d}\xi \\ &= \int_r^a t(\xi)\frac{1}{\sqrt{\xi^2-r^2}}\,\mathrm{d}\xi\end{aligned} \quad . \tag{2.34}$$

For the specific profile of $\tau_{N,z}$ given in Eq 2.29 this can be solved by setting:

$$t(\xi) = \frac{3Q}{2\pi a^3}\xi. \tag{2.35}$$

To solve the resulting integral formula Eq 2.31, we transform the integral path onto a complex curve:

$$\begin{aligned}P_z(x,y,z) = \operatorname{Im}\frac{3Q}{2\pi a^3}\int_\gamma (z-z_1)k(x,y,z_1)\,\mathrm{d}z_1 \\ \text{for } \gamma : \xi \in [0,a] \longmapsto z_1(\xi) = z + i\xi.\end{aligned} \tag{2.36}$$

Now, we find a function $\mathcal{M}_1$, such that $\mathcal{M}_1(x,y,z,\cdot)$ is holomorphic and

$$\frac{\mathrm{d}}{\mathrm{d}z_1}\mathcal{M}_1(x,y,z,z_1) = (z-z_1)k(x,y,z_1) \tag{2.37}$$

for all z_1 in a open set containing γ. By explicit calculation one can verify, that

$$\begin{aligned}&\mathcal{M}_1(x,y,z,z_1) = \\ &\frac{r^2\left(16z\left(4R_1+9z_1\right)-9z_1\left(R_1+8z_1\right)\right)}{576} + \frac{z_1^2 R_1(63z_1-88z)}{288} \\ &+\frac{\left(3r^4+24r^2z_1(z_1-2z)+8z_1^3(4z-3z_1)\right)\ln\left(R_1+z_1\right)}{192}\end{aligned} \tag{2.38}$$

is a suitable solution. The function $\mathcal{M}_1$ is holomorphic in z_1 except if $z_1 = im$ for $m \in \mathbb{R}$, $|m| > r$. We now find for P_z:

$$\begin{aligned}P_z(x,y,z) &= \operatorname{Im}\frac{3Q}{2\pi a^3}\left(\mathcal{M}_1(x,y,z,z+ia) - \mathcal{M}_1(x,y,z,z)\right) \\ &= \operatorname{Im}\frac{3Q}{2\pi a^3}\mathcal{M}_1(x,y,z,z+ia)\end{aligned} \tag{2.39}$$

In preparation of finding expressions for the deformation field, we also calculate an auxiliary function, $\mathcal{M}_2(x,y,z)$

$$\begin{aligned}\mathcal{M}_2(x,y,z) &= \partial_z\left(\mathcal{M}_1(x,y,z,z+ia)\right) \\ &= (\partial_z\mathcal{M}_1)(x,y,z,z_2) + (z-z_2)k(x,y,z_2) \\ &= \frac{4z_2^2+r^2}{9}R_2 - \frac{z_2^3}{3}\log\left(z_2+R_2\right) + zk(x,y,z_2)\end{aligned} \quad , \tag{2.40}$$

where $z_2 = z + ia$ and $R_2 = \sqrt{z_2^2+r^2}$.

Next, we insert the expression for the potential function $P_{N,z}$ into Eq 2.31 and simplify the partial derivative in z direction using $\mathcal{M}_2$. We find:

$$\begin{aligned} u_{N,x}(x,y,z) &= \frac{3Q}{4\pi\mu a^3}\,\mathrm{Im}\left((2\nu-1)\partial_x\mathcal{M}_2(x,y,z) - z\partial_x\partial_z\mathcal{M}_2(x,y,z)\right) \\ u_{N,y}(x,y,z) &= \frac{3Q}{4\pi\mu a^3}\,\mathrm{Im}\left((2\nu-1)\partial_y\mathcal{M}_2(x,y,z) - z\partial_y\partial_z\mathcal{M}_2\right) \\ u_{N,z}(x,y,z) &= \frac{3Q}{4\pi\mu a^3}\,\mathrm{Im}\left(2(1-\nu)\partial_z\mathcal{M}_2(x,y,z) - z\partial_z^2\mathcal{M}_2(x,y,z)\right) \end{aligned} \tag{2.41}$$

These equations can easily be solved analytically.

Next, I find a solution for $\boldsymbol{\tau}_T$. We note that $\boldsymbol{\tau}_{T,x}$ looks identical to $\boldsymbol{\tau}_{N,z}$. Since the equations for the 3 Boussinesq-Cerruti potential functions given in 2.21 do not couple, we can simply set

$$P_{T,x} = P_{N,x} = \mathrm{Im}\,\frac{3Q}{2\pi a^3}\mathcal{M}_1(x,y,z,z+ia) \qquad P_{T,y} = 0 \qquad P_{T,z} = 0. \tag{2.42}$$

Again, we can insert the expression for the potential function $P_{T,z}$ into Eq 2.31 and simplify the partial derivative in z direction using $\mathcal{M}_2$. We find:

$$\begin{aligned} u_{T,x}(x,y,z) &= \frac{3Q}{4\pi\mu a^3}\,\mathrm{Im}\left(2\nu\partial_x^2\mathcal{M}_1(x,y,z,z_2) + \left(2\partial_z - z\partial_x^2\right)\mathcal{M}_2(x,y,z)\right) \\ u_{T,y}(x,y,z) &= \frac{3Q}{4\pi\mu a^3}\,\mathrm{Im}\left(2\nu\partial_x\partial_y\mathcal{M}_1(x,y,z,z_2) - z\partial_x\partial_y\mathcal{M}_2(x,y,z)\right) \\ u_{T,z}(x,y,z) &= \frac{3Q}{4\pi\mu a^3}\,\mathrm{Im}\left((1-2\nu)\partial_x\mathcal{M}_2(x,y,z) - z\partial_x\partial_z\mathcal{M}_2(x,y,z)\right). \end{aligned} \tag{2.43}$$

Again, these equations can be solved analytically.

2.2.5 Surface displacement fields for a constant traction and Hertz-like contact profiles

In many cases only the deformations at the surface $\bar{\boldsymbol{u}} = \boldsymbol{u}|_{z=0}$ are needed, as these are the only ones observable using 2D TFM. In this case, the calculation can be greatly simplified and solutions are more widely available in literature, e.g. in Johnson's *Contact mechanics* [120].

Circular constant traction contact

The analytical solution for the surface deformation created by a tangential traction force $\boldsymbol{F} = (F_x, F_y)^T$ distributed equally over a circular area with radius a at the surface of a sufficiently thick substrate in the linear, isotropic elastic regime has recently been calculated in the context of traction force microscopy [14]. Employing polar coordinates $\boldsymbol{x} = r(\cos\theta, \sin\theta)$ centered around the middle of the circular adhesion, the surface traction profile is given by:

$$\boldsymbol{\tau}(r,\theta) = \begin{cases} \frac{\boldsymbol{F}}{\pi a^2} & r < a \\ 0 & r \geq a \end{cases} \tag{2.44}$$

The profile is shown in Fig 2.2 A and the corresponding deformation field is given by

$$\bar{u}_x(r,\theta) = \frac{1+\nu}{\pi^2 aE}\left[(1-\nu)N_1(r,\theta) + \nu N_2(r,\theta))F_x - \nu N_3(r,\theta)F_y\right] \tag{2.45}$$

$$\bar{u}_y(r,\theta) = \frac{1+\nu}{\pi^2 aE}\left[-\nu N_3(r,\theta)F_x + (1-\nu)N_1(r,\theta) + \nu N_4(r,\theta))F_y\right] \tag{2.46}$$

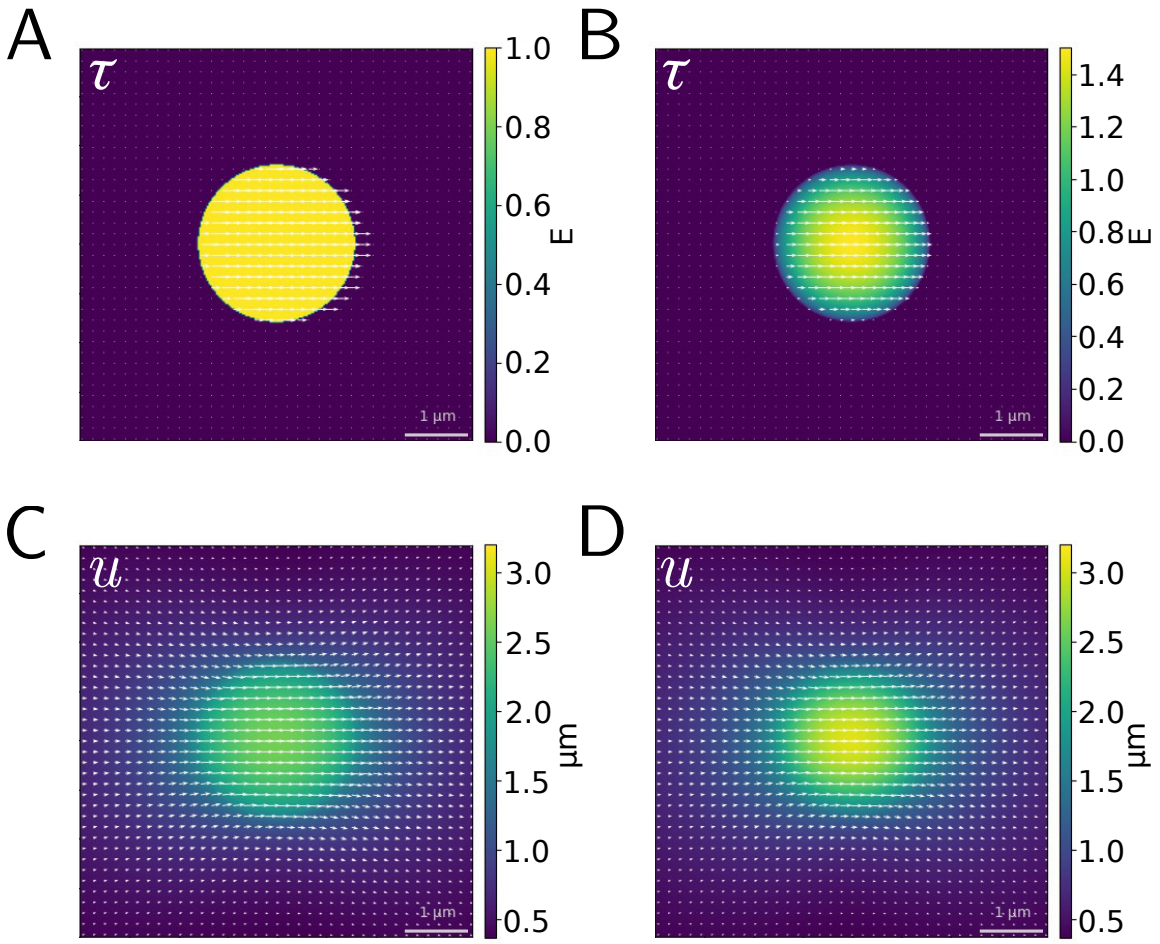

Figure 2.2: Visualization of constant traction and Hertz-like contact profiles. (A) Traction profile for a constant traction profile for a force field oriented in direction of the x-axis (B) Traction profile for a Hertz-like contact profile with same orientation and contact area. (C) Deformation field for the constant traction profile. (D) Deformation field for the Hertz-like traction profile

Here the E describes the substrate stiffness (Young's modulus) and ν the Poisson ratio. The functions N_1 to N_4 have the following form in the inner region where $r < a$ and $\xi_1 = r^2/a^2$:

$$N_1 = 4E_0(\xi_1) \tag{2.47}$$

$$N_2 = \frac{4\cos(2\theta)\left((r^2+a^2)E_0(\xi_1) + (r^2-a^2)K_0(\xi_1)\right)}{3r^2} + 4\sin^2\theta E_0(\xi_1) \tag{2.48}$$

$$N_3 = \frac{2\sin(2\theta)\left((r^2-2a^2)E_0(\xi_1) + (r^2-a^2)K_0(\xi_1)\right)}{3r^2} \tag{2.49}$$

$$N_4 = 4\cos^2\theta E_0(\xi_1) - \frac{4\cos(2\theta)\left((r^2+a^2)E_0(\xi_1) + (r^2-a^2)K_0(\xi_1)\right)}{3r^2}\,. \tag{2.50}$$

For the outer region where $r > a$ and $\xi_2 = a^2/r^2$ we have

$$N_1 = \frac{4\left(r^2 E_0(\xi_2) + (a^2 - r^2)K_0(\xi_2)\right)}{ar} \tag{2.51}$$

$$N_2 = \frac{\left(6r^2 - 2(r^2 - 2a^2)\cos(2\theta)\right)E_0(\xi_2) + 2(r^2 - a^2)(\cos(2\theta) - 3)K_0(\xi_2)}{3ar} \tag{2.52}$$

$$N_3 = \frac{2\sin(2\theta)\left((r^2 - 2a^2)E_0(\xi_2) + (a^2 - r^2)K_0(\xi_2)\right)}{3ar} \tag{2.53}$$

$$N_4 = \frac{\left(6r^2 + 2(r^2 - 2a^2)\cos(2\theta)\right)E_0(\xi_2) - 2(r^2 - R^2)(\cos(2\theta) + 3)K_0(\xi_2)}{3ar}\,. \tag{2.54}$$

In both cases, K_0 and E_0 are the complete elliptic integrals of the first and second kind [121]:

$$K_0(m) = \int_0^{\frac{\pi}{2}} \frac{d\theta}{\sqrt{1 - m\sin^2\theta}} \qquad E_0(m) = \int_0^{\frac{\pi}{2}} \sqrt{1 - m\sin^2\theta}\, d\theta \tag{2.55}$$

The shape of the deformation field is shown in Fig 2.2 C.

Circular Hertz-like contact

The surface deformation created by a tangential traction force distributed in a Hertz-like manner over a circular area is known from contact mechanics [120]. Employing Cartesian coordinates centered on the center of the circular adhesion, and the abbreviation $r = \sqrt{x^2 + y^2}$, the surface traction profile, presented in 2.2.4 is given by:

$$\boldsymbol{\tau}(x, y) = \begin{cases} \frac{3\boldsymbol{F}}{2\pi a^3}\sqrt{a^2 - r^2} & r < a \\ 0 & r \geq a \end{cases} \tag{2.56}$$

The corresponding deformation field is given by:

$$\bar{u}_x(x, y) = \frac{3(1 + \nu)}{8Ea^3}((W_1 + W_2)F_x + W_3 F_y) \tag{2.57}$$

$$\bar{u}_y(x, y) = \frac{3(1 + \nu)}{8Ea^3}(W_3 F_x + (W_1 + W_4)F_y) \tag{2.58}$$

The functions W_1 to W_4 have the following form in the inner region where $r < a$:

$$W_1 = \frac{1}{4}4(2 - \nu)a^2 \tag{2.59}$$

$$W_2 = -\frac{1}{4}((4 - 3\nu)x^2 + (4 - \nu)y^2) \tag{2.60}$$

$$W_3 = \frac{1}{4}2\nu xy \tag{2.61}$$

$$W_4 = -\frac{1}{4}((4 - 3\nu)y^2 + (4 - \nu)x^2)\,. \tag{2.62}$$

For the outer region where $r > a$ and $\xi_2 = a^2/r^2$ we have:

$$W_1 = \frac{2-\nu}{\pi}\left((2a^2 - r^2)\arcsin\frac{a}{r} + ar\sqrt{1-\frac{a^2}{r^2}}\right) \tag{2.63}$$

$$W_2 = \frac{\nu}{2\pi}\left(r^2\arcsin\frac{a}{r} + (2a^2 - r^2)\frac{a}{r}\sqrt{1-\frac{a^2}{r^2}}\right)\frac{x^2-y^2}{r^2} \tag{2.64}$$

$$W_3 = \frac{1}{\pi}\left(r^2\arcsin\frac{a}{r} + (2a^2 - r^2)\frac{a}{r}\sqrt{1-\frac{a^2}{r^2}}\right)\frac{xy}{r^2} \tag{2.65}$$

$$W_4 = \frac{\nu}{2\pi}\left(r^2\arcsin\frac{a}{r} + (2a^2 - r^2)\frac{a}{r}\sqrt{1-\frac{a^2}{r^2}}\right)\frac{y^2-x^2}{r^2}\,. \tag{2.66}$$

These expressions show the corrected version the equations found in [120], where a normalization factor $1/r^2$ is included in W_2 to W_4 [122].

The shape of the traction and deformation is shown in Fig 2.2 B and D. We can easily verify, that Eq 2.57 and 2.58 describe a special case of Eq 2.43.

Elliptical Hertz-like contact

Finally, I also present the results for an elliptical contact, that has been elongated to an elliptical shape. For simplicity, we assume that the direction of force and one of the semi-axes are both parallel to the x-axis. The general case where both the semi-axes and the direction of force do not align can be found using a combination of rotation and superposition, similar to 2.27. The traction field for this setup is given by

$$\boldsymbol{\tau}(x,y) = \begin{cases} \frac{3F_x\mathbf{e}_x}{2\pi ab}\sqrt{1-\frac{x^2}{a^2}-\frac{x^2}{b^2}} & \frac{x^2}{a^2}+\frac{y^2}{b^2} < 1 \\ 0 & \frac{x^2}{a^2}+\frac{y^2}{b^2} \geq 1 \end{cases}, \tag{2.67}$$

where we used a to designate the semi-axes parallel to the x and b to designate the semi-axes parallel to the y axes.

The deformation field for this kind of profile inside the contact area has been found by Vermeulen and Johnson [123]:

$$\bar{u}_x = \frac{3}{4\pi\mu}\left[\Gamma\left(\frac{a}{b}\right) - \Phi\left(\frac{a}{b}\right)\frac{x^2}{a^2} - \Psi\left(\frac{a}{b}\right)\frac{y^2}{b^2}\right] \tag{2.68}$$

$$\bar{u}_y = \frac{3}{4\pi\mu}\Theta\left(\frac{a}{b}\right)\frac{xy}{ab} \tag{2.69}$$

Here we used the definitions Γ, Φ, Ψ and Θ given by:

$$\Gamma\left(\frac{a}{b}\right) = \begin{cases} K_0(m) - \nu D(m) & a < b \\ \frac{\pi(2-\nu)}{4} & a = b \\ \frac{b}{a}\left[K_0(m) - \nu B(m)\right] & a > b \end{cases} \tag{2.70}$$

$$\Phi\left(\frac{a}{b}\right) = \begin{cases} B(m) - \frac{\nu}{m}\left(2B(m) - E_0(m)\right) & a < b \\ \frac{\pi(4-3\nu)}{16} & a = b \\ \frac{b}{a}\left[D(m) - \frac{\nu}{m}\left(2B(m) - E_0(m)\right)\right] & a > b \end{cases} \tag{2.71}$$

$$\Psi\left(\frac{a}{b}\right) = \begin{cases} D(m) - \frac{\nu}{m}\left(D(m) - B(m)\right) & a < b \\ \frac{\pi(4-\nu)}{16} & a = b \\ \frac{b}{a}\left[B(m) - \nu\frac{b^2}{a^2 m}(D(m) - B(m))\right] & a > b \end{cases} \tag{2.72}$$

$$\Theta\left(\frac{a}{b}\right) = \begin{cases} 2\nu\frac{a}{bm}\left(D(m) - B(m)\right) & a < b \\ \frac{\pi\nu}{8} & a = b \\ 2\nu\frac{b^2}{a^2 m}(D(m) - B(m)) & a > b. \end{cases} \tag{2.73}$$

$$\tag{2.74}$$

Here K_0 and E_0 are the complete elliptic integrals of the first and second kind as above and B as well as D are functions given by:

$$B(m) = K_0(m) - D(m) \qquad D(m) = \frac{1}{m}\left(K_0(m) - E_0(m)\right) \tag{2.75}$$

The modulus m is given by $m = 1 - a^2/b^2$ for $a < b$ and $m = 1 - a^2/b^2$ for $b > a$.

2.3 Green's function-based 2D force inference

2.3.1 Quantization approaches and regularization

As mentioned in the introductory chapter, Green's function-based approaches rely on the formulation of a direct problem, by means of which displacement can be predicted from current traction estimates in order to verify and improve the current estimate. In principle this problem has already been solved in Eq 2.19 and 2.20. In 2.5D TFM the Green's function can be used directly. In 2D TFM only the planar part is used. This is justified by the fact that the normal traction is on average significantly smaller than its normal counterpart and hydrogels are mostly incompressible ($\nu \approx 0.5$). This means that the factor $2\nu - 1$ becomes very small, which causes the in-plane and normal components of the displacement and traction field to decouple [47]. We can therefore neglect the in-plane normal interaction as well as the normal component itself entirely. In general, the embedding depth z of the beads is also considered to be negligible. Using these two simplifications the Greens function reduces to a simple 2D one,

$$\mathbf{G}(x, y) = \frac{1+\nu}{2\pi E r^3} = \begin{pmatrix} (1-\nu)r^2 + \nu x^2 & \nu xy \\ \nu xy & (1-\nu)r^2 + \nu y^2 \end{pmatrix}, \tag{2.76}$$

where the Fredholm integral simplifies to

$$\overline{\boldsymbol{u}}(x, y) = \int_S \mathbf{G}(x - x', y - y') \cdot \boldsymbol{\tau}(x', y')\, \mathrm{d}x'\, \mathrm{d}y'\,. \tag{2.77}$$

For simplicity and to agree with conventions found elsewhere (e.g. [12, 76]), we omit the bar over the deformation symbol in the following, when describing the surface deformation. In order to solve Eq 2.19 numerically, we must now discretize both $\boldsymbol{u}$ and $\boldsymbol{\tau}$ to reduce the problem to a numerically traceable operation.

Boundary element method

The first way to do so is using the so-called boundary element method (BEM)) [8, 10], a detailed description of which was given by Sabass *et al.* [101]. This method starts by determining a boundary of the computational mesh, that should encompass all points where non-zero traction is to be expected. Typically, an area larger than the one enclosed by the cell boundary is selected to avoid boundary effects. Next, each point $\boldsymbol{x}_n$ where the displacement vector $\boldsymbol{u}_n^{(\mathrm{exp})}$ has been predicted in the image registration step is marked and a triangulation network between the sampling points is established. Then, a linear interpolation and separation into a weighted element representation of $\boldsymbol{u}(\boldsymbol{x})$ is produced. Now using the procedure described in the appendix of Sabass *et al.* [101], a matrix formulation of Eq 2.77 is obtained:

$$u_{im} = \sum_{j=1}^{2} \sum_{n} \mathrm{M}_{ijmn} \tau_{jn} \tag{2.78}$$

$\boldsymbol{\tau}_n$ and $\boldsymbol{u}_n$ now describe the traction vector and the predicted displacement vector at each sampling point. The matrix elements relating adjacent (near field), mid-distanced and far-distanced matrix elements are treated differently. Only for mid distance nodes the integration over the matrix elements is performed explicitly. When calculating the near-field elements, angular coordinates are used to avoid the divergence in the limit $|\boldsymbol{x}^{'} - \boldsymbol{x}| \to 0$. For the far field an approximate procedure is used to simplify the calculation.

While the solution $\boldsymbol{\tau}_n$ fitting $\boldsymbol{u}_n^{(\mathrm{exp})}$ most faithfully can be found by inverting the matrix application Eq 2.78 directly, this will not produce robust traction estimates, since the inverse problem of elasticity is ill-posed. This is the case, because elastic effects are long-ranged, meaning that local changes in traction will have non-negligible effects on the displacement even over large distances. This is a problem because the input data for the displacement field will be always subject to experimental noise due to limitations in resolution or inhomogeneities in the medium [76]. A naive inversion will try to reproduce all the fine details of the input field by changing global properties of the force field, thus this ill-posed nature of the inverse problem will be reflected by a large condition number of the inverse matrix. This problem can be addressed either by filtering the displacement data, e.g. by image smoothing [8, 12], or by introducing a regularization scheme [11, 14].

While this can be explained purely numerically [124, 125], a probabilistic motivation for regularization was given by Huang *et al.* [14]: Taking into account the noise, Eq 2.78 can be written as

$$\boldsymbol{u} = \mathbf{M} \cdot \boldsymbol{\tau} + \boldsymbol{s}. \tag{2.79}$$

Here $\boldsymbol{s}$ now designates a random variable representing the noise and $\boldsymbol{u}^{(\mathrm{exp})}$ can be seen as one particular realization of $\boldsymbol{u}$ and we have collected all M sampling points into a $2M \times 1$ vector. Assuming the noise to be Gaussian distributed, which has been verified to be a good approximation [126], the probability density can now be written

$$p(\boldsymbol{u}|\boldsymbol{\tau}, \beta) = \frac{1}{Z_u} \exp\left(-\frac{\beta}{2} (\mathbf{M}\boldsymbol{\tau} - \boldsymbol{u})^T (\mathbf{M}\boldsymbol{\tau} - \boldsymbol{u}) \right). \tag{2.80}$$

Here β describes the spread of distribution due to noise and $Z_u = (2\pi/\beta)^M$. One can now postulate a certain prior-distribution on the force configuration:

$$p(\boldsymbol{\tau}|\alpha) = \frac{1}{Z_f}\exp\Big(-\frac{\alpha}{2}\boldsymbol{\tau}^T\boldsymbol{\tau}\Big)), \tag{2.81}$$

where $Z_f = (2\pi/\alpha)^M$. This prior describes the fact that when selecting between solutions with large force magnitude and those with small one, the large force magnitude is considered more energy expensive and thus less probable. According to Bayes' rule the distribution of $\boldsymbol{\tau}$ can be found as a posterior:

$$p(\boldsymbol{\tau}|\boldsymbol{u},\alpha,\beta) = \frac{p(\boldsymbol{u}|\boldsymbol{\tau},\beta)p(\boldsymbol{\tau}|\alpha)}{p(\boldsymbol{u}|\alpha,\beta)} = \frac{\exp\big(-\frac{\beta}{2}K(\boldsymbol{\tau})\big)}{Z_u Z_f p(\boldsymbol{u}|\alpha,\beta)}, \tag{2.82}$$

where

$$K(\boldsymbol{\tau}) = (\mathbf{M}\boldsymbol{\tau}-\boldsymbol{u})^T(\mathbf{M}\boldsymbol{\tau}-\boldsymbol{u}) + \frac{\alpha}{\beta}\boldsymbol{\tau}^T\boldsymbol{\tau} \tag{2.83}$$

and

$$p(\boldsymbol{u}|\alpha,\beta) = \int \frac{\exp\big(-\frac{\beta}{2}K(\boldsymbol{\tau})\big)}{Z_u Z_f}\,\mathrm{d}^{2M}\tau\,. \tag{2.84}$$

The highest posterior probability solution $\boldsymbol{\tau}_{\mathrm{MP}}$, maximizes $p(\boldsymbol{\tau}|\alpha)$ and can thus be found by minimizing $K(\boldsymbol{\tau})$:

$$\begin{aligned}\boldsymbol{\tau}_{\mathrm{MP}} &= \arg\min_{\boldsymbol{\tau}}\left((\mathbf{M}\boldsymbol{\tau}-\boldsymbol{u})^T(\mathbf{M}\boldsymbol{\tau}-\boldsymbol{u}) + \lambda^2\boldsymbol{\tau}^T\boldsymbol{\tau}\right)\\ &= \left(\mathbf{M}^T\mathbf{M}+\lambda^2\mathbf{I}\right)^{-1}\mathbf{M}^T\boldsymbol{u}.\end{aligned} \tag{2.85}$$

where we defined $\lambda^2 = \alpha/\beta$. The second term in the first row describes a regularization, in this case, the so-called L2 or 0^{th}-order Tikhonov regularization [124, 125]. This kind of regularization effectively results in smoothing of the underlying traction field and significantly increases the stability of our reconstruction [14].

While the L2 regularization is by far the most popular choice [11, 69, 101], other optimization criteria have also been discussed. The L1 regularization, also known as Lasso regression [127], has also been occasionally used [128–130]. It is defined by replacing the Euclidean norm in the regularization term by a Taxicab one, meaning

$$\boldsymbol{\tau}_{\mathrm{L1}} = \arg\min_{\boldsymbol{\tau}}\left((\mathbf{M}\boldsymbol{\tau}-\boldsymbol{u})^T(\mathbf{M}\boldsymbol{\tau}-\boldsymbol{u}) + \lambda_1\|\boldsymbol{\tau}\|_1\right), \tag{2.86}$$

where $\|\boldsymbol{\tau}\|_1 = \sum_{j=1}^{2}\sum_n |\tau_{jn}|$. In contrast to the L2 regularization, which optimizes against high magnitude, energy intensive configurations, this norm also minimizes the number of non-zero components in the traction vector $\boldsymbol{\tau}$ [128] which often improves the level of background noise [14].

The elastic net or EN regularization [131] combines the regularization terms of L1 and L2 in order to achieve the effects of both factors and is particularly suited for correlated entries. While it is rarely used in TFM, Huang *et al.* [14] showed that such a regularization could potentially improve force reconstruction.

Traction reconstruction with point forces

A second reconstruction method introduced by Schwarz *et al.* [11] has been suggested in the case focal adhesions are clearly locatable due to being tagged with a fluorescent label. This method is known as traction reconstruction with point forces (TRFP). As suggested by its name, the traction field is now modeled by a collection of singular force peaks located at the site of each focal adhesion $\boldsymbol{\tau}(\mathbf{x}) = \sum_i \boldsymbol{F}_i \delta(\mathbf{x} - \mathbf{x}'_i)$. This assumption neglects the finite extend of each adhesion. Due to their singular nature, the Fredholm integral now reduces to a simple matrix application,

$$\boldsymbol{u}(\boldsymbol{x}_n) = \sum_i \mathbf{G}(\mathbf{x} - \mathbf{x}'_i)\boldsymbol{F}_i, \tag{2.87}$$

in the direct problem. This can now be inverted by an L2 Regularization as described for the BEM.

Fourier Transform Traction Cytomety

Many of the computational issue of solving Eq 2.77 can be avoided by Fourier Transform Traction Cytomety (FTTC), which is the most widely used inverse method [12, 69, 101, 102, 128]. This approach uses the fact that the Fredholm integral from Eq 2.77 becomes a product in Fourier space and that fast Fourier transforms allow one to quickly switch between real and Fourier space numerically.

To use it, the displacement field $\boldsymbol{u}(\boldsymbol{x})$ must first be interpolated onto a regular, rectangular grid covering the whole image. We will designate the values at the sample points $\boldsymbol{x}_{ij}$ by $\boldsymbol{u}_{ij}$ in the following, where $i = 0 \dots (N_x - 1)$ and $j = 0 \dots (N_y - 1)$, yielding a total number of $M = N_x \cdot N_y$ nodes. Then the traction force $\boldsymbol{\tau}(x, y)$ is described by a set of plane waves $\hat{f}_{mn}(x, y)$

$$\boldsymbol{\tau}(x,y) = \sum_{m=0}^{N_x-1} \sum_{n=0}^{N_y-1} \hat{\boldsymbol{\tau}}_{mn} \hat{f}_{mn}(x,y) \ , \qquad \hat{f}_{mn}(\boldsymbol{x}) = \frac{1}{N_x N_y} e^{\mathrm{i}\boldsymbol{k}_{mn}\cdot\boldsymbol{x}} \ . \tag{2.88}$$

The wave vectors $\boldsymbol{k}_{mn}$ are chosen in accordance with the sampling grid. This choice ensures that the expansion coefficients $\hat{\boldsymbol{\tau}}_{mn}$ are in fact the 2D discrete Fourier transform of the traction sampled at the $\boldsymbol{x}_{ij}$. Due to the Fourier convolution theorem, Eq 2.77 reduces to

$$\hat{\boldsymbol{u}}_{mn} = \tilde{\mathbf{G}}\left(k_{mn,x}, k_{mn,y}\right) \cdot \hat{\boldsymbol{\tau}}_{mn}, \tag{2.89}$$

where $\hat{\boldsymbol{u}}_{mn}$ and $\boldsymbol{u}_{ij}$ are also related by a 2D discrete Fourier transform. The term $\tilde{\mathbf{G}}(k_x, k_y)$ describes the function obtained from applying a continuous Fourier transform in the two tangential directions to the real space Green's function, defined in Eq 2.76, which is given by [12, 101]

$$\tilde{\mathbf{G}}(k_x, k_y) = \frac{2(1+\nu)}{Ek^3} \begin{pmatrix} (1-\nu)k^2 + \nu k_y^2 & -\nu k_x k_y \\ -\nu k_x k_y & (1-\nu)k^2 + \nu k_x^2 \end{pmatrix}. \tag{2.90}$$

The full description of the direct problem relating the real space traction values $\boldsymbol{\tau}_{ij}$ to their displacement equivalents $\boldsymbol{u}_{ij}$ is now defined by:

$$\boldsymbol{u}_{ij} = \underset{mn}{\mathrm{IDFT}} \left[\tilde{\mathbf{G}}\left(\boldsymbol{k}_{mn}\right) \cdot \underset{i'j'}{\mathrm{DFT}}(\boldsymbol{\tau}_{i'j'})_{mn} \right]_{ij}, \tag{2.91}$$

where DFT and IDFT designate the Discrete Fourier Transform and its inverse respectively.

Eq 2.89 diverges when evaluating at $\boldsymbol{k}_{00} = 0$. This can be avoided by restricting our model to cases, where $\hat{\boldsymbol{\tau}}_{00} = 0$, which corresponds to a vanishing total integrated force in the entire field of view, thus removing this mode from our calculation. This limitation is generally not significant in traction force reconstruction due to the internal force balance of the cell. This topic will be further discussed in chapter 5.

Similar to the BEM, directly inverting Eq 2.91 to obtain the least-square fit force reconstruction of the experimentally obtained deformation field suffers from noise related overfitting issues. Some researches [12, 59] addressed this, by smoothing the deformation field using a series of filters prior to force reconstruction. Instead, and in close analogy to the BEM, a L2 regularization scheme can be introduced to find a robust traction reconstruction [69, 101]:

$$\boldsymbol{\tau}_{MP} = \arg\min_{\boldsymbol{\tau}} \left\| \boldsymbol{u}^{(\mathrm{exp})} - \underset{mn}{\mathrm{IDFT}} \left[\tilde{\mathbf{G}}\left(\boldsymbol{k}_{mn}\right) \cdot \underset{i'j'}{\mathrm{DFT}}(\boldsymbol{\tau}_{i'j'})_{mn} \right] \right\|_2^2 + \lambda^2 \|\boldsymbol{\tau}\|_2^2 \tag{2.92}$$

Using the fact that the Fourier transform is a unitary operation with respect to the Euclidean norm $\|\boldsymbol{x}\|_2^2 = \sum_i x_i^2$, the problem can be described in Fourier space, where the different Fourier modes decouple and the minimization problem can be solved analytically:

$$\begin{aligned} \hat{\boldsymbol{\tau}}_{MP,mn} &= \arg\min_{\boldsymbol{s}} \|\hat{\boldsymbol{u}}_{mn}^{(\mathrm{exp})} - \tilde{\mathbf{G}}\left(\boldsymbol{k}_{mn}\right) \cdot \boldsymbol{s}\|_2^2 + \lambda^2 \|\boldsymbol{s}\|_2^2 \\ &= \left[\left(\tilde{\mathbf{G}}^{\dagger} \tilde{\mathbf{G}} + \lambda^2 \mathbf{I} \right)^{-1} \tilde{\mathbf{G}}^{\dagger} \right] \hat{\mathbf{u}}_{mn}^{(\mathrm{exp})} =: \hat{\mathbf{G}}_{\lambda,mn}^{\#} \hat{\mathbf{u}}_{mn}^{(\mathrm{exp})}. \end{aligned} \tag{2.93}$$

Here the superscript † designates the Hermitian conjugate. Additionally, $\tilde{\mathbf{G}}\left(\boldsymbol{k}_{mn}\right)$ has been denoted simply by $\tilde{\mathbf{G}}$ for visual clarity in the second line.

The calculation can be performed for each mode individually making FTTC highly performant, while it has been shown to produce comparable results to the BEM [101]. Because of this, I selected FTTC as the primary method for my analysis.

The usage of a periodic discreet Fourier transform may result in boundary artifacts, known as *ringing*, when large deformations are found close to the boundary of the field of view. To address this, the image can either be augmented with additional sampling points set to zero, in process known as *padding* [52] or by applying a Tukey windowing function [132] that smoothly reduces the deformation values at the boundary [110].

2.3.2 Regularization parameter selection in FTTC

The regularization parameter λ must be chosen with care [14, 102] as each choice will result in a different reconstruction of the traction field. If the value is chosen too large, this will result in a loss of accuracy and resolution in the resulting force map. If it is chosen too small, the result will be dominated by noise [13]. Different methods have been introduced to automatically select a regularization parameter. An overview of selection methods in the general context of inverse methods was given by Bauer and Lukas [133]. In the following, I mention some of the approaches that are applicable to FTTC. For simplicity I use a vectorized notation where $\boldsymbol{\tau}_{\lambda}$ is a $2M$-element vector that contains all traction values reconstructed by Eq 2.93, $\hat{\mathbf{u}}^{(\mathrm{exp})}$ does similarly contain all displacement values obtained during image processing and $\hat{\mathbf{M}}$ as

well as $\hat{\mathbf{M}}^{\#}_{\lambda}$ are $2M \times 2M$ block-diagonal matrices containing the entries of $\tilde{\mathbf{G}}\left(\boldsymbol{k}_{mn}\right)$ and $\hat{\mathbf{G}}^{\#}_{\lambda,mn}$ respectively on their diagonal.

L-curve method

The L-curve method is a graphical motivated procedure developed by Hansen [134] that has seen wide adaption in TFM applications [11, 61, 69, 101, 128, 135]. The L-curve method uses the fact that when plotting the logarithms of the two terms in Eq 2.93,

$$\tilde{\eta} = \log \left\| \hat{\boldsymbol{\tau}}_{\lambda} \right\|_2, \qquad \tilde{\rho} = \log \left\| \hat{\boldsymbol{u}}^{(\mathrm{exp})} - \hat{\mathbf{M}} \hat{\boldsymbol{\tau}}_{\lambda} \right\|_2, \tag{2.94}$$

for different values of λ, an L-shaped curve is obtained whose corner defines a good compromise between under- and overfitting. Numerically, this point can be found by calculating the curvature $\kappa(\lambda)$ of the $(\tilde{\eta}, \tilde{\rho})$ graph and finding its maximal value. Hansen [134] also presented a scheme based on the singular value decomposition to calculate the curvature analytically at every point, avoiding numerical differentiation.

Bayesian parameter selection

Bayesian parameter selection[102] makes use of the Bayesian interpretation of regularization described in Eq 2.82, which we can express similarly for FTTC:

$$p(\hat{\boldsymbol{\tau}} | \hat{\boldsymbol{u}}, \alpha, \beta) = \frac{\exp\left(-\frac{\beta}{2M} K(\hat{\boldsymbol{\tau}})\right)}{Z_u Z_f p(\hat{\boldsymbol{u}} | \alpha, \beta)}, \tag{2.95}$$

where Z_u and Z_f are defined as above and

$$K(\hat{\boldsymbol{\tau}}) = \underbrace{(\hat{\mathbf{M}}\hat{\boldsymbol{\tau}} - \hat{\boldsymbol{u}})^T (\hat{\mathbf{M}}\hat{\boldsymbol{\tau}} - \hat{\boldsymbol{u}})}_{E_u(\hat{\boldsymbol{\tau}})} + \frac{\alpha}{\beta} \underbrace{\hat{\boldsymbol{\tau}}^T \hat{\boldsymbol{\tau}}}_{E_f(\hat{\boldsymbol{\tau}})}. \tag{2.96}$$

In addition, while adapting Eq 2.84 to FTTC, the Gaussian integral can be solved explicitly by completing the square which yields a formula

$$\begin{aligned} p(\hat{\boldsymbol{u}} | \alpha, \beta) &= \int \frac{\exp\left(-\frac{\beta}{2M} K(\hat{\boldsymbol{\tau}})\right)}{Z_u Z_f} \, \mathrm{d}^{2M}\tau \\ &= \frac{(2\pi)^M}{Z_u Z_f \sqrt{\det \mathbf{A}}} \exp\left(-\frac{\beta}{2M} K\left(\hat{\boldsymbol{\tau}}_{\lambda=\sqrt{\alpha/\beta}} \right) \right), \end{aligned} \tag{2.97}$$

where $\mathbf{A} = (-\alpha \mathbf{I} - \beta \hat{\mathbf{M}}^T \hat{\mathbf{M}})/M$. Bayesian parameter selection now treats α as a hyperparameter and its Bayesian optimal value can be found by maximizing the marginal probability $p(\boldsymbol{u}|\alpha, \beta)$, while β is determined directly by calculating the variance in some region far away from the cell. By taking the logarithm of $p(\boldsymbol{u}|\alpha, \beta)$ and using a corollary of Jakobi's formula, since $\mathbf{A}$ is non-singular, we have $\log\det \mathbf{A} = \mathrm{tr} \log \mathbf{A}$ [136], it can easily be shown that the optimal selection α_B must satisfy the equation

$$E_f\left(\hat{\boldsymbol{\tau}}_{\lambda=\sqrt{\alpha/\beta}} \right) = \mathrm{tr}\left(\mathbf{A}^{-1} \right) + \frac{2M^2}{\alpha}. \tag{2.98}$$

A solution to this equation can now be found iteratively and a regularization parameter $\lambda_B = \sqrt{\alpha_B/\beta}$ can be calculated.

Normalized Cumulative Periodogram

The Normalized Cumulative Periodogram (NCP) method [137] can be used to detect a bias in the residual vector $\boldsymbol{e}_\lambda = \hat{\mathbf{M}}\boldsymbol{\tau}_\lambda - \hat{\mathbf{u}}^{(\mathrm{exp})}$. based on its power spectrum $p_{\lambda,k} = |\mathrm{DFT1}(\boldsymbol{e}_\lambda)_k|^2$, using the one-dimensional discrete Fourier transform DFT1. We now define the NCP vector $\boldsymbol{c}(\boldsymbol{e}_\lambda) \in \mathbb{R}^M$ by

$$c(\boldsymbol{e}_\lambda)_k = \frac{\sum_{i=2}^{k+1} p_{\lambda,k}}{\sum_{i=2}^{M+1} p_{\lambda,k}}. \tag{2.99}$$

If $\boldsymbol{e}_\lambda$ only describes white noise, we expect $\boldsymbol{c}$, when plotted as a function of k, to describe a straight line going from the origin to $(M+1, 1)$. Assuming that noise is indeed Gaussian distributed as previously predicted, we can therefore select λ such that this condition is fulfilled.

Generalized Cross-Validation

Generalized Cross-Validation (GCV) [138] is a variation of the ordinary leave-out-one-value cross-validation method, that has been used more recently [139]. It uses an estimator function, which is defined by

$$G(\lambda) = \frac{\|\hat{\mathbf{M}}\hat{\boldsymbol{\tau}}_\lambda - \hat{\mathbf{u}}^{(\mathrm{exp})}\|_2^2}{(\mathrm{tr}(1 - \hat{\mathbf{M}}\hat{\mathbf{M}}_\lambda^{\#}))^2}, \tag{2.100}$$

and always has a minimum for a strictly positive value of λ, at which an optimal regularization can be found. It can easily be calculated for a large number of values using the singular value decomposition of $\tilde{\mathbf{G}}$, which is known. Using the determined value for λ, an estimate for the deformation field can be calculated. Probst [110] estimated this method to yield more reliable results than the L-curve approach.

Due to its ease of use, reliability and less dependence on the prior assumption of Gaussian noise, I have used GCV in this dissertation as the primary regularization parameter selection method.

Chapter 3

2.5D Fourier Transform Traction Cytometry on thick elastic substrates

In this chapter, we describe an elegant approach to include the dimension of normal vector components into FTTC to extend the technique from 2D to 2.5D. The theory to this section has been covered as a minor part of manuscript 1. The experimental analysis follows research conducted by Joel Christian under supervision of Ada Cavalcanti-Adam [140].

3.1 Motivation

As elaborated in the previous sections, two-dimensional methods for measuring cellular traction forces have been widely adapted and employed in experimental research. In reality however, 2D TFM must be considered as an incomplete measurement, potentially leading to errors even when estimating in-plane traction forces due to neglecting possible interactions with normal components [60]. In addition, these out-of-plane stress components are also crucial in biological processes, it has been shown, for example, that the underlying extracellular matrix is clearly deformed not only in-plane but also in out-of-plane direction during tumor growth and development [141, 142].

Early studies by Frank, Maskarinec and others [15, 143] used the direct method, which will be discussed in detail in the subsequent section, to calculate both tangential and normal traction forces on soft elastic substrates during fibroblast migration. This was extended by Hur *et al.* [103] who modelled the problem as a boundary value problem using the surface deformation as boundary condition and used the FEM to solve the problem and extract the deformations.

The inverse method was used for 2.5D TFM by Legant *et al.* [61] and del Álamo *et al.* [18]. Legant *et al.* used a BEM-like approach, where they first simulated the 3D deformation field created by a singular force on one of the tile corners on a regular 3D tetrahedral mesh with a triangular surface using the FEM. They then used the surface solutions of this calculation to construct a numerical discretization of the Green's kernel. This could then be used to construct the matrix $\mathbf{M}$ introduced in Eq 2.79 without the need to perform extensive problem specific calculations. On the other hand, del Álamo *et al.* analytically found a representation for the relation of traction and deformation in Fourier space, and introduce a function $\tilde{\mathcal{G}}$ whose inverse $\tilde{\mathcal{G}}^{-1} = \tilde{\mathrm{G}}$ can be substituted into Eq 2.89 to obtain a 2.5D extension of FTTC. Instead of a regularization they used a local averaging procedure to reduce the level of noise in their experimental dataset. In addition to not considering regularization, their

formula is rather impractical to use in the case of large substrate thickness.

In this chapter, we now derive a complementary approach by assuming a thick substrate and present a more straight-forward calculation to derive a closed form solution for the Green's function in Fourier space, that is consistent with the 2D formula presented in Eq 2.90 and effectively gives the same results as the procedure by del Álamo *et al.* in the limit of an infinite thick halfspace.

3.2 Theory

A general ansatz for solving Eq 2.18 can be made using the Boussinesq-Cerruti potential functions [113, 114].

The GF in real space is known as described by Eq 2.19 with the Boussinesq equation [100]. By making use of the convolution theorem, Eq 2.19 can be reduced into the simple product expression

$$\tilde{u}_i(k_x, k_y, z) = \sum_{j=1}^{3} \tilde{\mathrm{G}}_{ij}(k_x, k_y, z)\tilde{\tau}_j(k_x, k_y). \tag{3.1}$$

Here a tilde above the quantities represents the Fourier transform along the x and y axis. Unfortunately, finding an analytical expression for $\tilde{\mathrm{G}}_{ij}$ directly from transforming the real space Boussinesq solution would require us to solve a complex integral expression. Instead of doing so, we will derive the relation between $\tilde{\boldsymbol{\tau}}$ and $\tilde{\boldsymbol{u}}$ directly from the boundary problem stated in Eq 2.18. We can then extract the analytical expression for $\tilde{\mathrm{G}}_{ij}$ by comparing this relation to Eq 3.1. In general, our procedure follows the same steps as described in Ref [100] to derive the real space GF in the first place.

Now, by applying the mentioned two-dimensional Fourier transform to Eq 2.21, the different modes decouple and we obtain the following initial value problem:

$$\partial_z^2 \tilde{P}_i(k_x, k_y, z) - (k_x^2 + k_y^2)\tilde{P}_i(k_x, k_y, z) = 0 \ , \quad \partial_z^3 \tilde{P}_i|_{z=0} = -\tilde{\tau}_i \ . \tag{3.2}$$

Because the differential equation is linear, it can easily be solved and we find for the Fourier transform of the potential functions:

$$\tilde{P}_i(k_x, k_y, z) = \frac{1}{\sqrt{k_x^2 + k_y^2}^3} e^{-\sqrt{k_x^2+k_y^2}z}\tilde{\tau}_i(k_x, k_y). \tag{3.3}$$

In the next step, we apply the Fourier transform onto Eq 2.22 to Eq 2.25 and obtain:

$$\tilde{u}_i = \sum_{j=1}^{3} \tilde{u}_i^{(j)}, \tag{3.4}$$

together with the x-tangential contributions

$$\begin{aligned} 2\mu\tilde{u}_x^{(x)} &= -2\nu k_x^2 P_x + 2\partial_z^2 P_x + k_x^2 z\partial_z P_x \\ 2\mu\tilde{u}_y^{(x)} &= -2\nu k_x k_y P_x + k_x k_y z\partial_z P_x \\ 2\mu\tilde{u}_z^{(x)} &= \mathrm{i}k_x(1-2\nu)\partial_z P_x - \mathrm{i}k_x z\partial_z^2 P_x, \end{aligned} \tag{3.5}$$

the y-tangential contributions

$$\begin{aligned} 2\mu\tilde{u}_x^{(y)} &= -2\nu k_x k_y P_y - z\partial_z P_y \\ 2\mu\tilde{u}_y^{(y)} &= -2\nu k_y^2 P_y + 2\partial_z^2 P_y + k_y^2 z\partial_z P_y \\ 2\mu\tilde{u}_z^{(y)} &= \mathrm{i}k_x(1-2\nu)\partial_z P_y - \mathrm{i}k_x z\partial_z^2 P_y \end{aligned} \tag{3.6}$$

and the normal (z) contributions

$$\begin{aligned} 2\mu\tilde{u}_x^{(z)} &= -(1-2\nu)\mathrm{i}k_x\partial_z P_z - \mathrm{i}k_x z\partial_z^2 P_z \\ 2\mu\tilde{u}_y^{(z)} &= -(1-2\nu)\mathrm{i}k_y\partial_z P_z - \mathrm{i}k_y z\partial_z^2 P_z \\ 2\mu\tilde{u}_z^{(z)} &= 2(1-\nu)\partial_z^2 P_z - z\partial_z^3 P_z. \end{aligned} \tag{3.7}$$

We can now insert Eq 3.3 into these equations. This results in a simple product expression relating $\tilde{\boldsymbol{\tau}}$ to $\tilde{\boldsymbol{u}}$. By comparing the result to Eq 3.1 we can extract the following Green's function in Fourier space:

$$\tilde{\mathbf{G}}(k_x, k_y, z) = \\ \frac{e^{-kz}}{2\mu k^3} \begin{pmatrix} 2k^2 - (2\nu + kz)k_x^2 & -(2\nu + kz)\, k_x k_y & (1 - 2\nu - kz)\,\mathrm{i}kk_x \\ -(2\nu + kz)\, k_x k_y & 2k^2 - (2\nu + kz)k_y^2 & (1 - 2\nu - kz)\,\mathrm{i}kk_y \\ -(1 - 2\nu + kz)\,\mathrm{i}kk_x & -(1 - 2\nu + kz)\,\mathrm{i}kk_y & 2(1-\nu)k^2 + k^3 z \end{pmatrix}. \tag{3.8}$$

The procedure described for 2D FTTC in section 2.3 can now easily be extended to a 3D procedure by promoting all 2-component quantities ($\boldsymbol{u}_{ij}$, $\boldsymbol{\tau}_{ij}$, $\hat{\boldsymbol{u}}_{nm}$, $\hat{\boldsymbol{\tau}}_{nm}$) into 3-component ones. In addition, the deformation field must now be interpolated to a singular plane in a depth d relative to the surface and the Green's function in Eq 2.87 and Eq 2.93 is replaced by $\tilde{\mathbf{G}}(k_{mn,x}, k_{mn,y}, d)$ for where depth d is inserted.

3.3 Experimental evaluation: Particle uptake in epithelial cells

Particle uptake of cells plays an important role in many biological processes. For example, many intracellular pathogens, such as mammalian reovirus, must overcome the apical epithelium barrier to gain access to the cytoplasma of epithelial cells and subsequently penetrate the intestinal epithelium [144]. To do so, they mimic extracellular matrix motifs to specifically interact with the host membrane [145]. This process can be studied using protein coated nanoparticles, which decouples the processes of cellular uptake from the chemical and physical properties of viruses and allows for a variation in particle size [146]. However, the mechanical details of this process are difficult to observe when occurring on the ventral (substrate facing) side with methods like optical tweezers or AFM which are used on the dorsal side [147–149]. While the ventral uptake has been studied using molecular force sensors on glass substrates [149], using softer hydrogel substrates and observing forces with TFM is expected to offer a more physiological measurement [140] for the study of clathrin-mediated endocytosis (CME). 2.5D TFM provides a non-intrusive method to examine the forces exerted by the cell, including those under the influence of nanoparticles. Experiments conducted by my experimental collaborator, Joel Christian, on HeLa cells (immortal cervical cancer cells) [140] had already revealed that nanoparticles immobilized at the substrate can be grabbed by CME and he postulated that particles are then dragged along the ventral membrane to an area close to the cell center to be possibly internalized there. However, by simultaneously observing the expression of GFP florescence marked AP2, a protein complex involved in endocytosis, he has also shown, that AP2 is not found next to cell-matrix adhesions and that traction forces alone were insufficient to detach nanoparticles close to the periphery. Despite this, he observed the initiation, but not completion of CME in this area, which results in the formation of AP2 clusters around

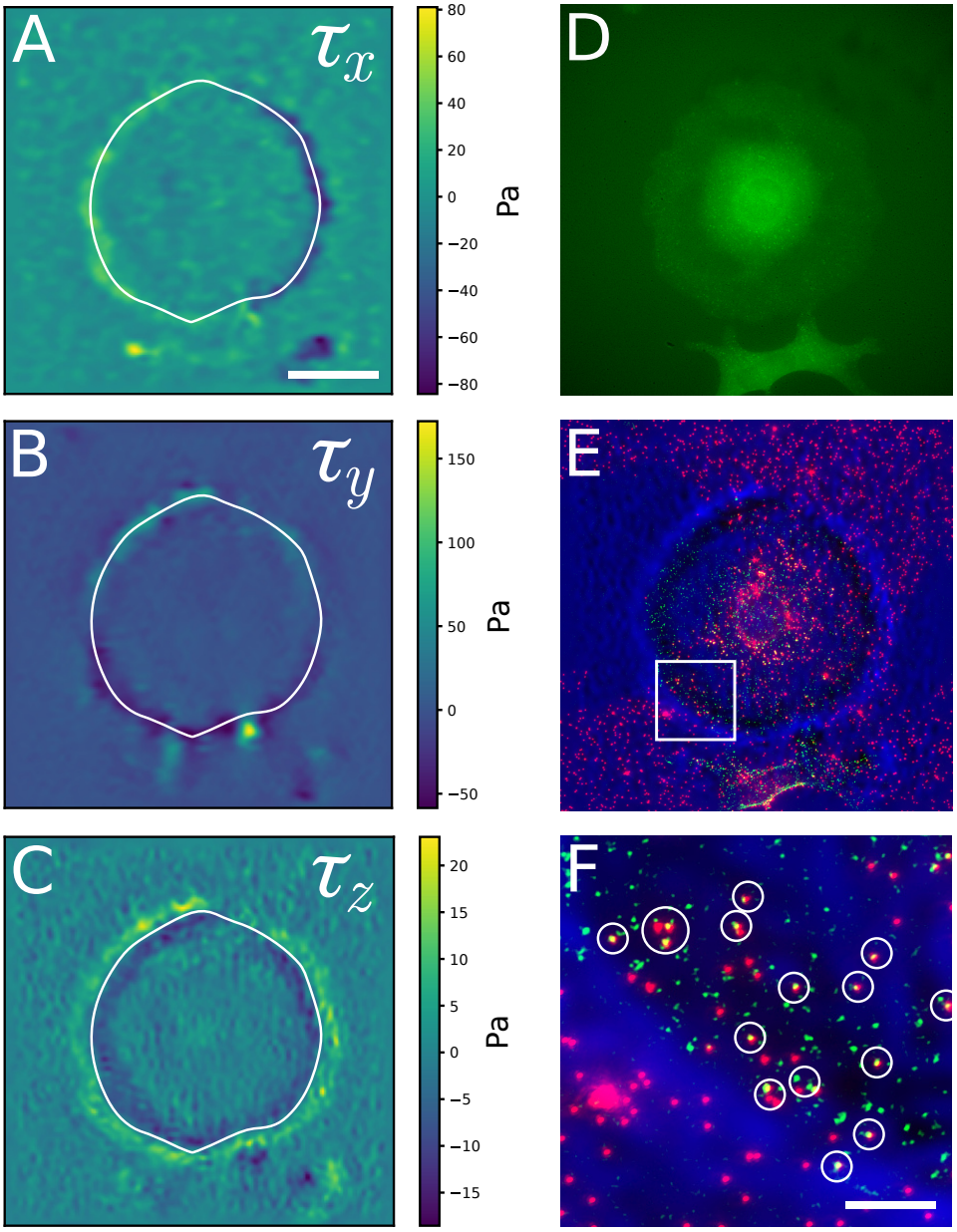

Figure 3.1: Traction forces exerted by HeLa cells on a 3 kPa fibronectin coated PAA substrate. (A to C) Different components of the traction exerted onto the substrate as reconstructed using 2.5D LUVI FTTC. Positive values indicate leftwards, downwards and cellwards facing adhesive traction exerted by the cell onto the substrate, in A,B and C respectively. The white contour indicates the transition between the pushing and pulling area in normal direction. (D) GFP strained AP2 (AP2-eGFP) distribution in a cell (E) Overlay of the distribution of AP2 (green, areal luminosity removed), immobilized 200 nm nanoparticles (red) and normal traction (blue). White square indicates focus region. (F) Insert shows the overlay in the focus area. Circles mark regions where clathrin mediated uptake occurs. Scale bar A to E 50 µm, F 10 µm — Experimental data obtained from [140]

nanoparticles. His research had also revealed that expression of AP2 was independent of substrate stiffness and AP2 clusters were highly distributed at the cells periphery. This was found by seeding AP2-eGFP expressing HeLa cells both on glass and 3 kPa stiff QGel920[1] substrates, both coated with immobilized 200 nm nanoparticles and biofunctionalized with fibronectin. TIRF microscopy was used to analyze the spatial distribution of AP2 around 4 hours after seeding.

An analysis shown in Fig 3.1 examplifies the cell's mechanical behavior on a 3 kPa fibronectin coated PAA substrate: We can clearly see that the cell uses adhesive contacts to exert a cell- and inwards pulling force on the its periphery, but exerts a pushing forces onto the substrate in a ring shaped domain a little bit more inside. By simultaneously observing the distribution of AP2 (D) and nanoparticles and correlating them to the normal component of the traction force (E and F), we can see that the appearance of AP2 clusters correlates with the region, the cell is pushing into the substrate. Correlation between AP2 and nanoparticle position was also found in the cell center. This corresponds well to the previous observations, but also highlights the importance of normal forces in this process.

3.4 Conclusion

In this section, I have presented a demonstration of how to extend the 2D regularized FTTC method to also consider normal forces (2.5D TFM) based on a newly derived Green's function with normal components. I successfully retained the benefits of this Fourier method, which is very fast and reliable when combined with a regularization scheme, for which here I have chosen zero-order Tikhonov regularization with generalized cross-validation for identification of the regularization parameter λ. Applying this new variant of 2.5D FTTC to experiments studying the role of traction forces in ventral endocytosis of nanoparticles, I have successfully shown that downward pressure exerted by the cell appears to be an decisive factor in the localization of AP2 clusters, an initial stage of the endocytotic process.

[1] QGel920 is a silicon polymer manufactured by CHT Germany GmbH, Tübingen with glass-like optical properties.

Chapter 4

Implementation and performance of the Direct Method

In this chapter, the direct method for TFM is introduced and compared to 2.5D FTTC introduced in chapter 3. The content of this chapter is published in manuscript 1, except that I omitted the introduction of 2.5D FTTC, which has been moved to chapter 3.

4.1 Motivation

As we have seen in the introductory chapter, a wide range of force reconstruction approaches have been devised, each of which has its advantages and disadvantages in a certain context. In particular, I have introduced the two fundamental approaches for force reconstruction, the inverse method and the direct method. Very rarely, however, are these different methods directly compared against each other. A notable exception is a recent work that compares FEM-based implementations of the direct and inverse methods for 3D TFM [98, 99]. Here I aim at a similar comparison, but for 2.5D TFM and with Green's function-based and finite difference methods. Rather than simulating experimental setups, I use simple test cases and simulations with displacement noise to provide a comprehensive comparison of the mathematical properties of direct versus inverse methods for 2.5D TFM.

In addition to its interest in fundamental questions of TFM, this work is also motivated by different recent experimental developments. As already mentioned in the introductory chapter, DM seems to be an attractive choice for non-planar geometries like elastic beads, for which it is very challenging to calculate appropriate Green's functions [63]. I expect that this line of research will become more important in the future with the promise of additive manufacturing to print 3D elastic materials that are compatible with cell culture and deform under cell traction [150–153]. Such systems might by approached best with FEM-approaches, but in some cases (like elastic beads) Green's function-based inverse methods are possible [64, 154]. Here I use this recent development as a motivation to compare direct and inverse methods in the traditional setup of 2.5D TFM for planar substrates.

Second, new microscopy methods have been used to achieve better image resolution for 2.5D TFM, including Stimulated Emission Depletion (STED) microscopy [69], Structured Illumination Microscopy (SIM) [71, 72], astigmatic SIM [75] and fluctuation-based TFM [73]. The displacement data resulting from these experimental advances is often analyzed with one of the different TFM-methods, but a systematic

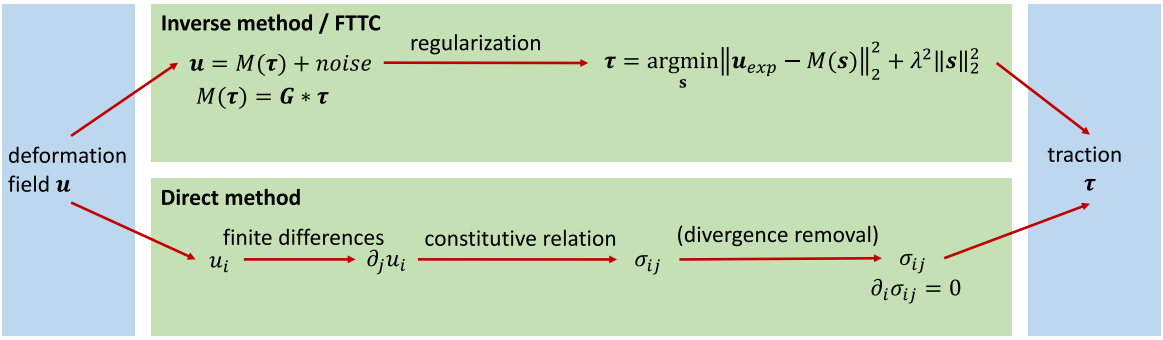

Figure 4.1: Comparison of the two fundamentally different methods for TFM: FTTC and the Direct method. The inverse method estimates a force distribution that results in an optimal match for the global displacement field. In Fourier Transform Traction Cytometry (FTTC) one makes use of fast Fourier transforms. A regularization scheme is introduced to address the fact that the inverse problem is ill-posed. In the direct method, point-wise computational methods are used to determine the stress tensor locally. A divergence correction can be applied to ensure that the physical force balance $\partial_i \sigma_{ij} = 0$ is satisfied.

comparison between different methods is usually not performed. In this context, it is interesting to know how direct and inverse methods compare in regard to improvements in sampling density. Here I use this recent development as a motivation to also study the effect of varying sampling distance.

The work presented in this chapter is structured as follows. I will first provide an in-depth introduction to direct methods for 2.5D TFM. I discuss different schemes for numerically calculating the required derivatives and introduce a divergence correction motivated by similar schemes from hydrodynamics. I define several simple test cases for force reconstruction based on analytical solutions for Hertz-like adhesion patches. To test the robustness of our different methods, I simulate different levels of displacement noise, which is a common method to lump noise that might originate from optical microscopy or gel preparation into one parameter. In addition, I investigate the effect of varying sampling distance.

4.2 Direct method and divergence correction

In contrast to the inverse approach, in the direct method (compare Fig 4.1), one starts directly with the observed deformation field and calculate the deformation gradient tensor from it using a suitable gradient kernel. Subsequently one can then calculate the strain and the stress within the substrate. From the strain tensor, one can then extract the surface deformation 2.3 The surface traction can be determined from the stress tensor using Eq 2.7. The direct method can be applied to both, 2.5D as well as 3D setups, in the case of 2.5D TFM, the substrate is delimited by a planar surface at the $z = 0$ plane and whose outwards normal is defined to be $(0, 0, -1)^T$ and thus Eq 2.7, reads:

$$\boldsymbol{\tau} = -\left(\sigma_{13}, \sigma_{23}, \sigma_{33}\right)|_{z=0} \ . \tag{4.1}$$

However, even in the 2.5D case, the direct method is fundamentally a 3D method and the deformation must be known not only in a single plane, but in a volume below the surface, in order to obtain the full stress tensor. It can easily be seen how in contrast to the IM based on Green's functions, the direct method can be extended easily to non-planar surfaces (going beyond Eq 2.18) and non-linear materials (going beyond

Eq 2.17).

The strains $\partial u_i/\partial x_j$ and the components F_{ij} of the deformation gradient tensor must be obtained numerically. To do so, the displacement field $\boldsymbol{u}$ is first sampled on a regularly spaced 3D grid. Then both quantities can easily be obtained using a finite difference scheme. Frank *et al.* [16, 143] determine the derivative by fitting a 1st order polynomial

$$\boldsymbol{u}(\boldsymbol{x}) = \boldsymbol{a}x + \boldsymbol{b}y + \boldsymbol{c}z + \boldsymbol{d} \tag{4.2}$$

to a local region in the resulting traction profile. The components of $\boldsymbol{a}$, $\boldsymbol{b}$ and $\boldsymbol{c}$ contain the strains $\partial u_i/\partial x_j$ directly. I refer to this technique as the 3x3x3 patch method as a 3 by 3 by 3 data point support is used to estimate the deformation field gradient. I investigate how well this approach performs in comparison to other approximation techniques. The simplest alternative is a simple two-point finite difference method (only the equation for z-derivatives is stated):

$$\left.\frac{\partial u_i}{\partial z}\right|_{klm} \approx \frac{u_{i,kl(m+1)} - u_{i,kl(m-1)}}{2\Delta x}. \tag{4.3}$$

Increasing the number of sampling points contributing to the derivatives as done in Eq 4.2 should in theory decrease the uncertainty of the result, but will decrease resolution. Another alternative to this constitutes a four-point scheme:

$$\left.\frac{\partial u_i}{\partial z}\right|_{klm} \approx \frac{-u_{i,kl(m+2)} + 8u_{i,kl(m+1)} - 8u_{i,kl(m-1)} + u_{i,kl(m-2)}}{12\Delta x}. \tag{4.4}$$

In all three cases special non-symmetric expressions are used close to the boundary that make use of the same number of support points, but avoid contributions outside the observed area. All methods for numerical derivatives are dependent on the sampling distance defined by the sampling lattice. A smaller sampling distance should reduce the systematic error, but on the other hand the statistical error on the deformation gradient is proportional to the ratio between the statistical error of the displacement field and the spacing and therefore will increase for smaller sampling distance.

While the inverse method always gives a valid displacement field because it is calculated from a force distribution as a direct problem, the direct method uses a displacement field that might not be valid as it violates force and torque balances. In a static system, the force balance leads to the Cauchy momentum equation 2.9 (here stated in the form used in linear elasticity):

$$\frac{\partial \sigma_{ij}}{\partial x_j} = 0\ . \tag{4.5}$$

In other words, the stress tensor must be divergence-free (*solenoid*). This property is not restricted to a specific geometry of the system. It describes a fundamental property resulting from the fact that the stress tensor represents local force densities that must be in balance for a static situation free of external forces. The coordinate of the initial deformation fields where the corresponding stress tensor field satisfies Eq 4.5 are called *compatible* [113]. The importance of this condition has been pointed out before in the context of monolayer stress microscopy [56] and 3D TFM[98].

While the true deformation field $\boldsymbol{u}^{(T)}$ is always compatible, the measured deformation field $\boldsymbol{u}^{(C)}$ is not, as it contains errors attributed to noise and thus, the obtained

stress tensor may not satisfy Eq 4.5. If I describe $\sigma_{ij}(\boldsymbol{u})$ to be the stress tensor obtained from a deformation field $\boldsymbol{u}$, we easily see by

$$\frac{\partial \sigma_{ij}(\boldsymbol{u}^{(C)})}{\partial x_j} = \frac{\partial(\sigma_{ij}(\boldsymbol{u}^{(C)}) - \sigma_{ij}(\boldsymbol{u}^{(T)}))}{\partial x_j} + \underbrace{\frac{\partial \sigma_{ij}(\boldsymbol{u}^{(T)})}{\partial x_j}}_{=0} = \frac{\partial \sigma_{ij}(\boldsymbol{u}^{(C)} - \boldsymbol{u}^{(T)})}{\partial x_j} \tag{4.6}$$

that only the noise part of the deformation field will contribute to the divergence of the obtained stress tensor $\sigma_{ij}(\boldsymbol{u}^{(C)})$. This means that one can use this divergence to determine what ratio of the input data is attributed to noise. The divergence of the calculated stress tensor $\sigma_{ij}(\boldsymbol{u}^{(C)})$ can be calculated on a local basis by using a symmetric two-point form. Although the relation between the divergence and the displacement noise contribution is less straight forward in the case of non-linear elasticity, a similar argument can be made here.

Instead of the tensor-based formulation Eq 4.5, the compatibility equation can also be represented as a condition for each column of the stress tensor:

$$\nabla \cdot \boldsymbol{a} = 0, \qquad \nabla \cdot \boldsymbol{b} = 0, \qquad \nabla \cdot \boldsymbol{c} = 0, \tag{4.7}$$

where I defined $\boldsymbol{\sigma} = (\boldsymbol{a}, \boldsymbol{b}, \boldsymbol{c})$. This observation immediately generates a relation to hydrodynamics, because a similar situation can be found for hydrodynamic descriptions of incompressible fluids, where the mass conservation equation reduces to

$$\nabla \cdot \boldsymbol{v} = 0 \tag{4.8}$$

for a flow field $\boldsymbol{v}$. This property has been exploited by various studies and using a variety of techniques to remove potential noise from $\boldsymbol{v}$ [155–157]. Because of the relation between the stress tensor and the surface traction Eq 2.7, removing the noise contributions from σ_{ij} for the full substrate might also yield a better result for the surface traction, similar to regularization for the inverse method. An efficient method for performing this kind of divergence correction on a flow profile has been described by Wang *et al.* [158] and this method can be generalized to any divergence-free vector field. A short description of their technique is given in the appendix, section A.1. This technique makes use of the particular structure of the problem to result in an algorithm that applies matrix operations only on one coordinate at the same time, which strongly reduces computational complexity as well as avoids complex operations like matrix inversion.

The noise removal technique now consists of an iterative process. One starts with the initial condition $\boldsymbol{\sigma}^{(0)} := \boldsymbol{\sigma}_{exp}$ and $i := 0$ and iterate the following steps [159]:

1. Split the stress tensor into column vectors:
   $(\boldsymbol{a}_{exp}, \boldsymbol{b}_{exp}, \boldsymbol{c}_{exp}) = \boldsymbol{\sigma}^{(i-1)}$

2. Find $\boldsymbol{a}_c$, $\boldsymbol{b}_c$ and $\boldsymbol{c}_c$ that satisfy Eq 4.7 using the mentioned procedure for vector fields using $\boldsymbol{a}_{exp}$, $\boldsymbol{b}_{exp}$ and $\boldsymbol{c}_{exp}$ as input.

3. Reassemble the vector fields into a new tensor
   $\mathbf{w} = \mathbf{w}^{(i)} := (\boldsymbol{a}_{exp}, \boldsymbol{b}_{exp}, \boldsymbol{c}_{exp})$.

4. Obtain a symmetric approximation for the stress tensor
   $\boldsymbol{\sigma}^{(i)} = (\mathbf{w} + \mathbf{w}^T)/2$.

In each iteration, the divergence of the resulting stress tensor $\boldsymbol{\sigma}^{(i)}$ is reduced. I tested this reduction for a number of different inputs, including a white noise input, and found that a fixed iteration of 20 cycles was sufficient to remove the noise of the input (compare appendix, section A.2).

4.3 Implementation and comparison to the inverse method

Design of simulated traction patterns

Because here I aim at testing different traction force reconstruction methods, I design traction patterns that are useful for the task at hand and for which I can calculate the deformations analytically. I then add displacement noise to these solutions and finally reconstruct the traction and compare with the original pattern. This process is illustrated in Fig 4.2 for an example that includes the two most important features known from adherent cells, namely tangential traction at focal adhesions and the normal push by the nucleus (which due to momentum conservation has to be balanced by counteracting normal forces at the focal adhesions). I discuss the properties of the different reconstructions in the subsequent section. For the analytically tractable patterns, I choose linear combinations of Hertz-like patches, which were introduced in Eq 2.2.4, here briefly repeated.

$$\boldsymbol{\tau}(\boldsymbol{x}) = \begin{cases} \frac{3}{2\pi a^3}\boldsymbol{F}\sqrt{a^2-(\boldsymbol{x}-\boldsymbol{x}_c)^2} & (\boldsymbol{x}-\boldsymbol{x}_c)^2 < a^2 \\ 0 & (\boldsymbol{x}-\boldsymbol{x}_c)^2 \geq a^2 \end{cases} \tag{4.9}$$

Using the derived analytical solution for this profile and the linear properties of the linear elastic half-space problem, the displacement field for a linear combination of Hertz-like patches can be found analytically using linear superposition.

The analytical solution is then sampled on an lattice grid with cuboid unit cells, where the distance between sampling points in x and y direction is equal. The distance in z-direction is usually chosen larger to reflect the anisotropy of the point spread function of traditional optical microscopes. In the next step, Gaussian noise is added to the displacements. For each data point in the grid sampled deformation field a random number is added. This number is drawn from a Gaussian distribution with mean $\mu = 0$ and standard deviation σ being fixed for all sampling points and chosen with respect to the amplitude of deformation averaged over the whole field, which I designate as $< ||u|| >$. In the following, I give the magnitude of the noise in $\sigma / < ||u|| >$. It has been shown before, that the noise distribution does indeed have a Gaussian shape [126]. The perturbed fields now form the input for the actual TFM-analysis. The determined traction profile $\boldsymbol{\tau}^{recon}$ can then be compared to the initial analytical profile $\boldsymbol{\tau}$. Studies that describe new methods to improve the image processing part of TFM often include a simulation of the bead distribution, sometimes also assuming a specific point spread function [85, 97, 99]. However, noise can also arise from different sources, e.g. inhomogeneities in the gel or the bead distributions. Because here I do not aim at simulating experimental setups, but focus on the mathematical properties of different TFM-procedures, I simply simulate displacement noise [11, 14, 101]. Every TFM-method will eventually fail at very high noise levels, but here I ask if direct or inverse methods perform better for low or high noise levels. For each dataset used, I list the full set of parameters, including the sample point spacing,

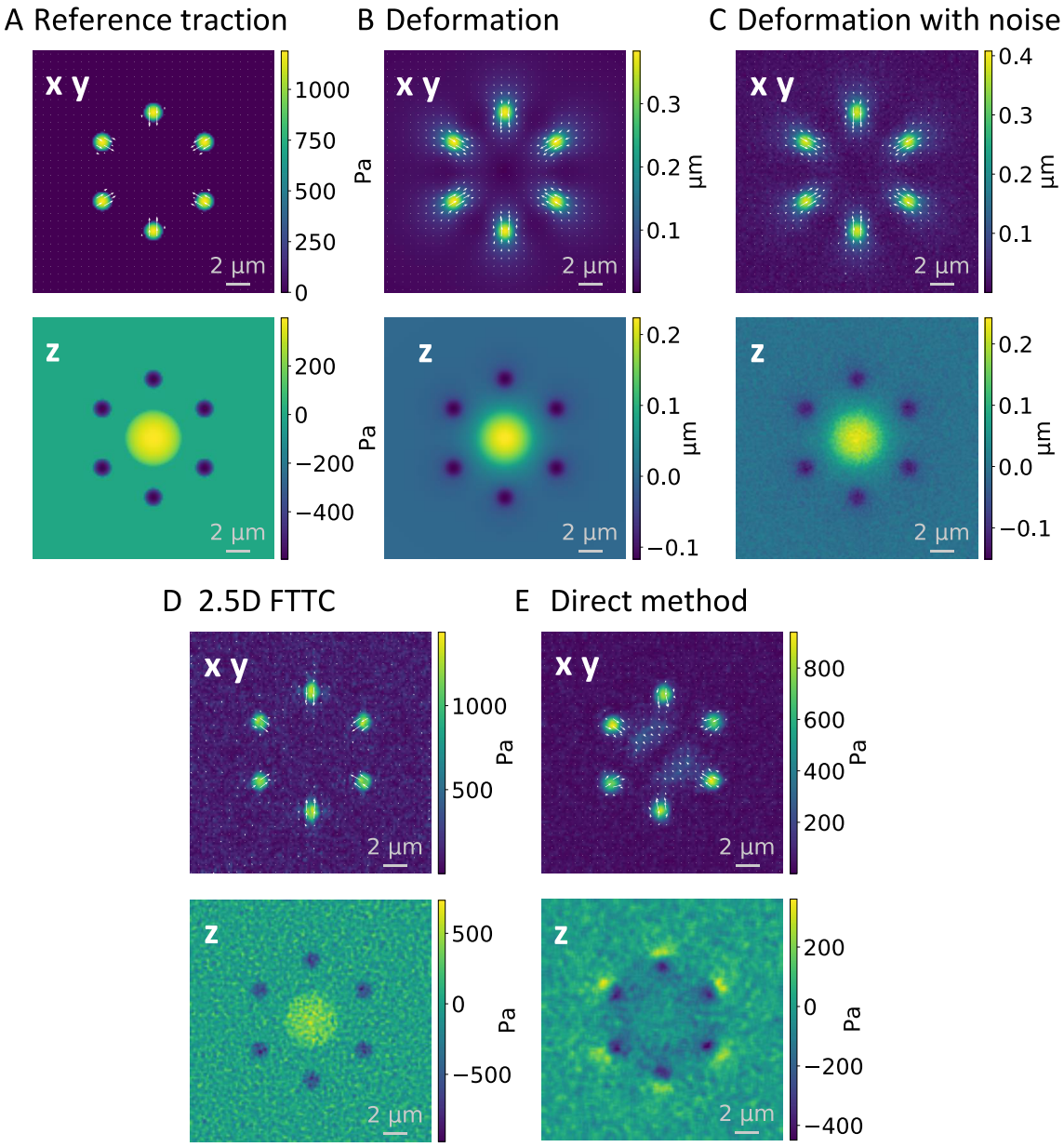

Figure 4.2: Workflow for reconstruction for cell-like traction pattern. The plots in the upper row show the tangential components, while the lower row contains the normal component. (A) As an introductory example, I include the two most important features of adherent cells, namely focal adhesions with mainly tangential traction and the normal push of the nucleus into the substrate. (B) From this given traction field one can then calculate the analytical solution for the deformation field. (C) Noise is added to simulate experimental data (here $\sigma_N / < \|u\| >= 0.2$). (D) For this low noise level, 2.5D FTTC works very well. (E) The direct method gives similar results for the tangential tractions, but performs less well for normal traction. Details on the simulation parameters for this profile can be found in the appendix, section A.3

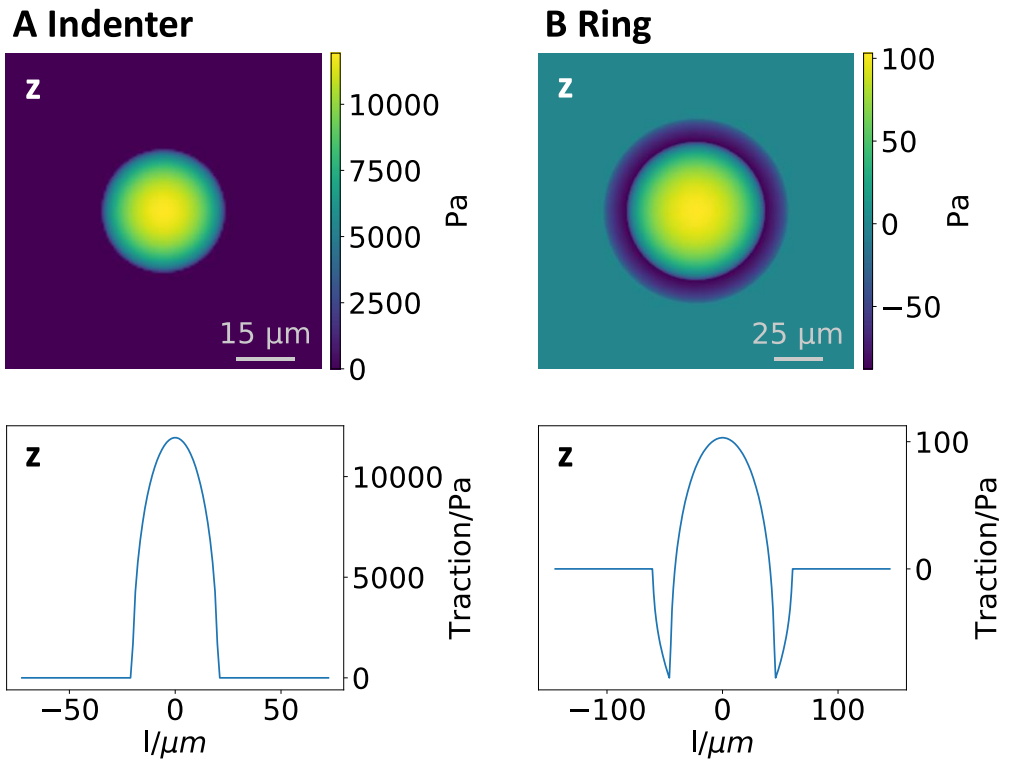

Figure 4.3: Two different Hertzian traction profiles used for normal analysis with the direct method. (A) Indenter monopole with $F_z = 10\ \mu N$. (B) Ring dipole with $F_z = 0\ \mu N$. The upper row presents a heat map of the normal traction τ_z at the substrate surface. There is no tangential traction in these cases. The lower row presents the change of the normal traction along a lower-left to upper-right diagonal section. The results of the analysis corresponding to these profiles are presented in Fig 4.4. The other simulation parameters for these profiles can be found in the appendix, section A.3.

the material parameters and the parameters of the Hertz-like patches superposition to generate the profile in the appendix (section A.3).

4.3.1 Performance of differentiation procedures

I first optimize the direct method by assessing the performances of the numerical derivatives and the importance of a divergence correction. Towards this aim, I choose traction profiles that emphasize the normal component. This is not the standard case in TFM, but in this way, I can best test the performance of the different approximations for derivatives that are required for the direct method. Moreover, this choice demonstrates our ability to deal with three dimensions. Fig 4.3 shows the two simple Hertzian traction patterns investigated below together with the cell-like profile presented in Fig 4.2. The first profile corresponds to a simple Hertz contact, which means that it is a force monopole pushing into the substrate. This setup could be recreated experimentally using a spherical indenter that presses into the substrate. Note that in contrast to FTTC, the direct method works in real space and also can reconstruct force monopoles. The second profile mimics a situation in which pushing and pulling tractions are exerted in different regions in a ring-like pattern. For example, this resembles the way cancer cells invade tissue with invadopodia or fungi invade plants. To quantitatively compare the different methods of determining the deformation gradient as well as the effects of our divergence correction scheme, I calculate different

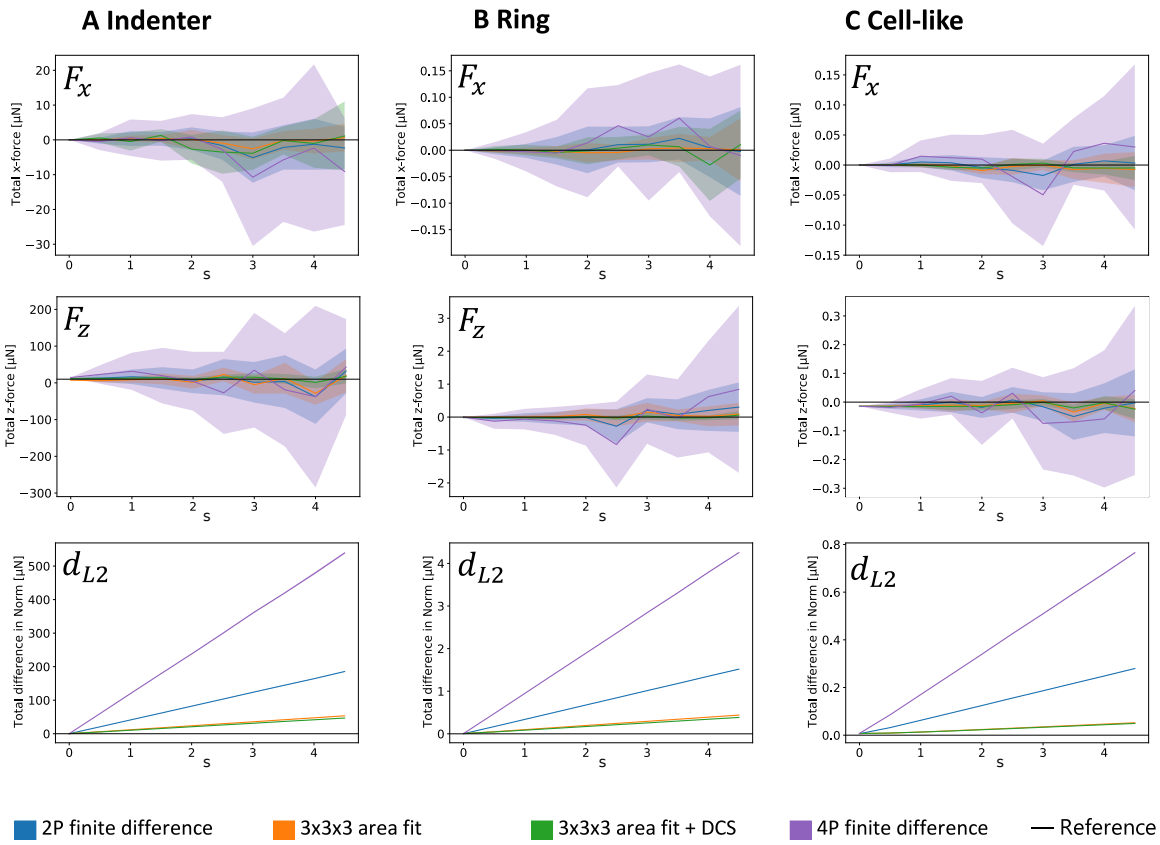

Figure 4.4: Quantitative comparison between different variants of the direct method. The plots use the Hertzian traction profiles introduced in Fig 4.2 and Fig 4.3. The normalization factor $< \|u\| >$ used to compare noise levels for different amplitudes is calculated by taking the mean of the amplitudes of the deformation field. The x axes shows $s = \sigma_N / < \|u\| >$. In the upper line, I plot the variation in the predicted total force in x direction as a function of the standard deviation of Gaussian noise added to the input data. The line indicates the mean and the colored area indicates the standard deviation. In the mid row the same is done for the total traction in z-direction. In the lower row, I plot the total difference in norm, where the variation between the different samples is shown to be negligible. The different colors designate the different ways of calculating the deformation gradients as well as whether the divergence correction scheme (DCS) is used. F_y is not shown due to its similarity to F_x.

quantities of interest. First, I calculate the force monopole components F_x, F_y, F_z defined by

$$F_i = \int_S \tau_i(x, y)\, \mathrm{d}x\, \mathrm{d}y \tag{4.10}$$

which describe the total force transmitted between the sample and the substrate in our field of view. Numerically, the integration is performed using the Simpson formula [160]. These quantities serve as indicators on numerical inaccuracies that add up. If they differ from their predicted value, they will therefore indicate asymmetric and systematic errors in the analysis. The amplitude of the tangential components F_x and F_y should be zero for all our normal indentation profiles, as no tangential force is transmitted. Due to symmetry, one expects the F_y component to show the same behavior as the F_x component. The F_z component should vanish for the dipolar patterns. If F_z was different from the expected value, this may indicate a systematic error due to the non-symmetric way of taking the derivative at the surface.

Next, I calculate the total L2-difference between the TFM results and the reference defined as

$$d_{L2} = \left\| \boldsymbol{\tau}^{recon} - \boldsymbol{\tau}^{true} \right\|_2 = \sqrt{\int_S \left| \boldsymbol{\tau}^{recon}(x,y) - \boldsymbol{\tau}^{true}(x,y) \right|^2 \mathrm{d}x\, \mathrm{d}y}. \tag{4.11}$$

This quantity measures how well the reconstructed field matches the analytical solution. Again, the integration is performed using the Simpson formula. In contrast to the monopole, this value will not only capture systematic aberration offset, but also general noise and gives a measure for the uncertainty of the results. A high d_{L2} indicates that the reconstruction contains a high amount of noise artifacts.

Fig 4.4 shows the performance of the different variants of the direct method as assessed through these metrics. First, I observe that as expected, the variance in the monopoles and the distance metrics increase with increasing noise levels such that $\sigma_N / < \|u\| >= 1$ has to be considered to be large noise. At much higher noise levels, all methods will fail. For the DM investigated here, I find that using a four-point (4P) form instead of a simple two-point (2P) form does not improve the result, but causes a significantly higher level of overall noise, likely due to overfitting. In contrast, using the 3x3x3 patch fit significantly improves the noise suppression, both in the full field as well as the background. However, it will result in an underestimate for the force monopole z-component F_z in case of the indenter profile (A). This is likely due to the fact that u_z/z will be underestimated due to the non-symmetric derivative. Applying the divergence correction algorithm does improve the result in this case and also offers a slightly better noise reconstruction. However, an opposite effect is found for F_z for profiles (B) and (C), where the noise removal introduces a systematic offset in the normal traction component, as well as for F_N, where it also increases the aberration in the force monopole normal components. Notably the difference in norm describes a straight line with negligible variance between the samples. This comes from the fact that for all methods, the deformation gradient and therefore also the resulting stress have a linear relation to the input deformation field. This implies a linear relation in the variance due to noise. This proportionality is then shared by the d_{L2} parameter. Although the divergence correction ensures that formally force and torque balance are satisfied, it does not improve the performance of the DM.

4.3.2 Comparison of direct method and FTTC

Now that I have optimized the direct method, I next compare it to the inverse method, namely with FTTC-calculations both in 2.5D (2.5D FTTC) as well as with calculations in which contributions in the normal dimension are not considered, as described by Eq 2.90 (2D FTTC). Because FTTC is often used as a 2D method, I adopt the standard choice for TFM on planar substrates, namely a collection of circular adhesion sites with mainly tangential tractions, as commonly observed for contractile cell types which adhere to flat substrates through focal adhesions.

Fig 4.2 presented traction reconstructions using different methods for the cell-like pattern with low noise ($\sigma_N / < \|u\| >= 0.2$). In contrast, Fig 4.5 displays such reconstructions for varying noise levels ($\sigma_N / < \|u\| >= 0, 1$ and 2 from top to bottom), but only for the components in the xy-plane for simplicity. Upon visual inspection, it appears that FTTC accurately reconstructs the deformation profile shape for low noise levels, but for high noise levels, it overestimates the force magnitude. At very high noise levels, the DM can identify adhesion sites more easily than FTTC. The DM,

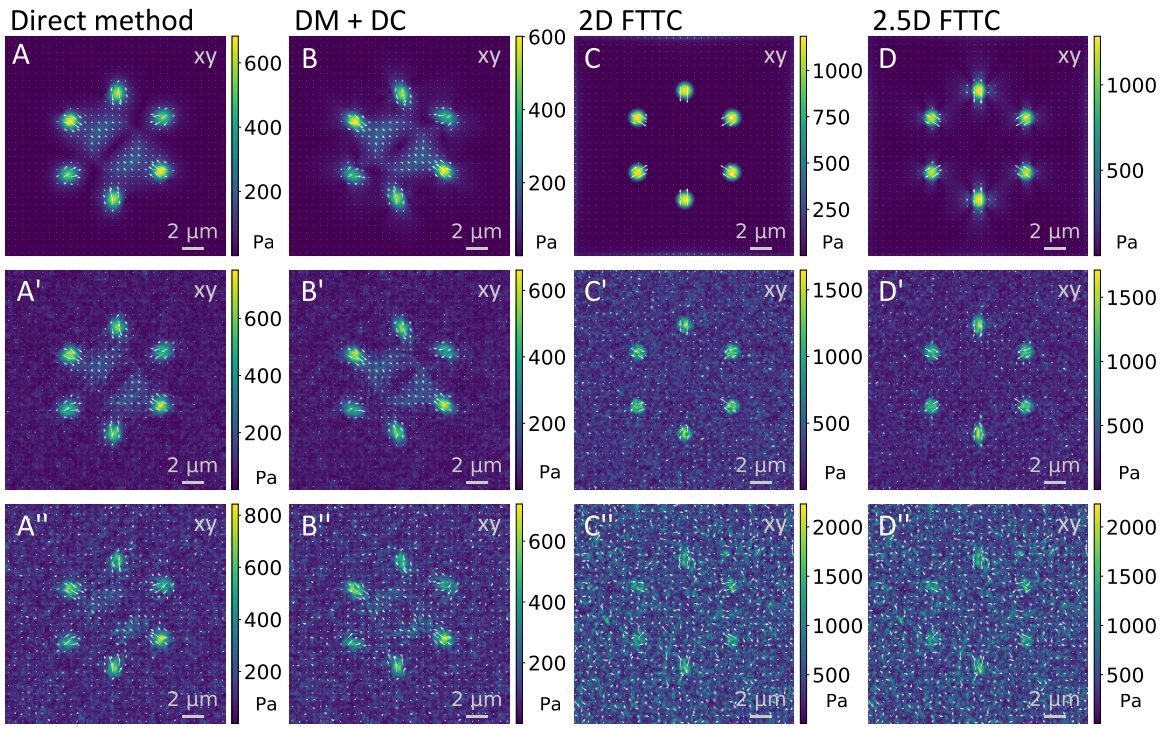

Figure 4.5: Reconstruction for cell-like traction pattern for different noise levels and reconstruction methods. The images show the reconstruction for no (upper row), large ($\sigma_N / < \|u\| >= 1$, mid row) and very large ($\sigma_N / < \|u\| >= 2$, lower row) Gaussian noise added to the analytical solution for the displacement before reconstruction with the different methods as indicated. The simulation parameters are identical to the ones used in Fig 4.2 and details can be found in the appendix, section A.3.

especially when using divergence correction, predicts a traction strength amplitude that is relatively insensitive to noise. However, the divergence correction scheme generates some artifacts that are independent of the noise level, indicating that the divergence removal algorithm transforms local noise into a more distributed signal that is not directly associated with the physical force generators.

In order to make these qualitative assessments more objective, I next evaluated a series of established metrics for the three different traction profiles shown in Fig 4.6. As before, the analytical solutions are known and it is easy to add Gaussian noise to the resulting deformation fields. The analysis results in a traction field described by a discrete sample vector $\boldsymbol{\tau}_j^{\text{recon}}$ for each site sampling point j, that can be compared to its theoretical equivalent $\boldsymbol{\tau}_j^{\text{true}}$ predicted from the analytical solution. I estimate the accuracy of the different reconstructions using the following five metrics [14, 101]:

- The deviation of traction magnitude at adhesions (DTMA) is given by:

$$\text{DTMA} = \frac{1}{N_P} \sum_i \frac{\text{mean}_{j(i)} \left(\left\| \boldsymbol{\tau}_{j(i)}^{\text{recon}} \right\|_2 - \left\| \boldsymbol{\tau}_{j(i)}^{\text{true}} \right\|_2 \right)}{\text{mean}_{j(i)} \left(\left\| \boldsymbol{\tau}_{j(i)}^{\text{true}} \right\|_2 \right)}. \tag{4.12}$$

  Here N_p is the number of adhesion patches and the index i iterates over the individual patches. For each patch, the mean is taken over all sampling points $j(i)$ belonging to the given patch. The DTMA determines how well the average magnitude of the patches is predicted. A good reconstruction would yield a

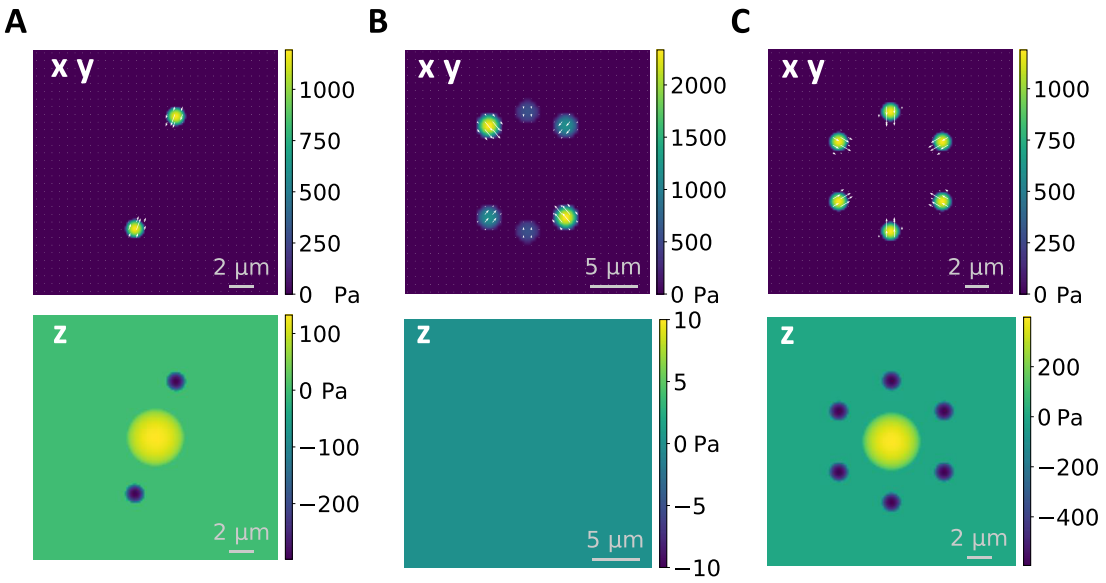

Figure 4.6: Profiles for comparison of direct and inverse method. In the first row, the heat map indicates the amplitude of the tangential traction, while the white arrows indicate their direction. In the second row, the heat map indicates the normal traction. Details on the simulation parameters for all three profiles can be found in the appendix, section A.3.

DTMA close to zero, while a positive or negative value would indicate an over- or underestimation, respectively.

- The deviation of traction magnitude at adhesions restricted to the two tangential dimensions (tDTMA) is given by:

$$\text{tDTMA} = \frac{1}{N_P} \sum_i \frac{\text{mean}_{j(i)} \left(n_2(\boldsymbol{\tau}^{\text{recon}}_{j(i)}) - n_2(\boldsymbol{\tau}^{\text{true}}_{j(i)}) \right)}{\text{mean}_{j(i)} \left(n_2(\boldsymbol{\tau}^{\text{true}}_{j(i)}) \right)}. \tag{4.13}$$

Here N_p is the number of adhesion patches and the index i iterates over the individual patches and $n_2(\boldsymbol{\tau}) = \sqrt{\tau_x^2 + \tau_y^2}$. For each patch, the mean is taken over all sampling points $j(i)$ belonging to the given patch. The tDTMA determines how well the average magnitude of the patches is predicted. In contrast to DTMA, I do only take into account the two tangential components. This focuses on situations in which the effect on the normal component behaves differently from the tangential one. A good reconstruction would yield an tDTMA close to zero, while a positive or negative value would indicate an over- or underestimation, respectively.

- The signal to noise ratio (SNR) is defined by:

$$\text{SNR} = \frac{\frac{1}{N_p} \sum_i \text{mean}_{j(i)} \left(\left\| \boldsymbol{\tau}^{\text{recon}}_j \right\|_2 \right)}{\text{std}_k \left(\left\| \boldsymbol{\tau}^{\text{recon}}_k \right\|_2 \right)}. \tag{4.14}$$

Here i,$j(i)$ and k are defined as above. The signal to noise ratio describes how well the adhesion sites are realized in comparison to background noise. The value should be significantly larger than 1 to indicate a good separation between traction sites and noise.

- The deviation of traction magnitude in the background (DTMB) is given by:

$$\mathrm{DTMB} = \frac{\mathrm{mean}_k \left(\left\| \boldsymbol{\tau}_k^{\mathrm{recon}} \right\|_2 \right)}{\frac{1}{N_p} \sum_i \mathrm{mean}_{j(i)} \left(\left\| \boldsymbol{\tau}_j^{\mathrm{true}} \right\|_2 \right)}. \tag{4.15}$$

  Here k runs over all sampling points not belonging to any patch. i and $j(i)$ again iterate over the patches and their sampling points respectively. The DTMB describes the level of background noise in the reconstruction. Ideally it takes a value close to zero indicating a low level of artifacts in the background.

- The deviation of traction maximum at adhesions (DMA) is defined by:

$$\mathrm{DMA} = \frac{1}{N_P} \sum_i \frac{\max_{j(i)} \left(\left\| \boldsymbol{\tau}_{j(i)}^{\mathrm{recon}} \right\|_2 \right) - \max_{j(i)} \left(\left\| \boldsymbol{\tau}_{j(i)}^{\mathrm{true}} \right\|_2 \right)}{\max_{j(i)} \left(\left\| \boldsymbol{\tau}_{j(i)}^{\mathrm{recon}} \right\|_2 \right)}. \tag{4.16}$$

  Again, i and $j(i)$ are defined as above. The DMA is similar to the DTMA, but rather than using the average traction over the whole adhesion site, the peak traction is taken into account. This emphasizes the reconstruction of the correct amplitude in core area over the correct profile close to the boundary. Like with the DTMA a good reconstruction would yield a DMA close to 0, while a positive or negative value would indicate an over- or underestimation, respectively.

Fig 4.7 shows the performance of the three different methods as a function of increasing noise level and for different traction patterns as shown in Fig 4.6. For all metrics except the SNR, the optimal value is shown as black horizontal line. In general, we see that all methods fail at very high noise levels. I find that FTTC is better than the DM in predicting the correct strength of the adhesions at low noise levels as seen in the DTMA, tDTMA and DMA results. However, the situation is reversed for higher noise, as the regularization is not sufficient to prevent overfitting above a certain noise level. While the application of the divergence correction scheme does reduce the SNR result, it improves the results for DTMB and DMA, by bringing them closer to zero, particular for high noise levels. A beneficial effect of the divergence removal is to reduce the difference between the DTMA and tDTMA scores, meaning that the algorithm does predict the orientation of the force vector more correctly. In contrast, the FTTC algorithm shows significantly better values for the DTMB metric, which means that it is more effective in preventing artifacts in the outside of adhesion sites. Surprisingly, the SNR is lower in the case of FTTC compared to the direct method. This can be attributed to the fact that FTTC works in Fourier space and errors in the reconstruction effect the whole field of view, not only the area close to the adhesion sites. I conclude that both methods perform similarly well, that the divergence correction as used here is in fact a disadvantage, that FTTC works best for small noise and that for larger noise the direct method becomes comparable and gives a clearer visualization due to the higher SNR.

4.3.3 Effect of sampling density

I finally study the effect of variation in sampling density, which experimentally is related to marker bead density and the resolution of the optical microscope. Because in practice displacement noise is expected to change with sampling distance and because

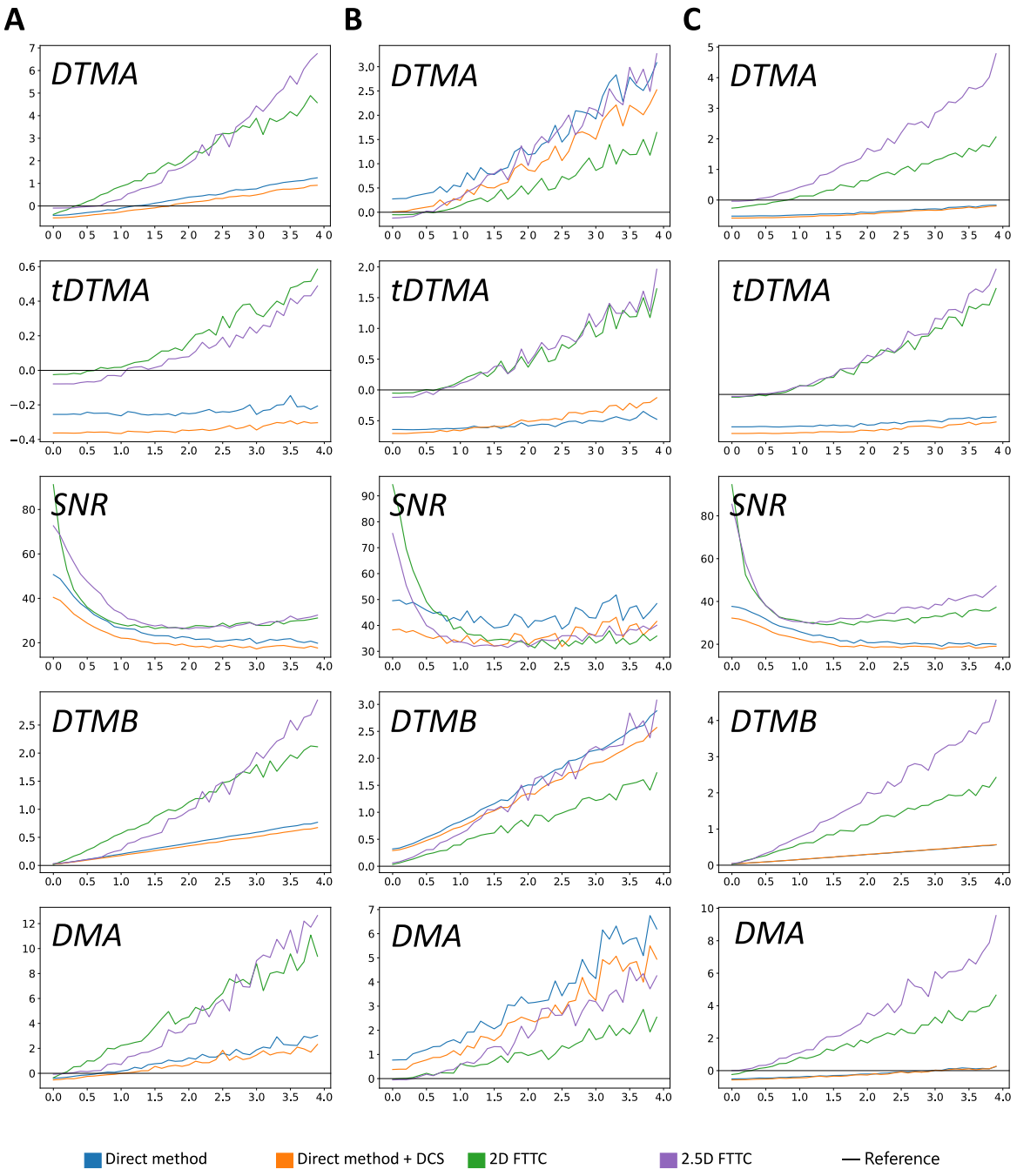

Figure 4.7: Quantitative comparison of direct and inverse methods. Performance of different force reconstruction techniques as a function of noise for different force profiles. The point profiles tested are the ones shown in Fig 4.6. Different metrics are shown, describing the quality of the reconstruction at different locations. The plots in one column all correspond to the same force profile. The x axis shows noise in units of $\sigma_N / < \|u\| >$

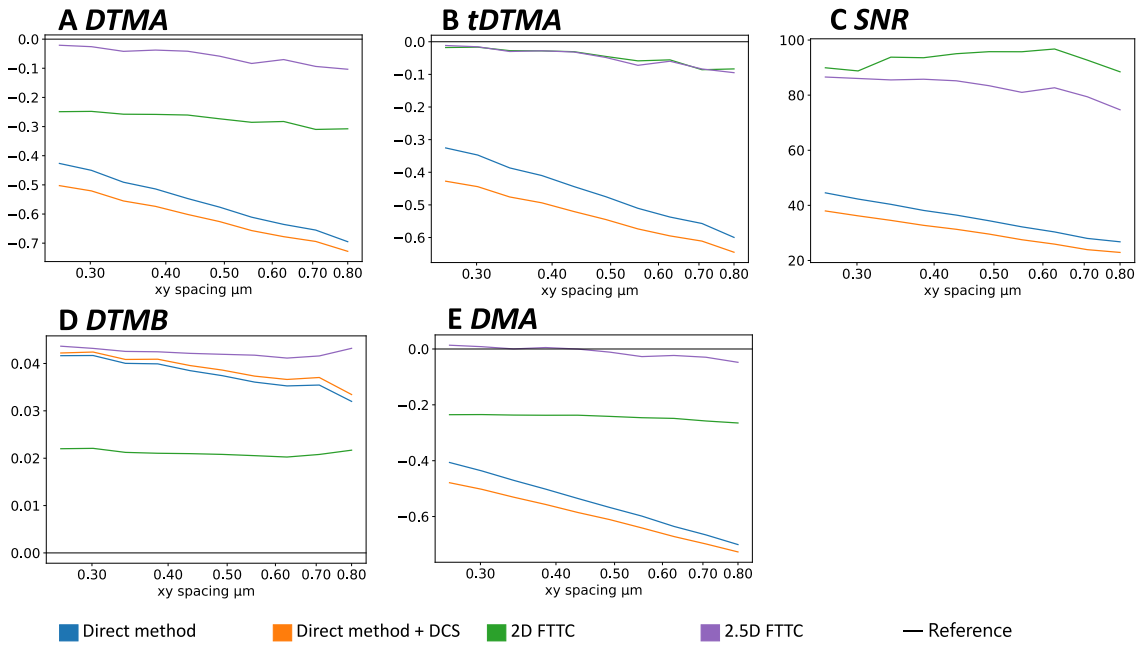

Figure 4.8: Effects of variation in sample density. Plots A to E show how the different metrics are affected when using a different distance of the sampling points when setting up the input data without adding any noise. The profile first shown in Fig 4.2 is used. The default sample point spacing in x and y for this profile is 0.4 µm and here is varied up and down. The z-component is scaled proportionally. Since there is no noise, in general FTTC performs much better. The direct method shows a consistent improvement for decreasing sampling point distance. Details on the simulation parameters can be found in the appendix, section A.4.

I now focus on the effect of sampling density, in Fig 4.8 I show the results for vanishing displacement noise. As expected, overall, all metrics become worse with increasing sampling distance. Interestingly, however, the performance of FTTC seems to be more robust, while the DM quickly decreases in performance. This implies that a decrease in sampling distance (that is an increase in sampling density) will be much more beneficial for the DM. I note that for FTTC, the SNR and (for 2.5D FTTC) also DTMB can even slightly improve with decreasing sampling density. This surprising (but weak) effect might be related to the fact that for the Fourier method, increasing sampling distance amounts to stronger filtering of the data, thus focusing on the overall adhesion pattern. I also checked that the same trends persist for variation of sampling distance at finite noise (appendix, section A.4). I noticed that for FTTC the SNR now significantly improves for a decrease in sampling density. This confirms that noise and sample point density are in fact correlated, because an increase in sampling density also increases the number of nodes that contribute noise towards the calculation. FTTC and DM are affected differently by an increase in sampling density in the presence of noise. For the DM the increase of the numbers of nodes improves the accuracy of the numerical gradients. For FTTC, the quality of reconstruction at the sampling points does not significantly improve when increasing the resolution, but the increase of the number of nodes increases the negative effect of noise on the result.

4.4 Conclusion

Motivated by the observation that different TFM-methods are often advanced in specific contexts, but rarely compared to each other, here I have conducted an in-depth comparison of inverse and direct methods in the framework of 2.5D TFM. This considers both the 3D-nature of the direct method as well as the fact, that the setup of a flat elastic substrate, common for high-resolution experiments, is usually treated by 2D TFM but can be expanded by considering also normal forces. By selecting 2.5D TFM both techniques could be directly compared to each other. For the inverse method, I have used the 2.5D version of FTTC introduced and tested in the previous session.

For each performance test, I have first designed traction patterns that are representative for experiments, suitable for the task at hand and analytically tractable. Motivated by the observation that experimental noise is Gaussian-distributed in experiments [126], I have added Gaussian noise to the displacements and than performed the reconstructions with different methods. In the future, this procedure could be complemented by a stronger focus on the actual image generation occurring in TFM-experiments, in particular by using specific image processing algorithms and point spread functions [85, 97, 99].

I have evaluated our reconstructions using commonly used metrics [14, 101]. This methodology then was used in three ways. I first optimized the direct method, then compared it with FTTC, and finally studied the effect of sampling distance. For the direct method, I found that the 3x3x3 patch calculation of the derivatives is indeed the best solution and that the standard divergence correction from hydrodynamics works, but does not necessarily improve our solutions and in fact worsens the visual appearance of the traction pattern. Assuming a perfect elastic material, divergence is generated only by noise, which is known to be essentially Gaussian in experimental TFM data. This means that it is uncorrelated between different dimensions. Divergence removal, however, couples the different dimensions and therefore does not counteract the process that generated the divergence. I conclude that although required from the viewpoint of elasticity theory, divergence removal is not really needed for the TFM procedures used here.

Our main result is the demonstration that the direct method for TFM can be used to reliably predict the traction field at the surface of a flat elastic substrate and in fact performs comparatively well to the best inverse method, that is FTTC, at least for large noise, when FTTC worsens more quickly. The direct method also offers an interesting alternative to costly FEM-simulations, in situations where FTTC cannot be applied. The 3x3x3 patch method that has proven to be a reliable method for deformation gradient calculation can in fact be easily adapted for curved surfaces. Although FTTC is expected to remain the standard method for 2D TFM, I believe that the direct method is a valuable alternative even in this case, e.g. because it can also reconstruct monopolar traction patterns. For 2.5D TFM I believe that the choice between the direct and inverse methods should depend on context, but that in principle, both might work well.

Chapter 5

The adaptive near-field method and cellular response to microneedle shearing

In this chapter, I introduce an alternative method to accurately quantify adhesion strength in unbalanced setups. This allows us to overcome some limitations of the FTTC method in 2D setups. The chapter is largely based on the work published in manuscript 3. This work was conducted in collaboration with Steven Huth and Christine Selhuber-Unkel from the Institute of Materials Science, Biocompatible Nanomaterials, Kiel University, who conducted the experiments and also closely collaborated in interpreting the results

5.1 Motivation

Traction force microscopy is mostly used to study the cell-mechanical response to a passive environment in the form of a static hydrogel substrate. Current traction force microscopy models are optimized for this setup and methods like FTTC assume an equilibrium of a cell's traction forces.

Cells do, however, not only react to passive stimuli like the resistivity to a planar substrate but also demonstrate a remarkable ability to respond to externally applied forces and mechanical cues by means of a process known as mechanotransduction [161, 162]. In nature, cells experience a variety of externally applied forces, for instance from blood flow, muscle contraction, movement of other cells, or wound opening. In particular, force transmission is important in tissue formation and adaption [57] as well as in collective cell migration, where many cells interact with each other and mechanically strong cells become leader cells [139, 163]. Therefore, to understand force transmission by cells more completely, it is crucial to study traction forces under external forces.

Techniques to exert mechanical stimuli to cells include atomic force microscopy (AFM), which can be employed to measure forces necessary to rupture cellular adhesions [164, 165] or forces exerted by cells [166, 167], hydrodynamic shear stress [168–170], optical or magnetic tweezers [171–174], microneedle assays [175–177] and optical stretchers [178, 179]. Despite the fact that such a large variety of physical cell manipulation techniques has been established and cellular forces exerted to surfaces can be measured via TFM or elastic resonator interference stress microscopy [180], a quantification of cellular force adaptation as a response to well-defined mechanical

stimuli applied to cells has not yet been realized.

Here, I present a new tool that combines TFM with externally applied mechanical stimulation by microneedle shearing. This setting allows to quantify cellular force transmission by measuring how cells distribute an external well-defined shear force to their adhesion sites. The spring constant of the microneedle is calibrated and thus the shear force exerted by the needle is known. I advanced current TFM procedures to create a novel procedure that analyzes traction forces in the presence of an external force monopole. This new force transmission assay is a versatile technique that is complementary to existing methods, as it can also be combined with other techniques such as AFM to broaden our understanding of the interplay of cellular biomechanics and adhesion.

5.2 Theory and Methods

5.2.1 Why FTTC is insufficient for this task

I have already demonstrated, that the FTTC algorithm would have to be modified in order to remove the divergence of the Green's function in the limit $\boldsymbol{k} \to 0$. Since this divergence is primarily attributed to the infinite thickness of the substrate, the most obvious approach would be to replace the elastic halfspace postulate by a finite thickness solution. However, one can use a simple multipole expansion to highlight the difficulties with this approach. As seen in the chapter 2, Eq 2.19, we know that:

$$u_i(\boldsymbol{x}) = \int \sum_j \mathrm{G}_{ij}(\boldsymbol{x} - \boldsymbol{x}')\tau_j(\boldsymbol{x}')\,\mathrm{d}x\,\mathrm{d}y \tag{5.1}$$

with the Green's function given in Eq 2.76 now expressed in component notation

$$\mathrm{G}_{ij}(\boldsymbol{x}) = \frac{1+\nu}{\pi E}\left((1-\nu)\frac{\delta_{ij}}{r} + \nu\frac{x_i x_j}{r^3}\right) \tag{5.2}$$

where $r = |\mathbf{x}|$. In this section, I fix the coordinate system in such a way, that the origin corresponds to a well-defined point within the cell, which I call the cell center.

In a common traction force setup, $\boldsymbol{\tau}$ is only non-zero in some region Ω around the cell center, where $|\boldsymbol{x}'| < R$. For a point far away from the cell center $R << |\boldsymbol{x}|$, only the moments of the traction distribution will dominate. To see the influence of different moments, I first find a Taylor expansion of the Green's function, yielding the following:

$$\mathrm{G}_{ij}(\boldsymbol{x} - \boldsymbol{x}') = \frac{1}{r}\mathrm{H}^{(0)}_{ij}\left(\frac{\boldsymbol{x}}{r}\right) + \sum_k \frac{1}{r^2}\mathrm{H}^{(1)}_{ijk}\left(\frac{\boldsymbol{x}}{r}\right)x'_k + \mathcal{O}(|\boldsymbol{x}'|^2) \tag{5.3}$$

The tensors $\mathbf{H}^{(0)}$ and $\mathbf{H}^{(1)}$ describe the angular dependency. They are given by.

$$\mathrm{H}^{(0)}_{ij}(\boldsymbol{n}) = r\mathrm{G}_{ij}(r\boldsymbol{n}) = \frac{1+\nu}{\pi E}\left((1-\nu)\delta_{ij} + \nu n_i n_j\right) \tag{5.4}$$

and

$$\begin{aligned}\mathrm{H}^{(1)}_{ijk}(\boldsymbol{n}) &= r^2\left.\frac{\partial \mathrm{G}_{ij}}{\partial x_k}\right|_{\boldsymbol{x}=r\boldsymbol{n}} \\ &= \frac{1+\nu}{\pi E}\left((\nu-1)\delta_{ij}n_k + \nu\delta_{kj}n_i + \nu\delta_{ki}n_j - 3\nu\frac{x_i}{r}n_i n_j n_k\right).\end{aligned} \tag{5.5}$$

Now for $R << |\boldsymbol{x}|$, I find approximately:

$$u_i(\boldsymbol{x}) \approx \sum_j \frac{\mathrm{H}_{ij}^{(0)}(\boldsymbol{x})}{r} \int \tau_j(\boldsymbol{x}')d^2x' + \sum_{jk} \frac{\mathrm{H}^{(1)}(\boldsymbol{x})_{ijk}}{r^2} \int x'_k \tau_j(\boldsymbol{x}')d^2x' \tag{5.6}$$

By inserting the definition of the force monopole, Eq 1.18 and the first order moment matrix, Eq 1.19, the far field solution takes an approximate form

$$u_i(\boldsymbol{x}) \approx \sum_j \frac{\mathrm{H}_{ij}^{(0)}(\boldsymbol{x})}{r} F_j + \sum_{jk} \frac{\mathrm{H}_{ijk}^{(1)}(\boldsymbol{x})}{r^2} \mathrm{M}_{kj} \tag{5.7}$$

In usual TFM measures, the solution is balanced, meaning that the force monopole has to be zero ($\boldsymbol{F} = 0$). This means, the deformation field decays relatively quickly with the inverse square of the distances. This fast decay is essential for FTTC as the transformation of the deformation field into Fourier space makes implicit assumptions about the structure of the deformation field at the boundaries of the observation frame. Usually, because the deformation field decays quickly, the integration cutoff at the boundary of the observation frame has little effect on the reconstructed traction, but this is no longer the case when a force monopole is introduced.

Another major issue is determining the $\boldsymbol{k} = 0$ mode of the deformation field. In a practical setup, we can only observe the displacement of beads relative to the stress-free configuration, but not the displacement of beads relative to the base of the substrate. This makes it impossible to distinguish bulk bead displacements from changes in the field of view due to slight movements of the sample tray relative to the microscope's objective.

FTTC is unable to handle this particular setup due to the presence of a monopole force. While the divergence of the Green's function at the $\boldsymbol{k} = 0$ mode has already been mentioned in chapter 2, I will demonstrate that this issue is fundamental to the fact, that we are working in Fourier space. The solution is therefore to avoid the widely used Fourier space force reconstruction algorithms entirely and use an approach based on the spatial domain. Although continuous force distributions can in principle be reconstructed with the boundary element method (BEM) [10, 128], here I make additional use of the fact that the cells used in our experiments have well-defined adhesion sites that are increasingly stressed as the cell is sheared by the microneedle. I can therefore use methods that are specialized for localized force distributions. However, force reconstruction by point forces as introduced by Schwarz *et al.* [11] as described in chapter 2, which assumed force transmission at singular points, often suffered from the divergence of the Green's tensor (Eq 2.90) at such singularities and thus avoided the near field and tried to estimate forces using far field deformations. A principal shortcoming of this approach is the high susceptibility to noise due to the often small deformation. In contrast, many modern approaches are near field ones but often rely on specific problem setups to fit an analytical model to the deformation field [181–183]. For this reason, here I present a technique that makes very little assumptions about the underlying geometry of adhesive regions.

5.2.2 Reconstruction of traction forces

As explained in the introductory sections, forces are primarily transmitted to cells via focal adhesions. By making use of the fact that the analytical field is known, we

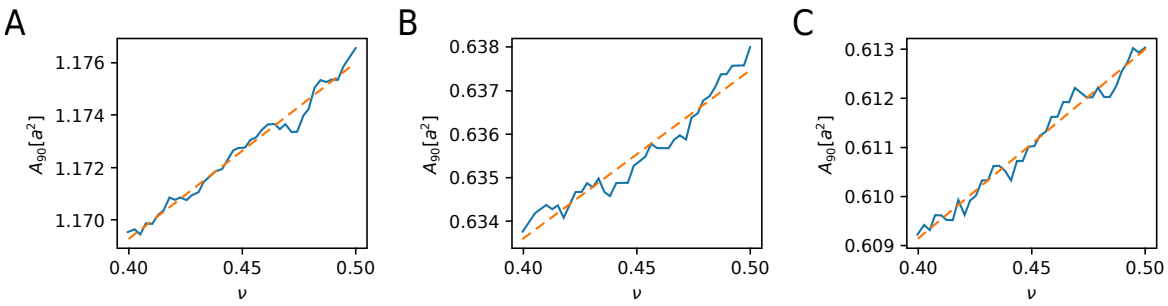

Figure 5.1: Effect of the Poisson's ratio on the contact area (A) Numerical relation betwen A_{90} and ν for the constant-traction profile (B) Same relation for the Hertz-like profile. (C) Numerical results relation between A_{95} and ν for the constant-traction profile. In all case a mostly linear dependence is observed.

can now reconstruct forces using a technique similar to the traction reconstruction method by point forces introduced in chapter 2. However, rather than sampling the deformation in random points, we sample the deformation field immediately below the predicted site of adhesion. In this point, both noise and contributions to the deformation field due to other sampling points are marginalized compared to the contribution due to the local adhesions and can thus be neglected. Thus, the reconstructions of the individual adhesion sites decouple, avoiding correlation errors between the individual force reconstructions. If the forces would be reconstructed from the far field, the exact adhesive profile can be ignored and the force transmission can be described by singular peaks. Since this approach uses the near field however, the solution heavily depends on the exact nature of the adhesive pattern. In particular, the adhesions' extent must be taken into account.

To compare the effect of different assumptions, I initially consider two types of circular adhesive patterns: the constant traction force pattern and radial decreasing Hertz-like traction force pattern. Noticeably while it has been suggested that focal adhesions have an elliptical shape [11, 13, 184–186], in this analysis, I will assume that focal adhesions have a circular shape. I will later show that choosing a circular rather than an elliptical model for the adhesions will have only limited effects.

The analytical solution for the surface deformation created by a tangential traction force $\boldsymbol{F} = (F_x, F_y)^T$ distributed equally over a circular area with radius a as defined in Eq 2.44 is described in Eq 2.45 and Eq 2.46. In the limit $r \to 0$ I find that

$$\boldsymbol{F} = \frac{\pi a E}{(1+\nu)(2-\nu)} \boldsymbol{u}(0) \ . \tag{5.8}$$

This is the relation between overall force and displacement in the middle of the focal adhesion. For the Green's function, this displacement would diverge, because it only describes the far field.

Similarly, the surface deformation created by a tangential traction force distributed in a Hertz-like manner over a circular area as defined in Eq 2.56 is described in Eq 2.57 and 2.58. In the limit $r \to 0$, I find, that:

$$\boldsymbol{F} = \frac{8 a E}{3(1+\nu)(2-\nu)} \boldsymbol{u}(0) \ . \tag{5.9}$$

Compared with Eq 5.8, we see that both scale linear in Young's modulus and patch size. Also, the contribution related to the Poisson ratio is equivalent. They differ only in the constant prefactor.

In general, the deformation fields in both cases share many similarities. In both cases the absolute value of the deformation field $u_{abs} = \sqrt{u_x^2 + u_y^2}$ takes its maximal value at the center of the deformation. In addition, the isolines of the u_{abs} field enclose simple connected regions always containing the center of the coordinate system. I define A_h to be the area where $u_{abs}(x, y) > h u_{abs}(0, 0)$. While the deformation field $\boldsymbol{u}$ is dependent on five parameters E, ν, a, F_x and F_y, only two of them, a and ν, will affect A_h. Because of the way we can choose the unit scale, it can be easily seen, that a contributes quadratically ($A_h \propto a^2$). A numerical analysis (Fig 5.1) reveals that the relation to ν can be estimated using a linear function. Therefore, the expression $A_h = (y_h + m_h \nu) a^2$ describes the relationship between A_h, a and ν. The constants y_h and m_h can be determined numerically by simulating the situation for an arbitrary choice of the five parameters mentioned above.

An estimation of the total force $\boldsymbol{F}$ of a Hertz-like or constant-traction contact based on the deformation field can be found using Eq 5.8 or 5.9, by finding the deformation at the center of the contact. The contact radius a can be calculated from the isoline-enclosed area A_h for some value h.

The overall algorithm to determine forces $\boldsymbol{F}_i$ within each adhesion now contains the following steps done individually for each adhesion search area i:

1. Interpolate the deformation field onto a regular spaced square grid for each time step.

2. Calculate the absolute value u_{abs} of the deformation field for each time step.

3. Locate the center of the adhesion by making use of the fact that u_{abs} should reach its maximum in this location for each time step.

4. A common issue in the above estimation is the fact that the adhesion in adjacent search areas might cause the center of the current adhesion not to correspond to the global maximum of u_{abs} within its search area, in which case the largest value for u_{abs} can be found right next to the adhesion search area boundary. In these cases, I rely on an interpolation from the other time steps to select the presumed location for the area estimate.

5. Now that I have determined the center of the adhesion for each time step and the radius a, I can determine the deformation $\boldsymbol{u}$ in the adhesion center.

6. Calculate the area A_h within the adhesion search area where u_{abs} lies within $1 - h = 5\,\%$, $10\,\%$, $20\,\%$, $30\,\%$ of its maximal value for each time step.

7. For each time step and each threshold value an estimate for the adhesion radius a can now be determined using the above-mentioned area formula $a = \sqrt{A_h / (y_h + m_h \nu)}$ using the predetermined values for y_h and m_h In general, all of these estimates should yield a similar value, as the radius of the adhesion is expected not to change during the procedure.

8. The final estimate for the adhesion radius can now be found by finding the mean of the estimates determined in the previous step. I explicitly emit those time steps from the calculation, where I had to use the interpolation from the other time-steps in step 4, as the estimates in these cases are particularly unreliable.

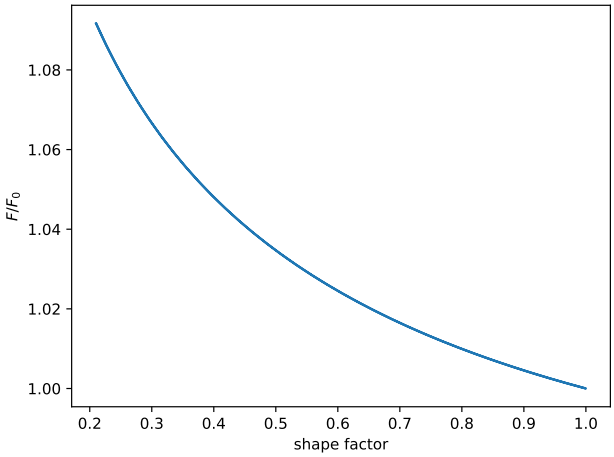

Figure 5.2: Ratio between the predicted force for an elliptical contact and a circular contact of equal contact area F/F_0 for $\nu = 0.5$ using Eq 5.10. The horizontal axis describes the shape factor given as defined by [184].

9. Now that I have determined the deformation $\boldsymbol{u}$ in the center of each adhesion for each time step and the radius a, I can determine the corresponding force $\boldsymbol{F}_i$ using Eq 5.8 or 5.9.

In the following I name this method the Adaptive Near-Field Method (AdNFM) or circular patch method of TFM

In order to determine whether adhesion sites can be better described by Hertz-like or the constant-traction profiles, one can compare the statistic variance between the radius estimates derived from different search area estimates in step 7. In the following, I select the setup using constant-traction profiles. During the experimental analysis, I will later show this choice is slightly superior to the one using Hertz-like profiles.

As mentioned above, many studies have suggested a more elliptic shape [184] rather than a circular one as assumed by the two approaches discussed. An elliptical variant of a Hertz like contact was introduced in Eq 2.67. Using the subsequent equation Eq 2.68 and Eq 2.69, I find that the deformation field for force central displacement relation at the center is given by:

$$\boldsymbol{F} = \frac{8\sqrt{ab}E}{3N(\nu, a/b)(2-\nu)(1+\nu)}\boldsymbol{u}(0) \ . \tag{5.10}$$

The function $N(\nu, a/b)$ is given by

$$N\left(\nu, \frac{a}{b}\right) = \begin{cases} \frac{4}{\pi(2-\nu)}\sqrt{\frac{a}{b}}\left(K_0(m_a) - \nu\frac{K_0(k_a)-E_0(k_a)}{k_a^2}\right) & a < b \\ 1 & a = b \\ \frac{4}{\pi(2-\nu)}\sqrt{\frac{b}{a}}\left((1-\nu)K_0(k_b) + \nu\frac{K_0(k_b)-E_0(k_b)}{k_b^2}\right) & a > b \end{cases} \tag{5.11}$$

with the definition $k_a = \sqrt{(1-a^2/b^2)}$ and $k_b = \sqrt{(1-b^2/a^2)}$. Its inverse $1/N$ describes the ratio between the force predicted using Eq 5.10 and the one predicted using Eq 5.9 for a circular adhesion of equal area. In Fig 5.2 $1/N$ is plotted against the shape factor

$\frac{\pi^2}{4}\frac{b}{a}\frac{1}{E_0(m_a)^2}$. Assuming a shape factor of 0.5 as observed by [184], we see that the force increase is only around 4% which is likely below the accuracy of the prediction.

5.2.3 Calculation of force moments

The calculation of force moments was introduced in the introductory chapter. However, procedures need to be adjusted due to the existence of a monopole moment.

The force monopole, the net directed force on the substrate was introduced in the introductory chapter and is also mentioned in Eq 1.18. Due to momentum conservation, it should be equivalent to the force transmitted by the cantilever into the cell. If the force contribution of each adhesion patch is known, the total force monopole vector can be obtained by simply summing up the force contributions of all adhesions:

$$\boldsymbol{F} = \sum_k \boldsymbol{F}_k \ . \tag{5.12}$$

Similarly, one can calculate the center of force (Eq 1.20) and the first order moment matrix (Eq 1.19) by inserting the traction profile for patches (Eq 2.56 or Eq 2.44) and making use of the fact that due to their symmetric nature they contribute in the same way as point forces:

$$\boldsymbol{x}_{\mathrm{CF}} = \left(\sum_k |\boldsymbol{F}_k| d^2x\right)^{-1} |\boldsymbol{F}_k| \boldsymbol{x}_k d^2x \ , \tag{5.13}$$

$$M_{ij} = \sum_k (\boldsymbol{x}_k)_i (\boldsymbol{F}_k)_j d^2x \ . \tag{5.14}$$

Without needle pulling, angular momentum conservation dictates that the net torque introduced in Eq 1.22 is zero and the moment matrix symmetric. In this case, one can find an orientation of the axis such that $\mathbf{M}$ is diagonal and the eigenvalues can be used to find the directed and isotropic contractile moment of the system. To also consider the case of needle pulling, I define a slightly modified version of the moment matrix, where I removed the torque contribution:

$$M^{\parallel}_{ij} = \int x_i x_j \frac{\boldsymbol{\tau}\cdot\boldsymbol{x}}{\boldsymbol{x}^2} d^2x \ . \tag{5.15}$$

If I again insert the definition of the patches, I obtain:

$$M^{\parallel}_{ij} = \sum_k (\boldsymbol{x}_k)_i (\boldsymbol{x}_k)_j \frac{\boldsymbol{F}_k\cdot\boldsymbol{x}_k}{\boldsymbol{x}_k^2} \ . \tag{5.16}$$

This matrix is symmetric and thus an orthogonal eigendecomposition can be found. The two eigenvalues describe the dipole moments and the eigenvector corresponding to the major dipole describes the main contractile axis. This can be proven by comparing the trace of $\boldsymbol{M}^{\parallel}$ to the contractile momentum μ introduced in Eq 1.21, which both yield the same value.

5.3 Quantifying force in fibroblasts under external shearing

To investigate the force transmission from the apical to the basal side of an adherent cell, my experimental collaborators conducted experiments during which they

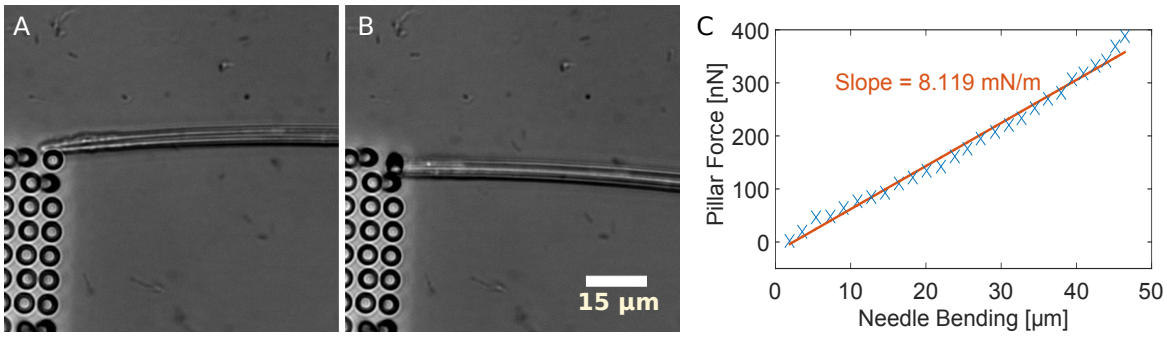

Figure 5.3: Microneedle shearing of an PDMS pillar. (A) and (B) show exemplary phase contrast images of the shearing. The needle moves downwards and bends the pillar. The pillar, on the other hand, exerts a force to the needle, which results in a bending of the needle. The force acting between needle and pillar is calculated from the bending of the PDMS pillar. (C) presents a plot of the pillar force versus the bending of the microneedle for each frame of the shearing experiment. The slope corresponds to the microneedle's spring constant.

exerted well-defined shear forces to the apical side of mouse embryonic fibroblasts (MEFs) while simultaneously measuring the change in traction forces at their basal side (manuscript 3). Details of the imaging and image analysis methods can be found in the appendix (section B.1); Details of the experimental methods can be found in the manuscript. We studied MEF fibroblasts expressing mNeonGreen (NeonG) labeled zyxin as a marker for focal adhesions. Cells were allowed to spread on a fibronectin-functionalized PAA gel with embedded red fluorescent marker beads so that traction forces could be derived from recording the displacement of the marker beads. A microneedle was installed into a micromanipulator such that the tip of the microneedle was parallel to the cell substrate. Moving the microneedle with a computer-controlled micromanipulator results in the application of a shear force to the apical cell surface. The spring constant of this microneedle was calibrated by shearing PDMS pillars prior to the cell experiments. To do so, first the Young's modulus of the PDMS sample was measured with an AFM-based indentation method [187]. Then, the calibration of a microneedle was carried out by moving the microneedle against a PDMS pillar (Fig 5.3) and measuring the associated PDMS pillar and microneedle bending. In Fig 5.3 A and B, representative phase contrast images of the shearing of a PDMS pillar with a microneedle show the bending of pillar and microneedle due to shear forces. Knowing the geometry as well as the Young's modulus of the pillar, the shear force is calculated from the pillar bending [188]. Fig 5.3 C shows a plot of the shear force versus the microneedle bending for each frame of the experiment. The slope of a linear fit to this curve corresponds to the microneedle's spring constant.

For the force transmission experiments, the microneedle was carefully inserted into the fibroblast cell directly below or above the nucleus. Subsequently, the microneedle was moved at a constant speed of 5 µm/s towards the nucleus to exert increasing shear forces to the cell until the cell detached from the underlying PAA substrate. My collaborators decided to shear the nucleus, as other modes of exerting shear forces to the cell caused the microneedle to quickly slip away. This is in agreement with published work by Riveline *et al.* [176] and Paul *et al.* [177] who have shown that nucleus shearing is the most efficient way to transmit forces to a cell with a microindenter. During the shearing process, phase contrast images of the cell and needle as well as fluorescent

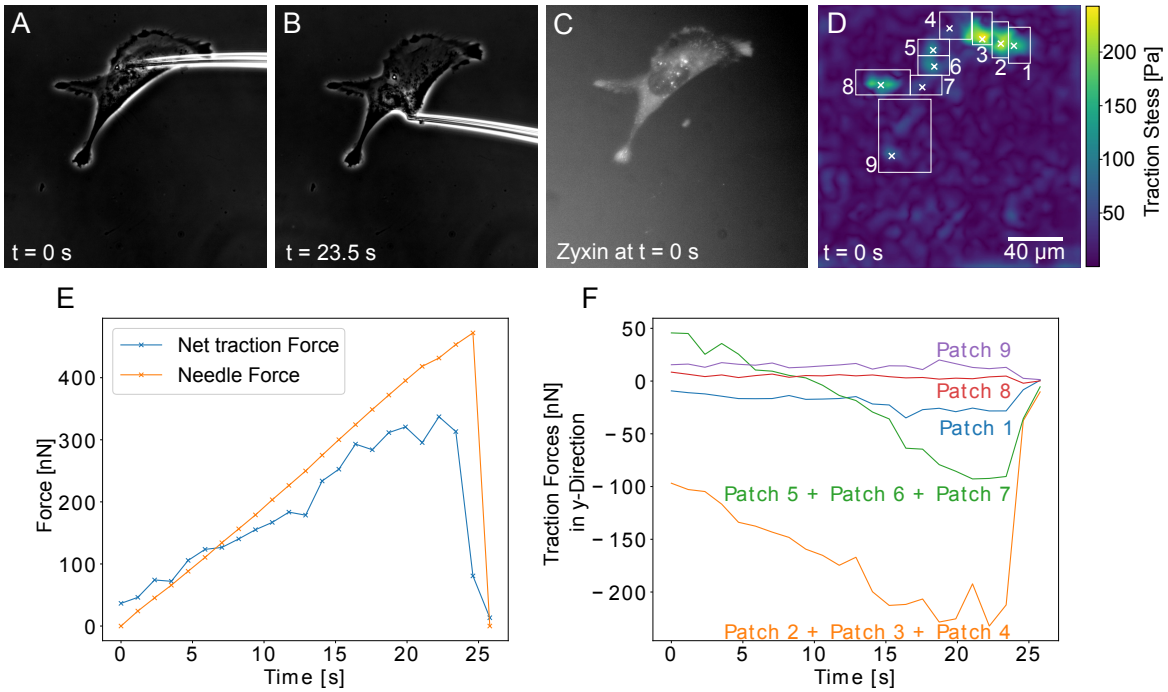

Figure 5.4: A microneedle is inserted into a fibroblast, which expresses fluorescently labelled zyxin and adheres to a TFM substrate. Subsequently, the needle is moved into the y-direction at a constant speed and exerts shear forces to the cell until it is detached. (A) and (B) Exemplary phase contrast images taken during cell shearing. Both the cell and the needle bending are monitored. The bending of the needle is used to calculate the shear force. (C) The cell's zyxin distribution prior to the shearing process is recorded via fluorescence microscopy. (D) Traction force map of the cell with adhesion search areas delimited by white rectangles and mean patch locations marked by crosses. Traction forces were reconstructed for $t = 0\,\mathrm{s}$ using Fourier Transform Traction Cytometry (FTTC). For the reconstruction of traction forces with the shear force monopole present ($t > 0$), we used the AdNFM. (E) The needle force and the cell's net traction force are plotted as a function of time. (F) The traction forces in y-direction are plotted for different adhesion patches (labelled in panel (D) to quantify how the cell loads its adhesion sites under the external shearing stimulus.

images of the marker beads embedded in the PAA gel were recorded. Fig 5.4 A and B present exemplary phase contrast images of such an experiment. These phase contrast images were used to monitor the cell as well as to calculate the degree of needle bending for each frame. Knowing the needle's spring constant, the needle bending is a measure for the shear force exerted to the cell. To correlate the measured traction forces with the distribution of adhesion sites, the zyxin distribution of the fibroblast prior to each experiment was recorded (Fig 5.4 C). This information is essential, as focal adhesions are the main site of traction force exertion [54, 101].

The images of the fluorescent marker beads embedded in the PAA sample to which the cell is adhering were used as the basis for computing the traction forces that the cell exerted to the PAA sample as a function of external shear force. As the microneedle applies external shear forces to the cell surface, cellular traction forces are no longer balanced by internal forces only, and the overall force balance has to include the overall force applied by the microneedle. In other words, the cell traction is not dominated by the force dipole contribution, as is usually the case, but also includes a force monopole.

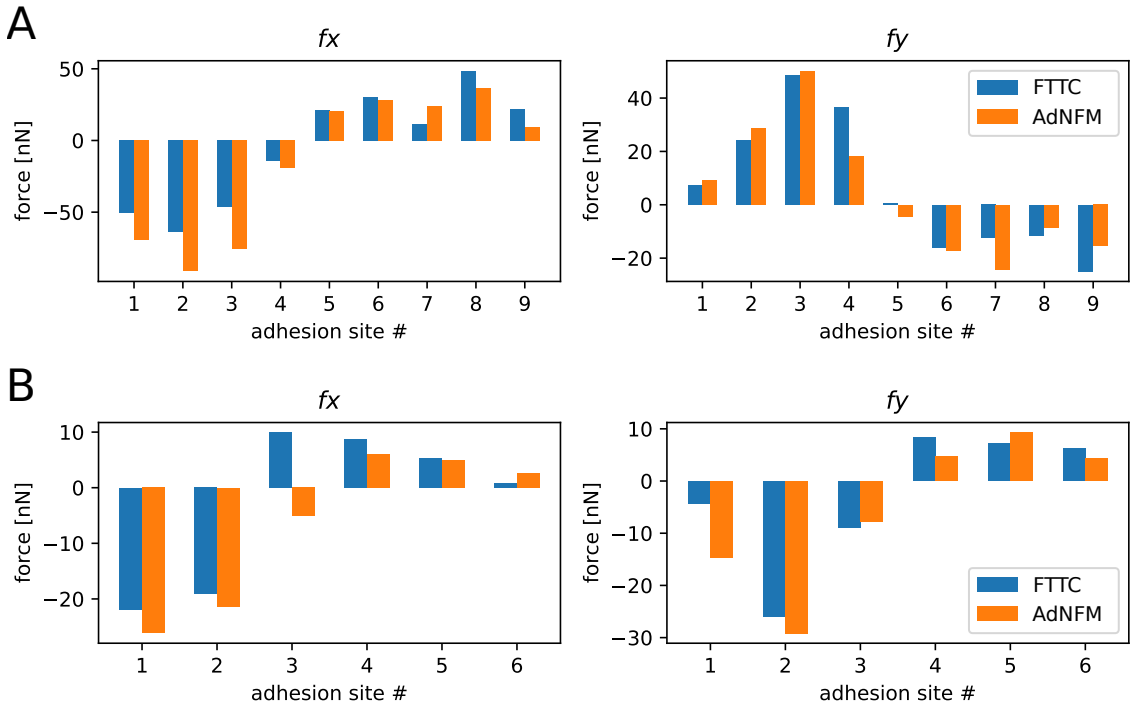

Figure 5.5: Comparison of the traction forces predicted in the absence of an external force monopole (at t = 0) using the Adaptive Near Field Method (AdNFM) and a regularized Fourier Transform Traction Cytometry (FTTC) [76] using generalized cross-validation [14]. (A) Profile for the cells introduced in Fig 5.4. (B) Profile for the cells introduced in Fig 5.8. In both cases, the agreement between the two methods is rather good.

Fig 5.4 D shows a traction force map computed using FTTC overlayed with estimates made using the AdNFM as described above. The algorithm first determines the main sites of traction force transmission from the cell to the PAA sample. These sites ("adhesion patches") are marked by white crosses and numbers in the figure panel. I then calculated the traction force vector of each adhesion patch and then determined the magnitude of the sum of all traction force vectors. This net traction force magnitude was then compared to the needle force. As traction forces without a force monopole are balanced, introducing an externally applied force must result in a change of traction forces to balance the externally applied force. The results shown in Fig 5.4 E demonstrate that the net traction force and the externally applied shear force closely matched during the entire experiment, validating our analysis approach. The fact that the shear force and net traction force do not match perfectly might have several reasons: force can be dissipated [165] or cells might resist deformation with cell specific responses. Furthermore, as several calibration steps are needed during force calculations, the results are prone to calibration errors: The needle spring constant was calibrated via shearing a PDMS pillar and the Young's modulus of the PDMS was measured for the computation of the needle's spring constant. Furthermore, the PAA's Young's modulus needed to be determined in order to reconstruct traction forces from the bead displacement data. Both materials' elastic properties were measured with a state-of-the-art atomic force microscopy procedure [187] naturally prone to measurement errors, which means that neither the needle force, nor the traction forces are perfectly accurate. Image analysis inaccuracies in the quantification of the

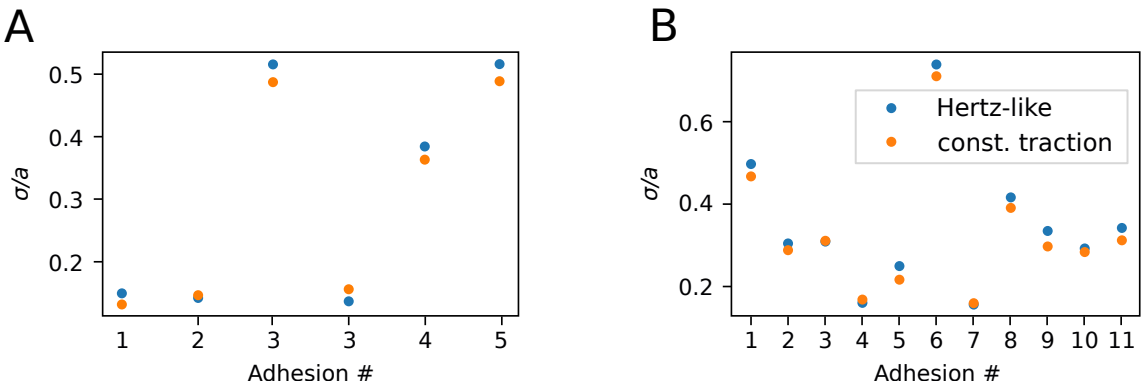

Figure 5.6: Comparison of the relative standard deviation of force reconstruction for Hertz-like and constant traction profiles (A) Comparison of force in the definition of areas for the cell presented in Fig 5.8 (B) Same for the cell presented in Fig 5.4

needle bending and bead displacement may further contribute to the slight mismatch between the net traction force and externally applied force.

In Fig 5.4 F, the y-components of traction force vectors are plotted for the different adhesion patches. For better visualization, some neighboring adhesion patches with similar force loading behavior are combined. (The data for each individual adhesion patch are presented in the appendix Fig C.1). As the needle pulled mainly in the y-direction, the x-components of the traction vectors were not influenced by the needle shear force, which is why we concentrate on discussing the y-components (the graph of the x-components of the traction vectors is also included in the plot in the appendix). One sees that the microneedle pulling mainly loads the adhesion patches 2, 3 and 4, and to a lesser extent also the adhesion patches 5, 6 and 7. This result had to be expected due to the position of these adhesions in the part of the cell that is tensed by the needle. On the other hand, Patches 8 and 9 are not or only slightly loaded, presumably because they are located in the part of the cell subjected to compressive forces during needle shearing. The plot shows that loading is not homogeneous and is most likely related to cytoskeletal elements (e.g. between adhesions and nucleus) not visible here. The asymmetric response of different adhesion patches can be explained by the fact that the cytoskeleton is made from semiflexible polymers, which respond differently to pulling and pushing. Pulling reduces entropy and increases stretching as well as bending energies, eventually leading to strain stiffening [189]. Pushing, on the other hand, meets little resistance, because cytoskeletal filaments tend to buckle under force and the cytoplasm can flow away, thus it is difficult to locally build up compression energy like in a solid [190, 191]. It is interesting to note that also in the physiological context, cell mechanics is probed mainly in pulling, not in pushing, e.g. in epithelial monolayers, which are under large prestress [192]. Therefore, pulling is the relevant mode and much more meaningful than pushing. Thus, patches 2 - 7 were loaded presumably because the needle pulling forces were transmitted efficiently to these adhesion patches through the polymers of the cytoskeleton. Correspondingly, patches 8 and 9 were probably not loaded because pushing forces are not transmitted well by cytoskeletal polymers [193]. This is in agreement with earlier studies [12, 176, 177], but our results quantify the traction forces for individual focal adhesion patches under an external mechanical stimulus in an unprecedented way. Our findings also demonstrate the complexity and non-uniform distribution of intracellular force

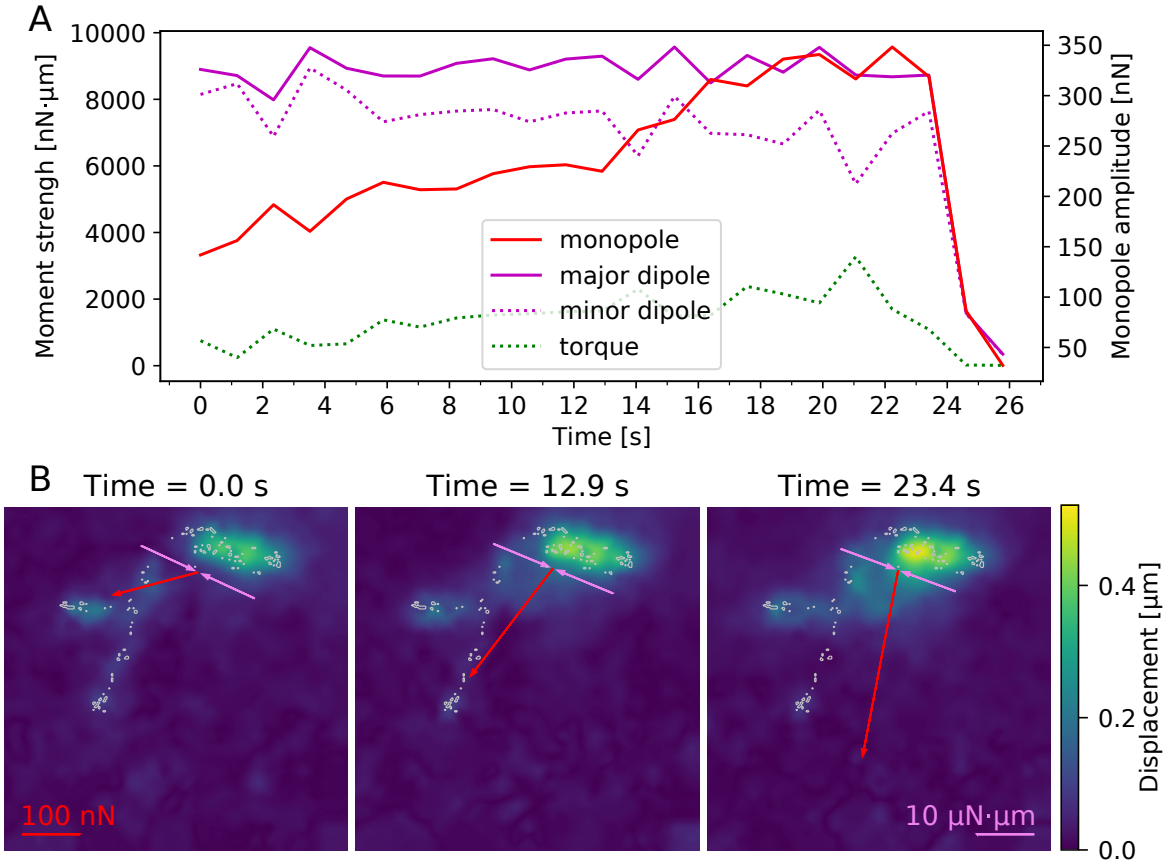

Figure 5.7: Change of force monopole and dipole moments of the cell presented in Fig 5.4 in response to needle shearing. (A) presents the magnitudes of the force monopole, as well as the major and minor dipole moments and the torque as functions of time. Our results show that the contractile forces are initially distributed mostly isotropically around the contractile center. However, the force monopole created by the needle shearing increases over time while the minor dipole, which describes the contractility in the direction of the force, deceases slightly. (B) shows the force monopole and the major dipole moment in exemplary force maps recorded during the shearing experiment. The force monopole is denoted by red arrows while the dipole moment is represented by purple arrows. All arrows follow the indicated color-coded length scale. Areas where adhesions are predicted from the cell's zyxin distribution are marked in gray.

transmission as a function of load and location.

The good agreement between the needle force and the net traction force predicted with AdNFM shown in Fig 5.4 E is a first and successful validation of my approach. To further validate it, I reconstructed forces at $t = 0$ (when there is no force monopole) at single patches with FTTC with 0^{th} order Tikhonov regularization, where the regularization parameter is determined by generalized cross-validation. Adhesion forces were then calculated by integrating the traction stress in each search window, both for the cell analyzed in Fig 5.4 and the cell analyzed in Fig 5.8. As shown in Fig 5.5, the agreement between the two methods is rather good in both cases. I also analyzed whether a better result can be reached by modelling the contacts using a Hertz-like profile. As shown in Fig 5.6, both approaches give a similarly consistent image in this regard. As the constant-force approach gives a slightly better estimate, I chose the constant traction estimate for the experimental analysis.

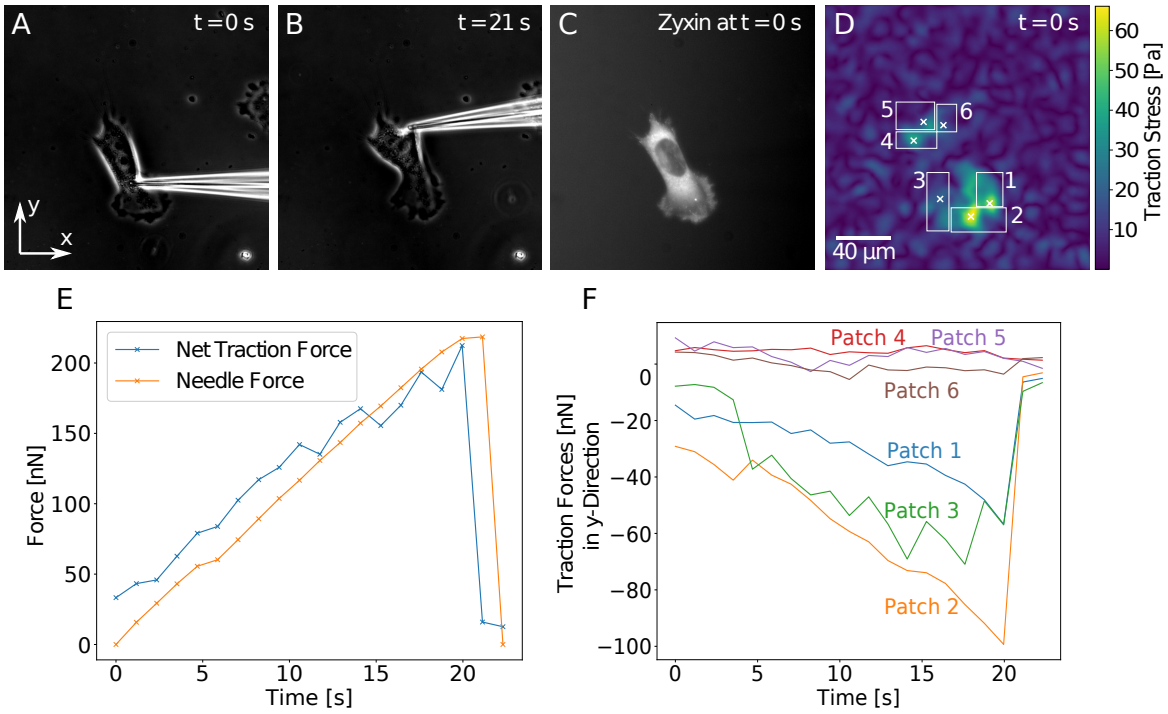

Figure 5.8: The change of traction forces as a response to microneedle shearing. (A) and (B) show phase contrast images of a cell adhering to a PAA substrate and a microneedle exerting shear forces to the cell. The cell's zyxin distribution prior to the shearing process is presented in (C) while (D) pictures a traction force map with cell's adhesion patch positions marked with white crosses and numbers. The force map is calculated using FTTC at t = 0 s. In (E) The shear force exerted by the needle to the cell is compared to the magnitude of the net traction force vector. The y-components of the traction vectors for the adhesion patches are plotted for each moment of the experiment in (F).

Because an unperturbed cell, to lowest order, forms a force dipole, while the needle presents a force monopole, we next calculated the force moments as a function of time using the special precautions mentioned in section 5.2.3. Fig 5.7 A shows, that for the cell displayed in Fig 5.4, the monopole increases with time, but the major dipole does not decrease as expected. The torque remains low but shows a slight upwards slope. The explanation is provided by Fig 5.7 B, which explicitly shows the monopole (in red) and the major dipole (in purple). Because they are oriented perpendicularly to each other, the microneedle pulling does not perturb the cellular dipole for a long time, until complete failure occurs.

We now turn to an example in which monopole and dipole orientations are co-linear. For the cell presented in Fig 5.8, only adhesion patches 1, 2 and 3, which - in contrast to patches 4, 5 and 6 - are loaded in tension, experience an increase in their traction forces. Furthermore, the traction forces exerted through patch 2 change most strongly. This is another indication that force components perpendicular to the shear force vector are not affected by the shearing process as patch 2 lies directly below the site of shear force exertion and thus has much weaker traction forces perpendicular to the shearing direction than patches 1 and 3. Fig 5.8 E shows that the total traction forces exerted through the cell have the same magnitude as the needle shear force, which confirms the validity of our approach. In Fig 5.9 I plot the force monopole as well as the major and minor dipole moments measured during the experiment

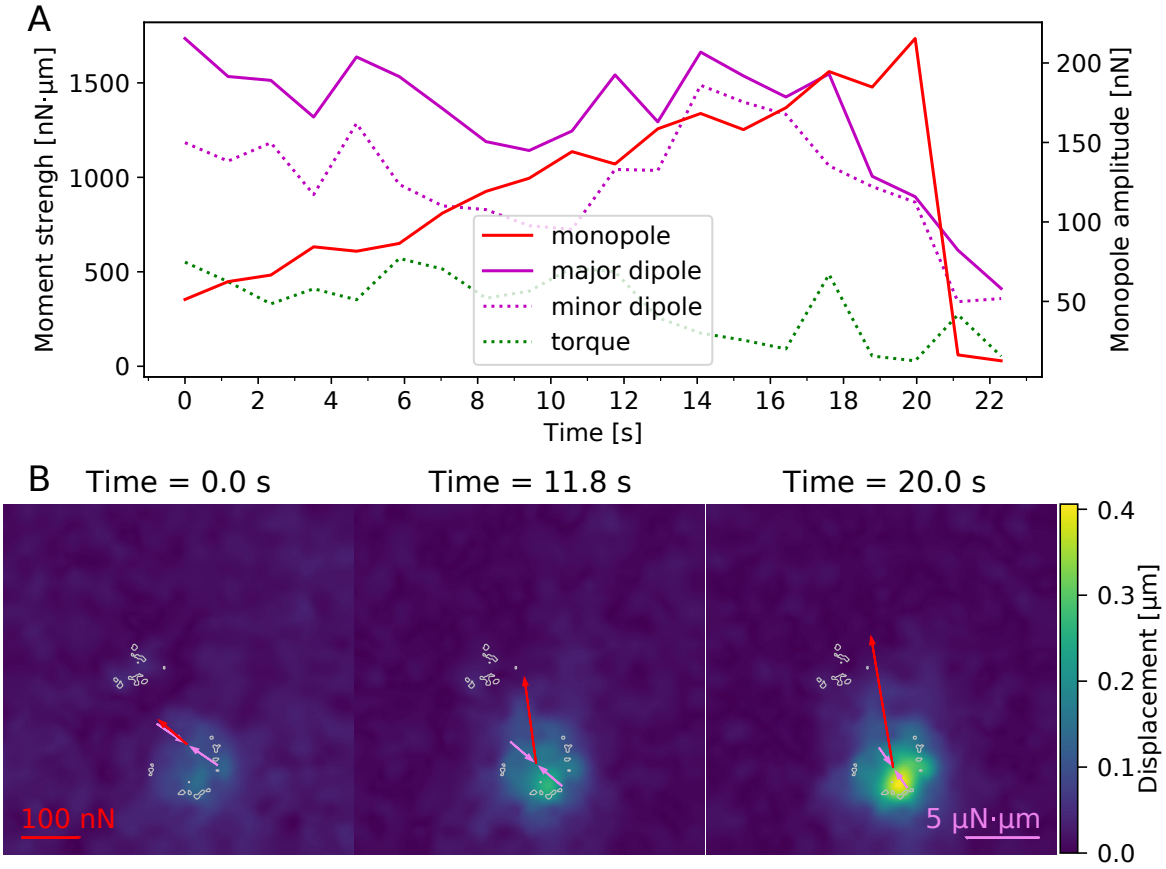

Figure 5.9: Change of force monopole and dipole moments of the cell presented in Fig 5.8 in response to needle shearing. (A) presents the magnitudes of the force monopole, as well as the major and minor dipole moments and the torque as functions of time. The results show that the force balance is initially governed by the major dipole moment. However, the force monopole created by the needle shearing increases over time and governs the force balance at high shearing forces. (B) shows the force monopole and the major dipole moment in exemplary force maps recorded during the shearing experiment. The force monopole is denoted by red arrows while the dipole moment is represented by purple arrows. All arrows follow the indicated color-coded length scale. Areas where adhesions are predicted from the cell's zyxin distribution are marked in gray.

presented in Fig 5.8 as functions of time. These data demonstrate that the force balance changes from a situation that is governed by the major dipole moment to one dominated by the force monopole that is created by the needle shearing. While the adhesions in front of the needle are less exposed to the stress, the ones behind are subjected to large tensile cytoskeletal forces. Interestingly, the cellular dipole becomes more and more localized to the tensed region, indicating a strong reorganization or rearrangement also inside the cell. This is supported by the torque that experiences a downward slope indicating that the adhesive center becomes more aligned with the microneedle.

The results presented in Fig 5.10 show once more that not all adhesion patches are loaded with forces. Patches 1 as well as 4 and 5 were not loaded under an external shear force. Interestingly, not only patches 2 and 3, which were closest to the external force application site were loaded, but also adhesion patches 10 and 11, even though they were further away from the needle than patches 1, 4 and 5. These data suggest

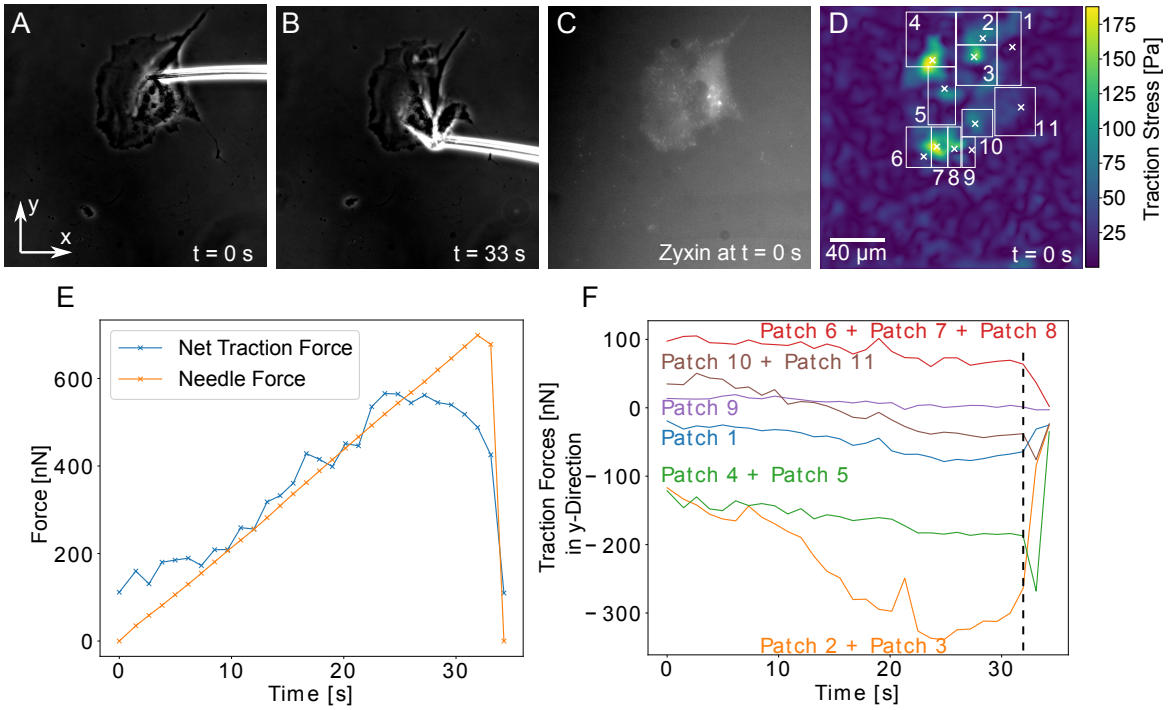

Figure 5.10: Redistribution of adhesion patch loading after a rupture event. (A) and (B) show phase contrast images of a microneedle shearing a fibroblast on a PAA substrate. The cell's zyxin distribution is visualized in (C). A map of the traction forces at t = 0 s exerted at the cell's adhesion patches is presented in (D). The white crosses mark the cell's adhesion sites. The force map is calculated using FTTC at t = 0 s. The sum of traction forces has roughly the same magnitude as the external shear force, as can be seen in (E). The y-components of the traction vectors for the adhesion patches are plotted in F). The dashed line marks the rupture of adhesion patches 1, 2 and 3 at t = 32 s

that internal transmission of tension can be long-ranged, for example through stress fibers, as recently demonstrated by optogenetic control of cell contractility [194]. In order to analyze this important aspect in detail, future work has to simultaneously image also the actin cytoskeleton. However, this is very challenging, as we also have to image the zyxin-marked focal adhesions and the fluorescent marker beads in the elastic substrates.

It is a well-established fact that focal adhesions rupture successively under external forces [165], nonetheless our results presented in Fig 5.10 quantify for the first time the redistribution of traction forces throughout the cell after the rupture of adhesion sites. When adhesion patches 1, 2 and 3 ruptured after 32 s (marked by the dashed line) - even though adhesion patch 1 had barely been loaded with force before that - the traction forces exerted through all other patches except patch 9 increased substantially. Interestingly, patches 10 and 11, which had been the only patches that were loaded strongly prior to the rupture event, were only loaded with a small amount of force upon the rupture event, while patches 4 and 5, which had been only marginally loaded, changed their traction forces much more strongly following the rupture event. In the future, one might use adhesive micropatterns to control the exact location of the adhesion patches and therefore the way individual adhesion sites are loaded by the shearing force.

In Fig 5.11 we present the force monopole as well as the major and minor dipole

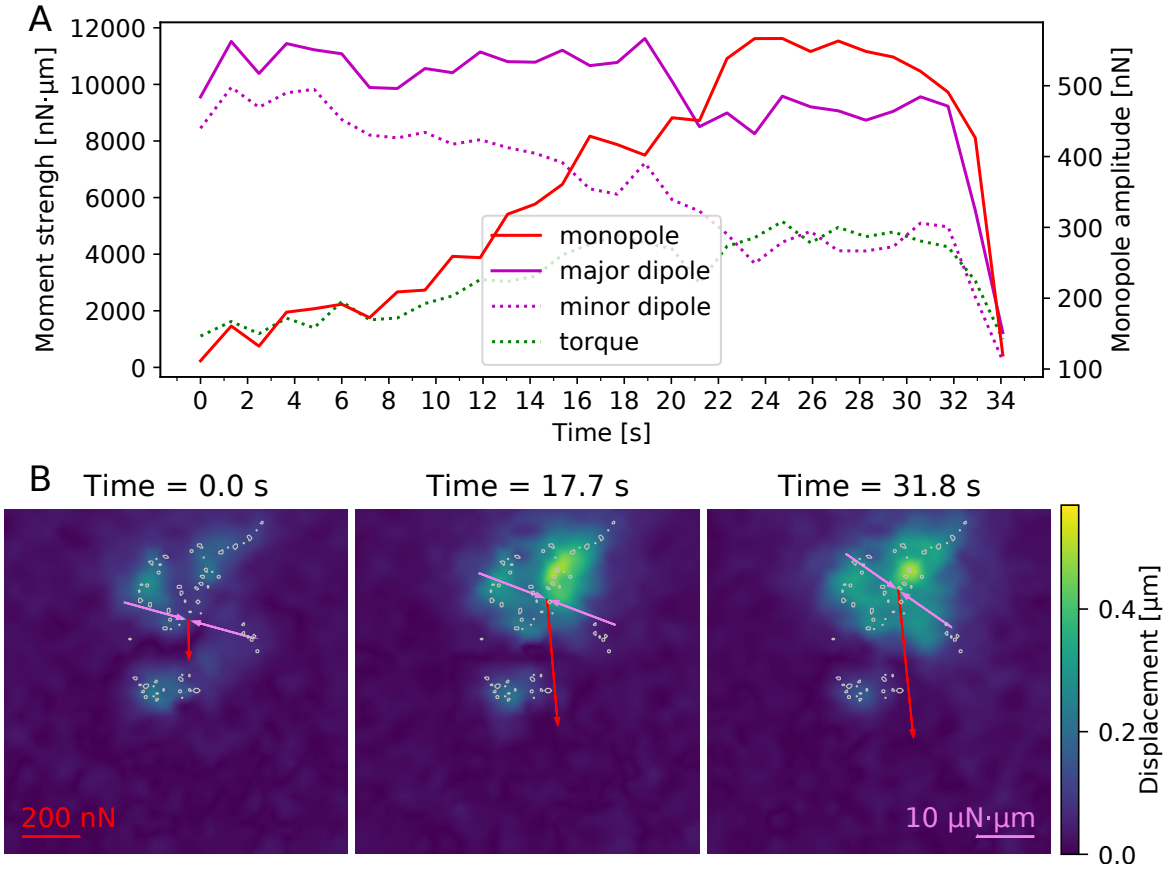

Figure 5.11: Change of force monopole and dipole moments of the cell presented in Fig 5.10 in response to needle shearing. (A) presents the magnitudes of the force monopole, as well as the major and minor dipole moments and the torque as functions of time. The results show that the force balance is initially governed by the major dipole moment. However, the force monopole created by the needle shearing increases over time and governs the force balance at high shearing forces. (B) shows the force monopole and the major dipole moment in exemplary force maps recorded during the shearing experiment. The force monopole is denoted by red arrows while the dipole moment is represented by purple arrows. All arrows follow the indicated color-coded length scale. Areas where adhesions are predicted from the cell's zyxin distribution are marked in gray.

moments measured during the experiment presented in Fig 5.10 as functions of time. The behavior is similar to the one presented in Fig 5.9.

Another striking aspect is the fact that the traction forces exerted through patches 2 and 3 started to slowly decrease several seconds prior to the rupturing event. We observed a similar behavior for adhesion patch 3 of the cell presented in Fig 5.8. This suggests that the rupture of focal adhesions is not necessarily an instantaneous event, but that there exist rupture processes of extended duration, which we recorded using our novel analysis approach. Strikingly, the load on some focal adhesions decreased prior to rupture while in others, the traction forces increased until they ruptured. Similar differences in adhesion site behavior have been described before as slip bonds and catch bonds [195], but in our experimental setting, which analyzes the behavior of intact cells, the mechanical properties of the cell and force transmission through the cytoskeleton likely play an important role, too. My new technique and the experiments of my collaborates hence enable us to reveal possible physical factors that influence

dynamic changes in force loading of adhesion sites.

5.4 Conclusion

Together with my collaborators, I have introduced a novel method for determining traction forces in cells under external shear forces. The applicability of this method has been proven by shearing fibroblasts off their underlying PAA substrates while monitoring the change in cellular traction forces at specific adhesion sites. We have shown that cells on soft substrates distribute an external shear force non-uniformly among their adhesion sites, as a function of location and load (tensile vs. compressive). Notably, we found that force transmission can be long ranged and mainly applies to adhesions that are under tensile load. This result may be due to the polymeric nature of the cytoskeletal network, which is better suited for the transmission of tensile forces. As our technique monitors the change in traction forces simultaneously to the shearing stimulation, it introduces a new quality to the recordings of rupture events to complement conventional techniques such as the single-cell force spectroscopy. Indeed, our method can be easily adapted to other force exertion methods and hence is very versatile and complementary to existing procedures. In the future, it could be combined with imaging of the cytoskeleton to achieve a more complete understanding of how force is transmitted through the cell. Moreover, adhesive micropatterns might be used to better control the positioning of the adhesion patches; with these two elements in place, we expect that our method can be used to achieve a comprehensive understanding of how force is transmitted through adherent cells.

Chapter 6

Using a conditional invertible neural network to extract traction forces

In this chapter, I describe a technique that not only predicts forces without the limitations previously presented, but in addition not just gives one dominant solution but also suggests alternatives by means of conditional invertible neural networks (cINNs). The design of the neural network and its training strategy has been developed in close collaboration with Felix Draxler and Ullrich Koethe from the "Computer vision and learning lab" at Heidelberg University (manuscript 6).

6.1 Motivation

As we have seen in the previous sections, each of the various variants of traction force inference methods displays certain limitations. While FTTC is sufficient to reconstruct forces in the majority of cases, we have seen that cases exist, that this approach is unable to handle due to internal limitations. Another fundamental issue is the regularization: It has been shown that regularization is essential to avoid incorrect reconstruction of traction profiles [14], but on the other hand, if a too large regularization is employed, the details of the reconstructed traction field are smoothed out and the overall force magnitude is then too small [13]. As such, a properly regularized reconstruction is only the best compromise between two undesired factors. Moreover, the noise conditions, and thereby the optimal parameter values, may also vary within a set of experiments, which may affect the comparability of different experiments.

In a more structural sense, TFM is a classical inverse problem [196] and neural networks (NNs) have proven to be an elegant alternative to numerical schemes for solving inverse problems in the context of elasticity. Exemplary applications can be found in the context of wrinkling force microscopy [197] and pendant drop tensiometry [24].

A non-linear reconstruction using deep learning can in principle improve the reconstruction of traction forces, as it can aim to distinguish noise from signal, but might face issues with generalization [196].

Deep NNs were first employed to implement TFM by Wang and Lin [23]. They introduced a framework labeled "deep learning for TFM" (DL-TFM), which utilized a convolutional neural network in a U-Net architecture to estimate the traction forces exerted by cells from a displacement map. The general ideas of a U-Net architecture will be described later in this chapter.

In order to train their model, Wang and Lin [23] created a synthetic dataset of

simulated TFM patterns, where both the deformation and the traction were known. For this, they used a model for cell migration and generated images that mimic the situation in amoeboid and mesenchymal cells and also contains artificial radial contractile circular patterns in order to improve the isotropy of cells. By doing so, they obtained a network optimized for circular contractile cells.

Wang and Lin then compared their networks performance to a FTTC reconstruction and showed that their NN method is able to perform with similar efficiency to FTTC. In addition, they also tested the model's robustness against variations in the input parameters by rescaling the input deformation fields to account for different deformation stiffness and force magnitudes and found a good generalization. Finally, they also compared DL-TFM and FTTC on experimental datasets obtained from NIH 3T3 cells on PAA substrates, where they reaffirmed their results.

An alternative approach was made by Kratz *et al.* [107]. This approach also features a U-Net architecture. In their study, they used a much simpler approach to generate training data. They also motivated their design by claiming that the innermost layers effectively take a similar role to the application of the Green's kernel in FTTC. Rather than doing an elaborate simulation of cell dynamics, they merely generated an image of randomly distributed traction spots of different sizes, traction magnitude and orientation. Despite this approach of sampling data generation being seemingly much less compatible with experimentally observed reconstructions, applied on experimental data, their results lead to a relatively comparable reconstruction.

Force reconstruction using deep-learning has also been implemented for 3D TFM by Duan *et al.* [26]. Training data were generated by subdividing an experimental observation into a range of sub-images each encompassing a piece of the cell-matrix-interface. Training the network on confocal microscopy images directly, they focused on reconstruction of the displacement and used a subsequent analytical layer to obtain the forces from the displacements. Doing so they were able to reconstruct cell forces on both numerically generated and experimentally obtained datasets with a similar accuracy to FEM-based inverse method, but computationally faster.

Neural networks can not only be used to study TFM but also to study cellular force generation itself, as shown by Schmitt *et al.* [25]. In their study, they first tried to predict observable cellular forces from the distribution of labeled proteins within the cells that are expected to show correlation with cellular force generation. By training a U-Net that tries to predict the traction forces based on each labeling factor, they then showed, that tractions could be predicted best from zyxin distribution, a protein found in the focal adhesions of cells. They then moved on to study the exact nature of the correlation by also building a network to predict the active stresses and adhesion points needed to describe the cell as a two-dimensional elastic medium. Despite not using the force distribution during training at all, they could again obtain traction forces that show close similarity to those obtained via traction force estimates. Finally, they also studied a setup, in which the neural network is extended by two analytical layers: First a long-range Green's function is applied to obtain a potential field χ and a weight field ξ, where the traction field itself is calculated from a weighted potential approach $\boldsymbol{\tau} = \xi(\boldsymbol{x})\nabla\chi(\boldsymbol{x})$. With this they show that force generation can be separated into a short-range contribution described by the weight field and a long-range adhesion correlation described by the potential field χ.

Another very recent approach in a similar direction focused on how forces can be predicted from the contour profile of cells. By training a generative adversarial

network, based on experimental datasets containing the cells profile as well as their traction forces, but also simulated ones obtained from a cell monolayer simulation, Li *et al.* [109] were able to mimic the distribution of forces.

While NNs have shown great potential in improving traction force reconstruction, by using any of the above-mentioned approaches, we do learn little on how this is achieved and how reliable and unique these reconstructions are. We have seen in chapter 2, that the inverse problem is possibly degenerate, which prompted us to include a regularization. However, regularization does not show how this degeneracy manifests: Both conventional methods without regularization and the neural network approaches mentioned do only yield one single solution for the traction forces. Regularized traction force microscopy offers some limited sampling options based on the choice of the regularization parameter. While some more advanced methods like Bayesian FTTC [102] use Bayesian-reasoning, they still arrive at a single unique solution $\boldsymbol{\tau}(\boldsymbol{u})$ and do not explore the full probability space $p(\boldsymbol{\tau}|\boldsymbol{u})$.

In recent years, significant research into generative networks has been conducted. Generative approaches, like generative adversarial networks [198, 199], variational autoencoders [200, 201] and diffusion-based models [202] have proven highly efficient in returning high likelihood samples from a certain high-dimensional probability space of reasonable solutions, for example the probability space of facial images.

A third method, invertible NNs [203], has proven to be particular useful in the case where not an unbounded probability distribution $p(\boldsymbol{\tau})$ is of interest, but one where we wish to explore the distribution of possible responses relative to an observable $p(\boldsymbol{\tau}|\boldsymbol{u})$. This approach, referred to as invertible neural networks (conditional invertible neural networks (cINNs)) [204], has been successfully used to study conditional probabilities, that arose when trying to solve inverse problems [205, 206].

In this chapter, we therefore study, how cINNs may be employed to enhance TFM in order to improve image not only increase the accuracy force reconstruction, but also to study the invertibility of the forward problem, point out any potential degeneracies due to noise and quantify the reliability of reconstruction by exploring the conditional probability $p(\boldsymbol{\tau}|\boldsymbol{u})$.

6.2 Theoretical background

6.2.1 Basic principles of machine learning and neural networks

Machine learning (ML) encompasses data-driven methods that aim to solve an information processing tasks in a manner similar to how they would be solved by human or biological agents [207]. The success of machine learning methods is based on growth of computation power and the advent of data availability as well as the desire to move beyond tasks that can be solved using a heuristic strategy [208].

ML problems can be predominantly classified into unsupervised and supervised learning problems [208]:

The first case, unsupervised learning consists of problems, where a set of data records is given and the task is to discover somehow relevant information therein. It consists of clustering and dimensionality reduction. The aim of clustering is to establish a partition of the data set into groups that categorize the input data based on common traits. Dimensionality reduction on the other hand aims to filter out the relevant features that set the different data records apart and as such condenses each record's information into a low set of parameters. Such techniques can be used to

identify quantities that can often be related to the cause of some observed phenomena.

In the latter case, supervised learning, a set of input-output pairs is given and the task is to devise a transformation function that can be used to extrapolate the input output mapping to other input data points where the corresponding output data point is unknown.

Supervised learning models distinguish between classification and regression problems. In a classification problem, the output space consists of a set of discrete labels. In contrast, in a regression problem the output is a continuous value or a set of such values [207].

The following description of supervised learning problems and loss functions can be found in text books, e.g. [207, 208]:

In a mathematical sense, a supervised problem is one where we have a quantity $\boldsymbol{Y}$ which we are interested in, but in general cannot observe directly. We do, however, know that there is another quantity $\boldsymbol{X}$ which we can observe directly and which we assume to have a strong correlation to our desired quantity $\boldsymbol{Y}$. In a regression problem, we can describe both quantities by potentially huge vectors of real numbers ($\boldsymbol{X}, \boldsymbol{Y} \in \mathbb{R}^N$). The $\boldsymbol{X}$ is known as the *features* while $\boldsymbol{Y}$ is known as the *response*. In the case of TFM, $\boldsymbol{X} = \mathbf{u}$ corresponds to the surface deformation, which can be directly observed, while $\boldsymbol{Y} = \boldsymbol{\tau}$ corresponds to the surface traction. Unfortunately we do not know the exact relationship between $\boldsymbol{X}$ and $\boldsymbol{Y}$. We only have a set of data pairs $[(\boldsymbol{X}_i, \boldsymbol{Y}_i)_{i=1,\ldots,N}]$, where we observed both the features and their responses, that can be used to make estimates about the general relationship between $\boldsymbol{X}$ and $\boldsymbol{Y}$. This set is known as the set of *training data*. The task is now to use this sample data to explore the relationship between $\boldsymbol{X}$ and $\boldsymbol{Y}$ in order to obtain information about the response for a particular observation of the features.

The most simplistic description is to assume that our sample data arose from a statistical model with a deterministic relationship, e.g. $\boldsymbol{Y} = f(\boldsymbol{X}) + \boldsymbol{\varepsilon}$ where $\boldsymbol{\varepsilon}$ is a random error with a vanishing expectation value ($\mathbb{E}(\boldsymbol{\varepsilon}) = 0$). Unfortunately, the exact nature of the mapping function $f(\cdot)$ is unknown. We therefore postulate a generic model $f(\cdot, \theta)$ that, for the right choice of the configuration parameter $\hat{\theta}$, should mimic $f(\cdot)$ closely. We can then for every set of features $\boldsymbol{X}$ find a prediction $\hat{\boldsymbol{Y}} = f(\boldsymbol{X}, \hat{\theta})$ of our responses $\boldsymbol{Y}$. In order to select $\hat{\theta}$ we apply our model to our sample data to obtain $\hat{\boldsymbol{Y}}_i = f(\boldsymbol{X}_i, \hat{\theta})$ and estimate the quality of our reconstruction using a so-called *loss function* $L(\boldsymbol{Y}_i, \hat{\boldsymbol{Y}}_i)$. We can then find a preferred reconstruction by finding $\hat{\theta}$ such that it minimizes the loss function averaged over all training samples:

$$\hat{\theta} = \arg\min_{\theta} \mathcal{L}(\theta) \tag{6.1}$$

where

$$\mathcal{L} = \mathbb{E}[L] = \frac{1}{N} \sum_{i=1}^{N} L(\boldsymbol{Y}_i, \hat{\boldsymbol{Y}}_i = f(\boldsymbol{X}_i, \theta)) \tag{6.2}$$

This optimization process is known as *training*.

The selection of the generic model $f(\cdot, \theta)$ is a particular challenging task. If the model is too restrictive, there is a real risk that even the best choice of $\hat{\theta}$ does not result in a function that mimics the true function closely. In contrast, if the model contains too many parameters this may result in over-fitting. An additional challenge lies in the fact that the model must be supplemented by a training procedure, an algorithm to solve Eq 6.1 at least approximately.

Loss function and model evaluation

Finding a suitable loss function can be motivated in different manners, in the following I will sketch out the motivation based on probabilistic reasoning, a summary of which can be found in the book of Barber *et al.* [207]. The simplest choice of the loss function is the square distance:

$$L(\boldsymbol{Y}_i, f(\boldsymbol{X}_i, \theta)) = ||\boldsymbol{Y}_i - f(\boldsymbol{X}_i, \theta)||_2^2. \tag{6.3}$$

This choice corresponds to the assumption that $\boldsymbol{\varepsilon}$ is uniformly Gaussian distributed meaning that the likelihood for our solution is given by:

$$p(\boldsymbol{Y}_i|\boldsymbol{X}_i, \theta) = \exp\left(-\frac{1}{2\sigma^2}||\boldsymbol{Y}_i - f(\boldsymbol{X}_i, \theta)||_2^2\right) \tag{6.4}$$

The most probable choice of parameters $\hat{\theta}$ is then found by maximizing the posterior probability $p(\theta|(\boldsymbol{Y}_i)_{i=1,\dots,N}, (\boldsymbol{X}_i)_{i=1,\dots,N})$ with respect to the parameters

$$\begin{aligned}
\hat{\theta} &= \arg\max_{\theta} p(\theta|(\boldsymbol{Y}_i)_{i=1,\dots,N}, (\boldsymbol{X}_i)_{i=1,\dots,N}) \\
&= \arg\min_{\theta}(-\log p(\theta|(\boldsymbol{Y}_i)_{i=1,\dots,N}, (\boldsymbol{X}_i)_{i=1,\dots,N}) \\
&= \arg\min_{\theta}\left(-\log\left(\prod_{i=1}^{N} p(\boldsymbol{Y}_i|\boldsymbol{X}_i, \theta)\right) - \sigma^2 \log p(\theta)\right) \\
&= \arg\min_{\theta}\left(\sum_{i=1}^{N} ||\boldsymbol{Y}_i - f(\boldsymbol{X}_i, \theta)||_2^2 - 2\sigma^2 \log p(\theta)\right),
\end{aligned} \tag{6.5}$$

where we have used Bayes' law in the third row to replace the posterior distribution by the likelihood and the prior. If we assume all configurations to be equally likely, $p(\theta)$ turns into a constant, the last term drops out and we obtain a least-square criterion.

Similar to the regularization in FTTC, we may also impose a non-constant prior distribution and assume that high model parameters will be unlikely,

$$p(\theta) = \exp\left(-\frac{1}{2N\sigma_\theta^2}||\theta||_2^2\right). \tag{6.6}$$

And again following the reasoning laid out while we regularized our inverse problem for force reconstruction, this results in an additional term in the loss function,

$$\mathcal{L} = \mathbf{E}_i\left(||\boldsymbol{Y}_i - f(\boldsymbol{X}_i, \theta)||_2^2\right) + \lambda^2||\theta||_2^2, \tag{6.7}$$

where we have collected the two variances into a regularization factor $\lambda = \sigma/\sigma_\theta$.

In order to ensure the reliability and effectiveness of our machine learning model, the introduction of *test data* becomes crucial. Test data are a second set of data tuples $[(\boldsymbol{X}_i, \boldsymbol{Y}_i)_{i=1,\dots,N_{\text{test}}}]$, similar to the set of training data, but must be clearly distinct. A common way to achieve this, is by randomly splitting a larger dataset into two subsets with one serving as training and one as test data. In particular, test data should not affect the training procedure in any way, to ensure unbiased evaluation and realistic expectation when encountering unseen data. Test data should also represent real-world scenarios the model will later encounter after training.

Test data allow us to assess the model's generalization and predictive accuracy on unseen examples. By evaluating the model's performance on test data, we can determine its effectiveness, identify overfitting or underfitting issues, compare different models or hyperparameters (model configuration parameters not optimized during training) and evaluate its readiness for deployment.

Calculating the loss function of the test data is the most straightforward way of comparing generalizability of the model. A large discrepancy in the numerical value of the loss function calculated from training and the one calculated from test data indicates overfitting and in this case the model or its hyperparameters need to be adjusted.

Neural networks

A very successful approach for selecting a model function has been inspired by the way information is processed in biological neuron cells and is known as neural networks (NNs), [209, 210].

The core structure of a (feed-forward) neural network is the so-called *neuron*, a combination of an affine mapping of the input vector x onto the real numbers, described by a weight vector $\mathbf{w}$, an offset b and a non-linear activation function ϕ

$$y = \phi(z) = \phi(\boldsymbol{w}^T \boldsymbol{x} + b) \tag{6.8}$$

The output y is commonly referred to as the *activation*, while z is often called the *pre-activation*.

Multiple neurons are joined in parallel to form a full network layer:

$$\begin{aligned} \boldsymbol{y} &= l(\boldsymbol{x}|\mathbf{W}, \phi) \\ &= \left[\phi\left(\mathbf{W}_0 \cdot \boldsymbol{x} + b_0\right), \phi\left(\mathbf{W}_1 \cdot \boldsymbol{x} + b_1\right), \ldots, \phi\left(\mathbf{W}_{L-1} \cdot \boldsymbol{x} + b_{L-1}\right)\right]^T \\ &= \phi\left(\mathbf{W} \cdot \boldsymbol{x} + \boldsymbol{b}\right) = \phi(\boldsymbol{z}). \end{aligned} \tag{6.9}$$

Here L now describes the number of outputs in this layer and the weights have been collected into a weight matrix $\mathbf{W}$, consisting of row vectors $\mathbf{W}_i$. Similarly, the offsets have been collected into an offset vector b. In the last row, we used the convention that applying ϕ onto a vector is understood to mean element-wise application over the elements of the pre-activation $\boldsymbol{z} = \mathbf{W} \cdot \boldsymbol{x} + \boldsymbol{b}$. As common in programming we employ a convention of starting array indices at 0 rather than one, hence $\boldsymbol{b} = (b_0, b_1, \ldots, b_{L-1})^T$.

A (deep) neural network is now created by taking a sequence of layers

$$f(\cdot, \theta) = l_N \circ \ldots l_2 \circ l_1 \tag{6.10}$$

$$\boldsymbol{y}^{(j)} = l_i(\boldsymbol{y}^{(j-1)}) = l(\boldsymbol{y}^{(i-1)}|\mathbf{W}^{(j)}, \boldsymbol{b}^{(j)}, \phi^{(j)}). \tag{6.11}$$

Each layer has its own set of weights. Combined, they form the parameter space $\theta = (\mathbf{W}^{(1)}, \boldsymbol{b}^{(1)}, \mathbf{W}^{(2)}, \boldsymbol{b}^{(2)}, \ldots, \mathbf{W}^{(N)}, \boldsymbol{b}^{(N)})$.

The first layer $\boldsymbol{y}^{(0)} = \boldsymbol{X}$ is known as the *input layer*, it is followed by a series of so-called *hidden layers* and finally the *output layer* $\boldsymbol{y}^{(N)} = \boldsymbol{Y}$. Notice that each layer may have a different size. It is quite common for hidden layers to have more nodes than both the input and output layer.

Training of NNs

Training a NN can be done using gradient descent methods. The simplest approach is stochastic gradient descent (SGD) [211, 212]. Here we first initialize the weights θ

randomly and then update them using the following procedure:

$$\theta_{k+1} = \theta_k - \eta \nabla_\theta \mathbb{E}[L]|_{\theta=\theta_k} \tag{6.12}$$

Due to the high number of parameters, in order to train a neural network, the training data set is fairly large, so using the loss averaged over all training data ($\mathbb{E}[L] = \frac{1}{N}\sum_{i=1}^{N} L(\boldsymbol{Y}_i, \hat{\boldsymbol{Y}}_i)$) at each step would be unfeasible. Therefore, we reorder the samples and only use a relatively small randomly selected subset I of a fixed size n (known as batch size) of all training data to average over ($\mathbb{E}[L] = \frac{1}{n}\sum_{i\in I} L(\boldsymbol{Y}_i, \hat{\boldsymbol{Y}}_i)$). This technique is therefore known as stochastic gradient descent. An *epoch* is defined as a sequence of steps, after which all training datasets have been used once. The convergence of this algorithm has been discussed in literature [213].

While SGD has proven to be relatively robust, it may suffer from a number of shortcomings. If the learning rate is set too high, SGD may reach an oscillatory state due to overshooting of the optimal parameters. In contrast, if the learning rate is set too low, this may result in slow or even non-existing convergence. In addition, a very anisotropic behavior of the loss function surrounding the global optimum may result in a slow oscillatory descent.

A wide range of different strategies, many of which have been empirically justified, have been developed [214]: Overshooting can be limited by decreasing the learning rate during training, however, this has to be done manually on a case-by-case bias, while other oscillatory behavior can be suppressed by introducing a form of momentum, where the gradient is first averaged with the gradient values of previous iteration steps before being used to adjust the model parameters.

A particularly widely used training strategy, that has proven to show a more rapid convergence in empirical use, is to introduce both momentum and a form of automatic learning rate adaptation. This strategy is known as ADAM [197, 215]. ADAM uses four meta-parameters each given a suggested value by Kingma and Ba [215]:

- β_1: First momentum decay rate (suggested value: 0.9).
- β_2: Second momentum decay rate (suggested value: 0.999).
- η: Learning rate (suggested value: 0.001).
- ϵ: Small constant for numerical stability (suggested value: 10^{-8}).

The ADAM optimization scheme can then be summarized by the following steps:

1. Initialize parameters: $k = 0$, $m_0 = 0$, $v_0 = 0$.
2. Repeat the following steps until a convergence criterion is reached:
   (a) Increment k.
   (b) Compute gradient:
   $g_k = \nabla_\theta \mathcal{L}|_{\theta=\theta_{k-1}}$.
   (c) Find updated biased first moment estimate:
   $m_k = \beta_1 \cdot m_{k-1} + (1-\beta_1)\cdot g_k$.
   (d) Find updated biased second moment estimate:
   $v_k = \beta_2 \cdot v_{k-1} + (1-\beta_2)\cdot (g_k)^2$.

(e) Correct bias in moment estimates:
$\hat{m}_k = \frac{m_k}{1-\beta_1^k}$, $\hat{v}_k = \frac{v_k}{1-\beta_2^k}$.

(f) Update parameters:
$\theta_k = \theta_{k-1} - \frac{1}{\sqrt{\hat{v}_k}+\epsilon}\eta\hat{m}_k$.

Non-linear function and representation theorem

One important choice is the selection of the nonlinear activation functions $\phi^{(i)}$ in the network. It is critical in order to make the network able to approximate the ideal solution f using training 6.1. The universal approximation theorem in its original form [216] states that at least one $\phi^{(i)}$ cannot be polynomial in order to achieve this, but that any function f can in principle be approximated by a single layer network provided that a sufficient non-polynomial function $\phi^{(1)}$ is chosen.

Early neural networks would frequently employ sigmoid functions like the hyperbolic tangent $\phi(z) = \tanh(z) = (\exp(z) - \exp(-z))/(\exp(z) + \exp(-z))$ or the logistic function $\phi(z) = 1/(1 + \exp(-z))$ [209]. However, in recent years the rectified linear unit (ReLU) $\phi(z) = max(0, z)$ has been most commonly used [210]. This function is not only more simple to implement computationally but also has a couple of practical benefits: First, ReLU avoids the problem of vanishing gradients by having a simple derivative that does not converge to zero for large pre-activation values. Second, this also avoids saturation allowing for faster convergence and better gradient flow during training. Finally, ReLU also promotes a sparse activation in the network, that may be used to reduce computational complexity and memory requirements [214].

A second form of the universal representation theorem states that if ReLU is chosen as the activation function for all interior layers, a sufficiently deep neural network is able to approximate any integrable function f [217].

Backward propagation

All iterative optimization schemes rely on the ability to compute the gradient of the loss function with respect to the weights ($\nabla_\theta [L(\boldsymbol{Y}, f(\boldsymbol{X}, \theta))]$). This can be achieved using a technique known as backward propagation or back-propagation, that makes use of backward automatic differentiation. For simplicity, we will omit the ground truth parameter $\boldsymbol{Y}$ in the following. Backward propagation was first popularized for NNs by Rumelhart *et al.* [218]. A more modern introduction into backward propagation can be found e.g. in [214].

The primary idea of backward automatic differentiation is the observation that just like we calculated the value of $f(\boldsymbol{X}, \theta)$ using an iterative scheme starting with $\boldsymbol{y}^{(0)} = \boldsymbol{X}$ and then applying Eq 6.11 recursively to transverse the network in a forward manner in order to finally arrive at $\boldsymbol{y}^{(N)} = \boldsymbol{Y}$ and then use this result to evaluate the loss function (forward propagation), we can use the chain rule to find a similar recursive condition for calculating the gradient of the loss function with respect to different quantities starting with the last layer and then move backward through the network (backward propagation).

The gradient of the loss function with respect to the pre-activation within the different layers is given by:

$$\overline{\boldsymbol{z}}^{(j)} = \nabla_{\boldsymbol{z}} L \circ l_N \circ \ldots \circ l_{j+1} \circ \phi|_{\boldsymbol{z}=\boldsymbol{z}^{(j)}}. \tag{6.13}$$

For the output layer, we can apply the chain rule to relate $\overline{\boldsymbol{z}}^{(j)}$ to the partial

derivatives of the loss function, which have to be analytically known.

$$\overline{\boldsymbol{z}}^{(N)} = \frac{\partial}{\partial y_k} L \bigg|_{\boldsymbol{y}=\boldsymbol{Y}} \odot \phi'^{(N)}(\mathbf{z}^{(N)})$$

Here, $\odot$ denotes the element-wise multiplication and we use $\phi'^{(j)}(\mathbf{z}^{(j)})$ to represent the derivative of the activation function in the jth layer with respect to its input evaluated at its corresponding pre-activation $\mathbf{z}^{(j)}$.

The other gradients can now be calculated using the chain rule, in order to yield a recursive relationship [219]:

$$\begin{aligned}
\overline{z}_k^{(j)} &= \frac{\partial}{\partial y_k} L \circ l_N \circ \ldots \circ l_{j+1} \bigg|_{\boldsymbol{y}=\phi(\boldsymbol{z}^{(j)})} \phi'\left(z_k^{(j)}\right) \\
&= \left(\nabla_{\boldsymbol{z}} L \ldots l_{j+2} \circ \phi|_{\boldsymbol{z}=\boldsymbol{z}^{(j+1)}} \cdot \frac{\partial \mathbf{W}^{(j+1)} \cdot \boldsymbol{y} + \boldsymbol{b}^{(j+1)}}{\partial y_k} \bigg|_{\boldsymbol{y}=\phi(\boldsymbol{z}^{(j)})} \right) \phi'\left(z_k^{(j)}\right) \\
&= \left(\overline{\boldsymbol{z}}^{(j+1)} \cdot \mathbf{W}^{(j+1)} \cdot \boldsymbol{e}_k\right) \phi'\left(z_k^{(j)}\right) \\
\overline{\boldsymbol{z}}^{(j)} &= \left((\mathbf{W}^{(j+1)})^T \cdot \overline{\boldsymbol{z}}^{(i+1)}\right) \odot \phi'^{(j)}(\mathbf{z}^{(j)})
\end{aligned} \tag{6.14}$$

Again, by applying the chain rule, one can now find the gradient contribution of the current sample with respect to the weights and offsets in each layer [219]:

$$\begin{aligned}
\overline{\mathrm{W}}_{kl}^{(j)} &= \frac{\partial L \circ f}{\partial \mathrm{W}_{kl}^{(j)}} \\
&= \nabla_{\boldsymbol{z}} L \circ l_N \circ \ldots \circ l_{j+1} \circ \phi|_{\boldsymbol{z}=\boldsymbol{z}^{(j)}} \cdot \frac{\partial}{\partial \mathrm{W}_{kl}^{(j)}} \left(\mathbf{W}^{(j)} \cdot \boldsymbol{y} + \boldsymbol{b}^{(j)}\right) \\
&= \overline{z}_k^{(j)} y_l^{(j)}
\end{aligned} \tag{6.15}$$

$$\begin{aligned}
\overline{b}_k^{(j)} &= \frac{\partial L \circ f}{\partial b_k^{(j)}} \\
&= \nabla_{\boldsymbol{z}} L \circ l_N \circ \ldots \circ l_{j+1} \circ \phi|_{\boldsymbol{z}=\boldsymbol{z}^{(j)}} \cdot \frac{\partial}{\partial b_k^{(j)}} \left(\mathbf{W}^{(j)} \cdot \boldsymbol{y} + \boldsymbol{b}^{(j)}\right) \\
&= \overline{z}_k^{(j)}
\end{aligned} \tag{6.16}$$

Modern machine learning frameworks like *pyTorch* [220] can typically perform back-propagation without the back-propagation steps being written explicitly in the program code. To achieve this, when the program code is evaluated in training mode, each field variable is extended by a gradient field, that is first initialized to zero. During the forward operation, the program will not only compute the results of each atomic operation but also build a computation graph culminating in the computation of the loss function value $L = \mathbb{E}[L]$. Then starting with $\overline{L} = \frac{\partial L}{\partial L} = 1$, the computation graph is evaluated and for each input, weight or intermediate result x the value $\overline{x} = \frac{\partial L}{\partial x}$ is found by making use of the fact, that for all intermediates y_i that directly depend on x via a relation $y_i = f_i(\ldots, x, \ldots)$ we can find a recursive relationship.

$$\overline{x} = \frac{\partial L}{\partial x} = \sum_i \frac{\partial L}{\partial y_i} \frac{\partial f_i}{\partial x} = \sum_i \overline{y_i} \frac{\partial f_i}{\partial x}. \tag{6.17}$$

This strategy allows for a more flexible network structure. For example, certain information can be passed alongside individual layers to be merged in again at a later point or normalization layers may be introduced in which the activations are divided by their average. Libraries such as *pyTorch* [220] contain an assortment of such structures.

Convolutional Neural networks

A slight variation of the standard neural network layer is often used when dealing with grid-structured data such as images and is also used in all machine learning methods for TFM: These data often have a huge number of input and output nodes and also generally show some kind of translational invariance, meaning that if we find a correspondence between an input field $X(x)$ and an output field $Y(x)$, we predict, that a translated input $X(x+a)$ should correspond to a translated output $Y(x=a)$. Linear operations that maintain this kind of relationship can be expressed as convolution of the input, meaning:

$$Y(x) = \int K(x-x')X(x')\,\mathrm{d}x \tag{6.18}$$

One idea is therefore to replace the general fully connected formula for calculating the pre-activation $\boldsymbol{z} = \mathbf{W}\cdot\boldsymbol{x}+\boldsymbol{b}$ by a convolution-based expression. For image-like data, the inputs are usually described by a field of grid-sampled data. However, the sampling is usually not over a grid of values, but instead each grid point is attributed a vector-valued observation. For an image, the different values may describe the different chromatic contributions, while for medical data, the different fluorescent channels may be used. In traction force microscopy these different channels hold the x and y component of the deformation, respectively. Consequently, in general the input field $\boldsymbol{X}$ contains elements $X_{i,j,k}$, where the first index i goes over the number of channels, while the other indices j and k would iterate over the width and height of the input data. Similar to the nodes in the hidden layers, the output layer may also have a different number of channels.

A convolutional layer may now be described by [214, 221]:

$$z_{i,j,k} = c(\boldsymbol{X}|\mathbf{K},s,\boldsymbol{b}) = b_i + \sum_{l=0}^{C_\mathrm{in}}\sum_{m=0}^{N-1}\sum_{n=0}^{N-1}\mathrm{K}_{i,l,m,n}X_{l,j\cdot s+m,k\cdot s+n}. \tag{6.19}$$

Here $\boldsymbol{b}$ now gives a bias for each layer, while the four-dimensional tensor $\mathbf{K}$ has the dimension $C_\mathrm{out}\times C_\mathrm{in}\times N\times N$. The parameters C_in and C_out describe the number of channels in the input and output of each layer. Each element $\mathrm{K}_{i,l,m,n}$ describes the m,n component of the connection kernel matrix connecting input channel l to the output channel i. The parameter N describes the size of the kernel support and thus the maximum distance in which input nodes affect the pre-activation at a given sampling point. s describes the so-called stride, the number of pixels the kernel moves forward to calculate the next datapoint in the pre-activation. A stride larger than 1 will result in a downsampling of the image.

Notice that the width and the height of the output is smaller than the input image. To avoid this, the input is often augmented before each convolution by inserting a specific number P of additional input nodes at the boundaries of the grid, which will increase the size of the input by $2P$ in each direction. The additional nodes are either filled with zero, or are found by imposing some kind of symmetry condition on the

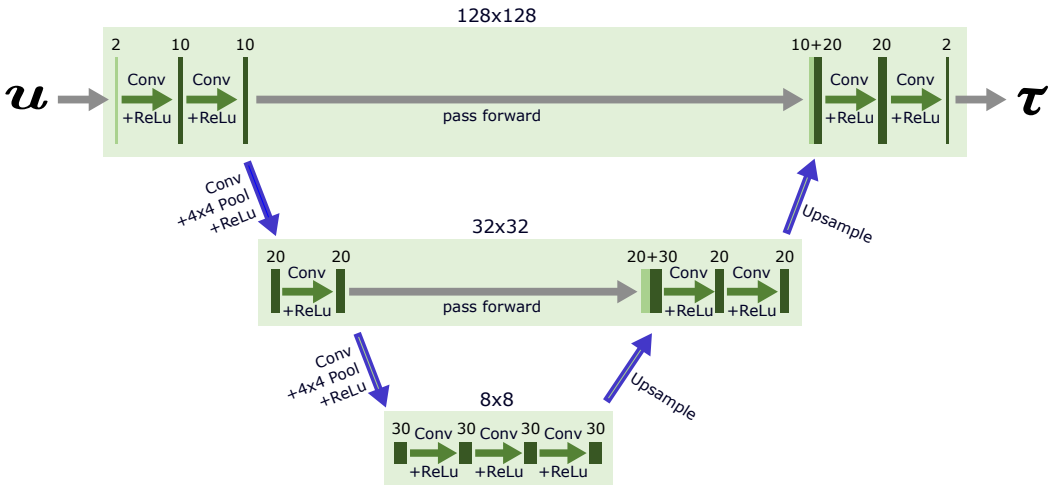

Figure 6.1: Schematic depiction of the UNet architecture used in this chapter. Downsampling reduces the image resolution enabling the detection of longer-ranged correlations. Upsampling reconstructs the image resolution. The model is fully convolutional. If the input size is larger, the pixel size in each layer changes appropriately. In the figure I use $\boldsymbol{u}$ for the input and $\boldsymbol{\tau}$ describing the U-Net configuration that would be used to predict tractions from deformations directly. In this study, however, I will use the U-Net only as a precondition step, details are explained in section 6.3.1

input data. The relationship in size prior to padding and after application of the convolution is now given by [220]:

$$W_{\text{out}} = \left\lfloor \frac{W_{\text{in}} - N + 2P}{s} \right\rfloor \qquad H_{\text{out}} = \left\lfloor \frac{W_{\text{in}} - N + 2P}{s} \right\rfloor \tag{6.20}$$

Like in the fully connected case, we can use backward propagation to calculate the gradients with respect to $\boldsymbol{b}^{(j)}$ and $\overline{K}^{(j)}_{i,l,m,n}$. They are given by [219]:

$$\overline{y}^{(j)}_{l,m,n} = \sum_{i=0}^{C_{\text{out}}} \sum_{p=0}^{H_{\text{out}}} \sum_{q=0}^{W_{\text{out}}} \sum_{m'=0}^{N-1} \sum_{n'=0}^{N-1} \mathrm{K}_{i,l,m',n'} \overline{z}^{(j+1)}_{l,p,q} \delta_{m,p\cdot s+m'} \delta_{n,q\cdot s+n'} \tag{6.21}$$

$$\overline{z}^{(j)}_{l,m,n} = \overline{y}^{(j)}_{l,m,n} \cdot \phi'(z^{(j)}_{l,m,n}) \tag{6.22}$$

$$\overline{b}^{(j)}_{i} = \sum_{m=0}^{H_{\text{out}}} \sum_{n=0}^{W_{\text{out}}} \overline{z}^{(j)}_{i,m,n} \tag{6.23}$$

$$\overline{K}^{(j)}_{i,l,m,n} = \sum_{p=0}^{H_{\text{out}}} \sum_{q=0}^{W_{\text{out}}} \overline{z}^{(j)}_{i,m,n} y^{(j)}_{l,p\cdot s+m,q\cdot s+n} \tag{6.24}$$

where C_{out}, H_{out}, W_{out}, N and M describe the corresponding quantities for layer j respectively.

A major benefit of using connected layers is also the flexibility in input size. A fully convolutional network, meaning a network without dense layers, can often be applied to images with a different size of what it has been trained on.

6.2.2 U-Net architecture

One principal shortcoming of simply using a set of convolutional layers is the limited context: Each convolutional layer has only a very restricted receptive field due to its

finite kernel size. In principle this could be overcome by increasing the kernel size, however, this would drastically increase the degrees of freedom. The U-Net, an architecture first proposed by Ronneberger *et al.* [108] for Biomedical Image Segmentation, tries to overcome this issue. A variant of the U-Net architecture is visualized in Fig 6.1. The principal idea is to intermix convolutional layers with downsampling steps, that merge neighboring nodes of the same channel into one pixel. Each downsampling step reduces the width and height of the intermediate output. Information can thus be processed at a different length scale. The downsampling steps are followed by an equal number of upsampling steps. In each upsampling step, we increase the width and height of the intermediate output and then concatenate it with the output of the last layer prior to downsampling. This procedure reintroduces local information. The U-Net architecture has been successfully employed in a wide range of problems including problems related to bio-imaging and traction force estimation techniques [23, 25, 107, 108, 222].

6.2.3 Conditional invertible neural networks

In the previous section we have always assumed a simple deterministic relationship between the features and the response $\boldsymbol{Y} = f(\boldsymbol{X}) + \boldsymbol{\varepsilon}$. In general, however, this is not true. There may be no deterministic relationship between the features and the response at all. Rather than trying to approximate the function $f(\cdot)$ we hence need to look into the full probabilistic picture. A very elegant solution to do so has been suggested by Ardizzone *et al.* [203, 204].

The relation between our features and our response can be described more generally by their full posterior probability density, $p(\boldsymbol{Y}|\boldsymbol{X})$. In many cases, however, the inverse relationship is better understood and can be described by a model $\boldsymbol{X} = s(\boldsymbol{Y}) + \boldsymbol{\varepsilon}$. Motivated by this, we now introduce a random variable $\boldsymbol{z} \in \mathbb{R}^K$ with the same dimensionality as $\boldsymbol{Y}$, and which we impose to have been distributed by a standard distribution

$$\boldsymbol{z} = f(\boldsymbol{Y}; \boldsymbol{X}) \qquad \boldsymbol{z} \sim p_Z(\boldsymbol{z}) = \mathcal{N}(\boldsymbol{z}|0, \mathrm{I}_K) = (2\pi)^{K/2} \exp\left(-\boldsymbol{z}^2\right) \quad . \tag{6.25}$$

The tilde here reads "distributed by". It can be shown that demanding such a pairwise independent Gaussian distribution for the so-called *latent variables* does not impose any additional restriction [223]. Just like in the simplistic description, we assume that we can approximate $f(\boldsymbol{Y}; \boldsymbol{X})$ by a traceable model $f(\boldsymbol{Y}; \boldsymbol{X}, \theta)$.

If we now assume that the mapping $f(\boldsymbol{Y}; \boldsymbol{X}, \theta)$ is invertible in its first component, meaning a $g(\boldsymbol{z}; \boldsymbol{X}, \theta)$ such that $g(\cdot; \boldsymbol{X}, \theta) = f^{-1}(\cdot; \boldsymbol{X}, \theta)$ exists, the new quantity $\boldsymbol{z}$ contains the latent variables, or information, which is contained in $\boldsymbol{Y}$ but cannot be reconstructed from $\boldsymbol{X}$.

We can now describe $p(\boldsymbol{Y}|\boldsymbol{X})$ by a coordinate transform [204]:

$$p_Y(\boldsymbol{Y}|\boldsymbol{X}, \theta) = p_Z(\boldsymbol{z} = f(\boldsymbol{Y}; \boldsymbol{X}, \theta)) \left| \det\left(\frac{\partial f}{\partial \boldsymbol{Y}}\right) \right| . \tag{6.26}$$

Here we used $\partial f / \partial \boldsymbol{Y}$ to describe the Jacobian of f.

In order to determine the model parameters θ we use Bayes' theorem which gives us the posterior over the model parameters

$$p(\theta|\boldsymbol{X}, \boldsymbol{Y}) \propto p_Y(\boldsymbol{Y}|\boldsymbol{X}) \cdot p_\theta(\theta). \tag{6.27}$$

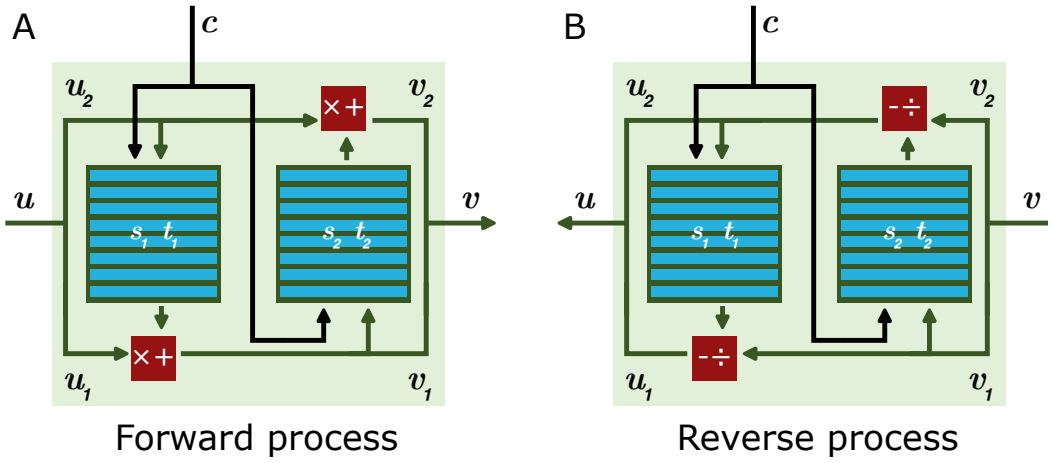

Figure 6.2: Visualization of an invertible coupling block. In the forward process (A) the input $\boldsymbol{u}$ is first split into two parts. The first sub-network is used to generate the transformation parameters $s_1(\boldsymbol{u}_2, c)$ and $t_1(\boldsymbol{u}_2, c)$ to transform the first component $\boldsymbol{u}_1$. The transformed first component $\boldsymbol{v}_1$ is then passed to the second network to generate the transformation parameters $s_2(\boldsymbol{v}_1, c)$ and $t_2(\boldsymbol{v}_1, c)$ to generate the transformed second component $\boldsymbol{v}_2$. (B) The transformation can be reversed without requiring the subnets to be invertible. Both transformations can be controlled by a conditioning parameter $\boldsymbol{c}$, that is passed to the subnets.

Like in Eq 6.5, our goal is to find the network parameters that maximize this posterior, which can be achieved by minimizing the loss [204]

$$\mathcal{L} = \mathbb{E}_i[-\log(p_Y(\boldsymbol{Y}_i|\boldsymbol{X}_i, \theta))] - \log(p_\theta(\theta)). \tag{6.28}$$

If we now insert Eq 6.26 with the standard Gaussian Eq 6.25 and also introduce a Gaussian prior on the weights like in Eq 6.6, we obtain

$$\mathcal{L} = \mathbb{E}_i \left[\frac{\|f(\boldsymbol{Y}_i; \boldsymbol{X}_i, \theta)\|_2^2}{2} - \log|J_i| \right] + \tau \|\theta\|_2^2 . \tag{6.29}$$

J_i is the determinate of the Jacobian introduced in Eq 6.26 and $\tau = 1/2\sigma_\theta^2$. The case of $\tau = 0$ corresponds to an equal probability prior.

The function f completely describes the distribution of $\boldsymbol{Y}$. For a given so-called *conditioning* input $\boldsymbol{X}$ we can now find realizations of $\boldsymbol{Y}$ by drawing realizations of $\boldsymbol{z}$ and calculate $\boldsymbol{Y}_{\text{gen}} := g(\boldsymbol{z}; \boldsymbol{X}, \theta)$.

Invertible architecture

If we now want to describe $f(\boldsymbol{Y}, \boldsymbol{X}, \theta)$ by a traceable model using a neural network, we need to construct this model in a specific manner, such that it is trivially invertible. This can be achieved by building our network based on invertible coupling blocks using an architecture first proposed by Dinh *et al.* [224], which is visualized in Fig 6.2. In order to do so, in each block, the block input $\boldsymbol{u}$ is split into two equal parts $[\boldsymbol{u}_1, \boldsymbol{u}_2]$ which are then passed through a layer of affine transformations

$$\boldsymbol{v}_1 = \boldsymbol{u}_1 \odot \exp(s_1(\boldsymbol{u}_2)) + t_1(\boldsymbol{u}_2), \tag{6.30}$$

$$\boldsymbol{v}_2 = \boldsymbol{u}_2 \odot \exp(s_2(\boldsymbol{v}_1)) + t_2(\boldsymbol{v}_1). \tag{6.31}$$

The outputs $[\boldsymbol{v}_1, \boldsymbol{v}_2]$ can then subsequently be rejoined and passed on to the subsequent coupling block. The functions $s_{1,2}$ and $t_{1,2}$ may also take the conditioning $\boldsymbol{X}$

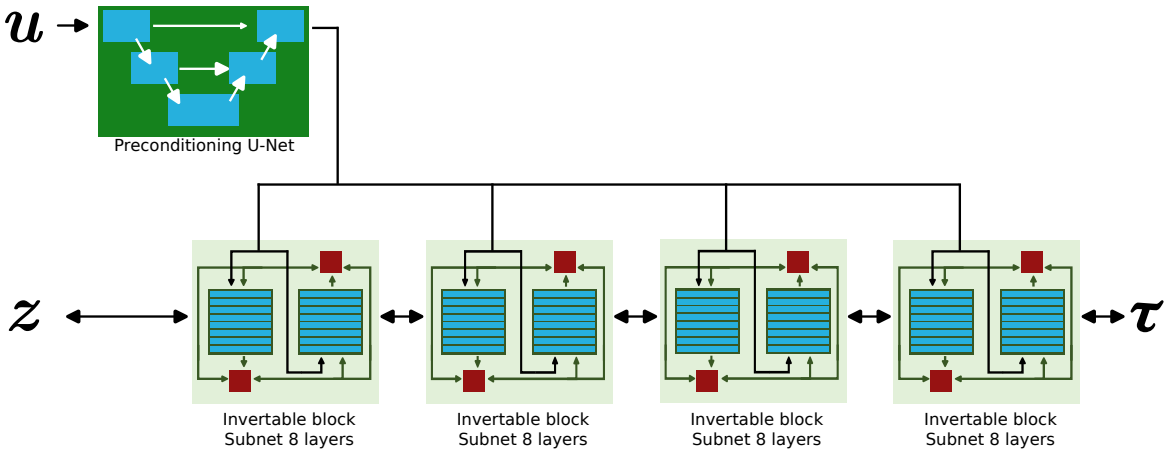

Figure 6.3: CINN architecture used for TFM. The input deformation field is first processed by a preprocessing network following the U-Net architecture the cINN itself consists of 4 individual subnet blocks. Each subblock is constructed out of 4 convolutional layers using a ReLU non-linear function.

as an additional input. They can be represented by arbitrary NNs. While the subnet functions $s_{1,2}$ and $t_{1,2}$ are not necessarily invertible and can only be evaluated in forward direction, the entire coupling block can be inverted:

$$\boldsymbol{u}_2 = (\boldsymbol{v}_2 - t_2(\boldsymbol{v}_1)) \oslash \exp(s_2(\boldsymbol{v}_1)), \tag{6.32}$$

$$\boldsymbol{u}_1 = (\boldsymbol{v}_1 - t_1(\boldsymbol{u}_2)) \oslash \exp(s_1(\boldsymbol{u}_2)). \tag{6.33}$$

The symbol $\oslash$ here describes element-wise division. As shown by Dinh *et al.* [224] the logarithm of the Jacobian determinant of this coupling block can be obtained by simply summing up the results of $s_1(\boldsymbol{u}_2)$ and $s_2(\boldsymbol{v}_1)$ over all output nodes. The functioning of an invertible coupling block is detailed in Fig 6.2.

Such a NN which describes, relative to a conditioning input, an invertible map between particular realizations of a certain quantity and its latent space equivalent is known as a conditional invertible neural network (cINN) [204].

6.3 Application to TFM

6.3.1 Model selection

For application in TFM, I use a cINN, whose network architecture is shown in Fig 6.3. I use a U-Net architecture with 2 downsampling steps as a preprocessing step for our conditioning input and use a network consisting of 4 consecutive invertible blocks, with subnets each consisting of 8 layers with a relatively large kernel size of 16x16. The idea is that the U-Net should ensure the distribution of the overall network, while the individual layers predict the local structure of the network. Using the U-Net for preconditioning ensures that the network is able to efficiently propagate long-range interactions.

6.3.2 Sample generation framework

The primary bottleneck of machine learning methods is the availability of training and test data: Either the goal of our algorithm must be sufficiently flexible to allow for unsupervised algorithms or we must have a relatively large set of realizations of

our problem where both the input and the correct response are known by a priori means.

For simple problems that mimic human perception and response and do not aim to excel human abilities one could simply manually perform this task [225], however, it is obvious that such an approach is not feasible for problems like TFM. Given that TFM is an inverse problem, the idea is to start with the traction field and solve the forward problem to obtain a deformation field. In a subsequent step, random perturbations are added to the resulting deformation field.

To obtain traction fields, there are now multiple strategies as well. One obvious approach would be to obtain datasets where the force is obtained using different, non-TFM based methods, however, this approach not only requires extensive data collection, but this strategy would maintain all shortcomings and issues of this alternative observation method.

The previous attempts to apply machine learning to TFM therefore used a different strategy to obtain training data [23, 107]: Generate synthetic data and then use them for the training. The main benefit of this approach is that it is in principle unbiased with respect to specific external observations. Also, shortcomings in the generalization of the model should be more apparent.

For my analysis, I have chosen a sample generation routine that is a somehow intermediate variant of the approaches described in [23] and [107]. The intention is to simulate adhesion profiles that superficially mimic the distribution of adhesions as seen in actively contracting cells like fibroblasts. By doing so, I hope to ensure that a certain correlation between different adhesion sites is maintained while avoiding biasing due to the use of a certain specific model.

We will build up the deformation profile analytically from circular adhesion profiles. To do so, we perform our generation in 3 steps:

- Define a "cell boundary" that references the rough position of each adhesion.
- Distribute the adhesion sites and obtain their radial and angular coordinates.
- Determine the force contribution of each adhesion site

Creating Cell boundaries

As adhesions are predominantly found close the cell boundary, in a first step, we generate a cell shape approximation. We can model each cell by an area

$$\Omega_{r\phi,x_0,y_0} = (x,y) \in \mathbb{R}^2 | (x-x_0)^2 + (y-y_0)^2 < r(\phi) \tag{6.34}$$

where (x_0, y_0) describes some reference point close to the cell center, ϕ describes the orientation of the vector $(x - x_0, y - y_0)^T$ and $r : [0, 2\pi) \to \mathbb{R}$ describes the radial extent of the cell. In order to get smooth contours, we model $r(\phi)$ by a Fourier like representation

$$r(\phi) = R_0 \left(a_0 + \frac{a_1}{2^\eta} + \sum_{k=3}^{N_{\text{sh}}} \frac{a_i}{k^\eta} \cos\left((k-1)(\phi + \alpha_i)\right) \right), \tag{6.35}$$

where R_0 describes the cell size and η describes a suppression factor that can be used to control the roundness of the cell. The special treatment of the first two coefficients avoids malformed cell shapes.

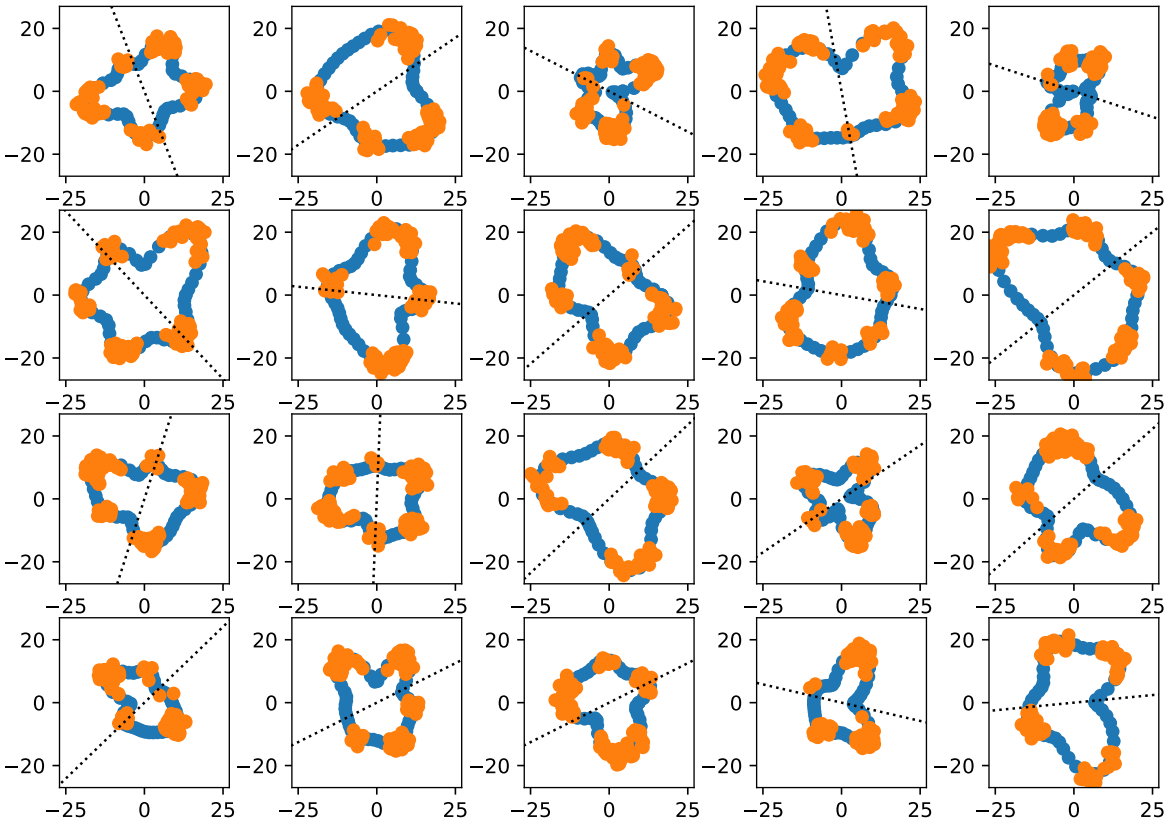

Figure 6.4: Samples of synthetic cell shapes. The blue contour indicates the cell shape, while orange indicates the regions where the adhesion sites are and forces act.

The full shape is now described in terms of its radial parameters a_i and its phase parameters α_i. The a_i are drawn from a uniform distribution $\mathcal{U}\left(\frac{1}{4}, 1\right)$, while the α_i are drawn from a uniform distribution $\mathcal{U}(0, 2\pi)$.

I also define the dominant axis for each cell such that it links up with the dominant direction of elongation. The algorithm can be found in the appendix, section A.5. In the following, I will use α to designate its orientation relative to the x axis.

The just described procedure generates a wide range of cell shapes as seen in Fig 6.4.

It should be noticed, that compared to real cell shapes, these synthetic cells do not necessarily represent the real cell shapes, as this procedure does not replicated details such as invaginated arcs or filopodia. However, as we will see in subsequent steps, only the protrusive parts of this contour line bear significant relevance.

Distribution of adhesion sites

In a subsequent step, we determine the positions ϕ_i of the individual adhesion sites. For this, we try to favor crypts and protrusive areas. To do so, we randomly draw angles from the distribution

$$p(\phi_i) \propto \begin{cases} \left(\frac{r(\phi)}{r_{\max}}\right)^f & \frac{r''(\phi_i)}{c_{\max}} \leq c_t \\ 0 & \frac{r''(\phi_i)}{c_{\max}} > c_t \end{cases}, \tag{6.36}$$

where $r_{\max} = \max_\phi r(\phi)$ and $c_{\max} = \max_\phi r''(\phi)$.

The case switching ensures that adhesions are predominantly found in protrusion like areas, which is controlled by a threshold parameter c_t. The inner term ensures

that placing adhesions at points close to the cell center is suppressed and is controlled by a parameter f.

Sampling this function can be easily conducted using the rejection method as described in [226], by drawing a trial ϕ_i from a suitable range of angles and a test parameter $u_i \in [0, 1]$ from a uniform distribution until the drawn value for u_i is smaller than the left-hand side of Eq 6.36.

I also avoid distributing all adhesion sites on one side of the cell. This is done by splitting the cell in halve orthogonal to its dominant axis and distributing the same number of adhesions in each halve.

In order to scatter the radial position, I introduce a specially designed random number distribution defined by a probability density $p_d(x)$ given by:

$$p_d(x|a,b,d) = \begin{cases} \frac{1}{b-a} - \frac{6c}{(b-a)^3}\left[\left(x - \frac{a+b}{2}\right)^2 - \frac{(b-a)^2}{12}\right] & x \in [a,b] \\ 0 & \text{else} \end{cases}. \tag{6.37}$$

Here, the variable c may be chosen arbitrarily and can be used to restrict how narrow the adhesions should be distributed relative to the contour line. This distribution is chosen such that parameters can be strictly restricted to a certain range $[a, b]$ with some emphasis on values being located close to the range's median and mean value.

We find the cumulant of this distribution to be:

$$P_d(X \leq x) = \begin{cases} 0 & x \leq a \\ \frac{2-c}{2(b-a)}(x-a) + \frac{2c}{(b-a)^3}\left(x - \frac{b+a}{2}\right)^3 + \frac{2c}{(b-a)^3}\left(\frac{b-a}{2}\right)^3 & x \in [a,b] \\ 1 & x > a \end{cases} \tag{6.38}$$

By using the transformation theorem [226], we can thus generate realizations of this distribution by drawing a realization z from the uniform distribution between 0 and 1 and then find the value x such that $z = P(x)$.

We finally calculate the radial position of each adhesion by:

$$\begin{aligned} r_i &= r(\phi_i) + \varepsilon \text{ where} \\ \varepsilon &\sim p_d(\cdot|c, -s \cdot r_{\max}, s \cdot r_{\max}) \end{aligned} \tag{6.39}$$

where the parameters s and d describe the degree of scattering.

Distribution of force strengths

We assume that the force vector at each adhesion site can be described by two components: A radial component pulling towards the reference point $(x_0, y_0)^T$ weighted with a factor a_i and a contractile component parallel to the cell's main axis, weighted with a factor b_i.

$$\boldsymbol{F}_i = \begin{pmatrix} b_i \cos(\alpha) - a_i \cos(\phi_i) \\ b_i \sin(\alpha) - a_i \sin(\phi_i) \end{pmatrix} \tag{6.40}$$

It can easily be shown, that this representation is merely a reparameterization and does not introduce any loss of generality. We now enforce two constraints that the overall adhesion distribution should fulfill. First we enforce that the overall cell should maintain force balance, meaning that:

$$\boldsymbol{F}_{\text{tot}} = \sum_i \boldsymbol{F}_i = 0, \tag{6.41}$$

which can be transformed into

$$0 = \sum_i b_i - a_i \cos\gamma_i, \tag{6.42}$$

$$0 = -\sum_i a_i \sin\gamma_i, \tag{6.43}$$

where we used the abbreviation $\gamma_i := \phi_i - \alpha$.

Second, we also define the contractile moment matrix with respect to the reference point:

$$\mathbf{M} = \sum_i \begin{pmatrix} F_{x,i}x_i & \frac{1}{2}(F_{x,i}y_i + F_{y,i}x_i) \\ \frac{1}{2}(F_{x,i}y_i + F_{y,i}x_i) & F_{y,i}y_i \end{pmatrix}. \tag{6.44}$$

We now impose the constraint that the contractile moment matrix should have dipole axes that correspond to the dominant axis and its normal, where we observe the major and minor dipole moments M_1 and $M_2 < M_1$ respectively:

$$\mathbf{M} = R(\alpha) \cdot \begin{pmatrix} M_1 & 0 \\ 0 & M_2 \end{pmatrix} \cdot R^T(\alpha) \qquad R(\alpha) = \begin{pmatrix} \cos(\alpha) & -\sin(\alpha) \\ \sin(\alpha) & \cos(\alpha) \end{pmatrix}. \tag{6.45}$$

This results in

$$M_1 = \sum_i r_i \cos\gamma_i \left(b_i - a_i \cos\gamma_i\right), \tag{6.46}$$

$$M_2 = -\sum_i r_i a_i \sin^2\gamma_i, \tag{6.47}$$

$$0 = \sum_i r_i \left(\sin\gamma_i \left(b_i - a_i \cos\gamma_i\right) - a_i \cos\gamma_i \sin\gamma_i\right). \tag{6.48}$$

In order to find a unique solution, we now fix M_1 and M_2 and impose an optimization criterion, namely that all a_i and b_i should be equal, this is to ensure that force contributions are all in a similar range and in absence of exterior constrains cells distribute forces equally over their focal adhesions. This results in a constrained optimization problem

$$\begin{gathered} \arg\min_{a,b,a_i,b_i} \sum_i (a_i - a)^2 + (b_i - b)^2 \\ \text{such that Eq 6.42, 6.43 and 6.46 to 6.48 hold.} \end{gathered} \tag{6.49}$$

This problem can now be efficiently formulated using Lagrangian multipliers and explicitly be reduced to a linear system of equations, where I first determine the values of a, b and all Lagrangian multipliers before using these 7 values to calculate a_i and b_i using a matrix multiplication and use them to find $\boldsymbol{F}_i$ using Eq 6.41.

Generation of force maps

Each adhesion site is now modeled by a circular adhesive patch. We use the analytical solutions described in section 5.2.2 for each individual patch.

We now specify $\boldsymbol{\tau}(x, y|a, \boldsymbol{F}, c = 1)$ to be a constant-traction profile with radius a and total transmitted force $\boldsymbol{F}$ as described in Eq 2.44 with the corresponding deformation profile $\boldsymbol{u}(x, y|a, \boldsymbol{F}, c = 1)$ as described in Eq 2.45 and 2.46.

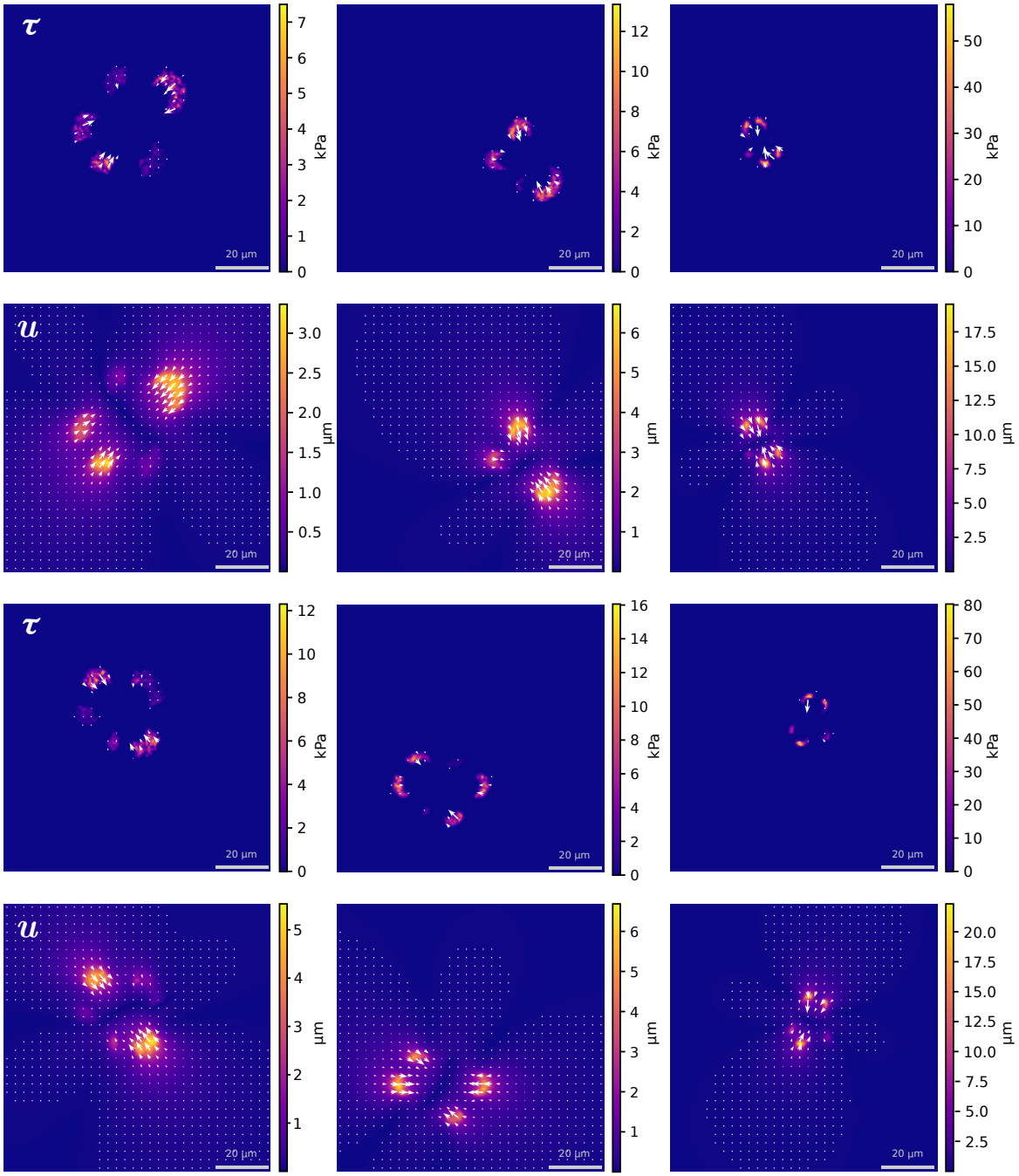

Figure 6.5: Generated traction and deformation samples. 6 samples are shown with their traction field $\boldsymbol{u}$ and their deformation field $\boldsymbol{\tau}$. The deformation is in all cases shown below the corresponding traction. For visualization a substrate stiffness of 6.7 kPa is assumed. Displacement is shown prior to the addition of noise.

Similarly, we specify $\boldsymbol{\tau}(x, y|a, \boldsymbol{F}, c = 0)$ and $\boldsymbol{u}(x, y|a, \boldsymbol{F}, c = 0)$ to be a Hertz-like profile as described in Eq 2.56, 2.57 and 2.58.

We can now generate a complete traction map by picking a position for the cell center, x_0, y_0 finding the positions and force magnitudes of all adhesions and build up an adhesive profile using the linearity of linear elasticity

$$\begin{aligned}\boldsymbol{\tau}(x, y) &= \sum_i \boldsymbol{\tau}(x - x_i, y - y_i|a_i, \boldsymbol{F}_i, c_i) \\ \boldsymbol{u}(x, y) &= \sum_i \boldsymbol{u}(x - x_i, y - y_i|a_i, \boldsymbol{F}_i, c_i).\end{aligned} \tag{6.50}$$

The values for $c_i \in 0, 1$ can be used to select between Hertz-like and Heavyside like profiles. A random selection between both profiles reduces the dependency of the network on one particular adhesion layout. In order to simulate experimental data, Eq 6.50 is evaluated on a regularly spaced grid. In order to simulate the reconstruction, a point-wise Gaussian noise is then added to the deformation components.

As seen in Fig 6.5 we can generate a wide variety of samples using this process.

6.3.3 Experimental Data

For an evaluation of my method, I use two different sets of experimental data from different cell lines.

The first dataset contains traction force imaging data for human induced pluripotent stem cell derived cardiomyocytes (hiPSCs). Cardiomyocytes are cells found in the heart which are responsible for contraction [227]. Somatic cells can revert to a pluripotent state under the influence of Yamanaka factors [228]. From this, hiPSCs can be derived [229]. hiPSCs behave similar to cardiomyocytes in early stages of cardiac development and are employed in the study of genetically caused diseases due to the more simple and systematic way to obtain them compared to the extraction of cells from an in vivo environment [230].

Protocols to grow hiPSCs showing highly phenotypic behavior of both atrial and ventricular cardiomyocytes have been well established [231–233]. The cardiomyocytes used in this study have been grown at the *Stem Cell Unit* of the University of Göttingen using a microcontact printing protocol established by Valentina Kuhn [234, 235] and were originally used as part of a study to observe the effects of the mutation R331Q of the *LMNA* gene found to be causing an increase of sudden death rates [236]. Experiments and gel deformation observations were conducted by Christina Goss, Valentina Kuhn, Anna Zelená, Isabelle Refke and Mangalika Sinha under the guidance of Sarah Köster and are presented in [234, 235, 237]. I briefly describe the experimental procedures in the appendix, section B.2

Their clearly bipolar, contractile peaks as well as the clearly predictable direction of force generation, makes this kind of data an ideal candidate for evaluation of my method. In this study I only use the wild type examples.

The second dataset used to evaluate cINN-based TFM is based on the study presented in manuscript 4 in which I, together with experimental collaborators, used traction force microscopy to study force generation in human blood platelets or thrombocytes by filamentous actomyosin structures.

Thrombocytes play an integral role in wound healing by facilitating blood clotting. When a blood vessel is damaged, thrombocytes adhere to the surrounding matrix and

Parameter		value
Cell scale	R_0	12 µm
Number of shape modes	N_{sh}	7
Mode suppression factor	η	1.1
Number of adhesions	N_{adh}	900
Scattering spread factor	c	0.5
Major dipole moment	M_1	$0.74 N_{\text{adh}} R_0$
Major dipole moment	M_2	$0.25 M_1$
Force map resolution		0.8 µm/pixel

Table 6.1: Parameters used for sample generation

contract to form a clot. This helps to restore normal blood circulation. The hemostatic function of thrombocytes is directly related to their mechanics and cytoskeletal organization. It is known that during spreading thrombocytes reorganize their cytoskeleton within minutes, which leads to the formation of contractile actomyosin bundles. However, previous research has not revealed a direct correlation between the emerging actin structures and the force field that is exerted to the environment. In our study, we therefore combined fluorescence imaging of the actin structures with simultaneous traction force measurements in a time-resolved manner and also imaged the final states with super-resolution microscopy. Our study found that both force fields and cell shapes had clear geometrical patterns defined by stress fibers and force generation was localized in a few hotspots, which appear early during spreading, and in the mature state anchor stress fibers in focal adhesions. The study also revealed that for gel stiffness in the physiological range, force generation is a very robust mechanism and we observed no systematic dependence on the amount of added thrombin in solution or fibrinogen coverage on the substrate. This suggested that force generation after thrombocyte activation is a threshold phenomenon that ensures reliable thrombus contraction in diverse environments. The experimental details are described in the appendix, section B.3.

Because super-resolution micrographs of the actin cytoskeleton and of vinculin, which is found in focal adhesions, are recorded in the experiment, the force generation mechanism of the cell could be observed directly. These additional observations can serve as an alternative indicator to reason about the plausibility of the observed force patterns. In combination with the more complex patterns of adhesion found in these cells, thrombocytes are another interesting candidate for evaluating the capabilities of cINN-base TFM.

6.4 Training

I generated a training dataset that consists of 10000 data-samples of a size of 128x128 pixels, with a resolution of 0.8 µm per pixel. 1000 data samples were used for validation, while the remaining 90% were used for training. Since force strength only depends on the choice of the Young's modulus E we used a unit-less convention $E = 0.5$ for the simulation. This factor improved training stability. Force predictions made by the network thus need to be multiplied by $2E$ to obtain physical dimensions. The configuration parameters used for training are given in Tab 6.1.

The ADAM optimization scheme was employed and training used 71 epochs until a high level of convergence was reached.

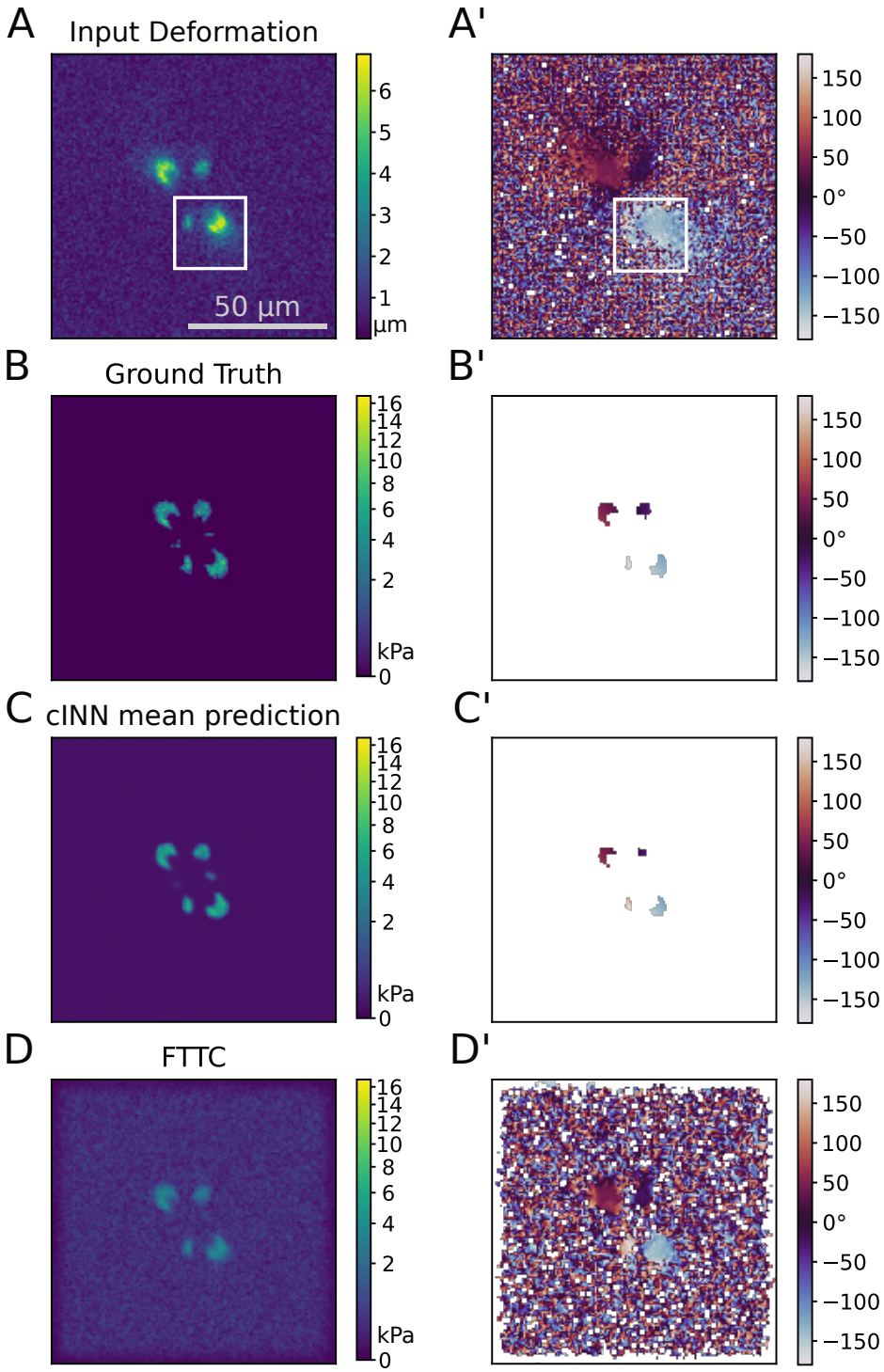

Figure 6.6: Reconstruction for a validation dataset. Plots (A, B, C, D) show field magnitudes, plots (A', B', C', D') show orientation. (A, A') Simulated deformation field. The white square indicates the focus area that will be used in Fig 6.8 and Fig 6.9 (B, B') Ground truth traction. (C, C') cINN prediction averaged over multiple traction realization. (D, D') FTTC traction prediction. An orientation of 0 degrees corresponds to a force in leftward direction. Positive angles indicate forces pulling in downward direction. Points with negligible traction magnitude are conventionally assigned a leftward orientation (0°). All coordinate axes show lengths in micrometers.

6.5 Network evaluation

I first verify our reconstruction on a simulated dataset taken from our validation data. The results of this are shown in Fig 6.6. Other datasets with different magnitudes show similar behavior and can be found in the appendix, Fig C.2 and Fig C.3. The first two plots, Fig 6.6 A and A', show the simulated input deformation field. Next, the true traction field, the deformation has been obtained from, is shown in Fig 6.6 B and B'. Because tractions and deformations are vector quantities, in the following, I show each field in two distinct plots, where the orientation plot is given the same letter as the magnitude plot, except that a prime is affixed to the plot label. After that, I show the force reconstructions using the cINN (Fig 6.6 C and C') and FTTC (Fig 6.6 D and D'). For the cINN reconstruction, I have averaged over 50 individual traction realizations obtained from our neural network to get sufficient statistics. For the FTTC reconstruction I used an optimized regularization parameter $\lambda = 0.55$ as well as a Tukey windowing function active in the outermost 10 pixels to avoid boundary artifacts. Both the cINN as well as the FTTC were able to reconstruct the layout. The cINN was in addition able to correctly recognize and remove the background noise in the signal. It can be verified that for an input where the deformation data purely consists of noise, our network is able to correctly predict the complete absence of forces. This proves that in principle a cINN architecture is able to solve the inverse problem of mechanical traction on an elastic halfspace on the macro-scale.

In order to study the micro-scale of the force reconstruction, I now focused closer onto the area immediately adjacent to the lower two adhesions that has been marked by a white square in Fig 6.6 A and A'. This detaining view is presented in figure Fig 6.7, where I again show the deformation field (Fig 6.7 A and A'), the true traction field (Fig 6.7 B and B'), as well as the force reconstructions using cINN (Fig 6.7 C and C') and FTTC (Fig 6.7 D and D'). We can see that the addition of noise in our

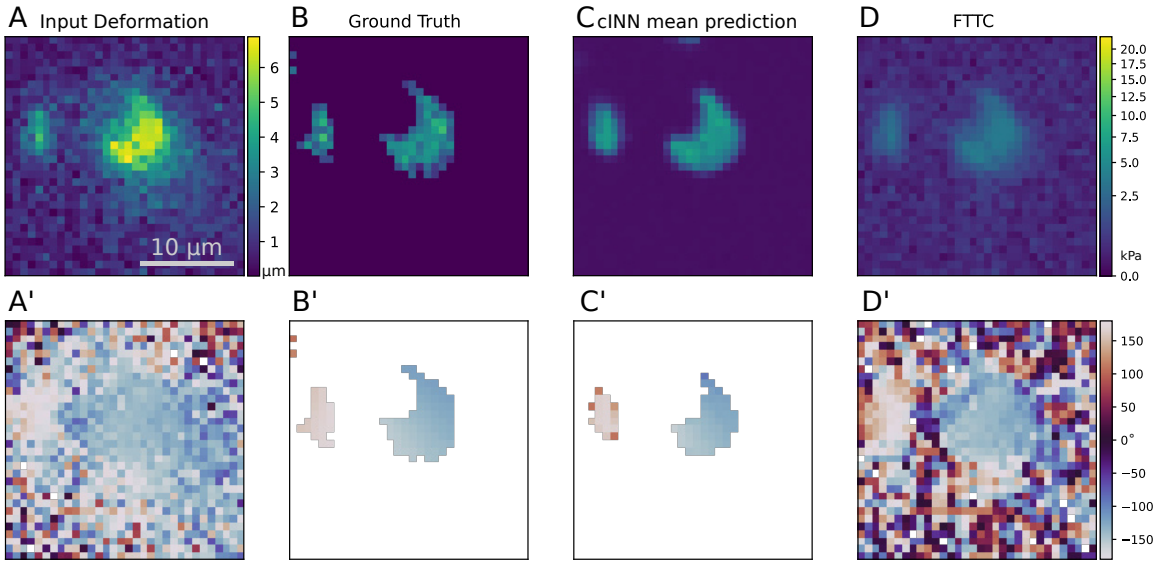

Figure 6.7: Zoomed-in view of validation dataset reconstruction showing the reconstruction in the area marked by a weight square in Fig 6.6. Plots (A, B, C, D) show field magnitudes, plots (A', B', C', D') show orientations. (A, A') Simulated deformation field. (B, B') Ground truth traction. (C, C') cINN prediction averaged over multiple traction realization. (D, D') FTTC traction prediction.

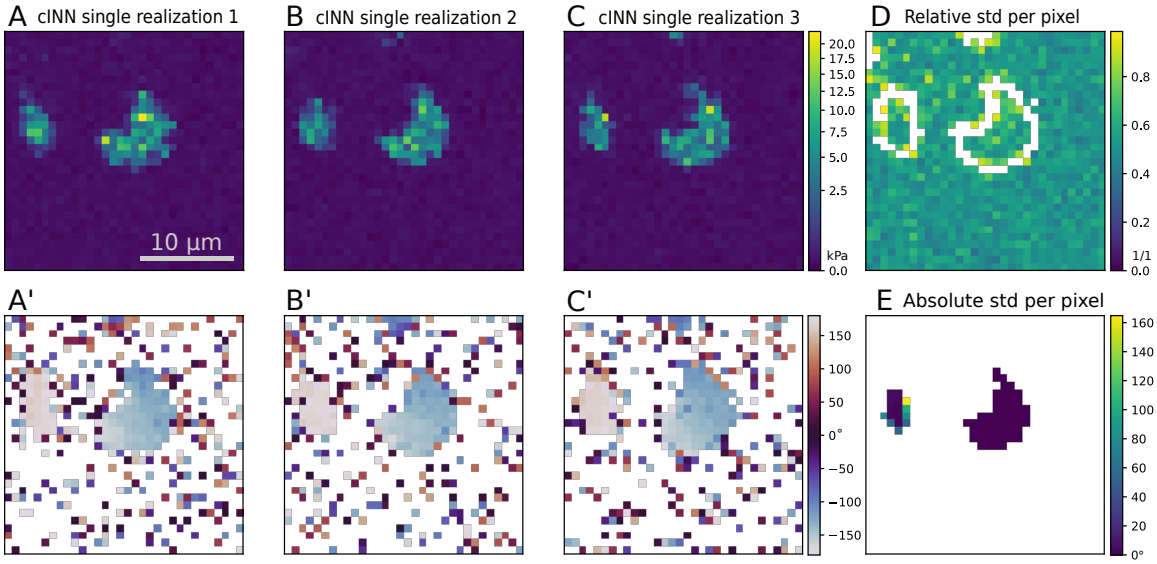

Figure 6.8: Probability space sampling for the validation dataset in the zoomed-in view. (A, A') Traction magnitudes (A) and orientation (A') for a singular cINN-realization. White color is used for points where traction magnitude is generally to small to calculate a meaningful orientation. (B, B') Another realization, again showing traction magnitudes (B) and orientation (B'). (C, C') A third realization. (D) Relative standard deviation (σ/μ) of traction magnitude at each sampling point. White corresponds to sampling points where the variation is exceeding 1, meaning that individual traction predictions at this locality are no longer significant statistically. (E) Standard deviation (σ) for traction orientation at each sampling point.

sample dataset resulted in a loss of traction resolution. The averaged prediction given by the cINN appears smoothed compared to the ground truth force and the contour line of each adhesion has been reduced in length and complexity. Despite of this, some details like the two locations of strong forces next to the outer edges of the adhesion have been retained. The cINN reconstruction on our validation dataset exceeds the prediction made using FTTC, both in predicting the correct magnitude as well as in signal clearness and orientation reconstruction.

Next, I try to explore the probability space of our sample reconstruction. The results of this analysis are shown in Fig 6.8. We can see that the different traction reconstructions feature significant variations in magnitude, but not in angle, which reflects the behavior of the input dataset. We can see that the network aims to recreate different distributions of adhesions with points of high force transmission situated at different sites of the adhesive area. The standard deviation of the traction magnitude, displayed in Fig 6.8 D shows that the variability of traction reconstruction is relatively consistent within the cell and only marginally lower than in the background. However, there is a huge uncertainty with respect to the exact cell boundary, which can be seen by the white contour line. In contrast, the reconstruction of the angle is relatively unambiguously based on the input data. In Fig 6.8 E, I present the variability in the reconstruction of orientation. Overall, the variability is very low, however, in small adhesions, the reconstruction in the left and right, when seen from the contractile center, delimiting point of the adhesive areas found to be very unreliable.

One primary benefit of the cINN architecture is the fact that it not only predicts the variability of the reconstruction in each sampling point but also detects strong

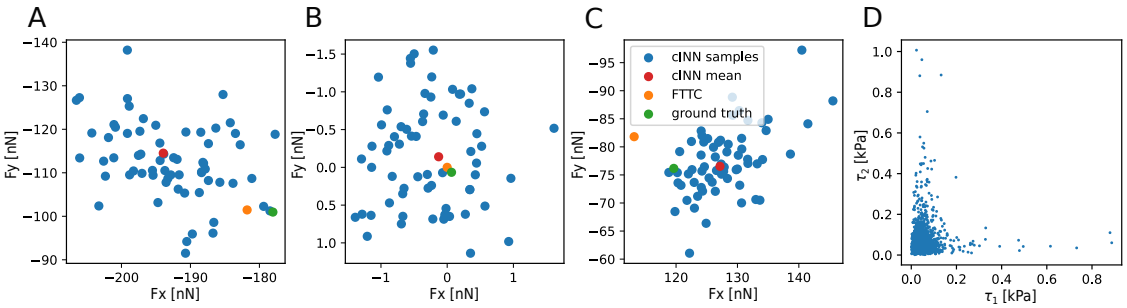

Figure 6.9: Regional quantitative behavior of the responsive field. (A to C) Integrated force in the zoomed-in view for differ realizations, in comparison to the ground truth, the force obtained from the averaged traction plot and the FTTC prediction for different configurations in the validation dataset. (A) corresponds to the configuration shown in Fig 6.6 to Fig 6.8. (D) Nearest neighbor correlation of traction magnitude reconstruction for two adjacent sampling points net to the point of maximal deformation.

correlations between different sampling points. We can see this when calculating the force transmitted in the zoomed-in window by integrating its traction. This is shown in Fig 6.9 A to C. The neural network predicts the integrated force to be distributed by a unimodal distribution and it shows a significant covariance and anisotropy in the distribution of traction in each sampling point.

The correlation in the reconstruction of traction magnitude between two adjacent sampling points is shown in Fig 6.9 D. We can see that in particular strong forces are show a highly level of correlation. While the distribution of traction magnitude in a single sampling point is unimodal and closely biased towards 0, a large traction magnitude in one sampling point never coincides with large traction value in the other sampling. I hence predict, that the value taken by the probability density function $p(\tau_1, \tau_2)$, where τ_1 and τ_2 are the realizations of the traction at the two adjacent sampling points, is somehow related to $d_p(\tau_1, \tau_2) = (\tau_1^p + \tau_2^p)^{\frac{1}{p}}$ for some $p \in (0, 0.5)$ via a monotonous transform.

6.6 Application to experimental data

After studying the networks performance on synthetic data, I applied my neural network to the experimental data obtained for cardiomyocytes. The results from this analysis are shown in Fig 6.10. These cells experience a strong periodic contractile behavior. Here we show the situation when the cardiomyocyte's contractility is at its peak. One can already predict from the plot of the deformation field Fig 6.10A and A' that the cell exerts contractile force between two points. For better resolution of details, we focus on the upper anchoring point, which is shown in the zoomed-in view. As we can see, the cINN (Fig 6.10F) is able to localize the contractile areas in a much cleaner manner, when compared to the FTTC prediction (Fig 6.10E). When looking into the individual force realizations (Fig 6.10 G and H) one apparent feature is the emergence of diagonal (from the upper left to the lower right) chains of sampling points with relatively large traction stresses. This is also reflected in the actin cytoskeleton presented in Fig 6.10 B, where the termination point of the actin strains also ends along two diagonal lines upon close inspection. This is a strong hint that the neural network is able to reconstruct substructures to a reasonable extent. When looking into the relative variation in the individual sampling points (Fig 6.10

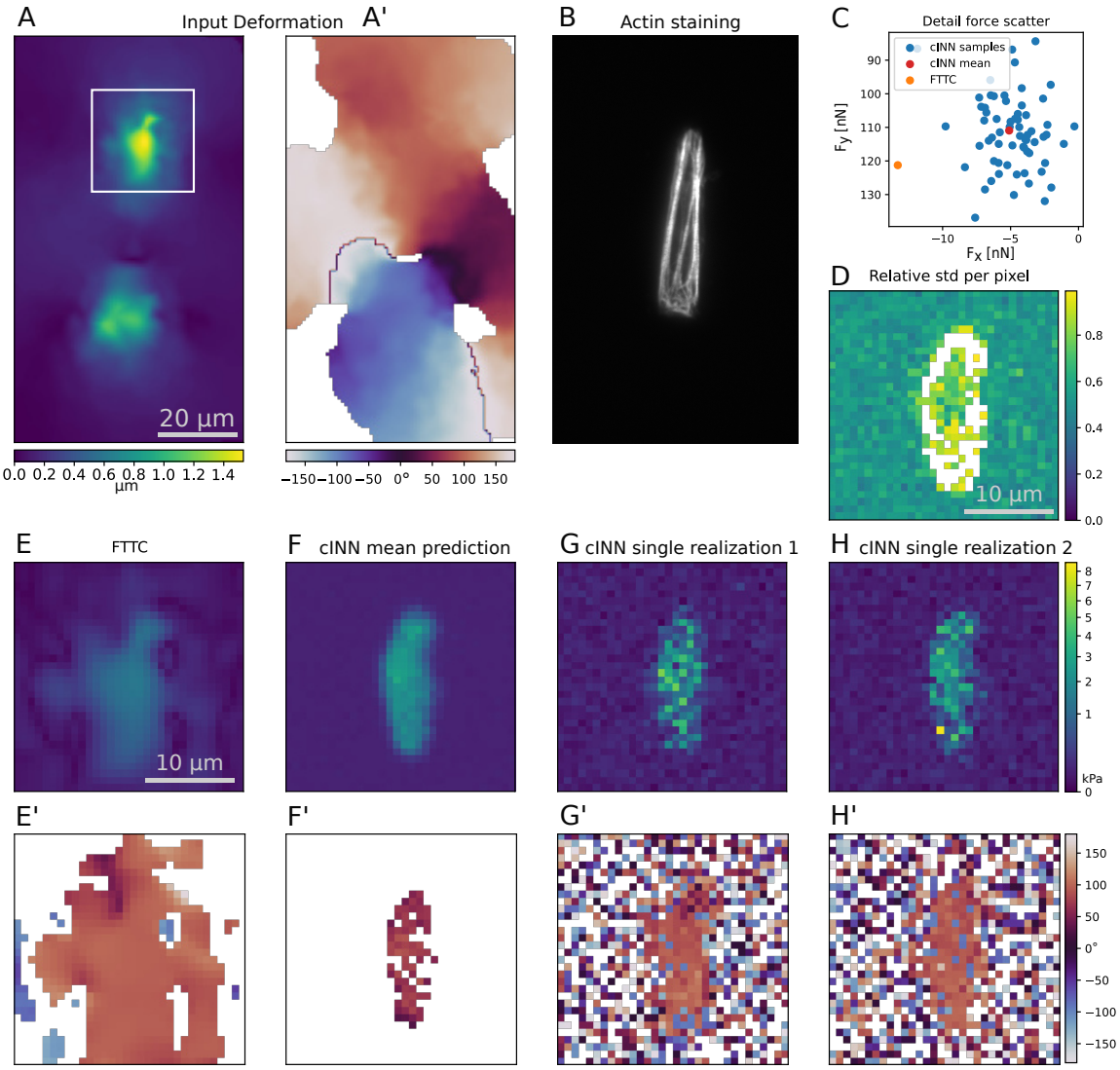

Figure 6.10: Reconstruction for a cardiomyocyte. The plots marked X' (where X is a letter) display the orientation of the corresponding magnitude plot X. (A, A') Deformation field, magnitude (A) and orientation (A'). The white square indicates the zoomed-in view. (B) Staining micrograph of the actin filament skeleton. (C) Integrated force in the zoomed-in view for different realizations, in comparison to the FTTC prediction. (D) Relative standard deviation of the reconstructed force magnitude. White corresponds to sampling points where the variation is exceeding 1, meaning that individual traction predictions at this locality are no longer significant statistically. (E, E') FTTC prediction. (F, F') cINN reconstruction averaged over multiple traction realization. (G, G') and (H, H') are two individual cINN reconstructions. Data presented in [237].

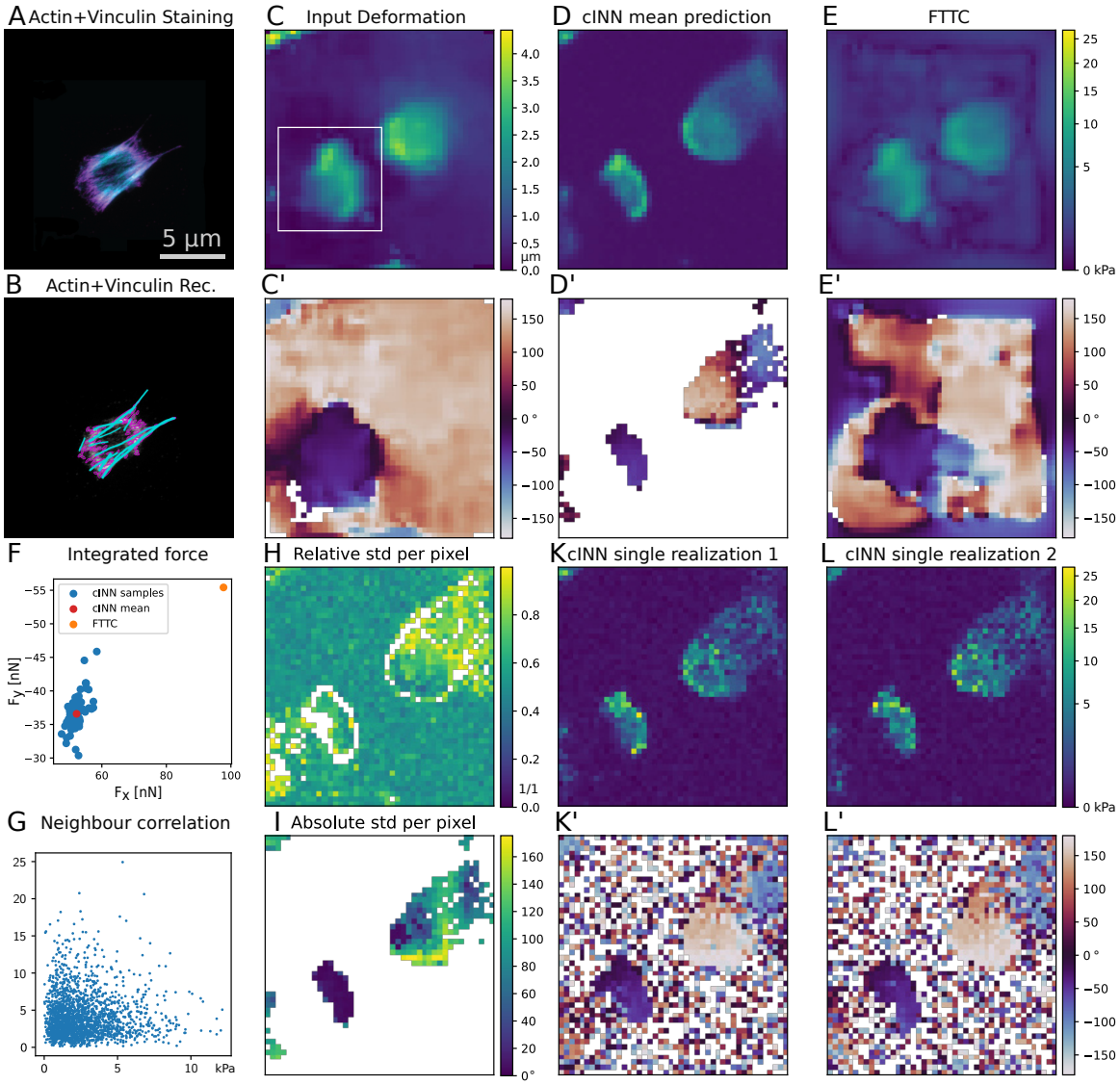

Figure 6.11: Traction force reconstruction for a thrombocyte. The plots marked X' (where X is a letter) display the orientation of the corresponding magnitude plot X. (A) Super-resolution STED-imaging; actin in cyan and vinculin in magenta. (B) Reconstruction of stress fibers and adhesions. Details can be found in the appendix, section B.3 (C, C') Substrate deformation field, magnitude and orientation, the white square indicates the force integration area. (D,D') cINN reconstruction averaged over multiple traction realizations. (E, E') FTTC reconstruction of the cell traction. (F) Integrated force in the integration area for different realizations, in comparison to the FTTC prediction. (G) Nearest neighbor correlation of traction magnitude reconstruction for to adjacent sampling points net to the point of maximal deformation. (H) Relative standard deviation of the reconstructed force magnitude. (I) Absolute standard deviation of the reconstructed force angle. (K,K') and (L,L') two individual cINN reconstructions. Data presented in manuscript 4.

D) we can see a relatively high uncertainty in each pixel within the cell in particular in the lower part of the adhesive area. This could be due to this area being in a region where the deformation contributions of all adhesons overlap making it more difficult to predict their exact location. When looking into the angular force distribution and taking into account the fact that the main axes of contraction are clearly observable, we see that both the FTTC reconstruction (Fig 6.10 E') as well as the reconstruction made by the cINN (Fig 6.10 F', G' and H') show close agreement with the orientation predicted by the orientation of the cardiomyocyte.

The results for a thrombocyte are shown in Fig 6.11, while some more examples can be found in the appendix, Fig C.4 and Fig C.5. In Fig 6.11A and B we first show the actin cytoskeletal structure and the locality of the adhesion sides and the present the deformation (Fig 6.11C and C'). As we can see, similar to the cardiomyocyte, the cINN (Fig 6.11D and D') was able to reconstruct the cell forces correctly and in a cleaner manner compared to FTTC (Fig 6.11E and E'). Interestingly, for this cell both FTTC and our cINN reconstruction predict a concentration of traction towards the lower end of the adhesive area, while predicting less force in the attachment of the two protrusions clearly visible in Fig 6.11 E. This, despite not being in the training set, correlates with the distribution of vinculin that is found predominantly along the two contractile lines. By looking into the standard deviation prediction (Fig 6.11 H and I), we find a high uncertainty being predicted in the upper right of our reconstruction. This indicates the difficulty of isolating the force contribution of the two protrusions and also correlates to the area where FTTC and cINN reconstructions are most different. The cINN here predicts an outward-facing traction, which is likely due to the presence of another cell in the vicinity.

When looking into the reconstructed force magnitude (Fig 6.11 F), which is integrated over the lower contractile area, we can see that the cINN makes a more conservative estimate of the traction but agrees with the FTTC concerning the overall force orientation. Like in the case of synthetic data, we can also find a correlation between neighboring sampling points (Fig 6.11 G), again confirming the notion of our network successfully recognizing areal force distribution more precisely than force magnitudes at a selected sampling point.

When looking into two individual realizations of the traction field as predicted by the cINN (Fig 6.11 K,K' and L,L') we notice the presence of multiple more or less equally distributed peaks in the traction distribution along the nucleus-facing edge of the adhesive area. These might represent individual focal adhesions. As seen in the analysis of the synthetic dataset, these fine structures are highly dependent on noise and can therefore not be seen in the averaged prediction (Fig 6.11 C and C').

6.7 Conclusion

In this part of my work, I successfully explored the ability of a generative NN approach, cINNs, to study the degeneracy of the inverse problem of traction force reconstructions. I showed that a force prediction network, even though trained using a rather abstract way for obtaining synthetic data, was able to return highly plausible traction reconstructions for experimental data showing a good generalization ability of the underlying reconstruction. I was able to demonstrate that due to noise, the traction force reconstruction is not unique on the scale of individual sampling points, but reliable and correlated on slightly longer length scales. Speculative interpretations even suggest that cINN-based methods could make out and detect smaller scale structures than possible using the standard Fourier-based technique. In addition, unlike the Fourier-based method and other established techniques, cINN-based TFM, is able to give a spatially resolved estimate of its force predictions, which can be used to more reliably judge the statistical relevance of observed differences in force distribution. Overall, these benefits are paving the way for deeper insights into cellular mechanics and behavior on a micro-scale.

Chapter 7

Summary and Outlook

By observing adhesive forces, cells exert on their environment, many insights into cellular mechanics can be obtained. In traction force microscopy these observations are made possible by a good understanding of the mechanics of the specifically designed extracellular environment, the fluorescent bead sprinkled elastic substrate used in this context. In this dissertation, I have used analytical calculations, numerical methods, neural networks and the results of experimental observations obtained in cooperation with my collaborators to gain a deeper understanding in how substrates respond to specific mechanical stimuli and how the cell's traction forces can be reconstructed from observable substrate deformations. In the process, these new predictions have helped to further understanding of processes like endocytosis or stress fiber dynamics in thrombocytes and fibroblasts.

In Chapter 2 I've laid down and collected the analytical insights traction reconstructions are based on. This essential step introduced many recurring concepts and gave a solid foundation of individual techniques I could build up on. In particular, we have shown how a diverse range of linear elasticity problems can be solved by separating them into elementary problems and using potential approaches to solve them.

In Chapter 3, I have made use of the potential approach introduced previously to derive a full solution of the Greens function in Fourier space. This allowed me to extend the well-established 2D regularized FTTC method into a 2.5D method which also considers normal forces. By doing so, I could successfully keep the procedure known from 2D, including the fast and reliable Fourier based reconstruction and the concept of using a generalized cross validation to find an optimal zero-order Tikhonov regularization parameter. I then applied this new method to experiments studying the effect of traction forces in the formation of AP2 clusters, an initial stage in the process of endocytosis. This allowed me to study the mechanics of endocytosis of nanoparticles of cells on their ventral side and gave the result that normal pressure exerted by the cell onto the substrate correlates with the formation of AP2 clusters. In the future, it would be interesting to integrate this method into more external processes to gain more insight into the three-dimensional nature of cellular force generation.

In Chapter 4, I have first introduced the direct method of traction force microscopy and compared how it performed when challenged with reconstructing traction from a dataset. in which the deformation field has been perturbed by Gaussian noise. I showed how a robust gradient scheme could successfully make the force reconstruction highly resilient, when tasked with the reconstruction of noised data. I directly

compared the performance of the direct method with the 2.5D FTTC method as a representative for inverse methods in general. I was able to demonstrate that FTTC works best if only tangential forces are reconstructed. I also showed that 2.5D FTTC is more precise for small noise, but that the performance of the direct method approaches the one of 2.5D FTTC for larger noise, before both fail for very large noise. Moreover, I found that mechanically tackling noise in the direct method by means of a divergence correction is not really needed. I was also able to show that the direct method profits more from increased resolution than the inverse method. In the future, the direct method might thus become more relevant due to several experimental developments: Image quality for TFM quickly improves, e.g. due to super-resolution microscopy [69, 71–73, 75], and this might play in favor of the direct method, which improves with smaller sampling distance. On the other hand, recent advances in microfabrication and additive manufacturing will lead to completely new geometries and setups [150–153], for which the analytical solutions required for methods like FTTC will not be possible anymore, except for simple geometries like elastic beads [64, 154]. Here, the direct method would provide a computationally attractive alternative to the currently dominating FEM-environments.

In Chapter 5, I have introduced the adaptive near field method. It allowed us to make quantitative predictions of location and force transmission via individual adhesion sides by observing only the areal contour of the deformation field. The applicability of our method has been proven experimentally for monitoring the change in cellular traction forces at specific adhesion sites, which occur when shearing fibroblasts off their underlying PAA substrates. By doing so, together with my collaborators, we could prove that force transmission can be long ranged and the shear force is not distributed uniformly among the cell's adhesion sites. This finding could potentially be explained by the polymeric nature of the cytoskeletal network. In the future, this technique could be combined with imaging of the cytoskeleton to directly correlate traction predictions with intracellular force transition or with micropatterning to control the area of adhesion more precisely thus improving the predictability of forces. Due to its areal nature, like the direct method, the adaptive near field approach could also prove to be an attractive technique for setups, where the planar nature can only be assumed locally, like in setups with completely new, less planar geometries.

Finally, in Chapter 6, I successfully explored the potential of using a cINN for traction reconstruction in TFM. By describing a method to generate a large amount of synthetic training data, I was able to predict not only the distribution of cell forces, but was also able to make estimates about the reliability of force predictions. My study showcases the potential of using a cINN in solving the inverse problem of mechanical traction of cells on surfaces. This neural network-based approach offers improved accuracy and more detailed force reconstructions compared to traditional FTTC methods as well as statistical estimates about the uncertainty of the force reconstruction. This paves the way for deeper insights into cellular mechanics and behavior on a micro-scale. In the future, I predict that traction force reconstructions can be improved by advances in the generation of experimental data, potentially by using machine learning processes in this setup itself or by including more information about the experimental structures. This could potentially even lead to the ability to not only predict areal traction distribution but the placement strength and shape of individual focal adhesions. In addition, newly devised analytics may better leverage the available statistical information on the variability in force generation to make more

statistically sound quantitative predictions about cellular effects resulting in deeper insights into the effects of different factors of the force reconstruction.

Summing up, this dissertation contributes to our understanding of the facets of traction force manifestation, enhancing our ability to make educated decisions on how experimental setups and evaluation techniques need to be designed to give reliable predictions and enable researches to also specify the experimental accuracy more precisely.

List of Publications

The following lists contains all manuscripts that have been prepared and submitted during the course of this theses. Only the content of three of the published manuscripts has been discussed in this dissertation, because the other ones predominantly focused on the applications of preexisting techniques. This should yield a focused monography. The other two are only mentioned in this thesis.

1.	**J. W. Blumberg** and U. S. Schwarz. **Comparison of direct and inverse methods for 2.5d traction force microscopy.** *PLOS ONE* 17(1):1–25, (2022). doi:10.1371/journal.pone.0262773	Chapter 3 Chapter 4
2.	J. Christian, **J. W. Blumberg**, D. Probst, C. Lo Giudice, S. Sindt, C. Selhuber-Unkel, U. S. Schwarz, and E. A. Cavalcanti-Adam. **Control of Cell Adhesion using Hydrogel Patterning Techniques for Applications in Traction Force Microscopy.** *J. Vis. Exp.* 179, e63121, (2022). doi:10.3791/63121	Introduction Chapter 3 (Mentioned)
3.	S. Huth, **J. W. Blumberg**, D. Probst, J. Lammerding, U. S. Schwarz, and C. Selhuber-Unkel. **Quantifying force transmission through fibroblasts: changes of traction forces under external shearing.** *Eur Biophys J* 51, 157–169 (2022). doi:10.1007/s00249-021-01576-8	Chapter 5
4.	A. Zelená*, **J. Blumberg***, D. Probst, R. Gerasimaitė, G. Lukinavičius, U. S. Schwarz, S. Köster **Force generation in human blood platelets by filamentous actomyosin structures** *In-press at Biophysical Journal* (2023). doi:10.1016/j.bpj.2023.07.010 * Contributed equally	Chapter 6 (Partially)
5.	J. L. Voigt, J. Timmer, F. Pennarola, J. Christian, N. Meng, **J. W. Blumberg**, U. S. Schwarz, D. Grimm and E. A. Cavalcanti-Adam. **Substrate stiffness regulates cellular uptake of nanoparticles and viruses from the ventral side.** *Accepted for Advanced Functional Materials* (2023).	Chapter 3 (Mentioned)
6.	**J. W. Blumberg**, F. Draxler, C. Goß, V. Kuhn, A. Zelená, S. Köster , U. Köhte, U. S. Schwarz. **Uncertainty aware cell force reconstruction with Conditional Invertible Neural Networks** *In preparation.*	Chapter 5

Bibliography

[1] Erwin Schrödinger. *What is Life? The Physical Aspect of the Living Cell*. Cambridge University Press, 1944.

[2] Kenneth M. Yamada and Michael Sixt. Mechanisms of 3d cell migration. *Nature Reviews Molecular Cell Biology*, 20(12):738–752, October 2019. doi:10.1038/s41580-019-0172-9.

[3] Farah Mustapha, Kheya Sengupta, and Pierre-Henri Puech. May the force be with your (immune) cells: an introduction to traction force microscopy in immunology. *Frontiers in Immunology*, 13, July 2022. doi:10.3389/fimmu.2022.898558.

[4] Fabiana Martino, Ana R. Perestrelo, Vladimír Vinarský, Stefania Pagliari, and Giancarlo Forte. Cellular mechanotransduction: From tension to function. *Frontiers in Physiology*, 9, July 2018. doi:10.3389/fphys.2018.00824.

[5] Nader Jalili and Karthik Laxminarayana. A review of atomic force microscopy imaging systems: application to molecular metrology and biological sciences. *Mechatronics*, 14(8):907–945, October 2004. doi:10.1016/j.mechatronics.2004.04.005.

[6] Christine Gourier, Antoine Jegou, Julien Husson, and Frédéric Pincet. A nanospring named erythrocyte. the biomembrane force probe. *Cellular and Molecular Bioengineering*, 1(4):263–275, November 2008. doi:10.1007/s12195-008-0030-x.

[7] Florian Hörner, Robert Meissner, Sruthi Polali, Jana Pfeiffer, Timo Betz, Cornelia Denz, and Erez Raz. Holographic optical tweezers-based in vivo manipulations in zebrafish embryos. *Journal of Biophotonics*, 10(11):1492–1501, February 2017. doi:10.1002/jbio.201600226.

[8] M. Dembo, T. Oliver, A. Ishihara, and K. Jacobson. Imaging the traction stresses exerted by locomoting cells with the elastic substratum method. *Biophysical Journal*, 70(4):2008–2022, April 1996. doi:10.1016/s0006-3495(96)79767-9.

[9] Albert K. Harris, Patricia Wild, and David Stopak. Silicone rubber substrata: a new wrinkle in the study of cell locomotion. *Science*, 208(4440):177–179, 1980. ISSN 0036-8075. doi:10.1126/science.6987736.

[10] Micah Dembo and Yu-Li Wang. Stresses at the cell-to-substrate interface during locomotion of fibroblasts. *Biophysical Journal*, 76(4):2307–2316, April 1999. doi:10.1016/s0006-3495(99)77386-8.

[11] U.S. Schwarz, N.Q. Balaban, D. Riveline, A. Bershadsky, B. Geiger, and S.A. Safran. Calculation of forces at focal adhesions from elastic substrate data: The effect of localized force and the need for regularization. *Biophysical Journal*, 83 (3):1380–1394, September 2002. doi:10.1016/s0006-3495(02)73909-x.

[12] James P. Butler, Iva Marija Tolić-Nørrelykke, Ben Fabry, and Jeffrey J. Fredberg. Traction fields, moments, and strain energy that cells exert on their surroundings. *American Journal of Physiology-Cell Physiology*, 282(3):C595–C605, March 2002. doi:10.1152/ajpcell.00270.2001.

[13] Jérôme R. D. Soiné, Christoph A. Brand, Jonathan Stricker, Patrick W. Oakes, Margaret L. Gardel, and Ulrich S. Schwarz. Model-based traction force microscopy reveals differential tension in cellular actin bundles. *PLoS Computational Biology*, 11(3):e1004076, March 2015. doi:10.1371/journal.pcbi.1004076.

[14] Yunfei Huang, Christoph Schell, Tobias B. Huber, Ahmet Nihat Şimşek, Nils Hersch, Rudolf Merkel, Gerhard Gompper, and Benedikt Sabass. Traction force microscopy with optimized regularization and automated bayesian parameter selection for comparing cells. *Scientific Reports*, 9(1), January 2019. doi:10.1038/s41598-018-36896-x.

[15] Stacey A. Maskarinec, Christian Franck, David A. Tirrell, and Guruswami Ravichandran. Quantifying cellular traction forces in three dimensions. *Proceedings of the National Academy of Sciences*, 106(52):22108–22113, December 2009. doi:10.1073/pnas.0904565106.

[16] Christian Franck, Stacey A. Maskarinec, David A. Tirrell, and Guruswami Ravichandran. Three-dimensional traction force microscopy: A new tool for quantifying cell-matrix interactions. *PLoS ONE*, 6(3):e17833, March 2011. doi:10.1371/journal.pone.0017833.

[17] Jennet Toyjanova, Eyal Bar-Kochba, Cristina López-Fagundo, Jonathan Reichner, Diane Hoffman-Kim, and Christian Franck. High resolution, large deformation 3d traction force microscopy. *PLoS ONE*, 9(4):e90976, April 2014. doi:10.1371/journal.pone.0090976.

[18] Juan C. del Álamo, Ruedi Meili, Begoña Álvarez-González, Baldomero Alonso-Latorre, Effie Bastounis, Richard Firtel, and Juan C. Lasheras. Three-dimensional quantification of cellular traction forces and mechanosensing of thin substrata by fourier traction force microscopy. *PLoS ONE*, 8(9):e69850, September 2013. doi:10.1371/journal.pone.0069850.

[19] Toshio Ando, Satya Prathyusha Bhamidimarri, Niklas Brending, H Colin-York, Lucy Collinson, Niels De Jonge, PJ De Pablo, Elke Debroye, Christian Eggeling, Christian Franck, et al. The 2018 correlative microscopy techniques roadmap. *Journal of physics D: Applied Physics*, 51(44):443001, 2018. doi:10.1088/1361-6463/aad055.

[20] Jeffrey A. Mulligan, François Bordeleau, Cynthia A. Reinhart-King, and Steven G. Adie. Traction Force Microscopy for Noninvasive Imaging of Cell Forces. In Cheng Dong, Nastaran Zahir, and Konstantinos Konstantopoulos,

editors, *Biomechanics in Oncology*, Advances in Experimental Medicine and Biology, pages 319–349. Springer International Publishing, Cham, 2018. ISBN 978-3-319-95294-9. doi:10.1007/978-3-319-95294-9_15.

[21] Wesley R Legant, Jordan S Miller, Brandon L Blakely, Daniel M Cohen, Guy M Genin, and Christopher S Chen. Measurement of mechanical tractions exerted by cells in three-dimensional matrices. *Nature Methods*, 7(12):969, 2010. doi:10.1038/nmeth.1531.

[22] Julian Steinwachs, Claus Metzner, Kai Skodzek, Nadine Lang, Ingo Thievessen, Christoph Mark, Stefan Münster, Katerina E Aifantis, and Ben Fabry. Three-dimensional force microscopy of cells in biopolymer networks. *Nature Methods*, 13(2):171–176, 2016. doi:10.1038/nmeth.3685.

[23] Yu li Wang and Yun-Chu Lin. Traction force microscopy by deep learning. *Biophysical Journal*, 120(15):3079–3090, 2021. ISSN 0006-3495. doi:10.1016/j.bpj.2021.06.011.

[24] Felix S. Kratz and Jan Kierfeld. Pendant drop tensiometry: A machine learning approach. *The Journal of Chemical Physics*, 153(9):094102, September 2020. doi:10.1063/5.0018814.

[25] Matthew S. Schmitt, Jonathan Colen, Stefano Sala, John Devany, Shailaja Seetharaman, Margaret L. Gardel, Patrick W. Oakes, and Vincenzo Vitelli. Zyxin is all you need: machine learning adherent cell mechanics, 2023.

[26] Xiaocen Duan and Jianyong Huang. Deep-learning-based 3d cellular force reconstruction directly from volumetric images. *Biophysical Journal*, 121(11): 2180–2192, 2022. ISSN 0006-3495. doi:doi.org/10.1016/j.bpj.2022.04.028.

[27] Florian Huber, Adeline Boire, Magdalena Preciado López, and Gijsje H Koenderink. Cytoskeletal crosstalk: when three different personalities team up. *Current Opinion in Cell Biology*, 32:39–47, February 2015. doi:10.1016/j.ceb.2014.10.005.

[28] Bruce Alberts, Alexander Johnson, Julian Lewis, David Morgan, Martin Raff, Keith Roberts, and Peter Walter. *Molecular Biology of the Cell*. Garland Science, 2017.

[29] W. K. Purves, D. Sadava, G. H. Orians, H. C. Heller, and W. H. Freeman. *Life: the science of biology*. W.H. Freeman, New York, NY, 7 edition, December 2003.

[30] R. Phillips, J. Kondev, J. Theriot, and H. Garcia. *Physical Biology of the Cell*. CRC Press, 2012. ISBN 9781134111589.

[31] M. Rubinstein and R.H. Colby. *Polymer Physics*. Oxford University Press, 2003. ISBN 9781613449431.

[32] Tetsuya Horio and Takashi Murata. The role of dynamic instability in microtubule organization. *Frontiers in Plant Science*, 5, 2014. ISSN 1664-462X. doi:10.3389/fpls.2014.00511.

[33] Anna Akhmanova and Lukas C. Kapitein. Mechanisms of microtubule organization in differentiated animal cells. *Nature Reviews Molecular Cell Biology*, 23 (8):541–558, April 2022. doi:10.1038/s41580-022-00473-y.

[34] Satish Bodakuntla, A.S. Jijumon, Cristopher Villablanca, Christian Gonzalez-Billault, and Carsten Janke. Microtubule-associated proteins: Structuring the cytoskeleton. *Trends in Cell Biology*, 29(10):804–819, 2019. ISSN 0962-8924. doi:10.1016/j.tcb.2019.07.004.

[35] Qi Wen and Paul A. Janmey. Polymer physics of the cytoskeleton. *Current Opinion in Solid State and Materials Science*, 15(5):177–182, October 2011. doi:10.1016/j.cossms.2011.05.002.

[36] Geoffrey M Cooper. *The Cell: A Molecular Approach. 2nd editon*, chapter Structure and Organization of Actin Filaments. Sinauer Associates, 2000.

[37] Laurent Blanchoin, Rajaa Boujemaa-Paterski, Cécile Sykes, and Julie Plastino. Actin dynamics, architecture, and mechanics in cell motility. *Physiological Reviews*, 94(1):235–263, 2014. doi:10.1152/physrev.00018.2013. PMID: 24382887.

[38] Pirta Hotulainen and Pekka Lappalainen. Stress fibers are generated by two distinct actin assembly mechanisms in motile cells. *Journal of Cell Biology*, 173 (3):383–394, May 2006. doi:10.1083/jcb.200511093.

[39] Markus Bender and Raghavendra Palankar. Platelet shape changes during thrombus formation: Role of actin-based protrusions. *Hämostaseologie*, 41(01): 014–021, February 2021. doi:10.1055/a-1325-0993.

[40] Brian T. Helfand, Lynne Chang, and Robert D. Goldman. Intermediate filaments are dynamic and motile elements of cellular architecture. *Journal of Cell Science*, 117(2):133–141, January 2004. doi:10.1242/jcs.00936.

[41] Miguel Vicente-Manzanares, Xuefei Ma, Robert S. Adelstein, and Alan Rick Horwitz. Non-muscle myosin II takes centre stage in cell adhesion and migration. *Nature Reviews Molecular Cell Biology*, 10(11):778–790, November 2009. doi:10.1038/nrm2786.

[42] Sarah F. Wulf, Virginie Ropars, Setsuko Fujita-Becker, Marco Oster, Goetz Hofhaus, Leonardo G. Trabuco, Olena Pylypenko, H. Lee Sweeney, Anne M. Houdusse, and Rasmus R. Schröder. Force-producing ADP state of myosin bound to actin. *Proceedings of the National Academy of Sciences*, 113(13), March 2016. doi:10.1073/pnas.1516598113.

[43] Allison L. Berrier and Kenneth M. Yamada. Cell–matrix adhesion. *Journal of Cellular Physiology*, 213(3):565–573, 2007. doi:10.1002/jcp.21237.

[44] Christian Frantz, Kathleen M. Stewart, and Valerie M. Weaver. The extracellular matrix at a glance. *Journal of Cell Science*, 123(24):4195–4200, 12 2010. ISSN 0021-9533. doi:10.1242/jcs.023820.

[45] B. Geiger and K. M. Yamada. Molecular architecture and function of matrix adhesions. *Cold Spring Harbor Perspectives in Biology*, 3(5):a005033–a005033, March 2011. doi:10.1101/cshperspect.a005033.

[46] Edna Cukierman, Roumen Pankov, Daron R. Stevens, and Kenneth M. Yamada. Taking cell-matrix adhesions to the third dimension. *Science*, 294(5547):1708–1712, November 2001. doi:10.1126/science.1064829.

[47] Andrea Zancla, Pamela Mozetic, Monica Orsini, Giancarlo Forte, and Alberto Rainer. A primer to traction force microscopy. *Journal of Biological Chemistry*, 298(5):101867, May 2022. doi:10.1016/j.jbc.2022.101867.

[48] Xavier Trepat, Michael R. Wasserman, Thomas E. Angelini, Emil Millet, David A. Weitz, James P. Butler, and Jeffrey J. Fredberg. Physical forces during collective cell migration. *Nature Physics*, 5(6):426–430, May 2009. doi:10.1038/nphys1269.

[49] Claude N. Holenstein, Unai Silvan, and Jess G. Snedeker. High-resolution traction force microscopy on small focal adhesions - improved accuracy through optimal marker distribution and optical flow tracking. *Scientific Reports*, 7(1), February 2017. doi:10.1038/srep41633.

[50] Jana Hanke, Dimitri Probst, Assaf Zemel, Ulrich S. Schwarz, and Sarah Köster. Dynamics of force generation by spreading platelets. *Soft Matter*, 14(31):6571–6581, 2018. doi:10.1039/c8sm00895g.

[51] Constance Oliver and Maria Célia Jamur. *Immunocytochemical methods and protocols*, chapter Permeabilization of Cell Membranes, page 63–66. Humana Press, 2010.

[52] Robert W. Style, Rostislav Boltyanskiy, Guy K. German, Callen Hyland, Christopher W. MacMinn, Aaron F. Mertz, Larry A. Wilen, Ye Xu, and Eric R. Dufresne. Traction force microscopy in physics and biology. *Soft Matter*, 10(23):4047, 2014. doi:10.1039/c4sm00264d.

[53] Francesco Silvio Pasqualini, Ashutosh Agarwal, Blakely Bussie O'Connor, Qihan Liu, Sean P. Sheehy, and Kevin Kit Parker. Traction force microscopy of engineered cardiac tissues. *PLOS ONE*, 13(3):e0194706, March 2018. doi:10.1371/journal.pone.0194706.

[54] Nathalie Q Balaban, Ulrich S Schwarz, Daniel Riveline, Polina Goichberg, Gila Tzur, Ilana Sabanay, Diana Mahalu, Sam Safran, Alexander Bershadsky, Lia Addadi, and Benjamin Geiger. Force and focal adhesion assembly: a close relationship studied using elastic micropatterned substrates. *Nature Cell Biology*, 3 (May):466–472, 2001. doi:10.1038/35074532.

[55] Martin Bergert, Tobias Lendenmann, Manuel Zündel, Alexander E. Ehret, Daniele Panozzo, Patrizia Richner, David K. Kim, Stephan J. P. Kress, David J. Norris, Olga Sorkine-Hornung, Edoardo Mazza, Dimos Poulikakos, and Aldo Ferrari. Confocal reference free traction force microscopy. *Nature Communications*, 7(1), September 2016. doi:10.1038/ncomms12814.

[56] Dhananjay T Tambe, Ugo Croutelle, Xavier Trepat, Chan Young Park, Jae Hun Kim, Emil Millet, James P Butler, and Jeffrey J Fredberg. Monolayer stress microscopy: limitations, artifacts, and accuracy of recovered intercellular stresses. *PLoS ONE*, 8(2):e55172, 2013. doi:10.1371/journal.pone.0055172.

[57] Mei Rosa Ng, Achim Besser, Joan S Brugge, and Gaudenz Danuser. Mapping the dynamics of force transduction at cell–cell junctions of epithelial clusters. *eLife*, 3:e03282, 2014. ISSN 2050-084X. doi:10.7554/eLife.03282.

[58] Ricardo Serrano, Aereas Aung, Yi-Ting Yeh, Shyni Varghese, Juan C. Lasheras, and Juan C. del Álamo. Three-dimensional monolayer stress microscopy. *Biophysical Journal*, 117(1):111–128, July 2019. doi:10.1016/j.bpj.2019.03.041.

[59] Andreas Bauer, Magdalena Prechová, Martin Gregor, and Ben Fabry. pyTFM: A tool for Traction Force and Monolayer Stress Microscopy. *bioRxiv*, page 2020.09.28.316430, September 2020. doi:10.1101/2020.09.28.316430. Publisher: Cold Spring Harbor Laboratory Section: New Results.

[60] Hélène Delanoë-Ayari, Tetsuya Hiraiwa, Philippe Marcq, Jean-Paul Rieu, and Thuan Beng Saw. 2.5d traction force microscopy: Imaging three-dimensional cell forces at interfaces and biological applications. *The International Journal of Biochemistry & Cell Biology*, 161:106432, August 2023. doi:10.1016/j.biocel.2023.106432.

[61] Wesley R. Legant, Colin K. Choi, Jordan S. Miller, Lin Shao, Liang Gao, Eric Betzig, and Christopher S. Chen. Multidimensional traction force microscopy reveals out-of-plane rotational moments about focal adhesions. *Proceedings of the National Academy of Sciences*, 110(3):881–886, December 2012. doi:10.1073/pnas.1207997110.

[62] Hendrik Schürmann, Fatemeh Abbasi, Antonella Russo, Arne D. Hofemeier, Matthias Brandt, Johannes Roth, Thomas Vogl, and Timo Betz. Analysis of monocyte cell tractions in 2.5d reveals mesoscale mechanics of podosomes during substrate-indenting cell protrusion. *Journal of Cell Science*, 135(10), May 2022. doi:10.1242/jcs.259042.

[63] Erfan Mohagheghian, Junyu Luo, Junjian Chen, Gaurav Chaudhary, Junwei Chen, Jian Sun, Randy H. Ewoldt, and Ning Wang. Quantifying compressive forces between living cell layers and within tissues using elastic round microgels. *Nature Communications*, 9(1), May 2018. doi:10.1038/s41467-018-04245-1.

[64] Daan Vorselen, Yifan Wang, Miguel M. de Jesus, Pavak K. Shah, Matthew J. Footer, Morgan Huse, Wei Cai, and Julie A. Theriot. Superresolved microparticle traction force microscopy reveals subcellular force patterns in immune cell-target interactions. *bioRxiv*, 2019. doi:10.1101/431221.

[65] N. Träber, K. Uhlmann, S. Girardo, G. Kesavan, K. Wagner, J. Friedrichs, R. Goswami, K. Bai, M. Brand, C. Werner, D. Balzani, and J. Guck. Polyacrylamide bead sensors for in vivo quantification of cell-scale stress in zebrafish development. *Scientific Reports*, 9(1), November 2019. doi:10.1038/s41598-019-53425-6.

[66] Nina Parker, Mark Schneegurt, Anh-Hue Thi Tu, Brian M. Forster, and Philip Lister. *Microbiology*. OpenStax, Houston, Texas, 2017. ISBN 978-1-938-16814-7.

[67] Daniel Axelrod. Total internal reflection fluorescence microscopy in cell biology. *Traffic*, 2(11):764–774, November 2001. doi:10.1034/j.1600-0854.2001.21104.x.

[68] Edgar Gutierrez, Eugene Tkachenko, Achim Besser, Prithu Sundd, Klaus Ley, Gaudenz Danuser, Mark H. Ginsberg, and Alex Groisman. High refractive index silicone gels for simultaneous total internal reflection fluorescence and traction force microscopy of adherent cells. *PLoS ONE*, 6(9):e23807, September 2011. doi:10.1371/journal.pone.0023807.

[69] Huw Colin-York, Dilip Shrestha, James H. Felce, Dominic Waithe, Emad Moeendarbary, Simon J. Davis, Christian Eggeling, and Marco Fritzsche. Super-Resolved Traction Force Microscopy (STFM). *Nano Letters*, February 2016. ISSN 1530-6984. doi:10.1021/acs.nanolett.6b00273.

[70] Huw Colin-York, Christian Eggeling, and Marco Fritzsche. Dissection of mechanical force in living cells by super-resolved traction force microscopy. *Nature Protocols*, 12(4):783–796, April 2017. ISSN 1754-2189. doi:10.1038/nprot.2017.009.

[71] Huw Colin-York, Yousef Javanmardi, Liliana Barbieri, Di Li, Kseniya Korobchevskaya, Yuting Guo, Chloe Hall, Aaron Taylor, Satya Khuon, Graham K. Sheridan, Teng-Leong Chew, Dong Li, Emad Moeendarbary, and Marco Fritzsche. Spatiotemporally Super-Resolved Volumetric Traction Force Microscopy. *Nano Letters*, 19(7):4427–4434, July 2019. ISSN 1530-6984. doi:10.1021/acs.nanolett.9b01196. Publisher: American Chemical Society.

[72] Morteza Aramesh, Simon Mergenthal, Marcel Issler, Birgit Plochberger, Florian Weber, Xiao-Hua Qin, Robert Liska, Georg N. Duda, Johannes B. Huppa, Jonas Ries, Gerhard J. Schütz, and Enrico Klotzsch. Functionalized Bead Assay to Measure Three-dimensional Traction Forces during T-cell Activation. *Nano Letters*, 21(1):507–514, January 2021. ISSN 1530-6984. doi:10.1021/acs.nanolett.0c03964. Publisher: American Chemical Society.

[73] Aki Stubb, Romain F. Laine, Mitro Miihkinen, Hellyeh Hamidi, Camilo Guzmán, Ricardo Henriques, Guillaume Jacquemet, and Johanna Ivaska. Fluctuation-Based Super-Resolution Traction Force Microscopy. *Nano Letters*, 20(4):2230–2245, April 2020. ISSN 1530-6984. doi:10.1021/acs.nanolett.9b04083. Publisher: American Chemical Society.

[74] Liliana Barbieri, Huw Colin-York, Kseniya Korobchevskaya, Di Li, Deanna L. Wolfson, Narain Karedla, Falk Schneider, Balpreet S. Ahluwalia, Tore Seternes, Roy A. Dalmo, Michael L. Dustin, Dong Li, and Marco Fritzsche. Two-dimensional TIRF-SIM–traction force microscopy (2d TIRF-SIM-TFM). *Nature Communications*, 12(1), April 2021. doi:10.1038/s41467-021-22377-9.

[75] Di Li, Huw Colin-York, Liliana Barbieri, Yousef Javanmardi, Yuting Guo, Kseniya Korobchevskaya, Emad Moeendarbary, Dong Li, and Marco Fritzsche. Astigmatic traction force microscopy (aTFM). *Nature Communications*, 12(1): 2168, April 2021. ISSN 2041-1723. doi:10.1038/s41467-021-22376-w.

[76] Ulrich S. Schwarz and Jérôme R.D. Soiné. Traction force microscopy on soft elastic substrates: A guide to recent computational advances. *Biochimica et Biophysica Acta (BBA) - Molecular Cell Research*, 1853(11):3095–3104, November 2015. doi:10.1016/j.bbamcr.2015.05.028.

[77] Th. Dracos. *Particle Tracking Velocimetry (PTV)*, pages 155–160. Springer Netherlands, Dordrecht, 1996. ISBN 978-94-015-8727-3. doi:10.1007/978-94-015-8727-3_7.

[78] Denis Fortun, Patrick Bouthemy, and Charles Kervrann. Optical flow modeling and computation: A survey. *Computer Vision and Image Understanding*, 134: 1–21, May 2015. doi:10.1016/j.cviu.2015.02.008.

[79] C. E. Willert and M. Gharib. Digital particle image velocimetry. *Experiments in Fluids*, 10(4):181–193, January 1991. doi:10.1007/bf00190388.

[80] J Westerweel. Fundamentals of digital particle image velocimetry. *Measurement Science and Technology*, 8(12):1379–1392, December 1997. doi:10.1088/0957-0233/8/12/002.

[81] Markus Raffel, Christan E. Willert, and Jürgen Kompenhans. *Image evaluation methods for PIV*, pages 105–146. Springer Berlin Heidelberg, Berlin, Heidelberg, 1998. ISBN 978-3-662-03637-2. doi:10.1007/978-3-662-03637-2_5.

[82] T. C. Chu, W. F. Ranson, and M. A. Sutton. Applications of digital-image-correlation techniques to experimental mechanics. *Experimental Mechanics*, 25 (3):232–244, September 1985. doi:10.1007/bf02325092.

[83] B K Bay. Methods and applications of digital volume correlation. *The Journal of Strain Analysis for Engineering Design*, 43(8):745–760, 2008. doi:10.1243/03093247JSA436.

[84] A. Buljac, C. Jailin, A. Mendoza, J. Neggers, T. Taillandier-Thomas, A. Bouterf, B. Smaniotto, F. Hild, and S. Roux. Digital volume correlation: Review of progress and challenges. *Experimental Mechanics*, 58(5):661–708, June 2018. doi:10.1007/s11340-018-0390-7.

[85] E. Bar-Kochba, J. Toyjanova, E. Andrews, K.-S. Kim, and C. Franck. A fast iterative digital volume correlation algorithm for large deformations. *Experimental Mechanics*, 55(1):261–274, August 2014. doi:10.1007/s11340-014-9874-2.

[86] K D Hinsch. Holographic particle image velocimetry. *Measurement Science and Technology*, 13(7):R61–R72, June 2002. doi:10.1088/0957-0233/13/7/201.

[87] Eize J. Stamhuis. Basics and principles of particle image velocimetry (PIV) for mapping biogenic and biologically relevant flows. *Aquatic Ecology*, 40(4): 463–479, September 2006. doi:10.1007/s10452-005-6567-z.

[88] JP Lewis. Fast Normalized Cross-Correlation. *Vision Interface*, 10(1):120–123, 1995. URL `http://scribblethink.org/Work/nvisionInterface/nip.pdf`. Accessed on 2023-07-31.

[89] J. Nogueira, A. Lecuona, P. A. Rodríguez, J. A. Alfaro, and A. Acosta. Limits on the resolution of correlation PIV iterative methods. practical implementation and design of weighting functions. *Experiments in Fluids*, 39(2):314–321, July 2005. doi:10.1007/s00348-005-1017-1.

[90] L. Lourenco and A. Krothapalli. On the accuracy of velocity and vorticity measurements with PIV. *Experiments in Fluids*, 18(6):421–428, April 1995. doi:10.1007/bf00208464.

[91] Ronald J. Adrian and Jerry Westerweel. *Particle Image Velocimetry*. Cambridge University Press, Cambridge, 2011. ISBN 978-0-521-44008-0.

[92] Jerry Westerweel and Fulvio Scarano. Universal outlier detection for PIV data. *Experiments in Fluids*, 39(6):1096–1100, August 2005. doi:10.1007/s00348-005-0016-6.

[93] Zachary J. Taylor, Roi Gurka, Gregory A. Kopp, and Alex Liberzon. Long-duration time-resolved piv to study unsteady aerodynamics. *IEEE Transactions on Instrumentation and Measurement*, 59(12):3262–3269, December 2010. doi:10.1109/tim.2010.2047149.

[94] Bruce Lucas and Takeo Kanade. An iterative image registration technique with an application to stereo vision (ijcai). In *Proceedings of the 7th International Joint Conference on Artificial Intelligence (IJCAI 81)*, volume 81, 04 1981.

[95] Jianbo Shi and Tomasi. Good features to track. In *Proceedings of IEEE Conference on Computer Vision and Pattern Recognition CVPR-94*. IEEE Comput. Soc. Press, 1994. doi:10.1109/cvpr.1994.323794.

[96] Jean-Yves Bouguet. Pyramidal implementation of the affine lucas kanade feature tracker description of the algorithm, 2001. URL `http://robots.stanford.edu/cs223b04/algo_affine_tracking.pdf`. Accessed on 2023-07-31.

[97] Alvaro Jorge-Peñas, Alicia Izquierdo-Alvarez, Rocio Aguilar-Cuenca, Miguel Vicente-Manzanares, José Manuel Garcia-Aznar, Hans Van Oosterwyck, Elena M. de Juan-Pardo, Carlos Ortiz de Solorzano, and Arrate Muñoz-Barrutia. Free form deformation–based image registration improves accuracy of traction force microscopy. *PLoS ONE*, 10(12):e0144184, December 2015. doi:10.1371/journal.pone.0144184.

[98] J. A. Sanz-Herrera, J. Barrasa-Fano, M. Cóndor, and H. Van Oosterwyck. Inverse method based on 3D nonlinear physically constrained minimisation in the framework of traction force microscopy. *Soft Matter*, October 2021. ISSN 1744-6848. doi:10.1039/D0SM00789G. Publisher: The Royal Society of Chemistry.

[99] J. Barrasa-Fano, A. Shapeti, J. de Jong, A. Ranga, J.A. Sanz-Herrera, and H. Van Oosterwyck. Advanced in silico validation framework for three-dimensional traction force microscopy and application to an in vitro model of sprouting angiogenesis. *Acta Biomaterialia*, 126:326–338, May 2021. doi:10.1016/j.actbio.2021.03.014.

[100] Lev D. Landau and Evgenij M. Lifshitz. *Theory of elasticity*. Pergamon Press etc., Oxford etc., 2. impression edition, 1963.

[101] Benedikt Sabass, Margaret L. Gardel, Clare M. Waterman, and Ulrich S. Schwarz. High resolution traction force microscopy based on experimental and computational advances. *Biophysical Journal*, 94(1):207–220, January 2008. doi:10.1529/biophysj.107.113670.

[102] Yunfei Huang, Gerhard Gompper, and Benedikt Sabass. A bayesian traction force microscopy method with automated denoising in a user-friendly software package. *Computer Physics Communications*, 256:107313, 2020. doi:10.1016/j.cpc.2020.107313.

[103] Sung Sik Hur, Yihua Zhao, Yi-Shuan Li, Elliot Botvinick, and Shu Chien. Live cells exert 3-dimensional traction forces on their substrata. *Cellular and Molecular Bioengineering*, 2(3):425–436, August 2009. doi:10.1007/s12195-009-0082-6.

[104] Florian Rehfeldt, André E. X. Brown, Matthew Raab, Shenshen Cai, Allison L. Zajac, Assaf Zemel, and Dennis E. Discher. Hyaluronic acid matrices show matrix stiffness in 2d and 3d dictates cytoskeletal order and myosin-II phosphorylation within stem cells. *Integrative Biology*, 4(4):422, 2012. doi:10.1039/c2ib00150k.

[105] Thorsten M Koch, Stefan Münster, Navid Bonakdar, James P Butler, and Ben Fabry. 3d traction forces in cancer cell invasion. *PLoS ONE*, 7(3):e33476, 2012. doi:10.1371/journal.pone.0033476.

[106] Zhaochun Yang, Jeen-Shang Lin, Jianxin Chen, and James H-C. Wang. Determining substrate displacement and cell traction fields—a new approach. *Journal of Theoretical Biology*, 242(3):607–616, October 2006. doi:10.1016/j.jtbi.2006.05.005.

[107] Felix S. Kratz, Lars Möllerherm, and Jan Kierfeld. Enhancing robustness, precision and speed of traction force microscopy with machine learning. *bioRxiv*, 2023. doi:10.1101/2022.09.02.506331.

[108] Olaf Ronneberger, Philipp Fischer, and Thomas Brox. U-net: Convolutional networks for biomedical image segmentation. In *Lecture Notes in Computer Science*, pages 234–241. Springer International Publishing, 2015. doi:10.1007/978-3-319-24574-4_28.

[109] Changhao Li, Luyi Feng, Yang Jeong Park, Jian Yang, Ju Li, and Sulin Zhang. Machine learning traction force maps of cell monolayers, 2023.

[110] Dimitri Probst. *Continuum Modeling of Cell Contractility*. PhD thesis, Heidelberg University, Heidelberg, 2019.

[111] Nik Abdullah Nik Mohamed. *Introduction to Continuum Mechanics for Engineers*. Springer Nature Singapore, Singapore, 1st ed. 2023. edition, 2023. ISBN 978-981-9908-11-0. doi:10.1007/978-981-99-0811-0.

[112] Holm Altenbach. *Kontinuumsmechanik*. SpringerLink : Bücher. Springer Vieweg, Berlin, Heidelberg, 4. aufl. 2018 edition, 2018. ISBN 978-3-662-57504-8. doi:10.1007/978-3-662-57504-8.

[113] Peter Howell, Gregory Kozyreff, and John R. Ockendon. *Applied solid mechanics*. Cambridge texts in applied mathematics. Cambridge Univ. Press, Cambridge etc., 2009. ISBN 978-0-521-85489-4 and 978-0-521-67109-5. Includes index.

[114] A. E. H. Love. *A Treatise on the mathematical theory of elasticity*. Dover books on engineering and engineering physics. Dover Publ., New York, repr. 4. ed. edition, 1972. Repr. Ausg. d. Ausg. 1944.

[115] R.W. Ogden. *Non-Linear Elastic Deformations*. Dover Civil and Mechanical Engineering. Dover Publications, 2013. ISBN 9780486318714.

[116] Allan F Bower. *Applied mechanics of solids*. CRC Press, Boca Raton, FL, October 2009.

[117] Rong Long, Matthew S. Hall, Mingming Wu, and Chung-Yuen Hui. Effects of gel thickness on microscopic indentation measurements of gel modulus. *Biophysical Journal*, 101(3):643–650, August 2011. doi:10.1016/j.bpj.2011.06.049.

[118] Wang Liangguo and Lin Xiao. On the general expression of fredholm integral equations method in elasticity. *Acta Mechanica Sinica*, 4(2):138–145, may 1988. doi:10.1007/bf02487715.

[119] G. M. Hamilton and L. E. Goodman. The stress field created by a circular sliding contact. *Journal of Applied Mechanics*, 33(2):371–376, June 1966. doi:10.1115/1.3625051.

[120] Kenneth L. Johnson. *Contact Mechanics*. Cambridge University Press, 1985. doi:10.1017/CBO9781139171731.

[121] Eugene Jahnke and Fritz Emde. *Tables of functions*. Dover Publications, Mineola, NY, may 1986.

[122] Benedikt Rennekamp. Sparse regularization in traction force microscopy, July 2015. Bachelor's thesis.

[123] P. J. Vermeulen and K. L. Johnson. Contact of nonspherical elastic bodies transmitting tangential forces. *Journal of Applied Mechanics*, 31(2):338–340, June 1964. doi:10.1115/1.3629610.

[124] David L. Phillips. A technique for the numerical solution of certain integral equations of the first kind. *Journal of the ACM*, 9(1):84–97, January 1962. doi:10.1145/321105.321114.

[125] A. N. Tikhonov. Solution of incorrectly formulated problems and the regularization method. *Soviet Math. Dokl.*, 4:1035–1038, 1963.

[126] Sergey V. Plotnikov, Benedikt Sabass, Ulrich S. Schwarz, and Clare M. Waterman. High-resolution traction force microscopy. In *Methods in Cell Biology*, pages 367–394. Elsevier, 2014. doi:10.1016/b978-0-12-420138-5.00020-3.

[127] Robert Tibshirani. Regression shrinkage and selection via the lasso. *Journal of the Royal Statistical Society. Series B (Methodological)*, 58(1):267–288, 1996. ISSN 00359246. URL http://www.jstor.org/stable/2346178. Accessed on 2023-07-19.

[128] Sangyoon J Han, Youbean Oak, Alex Groisman, and Gaudenz Danuser. Traction microscopy to identify force modulation in subresolution adhesions. *Nature Methods*, 12(7):653–656, June 2015. doi:10.1038/nmeth.3430.

[129] Jonatan Bohr Brask, Guillem Singla-Buxarrais, Marina Uroz, Romaric Vincent, and Xavier Trepat. Compressed sensing traction force microscopy. *Acta Biomaterialia*, 26:286–294, October 2015. doi:10.1016/j.actbio.2015.08.023.

[130] Alejandro Suñé-Auñón, Alvaro Jorge-Peñas, Rocío Aguilar-Cuenca, Miguel Vicente-Manzanares, Hans Van Oosterwyck, and Arrate Muñoz-Barrutia. Full l1-regularized traction force microscopy over whole cells. *BMC Bioinformatics*, 18(1), August 2017. doi:10.1186/s12859-017-1771-0.

[131] Hui Zou and Trevor Hastie. Regularization and variable selection via the elastic net. *Journal of the Royal Statistical Society Series B: Statistical Methodology*, 67(2):301–320, March 2005. doi:10.1111/j.1467-9868.2005.00503.x.

[132] John W. Tukey. An introduction to the calculations of numerical spectrum analysis, 1967.

[133] Frank Bauer and Mark A. Lukas. Comparingparameter choice methods for regularization of ill-posed problems. *Mathematics and Computers in Simulation*, 81(9):1795–1841, May 2011. doi:10.1016/j.matcom.2011.01.016.

[134] Per Christian Hansen. Analysis of discrete ill-posed problems by means of the l-curve. *SIAM Review*, 34(4):561–580, December 1992. doi:10.1137/1034115.

[135] Ankur H. Kulkarni, Prasenjit Ghosh, Ashwin Seetharaman, Paturu Kondaiah, and Namrata Gundiah. Traction cytometry: regularization in the fourier approach and comparisons with finite element method. *Soft Matter*, 14(23):4687–4695, 2018. doi:10.1039/c7sm02214j.

[136] Christopher S. Withers and Saralees Nadarajah. log det a = tr log a. *International Journal of Mathematical Education in Science and Technology*, 41(8):1121–1124, December 2010. doi:10.1080/0020739x.2010.500700.

[137] P. C. Hansen, M. E. Kilmer, and R. H. Kjeldsen. Exploiting residual information in the parameter choice for discrete ill-posed problems. *BIT Numerical Mathematics*, 46(1):41–59, March 2006. doi:10.1007/s10543-006-0042-7.

[138] Gene H. Golub, Michael Heath, and Grace Wahba. Generalized cross-validation as a method for choosing a good ridge parameter. *Technometrics*, 21(2):215–223, May 1979. doi:10.1080/00401706.1979.10489751.

[139] Medhavi Vishwakarma, Jacopo Di Russo, Dimitri Probst, Ulrich S. Schwarz, Tamal Das, and Joachim P. Spatz. Mechanical interactions among followers determine the emergence of leaders in migrating epithelial cell collectives. *Nature Communications*, 9(1), 2018. ISSN 20411723. doi:10.1038/s41467-018-05927-6.

[140] Joel Christian. *Role of Traction Forces in Initiating Clathrin-Mediated Endocytosis of Nanoparticles at the Cellular Ventral Side*. PhD thesis, Heidelberg University, Heidelberg, 2022.

[141] Vincent F. Fiore, Matej Krajnc, Felipe Garcia Quiroz, John Levorse, H. Amalia Pasolli, Stanislav Y. Shvartsman, and Elaine Fuchs. Mechanics of a multilayer epithelium instruct tumour architecture and function. *Nature*, 585(7825):433–439, September 2020. doi:10.1038/s41586-020-2695-9.

[142] Naoya Yamaguchi, Ziyi Zhang, Teseo Schneider, Biran Wang, Daniele Panozzo, and Holger Knaut. Rear traction forces drive adherent tissue migration in vivo. *Nature Cell Biology*, 24(2):194–204, February 2022. doi:10.1038/s41556-022-00844-9.

[143] C. Franck, S. Hong, S. A. Maskarinec, D. A. Tirrell, and G. Ravichandran. Three-dimensional full-field measurements of large deformations in soft materials using confocal microscopy and digital volume correlation. *Experimental Mechanics*, 47(3):427–438, March 2007. doi:10.1007/s11340-007-9037-9.

[144] Jacqueline L. Wolf, Donald H. Rubin, Robert Finberg, Robert S. Kauffman, Arlene H. Sharpe, Jerry S. Trier, and Bernard N. Fields. Intestinal m cells: A pathway for entry of reovirus into the host. *Science*, 212(4493):471–472, April 1981. doi:10.1126/science.6259737.

[145] Qiong Wei, Changjin Huang, Yao Zhang, Tiankai Zhao, Peng Zhao, Peter Butler, and Sulin Zhang. Mechanotargeting: Mechanics-dependent cellular uptake of nanoparticles. *Advanced Materials*, 30(27):1707464, May 2018. doi:10.1002/adma.201707464.

[146] Marta Fratini, Tina Wiegand, Charlotta Funaya, Zhongxiang Jiang, Pranav N. M. Shah, Joachim P. Spatz, Elisabetta Ada Cavalcanti-Adam, and Steeve Boulant. Surface immobilization of viruses and nanoparticles elucidates early events in clathrin-mediated endocytosis. *ACS Infectious Diseases*, 4(11):1585–1600, September 2018. doi:10.1021/acsinfecdis.8b00134.

[147] Bohua Ding, Yongmei Tian, Yangang Pan, Yuping Shan, Mingjun Cai, Haijiao Xu, Yingchun Sun, and Hongda Wang. Recording the dynamic endocytosis of single gold nanoparticles by AFM-based force tracing. *Nanoscale*, 7(17):7545–7549, 2015. doi:10.1039/c5nr01020a.

[148] Bo-Ying Tsai, Jyun-Yu Chen, Arthur Chiou, and Yueh-Hsin Ping. Using optical tweezers to quantify the interaction force of dengue virus with host cellular receptors. *Microscopy and Microanalysis*, 21(S3):219–220, August 2015. doi:10.1017/s1431927615001890.

[149] Tina Wiegand, Marta Fratini, Felix Frey, Klaus Yserentant, Yang Liu, Eva Weber, Kornelia Galior, Julia Ohmes, Felix Braun, Dirk-Peter Herten, Steeve Boulant, Ulrich S. Schwarz, Khalid Salaita, E. Ada Cavalcanti-Adam, and Joachim P. Spatz. Forces during cellular uptake of viruses and nanoparticles at the ventral side. *Nature Communications*, 11(1), January 2020. doi:10.1038/s41467-019-13877-w.

[150] Franziska Klein, Benjamin Richter, Thomas Striebel, Clemens M Franz, Georg von Freymann, Martin Wegener, and Martin Bastmeyer. Two-component polymer scaffolds for controlled three-dimensional cell culture. *Advanced Materials*, 23(11):1341–1345, 2011. doi:10.1002/adma.201004060.

[151] Christoph A Brand, Marco Linke, Kai Weißenbruch, Benjamin Richter, Martin Bastmeyer, and Ulrich S Schwarz. Tension and elasticity contribute to fibroblast cell shape in three dimensions. *Biophysical Journal*, 113(4):770–774, 2017. doi:10.1016/j.bpj.2017.06.058.

[152] Marc Hippler, Enrico Domenico Lemma, Sarah Bertels, Eva Blasco, Christopher Barner-Kowollik, Martin Wegener, and Martin Bastmeyer. 3d scaffolds to study basic cell biology. *Advanced Materials*, page 1808110, February 2019. doi:10.1002/adma.201808110.

[153] Marc Hippler, Kai Weißenbruch, Kai Richler, Enrico D. Lemma, Masaki Nakahata, Benjamin Richter, Christopher Barner-Kowollik, Yoshinori Takashima, Akira Harada, Eva Blasco, Martin Wegener, Motomu Tanaka, and Martin Bastmeyer. Mechanical stimulation of single cells by reversible host-guest interactions in 3D microscaffolds. *Science Advances*, 6(39):eabc2648, September 2020. ISSN 2375-2548. doi:10.1126/sciadv.abc2648. Publisher: American Association for the Advancement of Science Section: Research Article.

[154] Yifan Wang, Xiaohan Zhang, and Wei Cai. Spherical harmonics method for computing the image stress due to a spherical void. *Journal of the Mechanics and Physics of Solids*, 126:151–167, May 2019. ISSN 0022-5096. doi:10.1016/j.jmps.2019.01.020.

[155] Samuel M. Song, Sandy Napel, Gary H. Glover, and Norbert J. Pelc. Noise reduction in three-dimensional phase-contrast MR velocity measurementsl. *Journal of Magnetic Resonance Imaging*, 3(4):587–596, July 1993. doi:10.1002/jmri.1880030407.

[156] Ross Vennell and Rick Beatson. A divergence-free spatial interpolator for large sparse velocity data sets. *Journal of geophysical research*, 114, 10 2009. doi:10.1029/2008JC004973.

[157] Charitha M. de Silva, Jimmy Philip, and Ivan Marusic. Minimization of divergence error in volumetric velocity measurements and implications for turbulence statistics. *Experiments in Fluids*, 54(7):1557, Jun 2013. ISSN 1432-1114. doi:10.1007/s00348-013-1557-8.

[158] ChengYue Wang, Qi Gao, RunJie Wei, Tian Li, and JinJun Wang. Weighted divergence correction scheme and its fast implementation. *Experiments in Fluids*, 58(5), April 2017. doi:10.1007/s00348-017-2307-0.

[159] Johannes Wolfram Blumberg. Using elasticity theory for novel approaches in traction force microscopy, June 2019. Master's thesis.

[160] Milton Abramowitz and Irene A. Stegun. *Handbook of Mathematical Functions with Formulas, Graphs, and Mathematical Tables*. U.S. Goverment Printing Office, 10 edition, 1964.

[161] Diana E Jaalouk and Jan Lammerding. Mechanotransduction gone awry. *Nature Reviews Molecular Cell Biology*, 10(1):63–73, 2009. ISSN 1471-0080. doi:10.1038/nrm2597.

[162] Nicoletta I. Petridou, Zoltán Spiró, and Carl Philipp Heisenberg. Multiscale force sensing in development. *Nature Cell Biology*, 19(6):581–588, 2017. ISSN 14764679. doi:10.1038/ncb3524.

[163] Tamal Das, Kai Safferling, Sebastian Rausch, Niels Grabe, Heike Boehm, and Joachim P. Spatz. A molecular mechanotransduction pathway regulates collective migration of epithelial cells. *Nature Cell Biology*, 17(3):276–287, 2015. ISSN 14764679. doi:10.1038/ncb3115.

[164] Laith F. Kadem, Michelle Holz, Kristine Grace Suana, Qian Li, Constanze Lamprecht, Rainer Herges, and Christine Selhuber-Unkel. Rapid Reversible Photoswitching of Integrin-Mediated Adhesion at the Single-Cell Level. *Advanced Materials*, 28(9):1799–1802, 2016. ISSN 15214095. doi:10.1002/adma.201504394.

[165] C Selhuber-Unkel, T Erdmann, M López-García, H Kessler, U S Schwarz, and J P Spatz. Cell adhesion strength is controlled by intermolecular spacing of adhesion receptors. *Biophysical Journal*, 98(4):543–551, feb 2010. ISSN 1542-0086. doi:10.1016/j.bpj.2009.11.001.

[166] Steven Huth, Julia F Reverey, Matthias Leippe, and Christine Selhuber-Unkel. Adhesion forces and mechanics in mannose-mediated acanthamoeba interactions. *PLOS ONE*, 12(5):e0176207, may 2017. doi:10.1371/journal.pone.0176207.

[167] Claudia A. Brunner, Allen Ehrlicher, Bernd Kohlstrunk, Detlef Knebel, Josef A. Käs, and Michael Goegler. Cell migration through small gaps. *European Biophysics Journal*, 35(8):713–719, 2006. ISSN 01757571. doi:10.1007/s00249-006-0079-1.

[168] Peter F Davies. Flow-mediated endothelial mechanotransduction. *Physiological reviews*, 75(3):519–560, 1995. doi:10.1152/physrev.1995.75.3.519.

[169] Cecile M. Perrault, Agusti Brugues, Elsa Bazellieres, Pierre Ricco, Damien Lacroix, and Xavier Trepat. Traction Forces of Endothelial Cells under Slow Shear Flow. *Biophysical Journal*, 109(8):1533–1536, October 2015. ISSN 0006-3495. doi:10.1016/j.bpj.2015.08.036.

[170] Jana Hanke, Christiane Ranke, Eleonora Perego, and Sarah Köster. Human blood platelets contract in perpendicular direction to shear flow. *Soft matter*, 15(9):2009–2019, 2019.

[171] Matthias Rief, Filipp Oesterhelt, Berthold Heymann, and Hermann E Gaub. Single Molecule Force Spectroscopy on Polysaccharides by Atomic Force Microscopy. *Science*, 275(5304):1295 LP – 1297, feb 1997. doi:10.1126/science.275.5304.1295.

[172] Keir C Neuman and Attila Nagy. Single-molecule force spectroscopy: optical tweezers, magnetic tweezers and atomic force microscopy. *Nature Methods*, 5 (6):491–505, 2008. ISSN 1548-7105. doi:10.1038/nmeth.1218.

[173] Guoying Jiang, Grégory Giannone, David R Critchley, Emiko Fukumoto, and Michael P Sheetz. Two-piconewton slip bond between fibronectin and the cytoskeleton depends on talin. *Nature*, 424(6946):334–337, 2003. ISSN 1476-4687. doi:10.1038/nature01805.

[174] Pere Roca-Cusachs, Vito Conte, and Xavier Trepat. Quantifying forces in cell biology. *Nature Cell Biology*, 19(7):742 – 751, 2017. ISSN 14764679. doi:10.1038/ncb3564.

[175] Gregory Fedorchak and Jan Lammerding. Cell Microharpooning to Study Nucleo-Cytoskeletal Coupling. In Sue Shackleton, Philippe Collas, and Eric C. Schirmer, editors, *The Nuclear Envelope: Methods and Protocols*, chapter 16, pages 241–254. Springer Science+Business Media New York, New York, 2016.

[176] D. Riveline, E. Zamir, N. Q. Balaban, U. S. Schwarz, T. Ishizaki, S. Narumiya, Z. Kam, B. Geiger, and a. D. Bershadsky. Focal Contacts as Mechanosensors: Externally Applied Local Mechanical Force Induces Growth of Focal Contacts by an Mdia1-Dependent and Rock-Independent Mechanism. *Journal of Cell Biology*, 153(6):1175–1186, jun 2001. ISSN 0021-9525. doi:10.1083/jcb.153.6.1175.

[177] Raja Paul, Patrick Heil, Joachim P. Spatz, and Ulrich S. Schwarz. Propagation of mechanical stress through the actin cytoskeleton toward focal adhesions: Model and experiment. *Biophysical Journal*, 94(4):1470–1482, 2008. ISSN 15420086. doi:10.1529/biophysj.107.108688.

[178] Chii J. Chan, Andrew E. Ekpenyong, Stefan Golfier, Wenhong Li, Kevin J. Chalut, Oliver Otto, Jens Elgeti, Jochen Guck, and Franziska Lautenschläger. Myosin II Activity Softens Cells in Suspension. *Biophysical Journal*, 108(8): 1856–1869, apr 2015. ISSN 0006-3495. doi:10.1016/j.bpj.2015.03.009.

[179] Alexandre Micoulet, Joachim P Spatz, and Albrecht Ott. Mechanical Response Analysis and Power Generation by Single-Cell Stretching. *ChemPhysChem*, 6 (4):663–670, apr 2005. ISSN 1439-4235. doi:10.1002/cphc.200400417.

[180] Nils M. Kronenberg, Philipp Liehm, Anja Steude, Johanna A. Knipper, Jessica G. Borger, Giuliano Scarcelli, Kristian Franze, Simon J. Powis, and Malte C. Gather. Long-term imaging of cellular forces with high precision by elastic resonator interference stress microscopy. *Nature Cell Biology*, 19(7):864–872, 2017. ISSN 14764679. doi:10.1038/ncb3561.

[181] H. Delanoë-Ayari, J. P. Rieu, and M. Sano. 4d traction force microscopy reveals asymmetric cortical forces in MigratingDictyosteliumCells. *Physical Review Letters*, 105(24), December 2010. doi:10.1103/physrevlett.105.248103.

[182] Ingmar Schoen, Beth L. Pruitt, and Viola Vogel. The yin-yang of rigidity sensing: How forces and mechanical properties regulate the cellular response to materials. *Annual Review of Materials Research*, 43(1):589–618, July 2013. doi:10.1146/annurev-matsci-062910-100407.

[183] Morteza Aramesh, Simon Mergenthal, Marcel Issler, Birgit Plochberger, Florian Weber, Xiao-Hua Qin, Robert Liska, Georg N. Duda, Johannes B. Huppa, Jonas

Ries, Gerhard J. Schütz, and Enrico Klotzsch. Functionalized bead assay to measure three-dimensional traction forces during t-cell activation. *Nano Letters*, 21(1):507–514, December 2020. doi:10.1021/acs.nanolett.0c03964.

[184] Dong-Hwee Kim and Denis Wirtz. Focal adhesion size uniquely predicts cell migration. *The FASEB Journal*, 27(4):1351–1361, 2013. doi:10.1096/fj.12-220160.

[185] Eli Zamir, Ben Zion Katz, Shin ichi Aota, K. M. Yamada, Benjamin Geiger, and Zvi Kam. Molecular diversity of cell-matrix adhesions. *Journal of cell science*, 112 (Pt 11):1655–69, 1999. doi:10.1242/jcs.112.11.1655.

[186] Masha Prager-Khoutorsky, Alexandra Lichtenstein, Ramaswamy Krishnan, Kavitha Rajendran, Avi E. Mayo, Zvi Kam, Benjamin Geiger, and Alexander D. Bershadsky. Fibroblast polarization is a matrix-rigidity-dependent process controlled by focal adhesion mechanosensing. *Nature Cell Biology*, 13:1457–1465, 2011. doi:10.1038/ncb2370.

[187] Steven Huth, Sandra Sindt, and Christine Selhuber-Unkel. Automated analysis of soft hydrogel microindentation: Impact of various indentation parameters on the measurement of Young's modulus. *PLoS ONE*, 14(8):e0220281, 2019. ISSN 19326203. doi:10.1371/journal.pone.0220281.

[188] Ingmar Schoen, Wei Hu, Enrico Klotzsch, and Viola Vogel. Probing cellular traction forces by micropillar arrays: Contribution of substrate warping to pillar deflection. *Nano Letters*, 10(5):1823–1830, 2010. ISSN 15306984. doi:10.1021/nl100533c.

[189] Cornelis Storm, Jennifer J. Pastore, Fred C. MacKintosh, Tom C. Lubensky, and Paul A. Janmey. Nonlinear elasticity in biological gels. *Nature*, 435:191–194, 2005. doi:10.1038/nature03521.

[190] Clifford P. Brangwynne, Fred C. MacKintosh, Sanjay Kumar, Nicholas A. Geisse, Jennifer Talbot, Lakshminarayanan Mahadevan, Kevin Kit Parker, Donald E. Ingber, and David A. Weitz. Microtubules can bear enhanced compressive loads in living cells because of lateral reinforcement. *The Journal of Cell Biology*, 173:733 – 741, 2006. doi:10.1083/jcb.200601060.

[191] Ilka B. Bischofs, Franziska Klein, Dirk Lehnert, Martin Bastmeyer, and Ulrich Sebastian Schwarz. Filamentous network mechanics and active contractility determine cell and tissue shape. *Biophysical journal*, 95 7:3488–96, 2008. doi:10.1529/biophysj.108.134296.

[192] Andrew R. Harris, Loïc Peter, Julien Bellis, Buzz Baum, Alexandre J. Kabla, and Guillaume T. Charras. Characterizing the mechanics of cultured cell monolayers. *Proceedings of the National Academy of Sciences*, 109:16449 – 16454, 2012. doi:10.1073/pnas.1213301109.

[193] Margaret L. Gardel, Karen E. Kasza, Clifford P. Brangwynne, Jiayu Liu, and David A. Weitz. Chapter 19: Mechanical response of cytoskeletal networks. *Methods in cell biology*, 89:487–519, 2008. doi:10.1016/S0091-679X(08)00619-5.

[194] Patrick W. Oakes, Elizabeth Wagner, Christoph A. Brand, Dimitri Probst, Marco Linke, Ulrich S. Schwarz, Michael Glotzer, and Margaret L. Gardel. Optogenetic control of RhoA reveals zyxin-mediated elasticity of stress fibres. *Nature Communications*, 8:15817, June 2017. ISSN 2041-1723. doi:10.1038/ncomms15817.

[195] Yuriy V. Pereverzev, Oleg V. Prezhdo, Manu Forero, Evgeni V. Sokurenko, and Wendy E. Thomas. The Two-Pathway Model for the Catch-Slip Transition in Biological Adhesion. *Biophysical Journal*, 89(3):1446–1454, sep 2005. ISSN 0006-3495. doi:10.1529/BIOPHYSJ.105.062158.

[196] Yanna Bai, Wei Chen, Jie Chen, and Weisi Guo. Deep learning methods for solving linear inverse problems: Research directions and paradigms. *Signal Processing*, 177:107729, 2020. ISSN 0165-1684. doi:10.1016/j.sigpro.2020.107729.

[197] Honghan Li, Daiki Matsunaga, Tsubasa S. Matsui, Hiroki Aosaki, Genki Kinoshita, Koki Inoue, Amin Doostmohammadi, and Shinji Deguchi. Wrinkle force microscopy: a machine learning based approach to predict cell mechanics from images. *Communications Biology*, 5(1), April 2022. doi:10.1038/s42003-022-03288-x.

[198] Ian Goodfellow, Jean Pouget-Abadie, Mehdi Mirza, Bing Xu, David Warde-Farley, Sherjil Ozair, Aaron Courville, and Yoshua Bengio. Generative adversarial nets. In Z. Ghahramani, M. Welling, C. Cortes, N. Lawrence, and K.Q. Weinberger, editors, *Advances in Neural Information Processing Systems*, volume 27. Curran Associates, Inc., 2014. URL https://proceedings.neurips.cc/paper_files/paper/2014/file/5ca3e9b122f61f8f06494c97b1afccf3-Paper.pdf. Accessed on 2023-07-22.

[199] Mehdi Mirza and Simon Osindero. Conditional generative adversarial nets, 2014.

[200] Diederik P Kingma and Max Welling. Auto-encoding variational bayes, 2013.

[201] Kihyuk Sohn, Honglak Lee, and Xinchen Yan. Learning structured output representation using deep conditional generative models. In C. Cortes, N. Lawrence, D. Lee, M. Sugiyama, and R. Garnett, editors, *Advances in Neural Information Processing Systems*, volume 28. Curran Associates, Inc., 2015. URL https://proceedings.neurips.cc/paper_files/paper/2015/file/8d55a249e6baa5c06772297520da2051-Paper.pdf. Accessed on 2023-07-22.

[202] Robin Rombach, Andreas Blattmann, Dominik Lorenz, Patrick Esser, and Björn Ommer. High-resolution image synthesis with latent diffusion models, 2021.

[203] Lynton Ardizzone, Jakob Kruse, Sebastian Wirkert, Daniel Rahner, Eric W. Pellegrini, Ralf S. Klessen, Lena Maier-Hein, Carsten Rother, and Ullrich Köthe. Analyzing inverse problems with invertible neural networks, 2018.

[204] Lynton Ardizzone, Carsten Lüth, Jakob Kruse, Carsten Rother, and Ullrich Köthe. Guided image generation with conditional invertible neural networks, 2019.

[205] Govinda Anantha Padmanabha and Nicholas Zabaras. Solving inverse problems using conditional invertible neural networks. *Journal of Computational Physics*, 433:110194, May 2021. doi:10.1016/j.jcp.2021.110194.

[206] Alexander Denker, Maximilian Schmidt, Johannes Leuschner, and Peter Maass. Conditional invertible neural networks for medical imaging. *Journal of Imaging*, 7(11):243, November 2021. doi:10.3390/jimaging7110243.

[207] D. Barber. *Bayesian Reasoning and Machine Learning*. Cambridge University Press, 2012.

[208] Solveig Badillo, Balazs Banfai, Fabian Birzele, Iakov I. Davydov, Lucy Hutchinson, Tony Kam-Thong, Juliane Siebourg-Polster, Bernhard Steiert, and Jitao David Zhang. An introduction to machine learning. *Clinical Pharmacology & Therapeutics*, 107(4):871–885, March 2020. doi:10.1002/cpt.1796.

[209] Yann LeCun, Yoshua Bengio, and Geoffrey Hinton. Deep learning. *Nature*, 521 (7553):436–444, May 2015. doi:10.1038/nature14539.

[210] Frank Emmert-Streib, Zhen Yang, Han Feng, Shailesh Tripathi, and Matthias Dehmer. An introductory review of deep learning for prediction models with big data. *Frontiers in Artificial Intelligence*, 3, February 2020. doi:10.3389/frai.2020.00004.

[211] H. Robbins and S. Monro. A stochastic approximation method. *Ann. Math. Statist.*, 22:400–407, 1951.

[212] Léon Bottou, Frank E. Curtis, and Jorge Nocedal. Optimization methods for large-scale machine learning. *SIAM Review*, 60(2):223–311, 2018. doi:10.1137/16M1080173.

[213] Krzysztof C. Kiwiel. Convergence and efficiency of subgradient methods for quasiconvex minimization. *Mathematical Programming*, 90(1):1–25, March 2001. doi:10.1007/pl00011414.

[214] Ian Goodfellow, Yoshua Bengio, and Aaron Courville. *Deep Learning (Adaptive Computation and Machine Learning series)*. The MIT Press, hardcover edition, 11 2016. ISBN 978-0262035613.

[215] Diederik P. Kingma and Jimmy Ba. Adam: A method for stochastic optimization. In *Proceedings of the 3rd International Conference on Learning Representations (ICLR)*, 2015. doi:10.48550/arXiv.1412.6980.

[216] Kurt Hornik, Maxwell Stinchcombe, and Halbert White. Multilayer feedforward networks are universal approximators. *Neural Networks*, 2(5):359–366, 1989. ISSN 0893-6080. doi:10.1016/0893-6080(89)90020-8.

[217] Zhou Lu, Hongming Pu, Feicheng Wang, Zhiqiang Hu, and Liwei Wang. The expressive power of neural networks: A view from the width. In I. Guyon, U. Von Luxburg, S. Bengio, H. Wallach, R. Fergus, S. Vishwanathan, and R. Garnett, editors, *Advances in Neural Information Processing Systems*, volume 30. Curran Associates, Inc., 2017. URL https://proceedings.neurips.cc/paper_files/

paper/2017/file/32cbf687880eb1674a07bf717761dd3a-Paper.pdf. Accessed on 2022-07-20.

[218] David E. Rumelhart, Geoffrey E. Hinton, and Ronald J. Williams. Learning representations by back-propagating errors. *Nature*, 323(6088):533–536, October 1986. doi:10.1038/323533a0.

[219] Jake Bouvrie. Notes on convolutional neural networks, November 2006. URL http://web.mit.edu/jvb/www/papers/cnn_tutorial.pdf. Accessed on 2023-07-30.

[220] Adam Paszke, Sam Gross, Francisco Massa, Adam Lerer, James Bradbury, Gregory Chanan, Trevor Killeen, Zeming Lin, Natalia Gimelshein, Luca Antiga, Alban Desmaison, Andreas Kopf, Edward Yang, Zachary DeVito, Martin Raison, Alykhan Tejani, Sasank Chilamkurthy, Benoit Steiner, Lu Fang, Junjie Bai, and Soumith Chintala. Pytorch: An imperative style, high-performance deep learning library. In *Advances in Neural Information Processing Systems 32*, pages 8024–8035. Curran Associates, Inc., 2019. URL http://papers.neurips.cc/paper/9015-pytorch-an-imperative-style-high-performance-deep-learning-library.pdf. Accessed on 2023-08-01.

[221] Laith Alzubaidi, Jinglan Zhang, Amjad J. Humaidi, Ayad Al-Dujaili, Ye Duan, Omran Al-Shamma, J. Santamaría, Mohammed A. Fadhel, Muthana Al-Amidie, and Laith Farhan. Review of deep learning: concepts, CNN architectures, challenges, applications, future directions. *Journal of Big Data*, 8(1), March 2021. doi:10.1186/s40537-021-00444-8.

[222] Mikhail E. Kandel, Yuchen R. He, Young Jae Lee, Taylor Hsuan-Yu Chen, Kathryn Michele Sullivan, Onur Aydin, M. Taher A. Saif, Hyunjoon Kong, Nahil Sobh, and Gabriel Popescu. Phase imaging with computational specificity (PICS) for measuring dry mass changes in sub-cellular compartments. *Nature Communications*, 11(1), December 2020. doi:10.1038/s41467-020-20062-x.

[223] Aapo Hyvärinen and Petteri Pajunen. Nonlinear independent component analysis: Existence and uniqueness results. *Neural Networks*, 12(3):429–439, 1999. ISSN 0893-6080. doi:10.1016/S0893-6080(98)00140-3.

[224] Laurent Dinh, Jascha Sohl-Dickstein, and Samy Bengio. Density estimation using real nvp, 2016.

[225] Y. Le Cun, L.D. Jackel, B. Boser, J.S. Denker, H.P. Graf, I. Guyon, D. Henderson, R.E. Howard, and W. Hubbard. Handwritten digit recognition: applications of neural network chips and automatic learning. *IEEE Communications Magazine*, 27(11):41–46, November 1989. doi:10.1109/35.41400.

[226] Jean-François Le Gall. *Measure Theory, Probability, and Stochastic Processes*. Springer eBook Collection. Springer International Publishing, Cham, 1st ed. 2022. edition, 2022. ISBN 978-3-031-14205-5. doi:10.1007/978-3-031-14205-5.

[227] Benjamin Keepers, Jiandong Liu, and Li Qian. What's in a cardiomyocyte – and how do we make one through reprogramming? *Biochimica et Biophysica Acta (BBA) - Molecular Cell Research*, 1867(3):118464, March 2020. doi:10.1016/j.bbamcr.2019.03.011.

[228] Kazutoshi Takahashi, Koji Tanabe, Mari Ohnuki, Megumi Narita, Tomoko Ichisaka, Kiichiro Tomoda, and Shinya Yamanaka. Induction of pluripotent stem cells from adult human fibroblasts by defined factors. *Cell*, 131(5):861–872, November 2007. doi:10.1016/j.cell.2007.11.019.

[229] Christine L. Mummery, Jianhua Zhang, Elizabeth S. Ng, David A. Elliott, Andrew G. Elefanty, and Timothy J. Kamp. Differentiation of human embryonic stem cells and induced pluripotent stem cells to cardiomyocytes. *Circulation Research*, 111(3):344–358, July 2012. doi:10.1161/circresaha.110.227512.

[230] Jan W. Buikema and Sean M. Wu. Untangling the biology of genetic cardiomyopathies with pluripotent stem cell disease models. *Current Cardiology Reports*, 19(4), March 2017. doi:10.1007/s11886-017-0842-1.

[231] Alexandre J. S. Ribeiro, Yen-Sin Ang, Ji-Dong Fu, Renee N. Rivas, Tamer M. A. Mohamed, Gadryn C. Higgs, Deepak Srivastava, and Beth L. Pruitt. Contractility of single cardiomyocytes differentiated from pluripotent stem cells depends on physiological shape and substrate stiffness. *Proceedings of the National Academy of Sciences*, 112(41):12705–12710, September 2015. doi:10.1073/pnas.1508073112.

[232] Lukas Cyganek, Malte Tiburcy, Karolina Sekeres, Kathleen Gerstenberg, Hanibal Bohnenberger, Christof Lenz, Sarah Henze, Michael Stauske, Gabriela Salinas, Wolfram-Hubertus Zimmermann, Gerd Hasenfuss, and Kaomei Guan. Deep phenotyping of human induced pluripotent stem cell–derived atrial and ventricular cardiomyocytes. *JCI Insight*, 3(12), June 2018. doi:10.1172/jci.insight.99941.

[233] Mandy Kleinsorge and Lukas Cyganek. Subtype-directed differentiation of human iPSCs into atrial and ventricular cardiomyocytes. *STAR Protocols*, 1(1): 100026, June 2020. doi:10.1016/j.xpro.2020.100026.

[234] Valentina Kuhn and Anna Zelená. Traction froce microscopy to study protein mutation-associated atrial fibrillation. Presented at the Institut für Röntgenphysik Göttingen IPR Seminar Winter 22/23, 2022.

[235] Valentina Kuhn, Christina Goß, Aiste Liutkute, Anna Zelená, Ulrich Schwarz, Niels Voigt, and Sarah Köster. Traction force microscopy quantifies the contractility of laminopathic cardiomyocytes. Presented at DPG 2023 Spring Meeting of the Condensed Matter Section, 2023.

[236] Carlos Andres Sanchez Vallejo, Carlos Daniel Rodriguez Ariza, Jose Alfredo Restrepo Urbina, and Santiago Callegari Osorio. A case report of a novel mutation in lamin a/c gene related with risk of sudden death. *European Heart Journal - Case Reports*, 6(4), March 2022. doi:10.1093/ehjcr/ytac128.

[237] Christina Goß. Traction force microscopy of cardiomyocytes with lmna mutation R331Q, March 2023. Max Planck School Matter to Life Lab Rotation Report.

[238] Matthew Wheelwright, Zaw Win, Jennifer L. Mikkila, Kamilah Y. Amen, Patrick W. Alford, and Joseph M. Metzger. Investigation of human iPSC-derived cardiac myocyte functional maturation by single cell traction force microscopy. *PLOS ONE*, 13(4):e0194909, April 2018. doi:10.1371/journal.pone.0194909.

[239] Johannes Schindelin, Ignacio Arganda-Carreras, Erwin Frise, Verena Kaynig, Mark Longair, Tobias Pietzsch, Stephan Preibisch, Curtis Rueden, Stephan Saalfeld, Benjamin Schmid, Jean-Yves Tinevez, Daniel James White, Volker Hartenstein, Kevin Eliceiri, Pavel Tomancak, and Albert Cardona. Fiji: an open-source platform for biological-image analysis. *Nature Methods*, 9(7):676–682, June 2012. doi:10.1038/nmeth.2019.

[240] Sebastian Lickert, Simona Sorrentino, Jan-Dirk Studt, Ohad Medalia, Viola Vogel, and Ingmar Schoen. Morphometric analysis of spread platelets identifies integrin αIIbβ3-specific contractile phenotype. *Scientific Reports*, 8(1), April 2018. doi:10.1038/s41598-018-23684-w.

[241] Lara Hauke, Andreas Primeßnig, Benjamin Eltzner, Jennifer Radwitz, Stefan F. Huckemann, and Florian Rehfeldt. Filamentsensor 2.0: An open-source modular toolbox for 2d/3d cytoskeletal filament tracking. *PLOS ONE*, 18(2):1–21, 02 2023. doi:10.1371/journal.pone.0279336.

Appendix A

Simulation and algorithm details

A.1 Divergence correction of a vector field

Divergence correction can be used to correct a vector field $\boldsymbol{u}_{exp}$, which is expected to be divergence free. The input vector field $\boldsymbol{u}_{exp}$ is slightly perturbed into a corrected vector profile $\boldsymbol{u}_c$, which is free of divergence. A corrected profile can therefore be obtained by solving the optimization problem

$$\boldsymbol{u}_c = \arg\min_{\boldsymbol{u}} \int (\boldsymbol{u}_{exp}(\mathbf{x}) - \boldsymbol{u}(\mathbf{x}))^2 \, \mathrm{d}^3x \tag{A.1}$$

under the constraint

$$\nabla \cdot \boldsymbol{u}_c = 0. \tag{A.2}$$

When discretized to a mesh using a first order finite difference, the problem can be written [157]:

$$(u_c^{ijk}, v_c^{ijk}, w_c^{ijk}) = \arg\min_{(u,v,w)} \sum_{i,j,k=1}^{n_x,n_y,n_z} (u_{exp}^{ijk} - u^{ijk})^2 + (v_{exp}^{ijk} - v^{ijk})^2 + (w_{exp}^{ijk} - w^{ijk})^2 \tag{A.3}$$

under the constraint

$$\sum_{i'=1}^{n_x} \mathrm{d}_{n_x}^{ii'} u_c^{i'jk} + \sum_{j'=1}^{n_y} \mathrm{d}_{n_y}^{jj'} v_c^{ij'k} + \sum_{k'=1}^{n_z} \mathrm{d}_{n_z}^{kk'} w_c^{ijk'} = 0 \quad \text{for all } i,j,k = 1 \ldots n_x, n_y, n_z. \tag{A.4}$$

Here u_c^{ijk},v_c^{ijk} and w_c^{ijk} denote the three vector components sampled on a grid and $\mathrm{d}_{n_x}^{ii'}$,$\mathrm{d}_{n_y}^{jj'}$ and $\mathrm{d}_{n_z}^{kk'}$ are the coefficients of the one-dimensional finite difference operators in x, y and z direction. The coefficients $\mathrm{d}_{n_x}^{ii'}$s form $n_x \times n_x$ sparsely populated matrices $\mathbf{d}_{n_x}$ given by

$$\mathbf{d}_{n_x} = \frac{1}{\Delta x} \begin{pmatrix} -1 & 1 & & & \\ -\frac{1}{2} & 0 & \frac{1}{2} & & \\ & \ddots & \ddots & \ddots & \\ & & -\frac{1}{2} & 0 & \frac{1}{2} \\ & & & -1 & 1 \end{pmatrix}. \tag{A.5}$$

Here Δx corresponds to the grid spacing in the x direction. $\mathbf{d}_{n_y}$ and $\mathbf{d}_{n_z}$ can be defined analogously. An explicit solution for Eq (A.3) can be found by enforcing

Eq (A.4) using appropriate Lagrange multipliers as shown in by Wang *et al.* [158] (presented in appendix 1 of their study). This results in an algorithm that starts with calculating an eigenvalue decomposition of $\mathbf{d}_{n_x}\mathbf{d}_{n_x}^T$, $\mathbf{d}_{n_y}\mathbf{d}_{n_y}^T$ and $\mathbf{d}_{n_z}\mathbf{d}_{n_z}^T$:

$$\mathbf{d}_{n_x}\mathbf{d}_{n_x}^T = \mathbf{Q}_{n_x}\mathbf{L}_{n_x}\mathbf{Q}_{n_x}^T \tag{A.6}$$
$$\mathbf{d}_{n_y}\mathbf{d}_{n_y}^T = \mathbf{Q}_{n_y}\mathbf{L}_{n_y}\mathbf{Q}_{n_y}^T \tag{A.7}$$
$$\mathbf{d}_{n_z}\mathbf{d}_{n_z}^T = \mathbf{Q}_{n_z}\mathbf{L}_{n_z}\mathbf{Q}_{n_z}^T \tag{A.8}$$

Since each of these matrices has only the size of one of the three spatial dimensions of the sample, they are comparatively small compared to an algorithm that would target Eq (A.3) directly and would have to deal with $n_x \times n_y \times n_z$ components simultaneously. Furthermore, if the sample is a square ($n_x = n_y$) or multiple data sets need to be analyzed, an already calculated eigenvalue decomposition can be reused to increase the computational efficiency.

If we now denote the components of $\mathbf{Q}_{n_x}$, $\mathbf{Q}_{n_y}$ and $\mathbf{Q}_{n_z}$ by $Q_{n_x}^{ij}$, $Q_{n_y}^{ij}$, $Q_{n_z}^{ij}$ and the diagonal elements of $\mathbf{L}_{n_x}$,$\mathbf{L}_{n_y}$ and $\mathbf{L}_{n_z}$ by $\lambda_{n_x}^k$, $\lambda_{n_y}^k$, $\lambda_{n_z}^k$, the algorithm has the following steps, that contain only basic algebra and matrix multiplications.

- Calculate the divergence residue field of the uncorrected data

$$S_{exp}^{ijk} = \sum_{i'=1}^{n_x} \mathrm{d}_{n_x}^{ii'} u_{exp}^{i'jk} + \sum_{j'=1}^{n_y} \mathrm{d}_{n_y}^{jj'} v_{exp}^{ij'k} + \sum_{k'=1}^{n_z} \mathrm{d}_{n_z}^{kk'} w_{exp}^{ijk'} \tag{A.9}$$

- Calculate the helper variables Γ^{lmn} given by:

$$\Gamma^{lmn} = \lambda_{n_x}^l + \lambda_{n_y}^m + \lambda_{n_z}^n \tag{A.10}$$

- Calculate another set of helper variables μ^{ijk} given by:

$$\mu^{ijk} = \sum_{l,m,n=1}^{n_x,n_y,n_z} \frac{Q_{n_x}^{il} Q_{n_y}^{jm} Q_{n_z}^{kn}}{\Gamma^{lmn}} \left(\sum_{i',j',k'}^{n_x,n_y,n_z} Q_{n_x}^{i'l} Q_{n_y}^{j'm} Q_{n_z}^{k'n} S_{exp}^{i'j'k'} \right) \tag{A.11}$$

  Γ^{lmn} contains a single zero element. In order to calculate μ^{ijk}, this zero element must be replaced by a non-zero value (for example one). This particular value does not affect the result for the corrected vector field. The situation is similar to the calculation of a scalar potential, where a constant offset will also have no effect on its gradient field.

- Finally, the corrected field can be obtained by:

$$u_c^{ijk} = u_{exp}^{ijk} - \sum_{i'=1} \mathrm{d}_{n_x}^{i'i} \mu^{i'jk}, \tag{A.12}$$
$$v_c^{ijk} = v_{exp}^{ijk} - \sum_{j'=1} \mathrm{d}_{n_y}^{j'j} \mu^{ij'k}, \tag{A.13}$$
$$w_c^{ijk} = w_{exp}^{ijk} - \sum_{k'=1} \mathrm{d}_{n_z}^{k'k} \mu^{ijk'}. \tag{A.14}$$

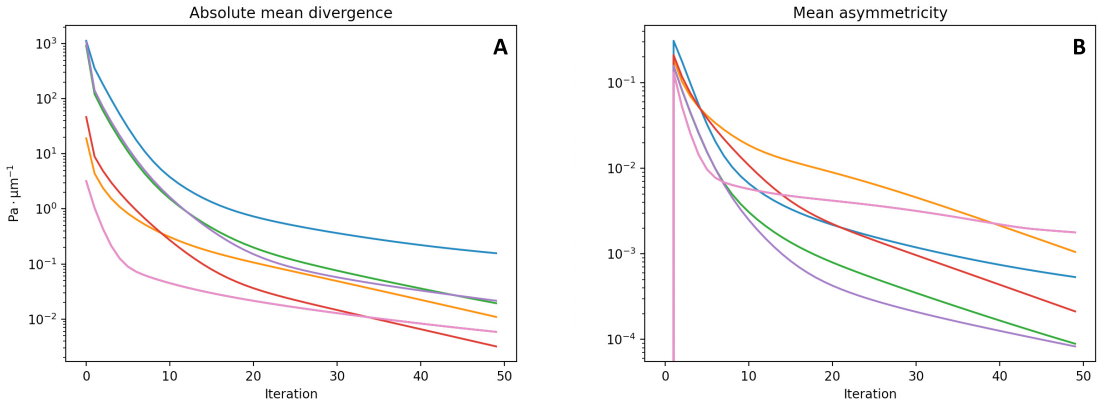

Figure A.1: Absolute mean divergence of $\boldsymbol{\sigma}^{(i)}$ and mean value of the asymmetricity for $\boldsymbol{w}^{(i)}$ plotted with respect to the iteration number i. The blue line represents the effect of the divergence correction on random data ($\boldsymbol{\sigma}^{(0)}$ is filled with white noise.) The other lines represent data for $\boldsymbol{\sigma}^{(0)}$ obtained from different pressure and point adhesion profiles with and without noise perturbations.

A.2 Convergence of the divergence correction algorithm

The iterative divergence correction scheme used for the Divergence-free Direct method 3D traction force microscopy tries to optimize the result according to two criteria:

- Minimize the divergence of $\boldsymbol{\sigma}^{(i)}$.
- Reduce the asymmetry of $\boldsymbol{w}$

We estimate the level divergence of $\boldsymbol{\sigma}^{(i)}$ by first calculating

$$S_r^{ijk} = \sum_{i'=1}^{n_x} \mathrm{d}_{n_x}^{ii'} \sigma_{r1}^{i'jk} + \sum_{j'=1}^{n_y} \mathrm{d}_{n_y}^{jj'} \sigma_{r2}^{ij'k} + \sum_{k'=1}^{n_z} \mathrm{d}_{n_z}^{kk'} \sigma_{r3}^{ijk'} \tag{A.15}$$

for $\sigma_{rl} = (\boldsymbol{\sigma}^{(i)})_{rl}$ for $r = 1, 2, 3$ using the first order discrete derivatives and then taking the L2 norm

$$\sum_{i,j,k} \sqrt{(S_1^{ijk})^2 + (S_2^{ijk})^2 + (S_3^{ijk})^2} \tag{A.16}$$

The asymmetricity of a matrix can be described by

$$\mathrm{asym}(\mathbf{w}) = \frac{\left\|\mathbf{w} - \mathbf{w}^T\right\|}{2\|\mathbf{w}\|} \tag{A.17}$$

where $\mathrm{asym}(\mathbf{w}) = 1$ indicates a fully asymmetric and $\mathrm{asym}(\mathbf{w}) = 0$ a symmetric matrix.

As we can see in figure A.1, every iteration improves both quantities. The symmetricity of $\boldsymbol{u}$ is improved and the remaining divergence $\nabla\boldsymbol{\sigma}$ is reduced. However, no universal termination criterion can be extracted from either improvement. Notice that the rate of improvement reduces after 5 to 20 iterations. For this reason, we assume that a sufficient level of improvement is reached after 20 iterations and terminate the divergence correction algorithm at this point.

A.3 Parameters used for simulated profiles

In general, profiles can be described by

$$\boldsymbol{\tau}(x,y) = \sum_i \boldsymbol{H}(x,y,x_i,y_i,a_i,\boldsymbol{F}_i) \tag{A.18}$$

with the definition

$$H(x,y,x',y',a,\boldsymbol{F}) = \frac{3}{2\pi a^3}\boldsymbol{F}\sqrt{a^2-\rho^2}\,\Theta(a-\rho) \tag{A.19}$$

where $\rho = \sqrt{(x-x')^2+(y-y')^2}$.

- Profile of Fig 4.2, Fig 4.4 C, Fig 4.5, Fig 4.6 C, Fig 4.7 C and Fig 4.8

Substrate properties		
Young's Modulus	E	10 kPa
Poisson Ratio	ν	0.5
Simulation properties		
Spacing x and y direction	d_{xy}	0.4 µm
Spacing z direction	d_z	0.8 µm
Number of sampling points x and y direction	n_{xy}	128
Number of sampling points z direction	n_z	6

Profile parameters						
i	x'	y'	a	F_x	F_y	F_z
1	0.0 µm	0.0 µm	6.0 µm	0.0 nN	0.0 nN	300 nN
2	−10.8 µm	6.2 µm	2.0 µm	86.6 nN	−50.0 nN	−50.0 nN
3	10.8 µm	−6.2 µm	2.0 µm	−86.6 nN	50 nN	−50.0 nN
4	7.7 µm	12.5 µm	2.0 µm	0.0 nN	−100 nN	−50.0 nN
5	−7.7 µm	−12.5 µm	2.0 µm	0.0 nN	100 nN	−50.0 nN
6	10.8 µm	6.2 µm	2.0 µm	−86.6 nN	−50.0 nN	−50.0 nN
7	−10.8 µm	−6.2 µm	2.0 µm	86.6 nN	50 nN	−50.0 nN

- Profile of Fig 4.3 A and Fig 4.4 A

$$\tau_x = 0 \qquad \tau_y = 0 \qquad \tau_z = \frac{3F}{2\pi a^3}\sqrt{a^2-r^2}\,\Theta(a-r) \tag{A.20}$$

Substrate properties		
Young's Modulus	E	10 kPa
Poisson Ratio	ν	0.45
Force profile parameters		
Total Force	F	10 µN
Radius of force affect region	a	20 µm
Simulation properties		
Spacing x and y direction	d_{xy}	0.8 µm
Spacing z direction	d_z	2.0 µm
Number of sampling points x and y direction	n_{xy}	128
Number of sampling points z direction	n_z	10

- Profile of Fig 4.3 B and Fig 4.4 B

$$\tau_x = 0 \quad \tau_y = 0$$
$$\tau_z = F\left(\frac{3}{2\pi a_I^3}\sqrt{a_I^2 - r^2}\,\Theta(a_I - r) - \frac{3}{2\pi a_O^3}\sqrt{a_O^2 - r^2}\,\Theta(a_O - r)\right) \tag{A.21}$$

Substrate properties		
Young's Modulus	E	3 kPa
Poisson Ratio	ν	0.45
Force profile parameters		
Force amplitude	F	1 µN
Radius of force affect region	a_O	60 µm
Radius of inner region	a_I	45 µm
Simulation properties		
Spacing x and y direction	d_{xy}	0.8 µm
Spacing z direction	d_z	2.0 µm
Number of sampling points x and y direction	n_{xy}	256
Number of sampling points z direction	n_z	10

- Profile of Fig 4.6 A and Fig 4.7 A

Substrate properties		
Young's Modulus	E	10 kPa
Poisson Ratio	ν	0.5
Simulation properties		
Spacing x and y direction	d_{xy}	0.4 µm
Spacing z direction	d_z	0.4 µm
Number of sampling points x and y direction	n_{xy}	128
Number of sampling points z direction	n_z	6

Profile parameters						
i	x'	y'	a	F_x	F_y	F_z
1	0.0 µm	0.0 µm	6.0 µm	0 nN	0 nN	100 nN
2	4.3 µm	11.7 µm	2.0 µm	−34.2 nN	−93 nN	−25 nN
3	4.3 µm	−11.7 µm	2.0 µm	−34.2 nN	93 nN	−25 nN

- Profile of Fig 4.6 B and Fig 4.7 B

Substrate properties		
Young's Modulus	E	10 kPa
Poisson Ratio	ν	0.45
Simulation properties		
Spacing x and y direction	d_{xy}	0.8 µm
Spacing z direction	d_z	4.0 µm
Number of sampling points x and y direction	n_{xy}	64
Number of sampling points z direction	n_z	4

Profile parameters						
i	x'	y'	a	F_x	F_y	F_z
1	−6.4 µm	7.7 µm	2.0 µm	128.5 nN	−153.2 nN	0.0 nN
2	6.4 µm	−7.7 µm	2.0 µm	−128.5 nN	153.2 nN	0.0 nN
3	6.1 µm	10.0 µm	2.0 µm	0 nN	−50.0 nN	0.0 nN
4	−6.1 µm	−10.0 µm	2.0 µm	0 nN	−50.0 nN	0.0 nN
5	6.4 µm	7.7 µm	2.0 µm	−64.3 nN	−76.6 nN	0.0 nN
6	−6.4 µm	−7.7 µm	2.0 µm	64.3 nN	76.6 nN	0.0 nN

A.4 Effect of sampling density in combination with displacement noise

As complement to Fig 4.8, which was calculated without noise, here I document the effect of changing sampling density in the presence of noise in the displacement field. In Fig A.2 and Fig A.3 I simulated the effects of variation in sampling density for a high ($\sigma_N / < \|u\| >= 1$) and very high ($\sigma_N / < \|u\| >= 2$) noise level, respectively. Surprisingly, we see that the SNR of FTTC now significantly improves when decreasing the sample density (increasing the sample distance). This is due to the fact that while for the DM only neighboring points are used to calculate the local traction, in FTTC even points far away contribute. This means that increasing the sample distance decreases the number of sampling points and as such the number of points that contribute to the error in traction at each sampling point.

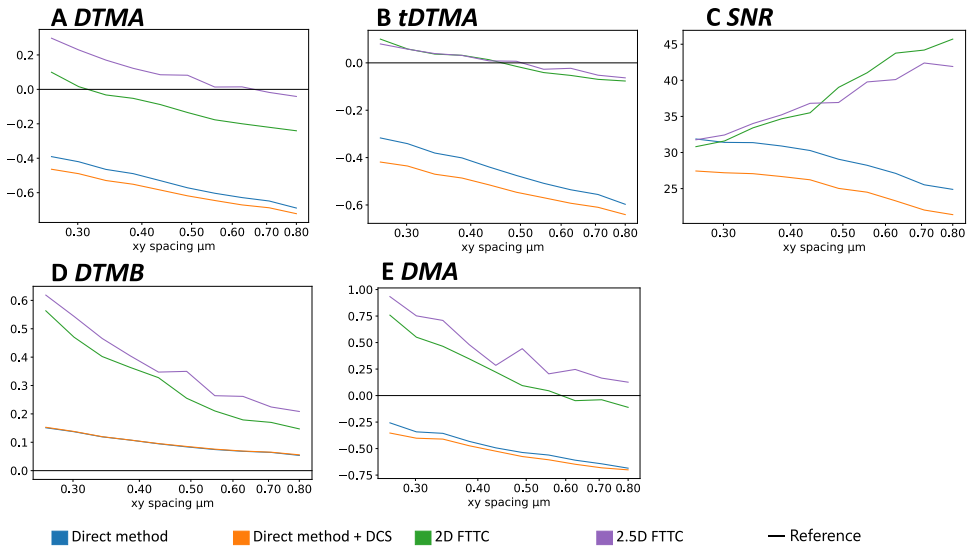

Figure A.2: Effects of variation in sampling density for a high noise level. Plots A to E show how the different metrics are affected when using a different distance of the sampling points when setting up the input while adding noise with a standard deviation that is equivalent to the average of the mean deformation field of the unperturbed profile ($\sigma_N / < \|u\| >= 1$). Moving to higher levels of noise worsens the performance of the Fourier-based methods, while the performance of the direct method is affected less.

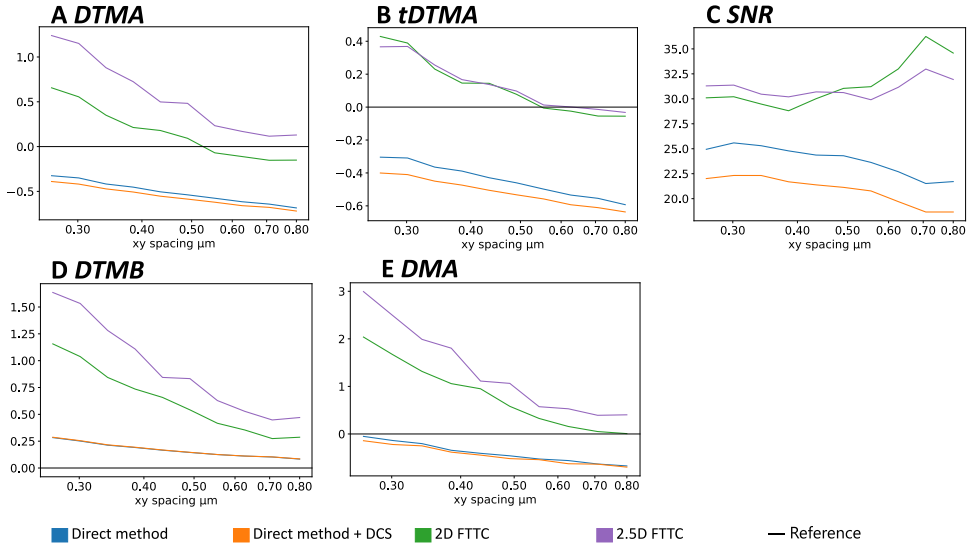

Figure A.3: Effects of variation in sampling density for a very high noise level. Plots A to E show how the different metrics are affected when using a different distance of the sampling points when setting up the input while adding noise that is equivalent to twice of the average of the mean deformation field of the unperturbed profile ($\sigma_N / < \|u\| >= 2$).

A.5 Determination of the dominant axis of a synthetic cell

For each cell, we define the centered moment of area matrix by

$$\boldsymbol{M} = \int_{\Omega_{r,\phi,x_0,y_0}} \begin{pmatrix} (x-x_0)^2 & (x-x_0)(y-y_0) \\ (x-x_0)(y-y_0) & (y-y_0)^2 \end{pmatrix} \mathrm{d}x\,\mathrm{d}y\,. \tag{A.22}$$

The radial integration can be performed analytically and one obtains

$$\boldsymbol{M} = \frac{1}{4}\int_0^{2\pi} r(\phi)^4 \begin{pmatrix} \cos^2(\phi) & \cos(\phi)\sin(\phi) \\ \cos(\phi)\sin(\phi) & \sin^2(\phi) \end{pmatrix} \mathrm{d}\phi\,. \tag{A.23}$$

The dominant axis can be found by finding the eigenvector of this matrix attributed to it's largest eigenvalue. This vector is given by:

$$\boldsymbol{e}_1 = C \begin{pmatrix} \cos(\alpha) \\ \sin(\alpha) \end{pmatrix}, \tag{A.24}$$

where C is an arbitrary constant and

$$\alpha = \frac{1}{2}\arctan 2(2M_{xy}, M_{xx} - M_{yy}). \tag{A.25}$$

The $\arctan 2$ function follows the convention established in section B.3. This formula can be verified by direct matrix application. The dominant axis of the cell is now the straight line obtained when rotating the x-axis by α counterclockwise.

Appendix B

Materials and Methods

B.1 Microneedle shearing of fibroblasts

In this section we describe the methods used to obtain the experimental data presented in the application section 5.3 of chapter 5. A detailed description, also including preparation procedures can be found in manuscript 3.

Cell shearing and imaging

Imaging was conducted by Steven Huth. A fluorescence image of the zyxin distribution of a well-spread fibroblast was recorded. The calibrated microneedle was inserted into this cell directly above or below the nucleus and a phase contrast image of cell and needle was recorded. Subsequently, the needle was moved horizontally at 5 µm/s against the nucleus. During the shearing process, phase contrast images of cell and needle as well as fluorescent images of the marker beads embedded in the underlying PAA substrate were recorded alternately at a frame rate of 0.85 fps. After cell detachment, an additional pair of fluorescent microscopy and phase contrast images was recorded. This last fluorescent image pair recorded the bead position of the PAA sample without any influence of traction forces and served as reference image for traction force calculations.

Images were recorded using an inverted microscope (Z1 Observer, Zeiss) equipped with a CMOS Camera (Hamamatsu ORCA Flash 4.0) and a 40x objective with phase contrast (Zeiss EC Plan-Neofluar 40x/0.75 Ph2 M27). Both, the phase contrast images and the fluorescence images were recorded using the RFP filtercube (necessary to image the fluorescent marker beads) to minimize the time between the measurement of shear force and traction forces. The microneedle was handled using a Eppendorf InjectMan NI2 micromanipulator. For each frame, the bending of the needle was calculated as described in the calibration section above. The shear force was computed by multiplying the needle bending with the needle's spring constant calibrated prior to each experiment.

Image registration

The substrate deformation field was obtained from fluorescent bead images using PIV. A windows size of 64 pixels and a 50% window overlap were used. Spurious vectors were removed using a minimal signal-to-noise ratio in the correlation function of 1.5 and a threshold of 2.0 for the normalized median test. The reference image was taken after cell detachment.

B.2 Traction force microscopy of cardiomyocyte

The cardiomyocyte sample preparation is described in detail by Goß and Kuhn [234, 235, 237] and follows procedures outlined by Ribeiro *et al.* [231] and Wheelwright *et al.* [238].

Imaging

Imaging was conducted by Christina Goß and Valentina Kuhn on an inverted microscope (IX81, Olympus) equipped with a stage top incubator and a 60x immersion oil objective. For each cell, first a snapshot was taken using the Bright-field channel. Then the fluorescent beads beneath it are recorded for 250 frames and finally the cell's actin structure is recorded for 250 frames. A relaxed cell phase was chosen as reference configuration, while a maximal contracted phase was used for traction reconstruction.

Image registration

First a Shi-Tomasi corner detector was used to find the position of beads. In this step, the number of detectable features was limited to 5000 to prevent mismatches. To avoid double-counting of clusters, a minimum distance between registered beads was set to 3 pixels. The pyramidal KLT algorithm was used to track the intensity gradients around the detected beads within search windows of size 64×64 pixels and in the second round of size 32×32 pixels. Drift correction was performed by selecting a region far from the cell where the displacements due to the traction of the cell are assumed to have vanished, calculating its mean displacement and subtracting this value from the displacement field [110]. To calculate the traction stresses from the displacement field, a Young's modulus of 9.8 kPa (determined via nanoindentation of a gel) and a Poisson's ratio of 0.5 were used. The objective used to capture the video of the fluorescent beads resolved 0.1 microns per pixel, and the nodal distance of the grid the Fourier Space methods were performed on was 8 pixels.

FTTC force reconstruction

For FTTC reconstructions, a Tukey filter with $\alpha = 0.1$ was used to suppress artifacts caused by the discretization in Fourier space. The General-Cross-Validation method was used to find the optimal value of the regularization factor λ for several cardiomyocytes. A representative value of $\lambda = 2.6 \times 10^{-3}$ was found and subsequently used for all force reconstructions.

B.3 Traction force microscopy of thrombocytes

In this section we describe the experimental methods applied to obtain data used in the experimental analysis of chapter 6. Experiments and data collection were conducted by Anna Zelená and Sarah Köster at the Research Group Cellular Biophysics, Institut für Röntgenphysik, University of Göttingen. The experimental and analytical procedures are described in detail in manuscript 4.

Live cell traction force microscopy and epi-fluorescence imaging

Sample growth and preparation was conducted by Anna Zelená with the help of Rūta Gerasimaitė and Gračvydas Lukinavičius for the super-resolution microscopy measurements.

The observation was conducted in two process steps, confocal imaging of cellular structures and traction force marker beads and STED microscopy on fixed thrombocytes:

In the first step, the actin filaments were stained with SiR-actin (Spirochrome Ltd., Stein am Rhein, Switzerland) and cells are placed on an PAA substrate, with a thickness of at least 50 µm. Fluorescent images of the cells on a PAA TFM-substrate were recorded on an inverted microscope (IX81, Olympus), equipped with a 60× water immersion objective (UPlanSApo, NA = 1.2, WD = 0.28 mm, Olympus) an MT20 Xenon arc lamp (150 W, Olympus) lamp operated at 23% of the maximum intensity and a CMOS camera (Orca Flash 4.0, Hamamatsu Photonics Deutschland GmbH, Herrsching am Ammersee, Germany). Fluorescence imaging employed a dual-band filter (FITC/Cy5; excitation at 470 nm and 628 nm and emission at 537 nm and 694 nm (AHF Analysentechnik AG, Tübingen, Germany)). Thrombocyte spreading was recorded for 2 hours at one frame every 7.5 s with an exposure time of 50 ms each for the actin structures and the beads. A total recording time of 2 hours was chosen to account for different thrombocytes to adhere and start spreading at different time points and so as to capture 30 mins of spreading and contraction time for each thrombocyte. After 30 mins the thrombocytes were fully contracted. Some remain in this contracted state, whereas, for some, the underlying gel relaxes, possibly due to detachment of the thrombocyte.

In a second step, thrombocytes were fixed and permeabilized. Next cells were incubated with a primary antibody against vinculin (monoclonal mouse anti-vinculin V9131, Sigma-Aldrich, St. Louis, Missouri, USA). The samples were imaged through the glass slide using super-resolution STED-microscopy (see manuscript 4, Supplemental Material, Fig. S3B), using an Abberior STED Facility Line microscope (Abberior Instruments GmbH, Göttingen, Germany) built on a motorized inverted microscope IX83 (Olympus) equipped with an 60× silicone oil immersion objective (UPlanSApo, NA = 1.3, WD = 0.3 mm, Olympus). For this setup the pixel size is 30 nm and the pinhole is set to 0.92 AU (Airy units with 1 AU = 1.22 λ/NA) for STED-imaging. The dwell time was set to 20 µs. The fluorescent probe SiR-actin was excited by 2 % power of a 640 nm laser and detected in the emission range 650-755 nm. For STED a 775 nm laser with 10 % power was used and each line scanned 10 times. The spherical correction was set to 1 to improve the image quality.

Image registration

The image sequences with the recorded beads are down-sampled from 16 to 8 bit in ImageJ [239]. The Shi-Tomasi corner detector tracked the position of at maximum 1000 beads. To avoid double-counting of clusters, a minimum distance between beads is set to 3 pixels. The pyramidal KLT algorithm is used to track the intensity gradients around the detected beads within search windows of size 48 × 48 pixels and in the second round of size 24 × 24 pixels. The displacements are tracked between successive images and the complete trace is reconstructed with reference to the undeformed image before adhesion of the thrombocytes. We assume a linear movement inside each of the search windows using a forward Euler approach. The drift correction is applied on a small area of the image sequence without deformation and the detected drift is subtracted from all calculated displacements.

FTTC force reconstruction

Application of a Tukey filter ($\alpha = 0.4$) ensured a zero velocity field at the border of the grid with drift-corrected displacements. The traction forces are calculated by FTTC with Tikhonov regularization using regularization parameters defined by a generalized cross-validation function. A new optimal regularization parameter was found for each reconstruction.

Stress fiber reconstruction

To extract the stress fibers, I used a combination of MATLAB scripts for morphometric analysis by Lickert *et al.* [240] and the tool *FilamentSensor* [241]. First, I used the MATLAB scripts *Define Cells* and *Process Cells* of the morphometric analysis toolbox, to obtain a binarized bitmap of the actin staining as well as a prediction of the local stress fiber orientation angle. I then determined the dominant orientation angle and produced two bitmap images: one in which only those bits of the actin image are retained, in which the corresponding orientation angle is roughly parallel to the dominant orientation angle (angles differ by less than 45°), and one in which only those bits of the actin image are retained, in which this is not the case. I found that this procedure of processing stress fibers in these two groups improves their reconstruction. Both bitmap images were then processed independently using the *FilamentSensor*. I loaded the images using the *Stack View* option and selected "As straight pieces" in the *Line Sensor* menu in order to obtain the filaments in a segment-wise manner. I then used the "Export filaments as .cs" option to extract the segments. In a post processing step, I first assembled the segments into piece-wise straight lines and then merged the filament data sets obtained from the parallel and non-parallel bitmap images.

Focal adhesion localization procedure

In order to compare the localization of vinculin to actin in the STED-images, I first apply a 2nd order Sobel filter on the vinculin data to compute the Laplacian. This identifies the points where the intensity is maximal. I apply a threshold to create a bitmap around these points. I then perform a connected component analysis and only retain sufficiently large patches. For each component i, the orientation ϕ_i, the length a_i of its semi-major axis and its eccentricity ε_i can be calculated using a moment analysis. I calculate the center of the adhesion $(x_0, y_0)^T$ as

$$\begin{pmatrix} x_0 \\ y_0 \end{pmatrix} = \int_{\Omega_i} \begin{pmatrix} x \\ y \end{pmatrix} \mathrm{d}x\,\mathrm{d}y, \tag{B.1}$$

where Ω_i is the area of the patch found in the component analysis. We then find the centered moment matrix of area $\boldsymbol{M}_i$ by

$$\boldsymbol{M}_i = \int_{\Omega_i} \begin{pmatrix} (x-x_0)^2 & (x-x_0)(y-y_0) \\ (x-x_0)(y-y_0) & (y-y_0)^2 \end{pmatrix} \mathrm{d}x\,\mathrm{d}y\,, \tag{B.2}$$

using summation to numerically solve the integral. If the adhesion was an ellipse, we would have for the moment matrix

$$\boldsymbol{M}_{el} = \alpha a^4 \sqrt{1+\varepsilon^2} \begin{pmatrix} 1+\varepsilon^2 \sin^2(\phi) & \varepsilon^2 \cos(\phi)\sin(\phi) \\ \varepsilon^2 \cos(\phi)\sin(\phi) & 1+\varepsilon^2 \cos^2(\phi) \end{pmatrix}, \tag{B.3}$$

where the factor α takes into account that the threshold will only retain the innermost parts of the adhesion. By comparing both expressions for the moment matrix, we find

that

$$\begin{aligned}
\phi &= \frac{1}{2}\arctan 2(2M_{i,xy}, M_{i,xx} - M_{i,yy}) \\
S &= \alpha a^4\sqrt{1+\varepsilon^2}(2+\varepsilon^2) = M_{i,xx} + M_{i,yy} \\
T &= \alpha a^4\sqrt{1+\varepsilon^2}\varepsilon^2 = \sqrt{(M_{i,xx} - M_{i,yy})^2 + 4 * M_{i,xy}} \\
\varepsilon &= \sqrt{\frac{2T}{S-T}} \\
a &= \left(\frac{2T}{\alpha\sqrt{1+\varepsilon^2}\varepsilon^2}\right)^{1/4}.
\end{aligned} \tag{B.4}$$

The arctan 2 function follows the usual convention of taking y as its first parameter. This means $\arctan 2(y, x) = \arctan(y/x)$ for positive y and x values. In my analysis, I empirically selected a threshold value of -2.5, retained components comprising more than 25 pixels and used a scaling factor $\alpha = 3^{-4}$.

Appendix C

Additional Results

C.1 Qualifying traction forces in fibroblasts under external shearing

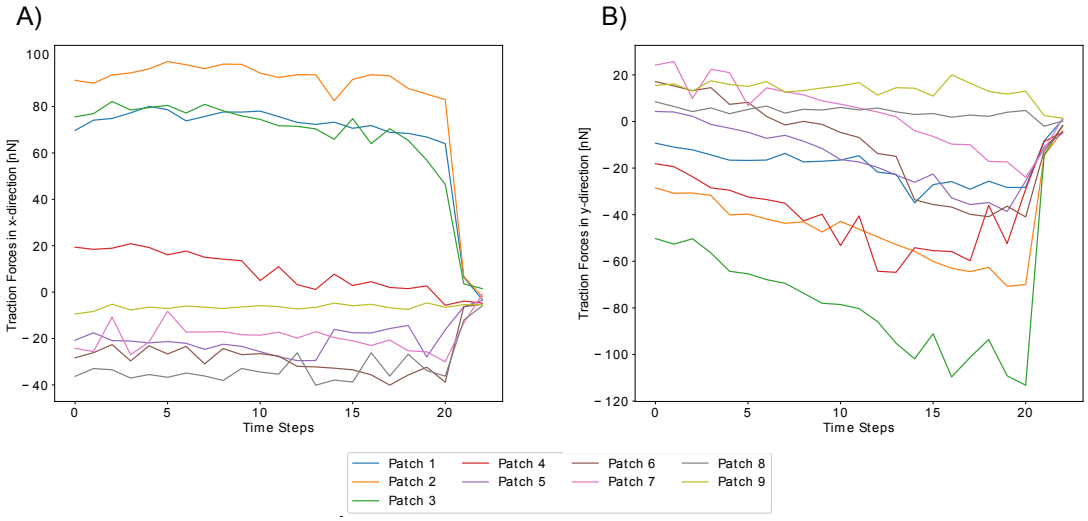

Figure C.1: Traction force data from the cell presented in Fig 5.4. (A) shows the x-components of the traction force vectors. It is very clear the these are not influenced by the shearing in y-direction, which is why we focus our discussion on traction forces in y direction. (B) shows the y-components of the traction forces for each adhesion patch. We decided to combine some neighboring patches with similar behavior for better visualization. We combined patches 2,3 and 4 as well as 5,6 and 7.

C.2 Additional cINN-ML-TFM reconstructions

cINN-ML-TFM reconstruction for some additional validation data samples

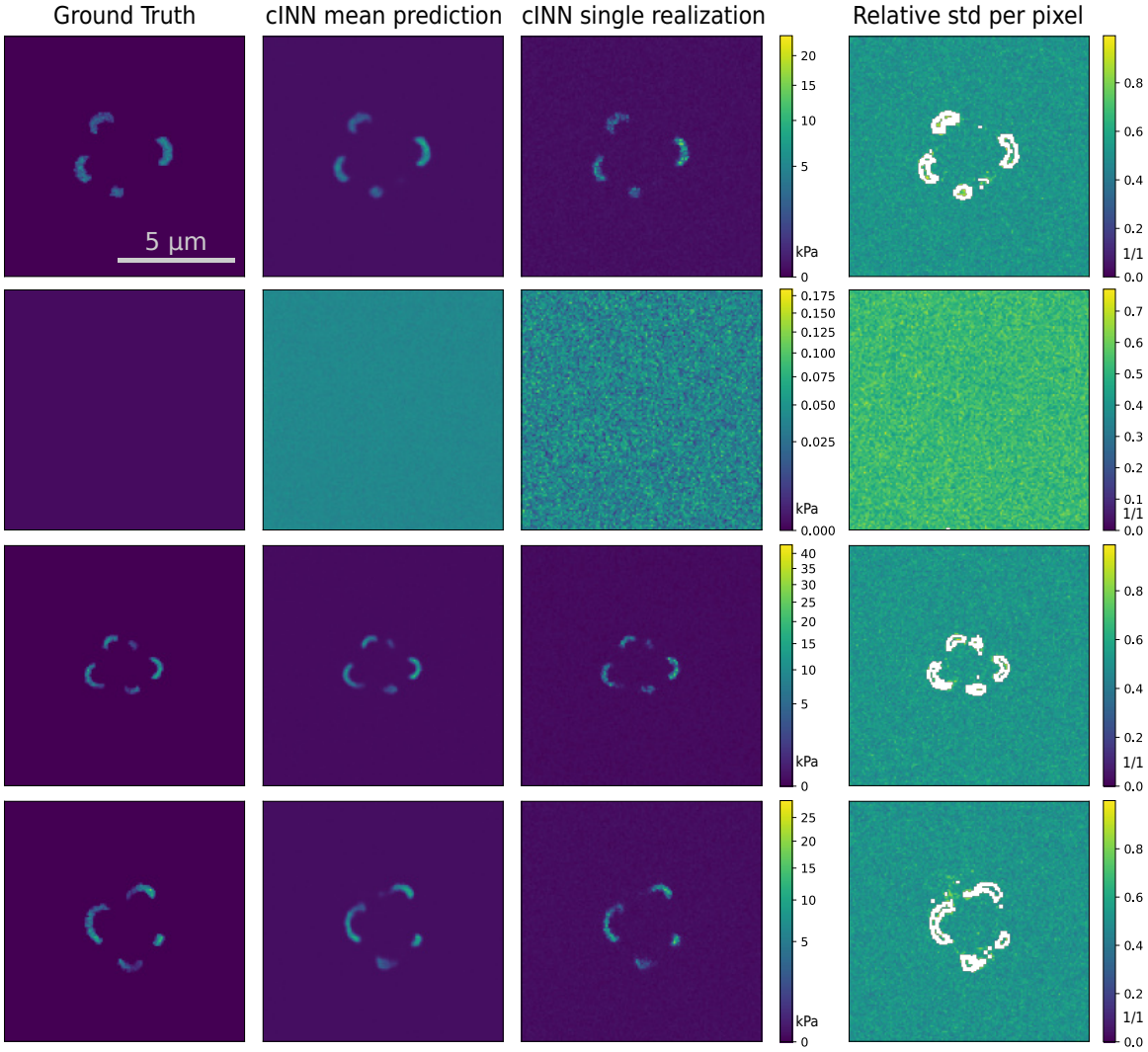

Figure C.2: cINN-ML-TFM magnitudes reconstruction for some additional validation datasets. For each dataset, we show the ground truth traction field, the cINN prediction averaged over multiple traction realizations, a single cINN realization and the relative standard variation in each pixel. Plots in one row all belong to the same cell. The second row displays an input containing no nonzero tractions.

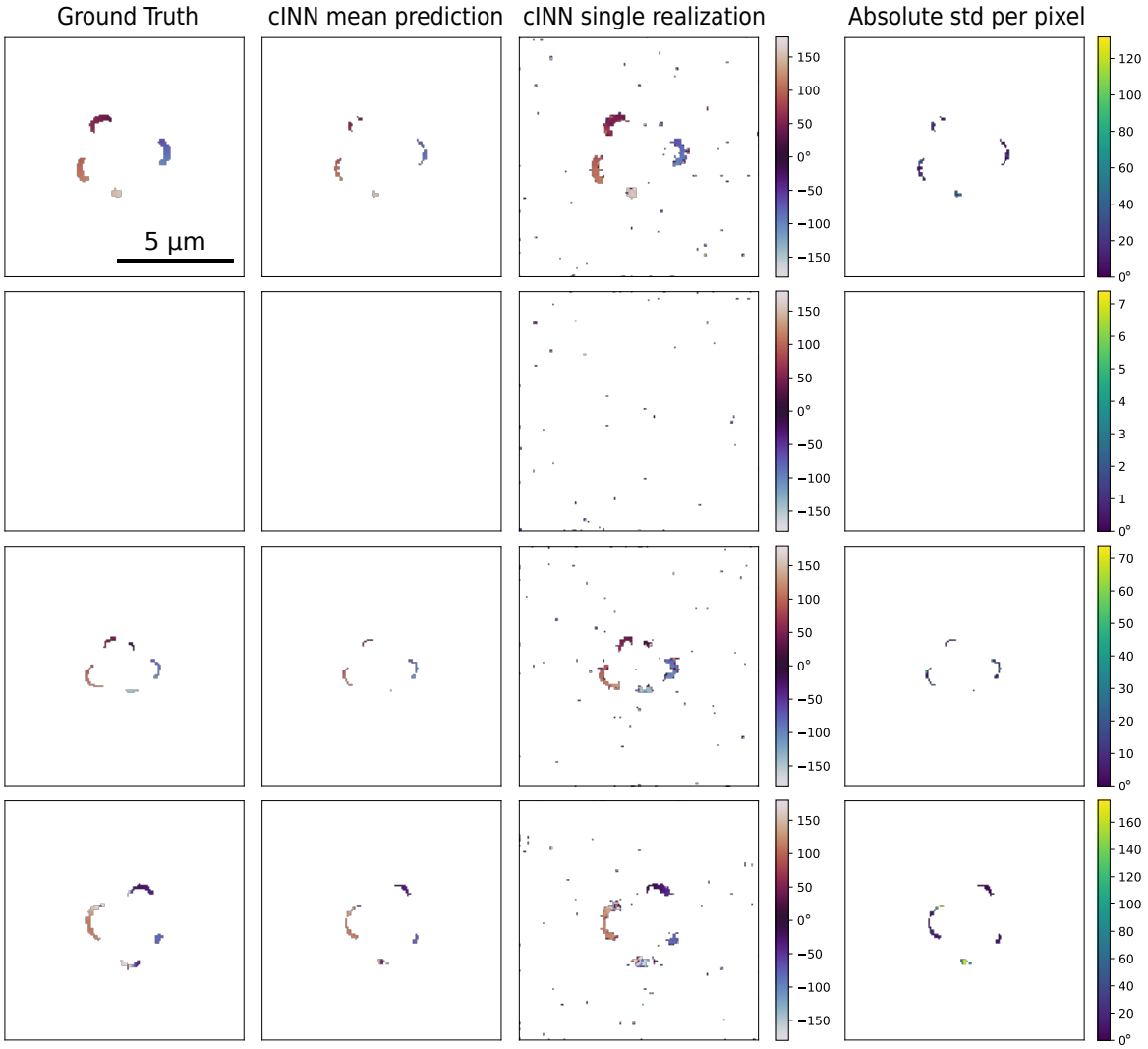

Figure C.3: cINN-ML-TFM magnitudes reconstruction for some additional validation datasets. For each dataset, we show the ground truth traction field, the cINN prediction averaged over multiple traction realizations, a single cINN realization and the relative standard variation in each pixel. These plots are complementary to the ones shown in Fig C.2. Each plot in this figure corresponds to the magnitude plot in the same position in Fig C.2. An orientation of 0 degrees corresponds to a force in leftward direction. Positive angles indicate forces pulling in downward direction. Points with negligible traction magnitude are conventionally assigned a leftward orientation (0°). Some plots displayed in the second row are empty due to small magnitude but have been kept to maintain correlation to Fig C.2.

cINN-ML-TFM reconstruction for some additional thrombocytes

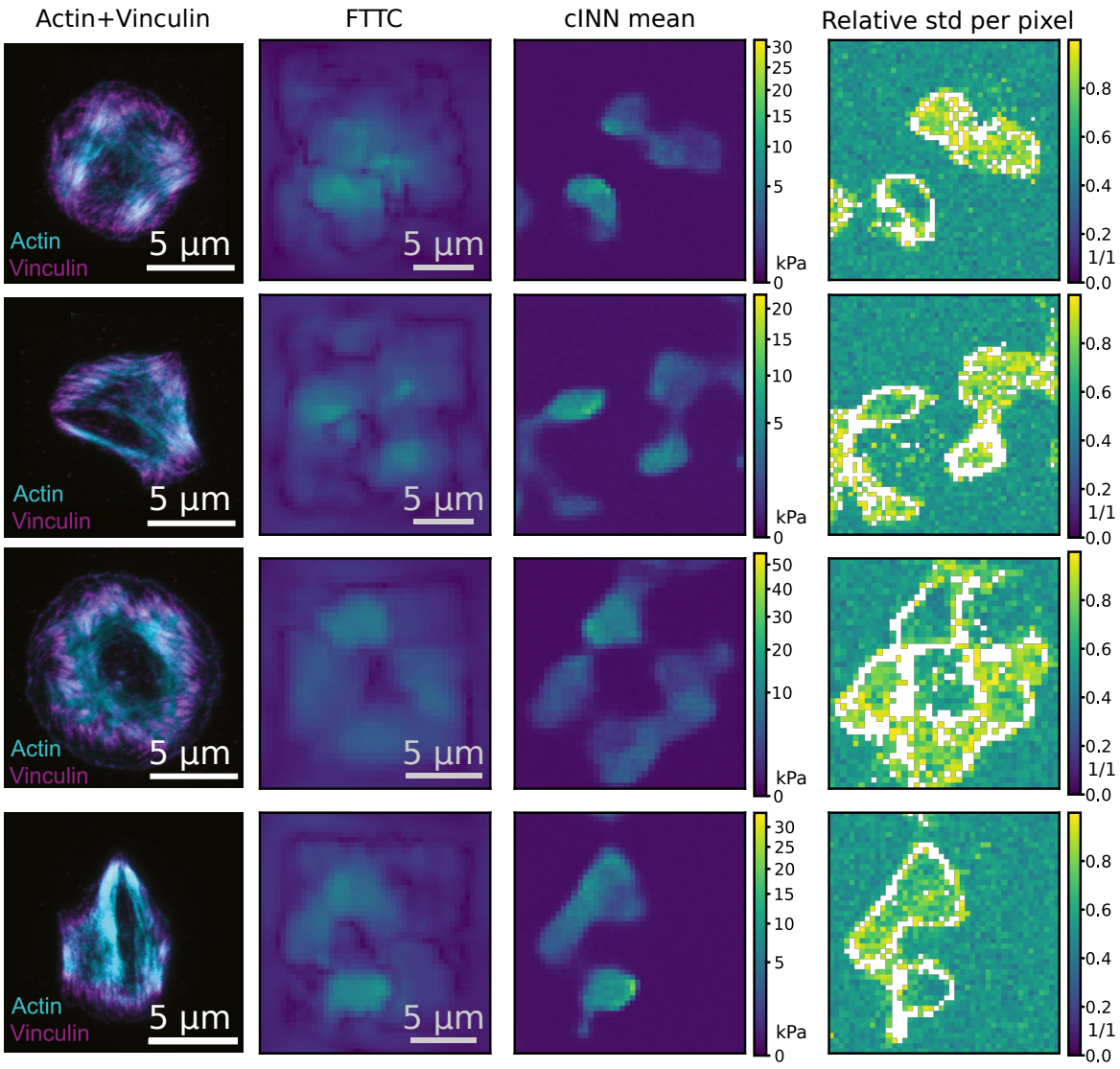

Figure C.4: cINN-ML-TFM reconstruction for some additional thrombocytes. In each row, I present one example. In the first column, I show the actin and vinculin staining, for each cell, where actin is shown in cyan and vinculin is shown in magenta. In the second column I show the force reconstruction as presented by FTTC. In the third column, I present the force reconstruction according to cINN averaged over multiple traction realizations. The rightmost column displays the variation in the relative error of the cINN reconstruction. Notice that all reconstruction plots have been rescaled to fit a common size of the plot. The scalebar shown after the cINN mean plot is also valid for the FTTC plot and the relative error plot left to it.

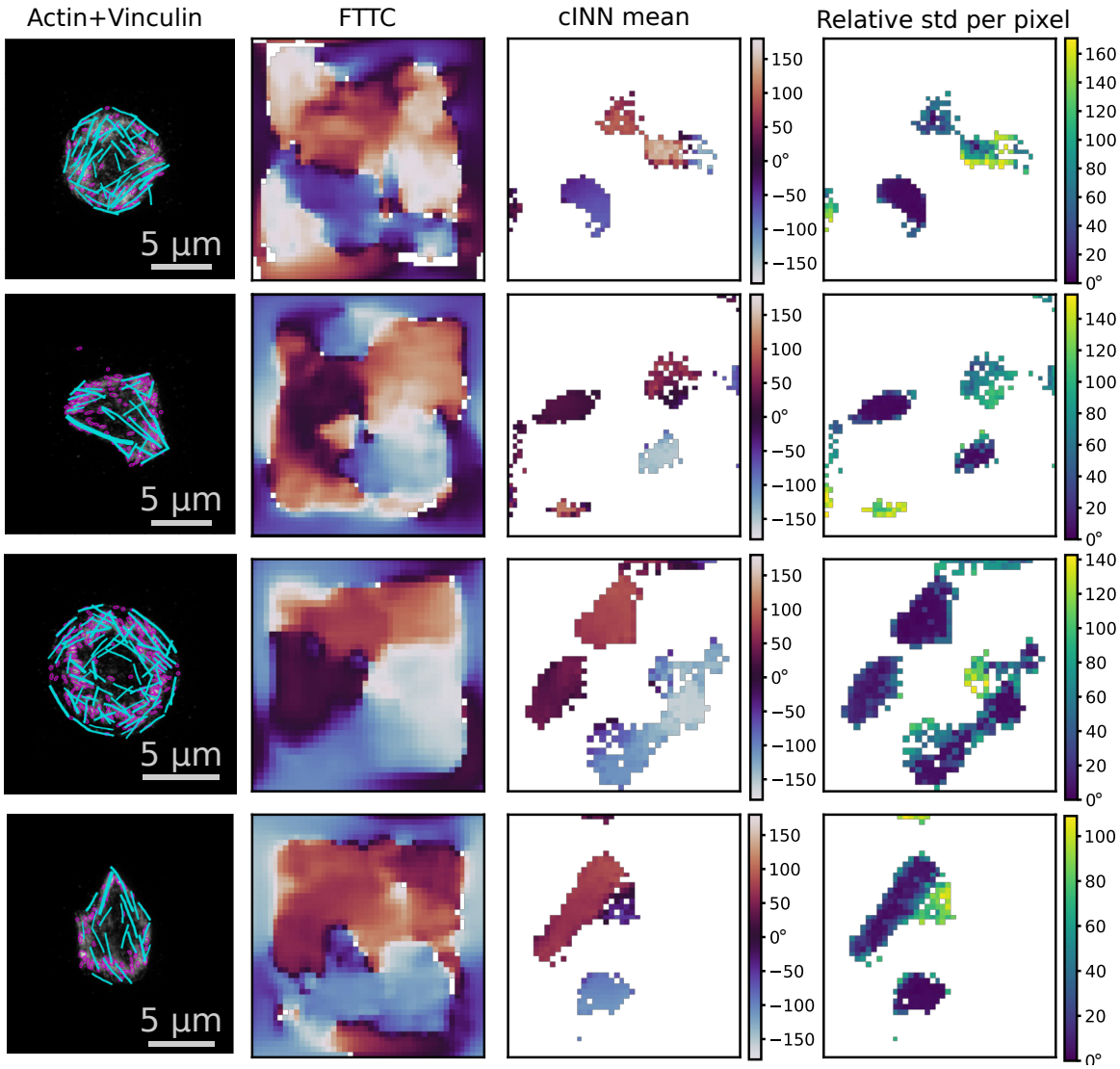

Figure C.5: cINN-ML-TFM angle reconstruction for some additional thrombocytes. In the first collumn, I present the reconstruction of stress fibers and adhesions. Details can be found in the appendix, section B.3. The second collumn shows the FTTC and the third one the cINN reconstraction averaged over multiple realizations. The plots in these two correspond directly to the magnitude presented in Fig C.4 except that they show angle not magnitude. Each plot corresponds to the plot found in the same position in Fig C.4. Positive angles indicate forces pulling in downward direction. Points with negligible traction magnitude are conventionally assigned a leftward orientation (0°). The final collumn shows the standard deviation in the angle reconstruction. Each scalebar is valid for all plots in the same row.

Danksagung

Zuallererst möchte ich mich bei meinem Betreuer Prof. Dr. Ulrich Schwarz, für seine Unterstützung und Betreuung, seine Anregung in Form von Ideen, Fragen und Kritik, aber auch für seine aufmunternde Worte danken. Trotz der Schwierigkeiten einer globalen Pandemie ermöglichte er es mir, an Konferenzen teilzunehmen und durch ihn konnte ich viel über Biophysik und insbesondere auch über wissenschaftliche Kommunikation lernen.

Des Weiteren bedanke ich mich bei Prof. Dr. Tristan Bereau für das Interesse an meiner Arbeit und die Bereitschaft diese Dissertation als zweiter Gutachter zu bewerten.

Ein großer Dank geht auch an die Exzellenzinitiative 3DMM2O für ihre Förderung meiner Arbeit durch zahlreiche Seminare und Events, die einen regen Austausch mit anderen jungen Wissenschaftlern ermöglichten. Insbesondere danke ich auch Stefanie Peer für ihre Rolle als verlässlicher Ansprechpartner. Ich danke auch der Carl-Zeiss-Stiftung für ihre finanzielle Unterstützung.

Ohne die Arbeit meiner Kollaborationspartner hätte diese Dissertation vermutlich deutlich weniger experimentellen Rückhalt. Im Zuge dessen möchte ich insbesondere Anna Zelená, Steven Huth, Christine Selhuber-Unkel, Joel Christian, Ada Cavalcanti-Adam, Sarah Köster, Mishal Khan, Phillip Kollenz, Aldo Leal-Egana, Felix Draxler und Ullrich Koethe für die gute Zusammenarbeit danken.

Ein besonderer Dank geht an alle derzeitigen und ehemaligen Mitglieder der Arbeitsgruppe Schwarz für die allzeit gute Arbeitsatmosphäre. Rabea Link danke ich für die allzeit warmherzige Büroatmosphäre und ihre Rolle als guter Orientierungsanker bei Unsicherheiten zum Promotionsfortschritt oder zu 3DMM2O. Ohne Gonen Golani wäre es im Büro zu Covid-Zeiten wohl sehr einsam geworden und ich hätte wohl viele kulturelle und philosophische Einblicke missen müssen. Oliver Drozdowski gab mir nicht nur in fachlicher Hinsicht viele neue Impulse, ohne ihn wäre ich auch um viele Anekdoten und den Geschmack zahlreicher Biersorten ärmer. Leon Lettermann möchte ich besonders für seine Programmiertipps, seine positive Art und seine Bemühungen um das Gruppenklima danken. Pintu Patra danke ich für einige nützliche Tipps für das weitere Berufsleben. Julia Jäger danke ich für ihre lockere und freundliche Art.

Ich danke auch den Leuten im Philosophenweg: Robert Chojowski, für seinen aufmunternden Optimismus, Dennis Woerthmueller, für Dinge, die gesagt werden müssen, Justin Grewe, für seine hilfsbereite und humoristische Art, Felix Frey, für seine große Professionalität und Hilfsbereitschaft und Santiago Gomez-Melo, für sein lateinamerikanisches Temperament. Falko Ziebert danke ich dafür, die Leitung der Schwarz Gruppe optimal zu komplettieren und in den Gruppensitzungen stets gute Fragen zu stellen.

Auch die von mir betreuten Master- und Laborrotationsstudierenden, haben meine Promotion fachlich und intellektuell bereichert: Timothy Herbst, mit seinem grenzenlosen Enthusiasmus und seinem bedingungslosen Glauben in die Leistungsfähigkeit von künstlicher Intelligenz, Simon Brauburger, dank seiner beneidenswerte Work-Life-Balance und seinem ausgezeichneten Musikgeschmack und Christina Goß, durch viele interessante Gespräche.

Ich danke auch den Sekretärinnen Sonja Bartsch und Melanie Steiert, ohne deren

Hilfe ich so manches bürokratisches Abenteuer nicht hätte bewältigen können.

Natürlich danke ich auch den anderen Gruppenmitgliedern die hier platzbedingt unerwähnt bleiben müssen.

Oliver Drozdowski, Falko Ziebert, Simon Brauburger und Wolfram Blumberg danke ich für das Gegenlesen dieser Dissertation.

Mein ganz persönlicher Dank gilt auch meinen Freunden, besonders Fabian Klein, Alexander Hubig und Paul Rosendahl, die mich während meiner Promotion stets begleitet haben.

Zu guter Letzt danke ich meinen Eltern, Margarete und Wolfram, meinen Geschwistern Celine, Stefan und Alexander und deren Begleitern, Leonie und Tania, die immer an meinen Erfolg geglaubt und mir in dieser Promotion stets geistige Unterstützung geleistet haben.